Single-molecule and super resolution investigations into the onco-immunogenic CCR5 receptor

Patrick Hunter

PhD

University of York

Biology

April 2025

Abstract

Chemokine receptors play a key role in the inflammatory response, facilitating immune cell migration and recruitment via G-protein-mediated signalling triggered by chemokine recognition. Despite the immunogenic role that the CC chemokine receptor CCR5 plays in signal transduction, CCR5 has been implicated in the pathogenesis of a range of diseases, notably acting as a key facilitator of the HIV-1 lifecycle. In addition, the CCR5-CCL5 chemotactic axis has been implicated in the formation of pro-tumorigenic microenvironments. Therapeutic targeting of CCR5 has seen the development of successful HIV-1 therapeutics considered for repurpose in cancer treatment. However, the advent of resistant HIV-1 strains necessitates our continued understanding of CCR5 behaviour and its interaction with binding partners. With several conformational pools being reported and little known of individual receptor characteristics, phenotypic investigations would benefit from advanced biophysical techniques capable of probing the receptor on a super-resolved and single-molecule level.

Structured illumination microscopy was used to visualise the super-resolved spatial distribution of CCR5 in adherent cells, revealing non-randomly distributed CCR5-enriched puncta across the membrane. Investigations employing a novel cell-line and imaging technique, tailored to the single-molecule investigation of adherent cells, revealed the number of constituent receptors within individual puncta, indicating the presence of dimeric CCR5 sub-units.

Extension of these techniques to the study of CCL5, alongside the HIV-1 therapeutic Maraviroc and alternative prospective therapeutics, allowed the visualisation of CCL5 cell-association and ligand-induced effects on CCR5 presentation. Thereby affording insights into CCL5-induced internalisation and the interference of CCR5-targetting therapeutics on this process. These investigations provided evidence suggesting the CCL5-induced reorganisation of CCR5 assemblies coinciding with internalisation and the non-interference of Maraviroc on redistribution despite its demonstrable antagonistic effect. Finally, this thesis presents findings from the attempted development of alternative CCR5-expressing cell lines tailored to assays of increased complexity and biological relevance.

Table of contents

Table of Figures

Acknowledgements

Firstly, I would like to thank my supervisors Mark Leake, Nathalie Signoret and Mike Shaw for allowing me the opportunity to pursue this research and for their constant support and encouragement along the way. Receiving guidance and insight from a truly interdisciplinary group of researchers has afforded me a unique outlook on the interplay of the biological and physical sciences that I will carry with me for the rest of my life. Mike, your passion for microscopy, and its many challenges, is truly contagious and I thank you for the keen insight that you have brought to this project. Nathalie, you have always made time to help me be the best researcher that I could be, thank you for having my back through this journey and for coaching me in the arts of biological research. Mark, you have been a fount of encouragement and sound advice, offering perspective in the face of difficult decisions. I would like to thank you for your unwavering support throughout this journey and your nurturing of my passion for the teaching of biophysics.

I would also like to thank my thesis advisory panel chair Gareth Evans for his support and excellent advice throughout my PhD. Thank you to Monica Bandeira for her guidance in difficult times. Thank you to Grant Calder for training me in the use of confocal microscopy and to the rest of the Imaging and Cytometry team of the technology facility for their guidance and support. Thank you to Mike Shaw, Camilla Dondi, Junqing Jiang and other members of the Biometrology group at NPL for training in the use of SIM. Thank you to Zoe Richmond Mynett for easing my first steps into the world of PhD research and for your training in cell-culture, immunolabelling and flow cytometry. Thanks, must also go to Afzaal Tufail for always offering to lend a hand, always being a good friend and always remembering where everything is stored. Thank you to Amanda noble and all other members, past and present, of the Signoret group.

Additionally, I would like to thank Alex Payne-Dwyer for being my mentor in single-molecule imaging and data analysis. It has been a pleasure to know you these years, thank you for your training, advice and support. Thanks, must also go to Jamieson Howard, Sébastien Guilbaud, Aisha Syeda and all other members, past and present, of the Physics of Life group for their support and their contribution to an amazing sense of community.

I thank all of my family and friends for their support in this journey. Thank you to my best friend William for all of our adventures along the way and thank you to his family for providing food and shelter during my visits to NPL. Thank you to all of my many siblings for each offering their love and unique perspectives in difficult times. Thank you to my parents for creating such a strong network of support and for always being there for me. Thank you to my closest sibling Felicity, you have been by my side from the beginning, taking each step

in unison. We have each other to blame for our future successes and failures and I wouldn't have it any other way. Finally, thank you to Fiona for always believing in me, even when I did not believe in myself.

Author's Declaration

I declare that this thesis is a presentation of original work. All work presented here was carried out by Patrick Hunter, with the exception of the following:

The interpretation and analysis of data shown in Figures: 3-4, 4-10 and 4-11 were performed in collaboration with Dr Alex Payne-Dwyer. The data shown in Figures: 4-3 and 4-4 was collected and analysed by Dr Nathalie Signoret.

A portion of this work was presented for publication[1], namely data shown in Figures: 3-1, 3-2, 3-3, 3-4, 4-1, 4-3, 4-3, 4-5, 4-7, 4-9, 4-10 and 4-11.

This work has not previously been presented for an award at this, or any other, University. All sources are acknowledged as References.

1. Introduction

1.1. Background immunology

1.1.1. The immune system

Living organisms are capable of surviving in an environment that contains a threat of exposure to a wide range of pathogens that can cause harm. This survival is dependent on a given organism's ability to defend against constant exposure to pathogens. This defence exists within all animals in its most primitive form, however complex vertebrates exhibit a more advanced system of immunity. This complex immune system can be described as a network of cells, chemicals and processes, which orchestrate the protection of the body against foreign substances, such as toxins, microbes and cancerous cells. The mammalian immune system is a multilayered system comprising three main defence mechanisms. The first line of defence consists of both physical and chemical barriers such as the skin, mucosal membranes and stomach acids blocking the entry of pathogens into the body. Beyond these preventative barriers, the body is thought to exhibit two further lines of defence, the innate and adaptive immune responses[2,3].

1.1.2. The innate immune response

The distinction between the early stage innate response and its later stage adaptive response can be characterised by the difference in their ability to recognise antigens and the timeline over which they perform their functions. The innate immune response comprises non-specific (antigen-independent) processes that serve to provide rapid defence against any pathogens. Although this system can respond immediately to threat, it lacks any immunological ‘memory’ and is unable to execute a learning process that may aid future defence against a given pathogen should it be encountered again. The cells involved in the innate immune system comprise tissue resident cells such as macrophages and dendritic cells, as well as circulating cells such as monocytes and neutrophils. Cells of the innate immune system use phagocytosis to engulf and destroy pathogens using stored digestive enzymes and reactive oxygen species produced within the cell[4,5]. These cells can recognise pathogens through cell receptors known as pattern-recognition receptors (PRRs) which can interact with pathogen-associated molecular patterns (PAMPs), a series of molecular structures common to a set of pathogens, such as bacterial cell wall components[6]. Innate immunity forms the basis of the inflammatory response in which phagocytic cells are recruited rapidly to a site of infection. This process is dependent on the ability of non-

lymphoid cells such as macrophages to recognise pathogens and in response secrete small proteins known as chemokines that serve to direct the migration of circulating phagocytes to the site of infection. The phagocytic nature of the innate immune response not only provides the clearance of pathogens, dead cells and antibody complexes within the body, it also serves to activate the adaptive immune response through the facilitation of antigen-presenting cell (APC) activation and mobilisation, whereby phagocytic macrophages and dendritic cells, upon activation, are able to inform cells of the adaptive immune response[2].

1.1.3. The adaptive immune response

Despite the efficacy of the innate immunity to carry out a rapid response to pathogens, complexity within the life cycle of many pathogens necessitates a more sophisticated response that displays specificity to a wider range of pathogenic markers and an immunological 'memory' that aids in the response to repeated exposure to the same pathogen. Many pathogens display a high mutation rate that allow evasion from the limited range of PRRs expressed by cells of the innate immune response. Further, intracellular replication of certain pathogens limits the utility of PRR-mediated detection[7]. Heightened response to pathogens is provided by the adaptive immune response, with the principal cells of this response being a class of white blood cells produce in the bone marrow known as lymphocytes, including T-cells activated by APCs and B cells which, upon activation, differentiate into plasma cells to facilitate the production of antibodies[8].

Antibodies constitute a set of proteins which display an exceptional level of diversity, with each member possessing a distinctive binding site for a complementary antigen. Individual B-cells express copies of a unique antibody in the form of a cell surface B-cell receptor (BCR) with the innate ability to recognise a single antigenic molecule[9]. In the event of stimulation of a given B-cell by its complementary antigen, differentiation and division of the cell into plasma cells and memory B cells occurs. Activated plasma cells can return to the bone marrow to produce large amounts of the corresponding antibody into the bloodstream, these circulating antibodies can coat the pathogen, preventing their movement and subject the pathogen to the complement system which in turn attracts phagocytic cells. Unlike plasma cells, which undergo apoptosis upon elimination of the inciting pathogen, memory B cells survive long after infection and can produce a rapid antibody response upon re-exposure to the pathogen[10].

Although providing a highly specific and long-lived response to a wide range of pathogens, the antibody-mediated immune response lacks the ability to effectively manage intracellularly

replicating pathogens such as viruses due to the inability of large antibody proteins to cross the plasma membrane[3]. In such cases, the adaptive immune response relies on the cell-mediated immune response characterised by the interaction of T-cells and APCs. T-cells express antigen-binding receptors on their surface, known as the T-cell receptor (TCR). T-cell antigen recognition is facilitated by APCs major histocompatibility complex (MHC) molecules. These complexes exist in two distinct classes, the first of which Class I MHC are expressed on all nucleated cells and serve to present endogenous peptides either from self or from internal pathogens. Class II MHC molecules, however, are expressed on the surface of APCs and serve to present exogenous antigen fragments often associated with pathogens taken up by phagocytosis[8]. TCR activation by an antigen loaded MHC complex and formation of an immunological synapse[11,12] leads to T-cell activation and/or differentiation to perform a range of tasks. $CD8^+$ T-cells (cytotoxic) recognise MHC I complexes, killing infected and cancerous cells, while $CD4^+$ T cells perform effector functions (T-helper or Th cells), maximising the immune response through the recruitment and direction of a range of other immune cells via the release of cytokines. Both $CD8^+$ and $CD4^+$ T cells can modulate the host response to prevent overzealous inflammation, such as that seen in autoimmune disorders, via a subset of T regulatory cells (Tregs)[13]. Adaptive immune cells can differentiate into memory cells to facilitate the response to repeated infection[2,3,8].

1.1.4. Signalling in immunity

Both the innate and adaptive immune responses rely on the spatiotemporal control of immune cells both within the lymphoid organs, such as the bone marrow and thymus, as well as in the peripheral tissues. Communication between immune cells is generally controlled through their interaction with inflammatory mediators. These constitute a wide range of molecules such as small proteins, lipids and peptides that induce and regulate immune cell response, migration, positioning and cell-cell interactions. The primary intercellular messengers within the immune response are a wide range of small proteins known as cytokines. Produced by all nucleated cells, cytokines facilitate the orchestration of immune cells into an effective immune response through their interaction with cytokine-specific receptors on cell surfaces. The migration of immune cells within the body is controlled mainly by a subset of cytokines known as chemokines (chemotactic cytokines). The release of chemokines can be induced at the site of infection during an active immune response to promote the recruitment of immune cells to the site. Further, chemokines play a homeostatic role in the migration of cells during tissue development, lymphocyte trafficking and immune surveillance. Chemokines are distinguished from other cytokines by the presence of conserved cysteine residue motifs that form disulfide bonds in the protein[14]. In general, these

soluble extracellular cellular proteins interact with immune cells via a chemotactic branch of the family of transmembrane proteins known as G-protein coupled receptors (GPCRs) which, upon activation, can induce a pro migratory response via intracellular signalling cascades[15]. However, a second group of chemokine receptors known as atypical chemokine receptors also play a role in the downregulation of the inflammatory response through chemokine scavenging in a G-protein independent manner[16].

1.2. GPCRs and chemokine receptors

1.2.1. G-protein coupled receptors

GPCRs are proteins embedded in the membrane of eukaryotic cells that serve to transduce chemical signals into the cell from the surrounding extracellular environment. This family of proteins forms the largest group of human membrane proteins with roughly 800 members being described[17]. Common features of this family of proteins include a 7-transmembrane structure that facilitates the transduction of signals, originating from external stimuli, through the plasma membrane, thereby allowing a subsequent intracellular signalling cascade to occur. Signal transduction depends on the ability of the transmembrane structure to undergo a major conformational reorganisation upon ligand binding. Through the rearrangement of the transmembrane helices, namely the 6th transmembrane helix (TM6), ligand induced reorganisation facilitates the exposure of an intracellular binding pocket favouring the membrane-resident G proteins that lend this family of receptors its name. Through this mechanism, this family of proteins can recognise a plethora of molecules ranging from chemokines to small hormones[17–20].

1.2.2. G protein activation

Prior to GPCR mediated activation, G-proteins exist at steady state as a heterotrimer consisting of three sub-units, Gα, Gβ and Gγ. The formation of this heterotrimer requires the binding of energy transfer protein guanosine diphosphate (GDP) to the sub-unit Gα which allows this complex to bind with a dimer formed between Gβ and Gγ sub-units. Inactive Gαβγ heterotrimers reside on the intracellular side of the plasma membrane, anchored by the Gγ sub-unit via a fatty acid chain inserted in the membrane and may or may not be pre-coupled with a GPCR. Upon ligand-induced activation of the GPCR, the conformational changes within the GPCR facilitate binding with Gαβγ, instigating a loss of GDP on the Gα sub-unit. Due to the high concentration of guanosine triphosphate (GTP) found within cells, binding of GTP to the now nucleotide-free Gαβγ occurs rapidly. GTP binding facilitates a

conformational change to the Gα, which in turn results in the dissociation of the GTP-bound Gα sub-unit and the Gβγ dimer. These two complexes represent the active forms of the G-protein sub-units, with each capable of enacting distinct signalling cascades. GTP-bound Gα sub-units target effector enzymes such as adenylyl cyclases and phospholipase C, whereas Gβγ sub-units can additionally serve to activate and regulate ion channels and kinases[18,21–23].

1.2.3. G protein and GPCR regulation

The ability of Gα to act as a GTPase allows activated Gα sub-units to eventually hydrolyse their bound GTP to GDP. Upon hydrolysis, the now inactive Gα can bind to a Gβγ dimer to reform the inactive Gαβγ heterotrimer. This activation cycle can be regulated through the presence of GTPase-activating proteins (GAPs) which serve to increase GTP hydrolysis and thereby moderate GPCR related signalling[24]. Repeated activation of a GPCR by ligand stimulation results in further activation of G proteins, however after a period of sustained activation, GPCRs eventually undergo phosphorylation by receptor kinases, followed by inactivation via the binding of the GPCR adaptor protein β-arrestin. As well as halting further interaction of the GPCR with G proteins, β-arrestin serves to facilitate the navigation of these GPCRs to sites of internalisation, which for a large number of receptors are clathrin-coated pits mediating endocytosis leading to later recycling or degradation of these GPCRs[18,25,26].

1.2.4. GPCR ligands

GPCR-facilitated signal transduction across the plasma membrane can access many distinct downstream signalling pathways via G proteins, however the specificity of this response is fundamentally controlled by the individual ligand able to activate a GPCR, also known as an agonist[18]. In addition to agonistic ligand activators of GPCRs, antagonistic ligands can interfere or regulate the signalling activity of GPCRs. Antagonists can prevent the binding of agonistic ligands either through the occupation of the GPCR binding site (inverse agonists) or by affecting conformational changes within the GPCR through allosteric binding[27,28].

1.2.5. Chemokine receptors

Although sharing the same transmembrane structure and G-protein dependent signalling activity, the GPCR family of receptors displays a large range of diversity associated with a wide spectrum of utility within the body. One subset of the GPCR family, for which this study focuses, is that of the aforementioned chemokine receptors. The primary function of these receptors is to facilitate the recruitment and migration of immune cells. This is achieved via the recognition of small protein chemoattractants known as chemokines, which act as

agonist ligands for G-protein activation. Chemokine receptors are classified into four distinct groups according to the class of chemokines with which they interact. Chemokines themselves are distinguished from within the wider class of cytokines by the presence of conserved N-terminal cysteine residue motifs with most displaying four invariant cysteine residues, with the arrangement of the first two residues dictating the subfamily to which the chemokine belongs, CXC, CC, XC and CX3C. At least 19 conventional G protein coupled chemokine receptors exist within the four classes, with seven CXC, ten CC, one XC and one CX3C associated receptors being so far identified[14,29–31]. The pro-migratory role of chemokine receptors within the innate inflammatory response is vital and relies on the release of chemokines by both immune and non-immune cells. Upon recognition of PAMPs, patrolling immune cells, such as monocytes, secrete chemokines[32]. The release of chemokines at the site of infection establishes a chemokine gradient capable of guiding immune cell movement. The activation of chemokine receptors by secreted chemokines induces polarisation of the cell and the subsequent alignment of chemokine receptors towards the cell leading edge, allowing directed cell migration along the chemokine gradient to the site of chemokine production, thereby resulting in the recruitment of immune cells to the site of infection[32].

The role of chemokine receptors within the immune response is not limited to the innate response however, antigen presenting dendritic cells can be directed to lymphoid tissues via chemokine receptors CXC chemokine receptor 4 (CXCR4) and CC chemokine receptor 7 (CCR7) upon which they can attract naive T-cells as part of the adaptive immune response[33]. T-cells are attracted to these antigen presenting cells via the interaction between the CC chemokine receptor 5 (CCR5) and its agonist ligands chemokine (CC motif) ligand 3 (CCL3), chemokine (CC motif) ligand 4 (CCL4) and chemokine (CC motif) ligand 5 (CCL5/RANTES), upon which, in the case of naive CD4+ T-cells, they can be activated to form Th cells.

In addition to mediating the activation of immune cells, chemokines are also known to play a large homeostatic role in both immune and non-immune cells. For example, the proliferation of progenitor cells and the maturation of innate immune cells is in part governed by chemokine receptor signalling[34]. Further, the maturation and migration of adaptive immune cells to secondary lymphoid tissues is governed by chemokine signalling, such as the migration of T-cells to the thymus via CCR7 and CC chemokine receptor 9 (CCR9) signalling and subsequent migration to lymph nodes[35].

1.3. Chemokine receptor CCR5

1.3.1. CCR5 structure

This thesis focuses on the chemokine receptor CCR5, which is expressed primarily on leukocytes from the human immune system, facilitating cellular migration and activation[36]. The 2D and 3D structure of CCR5 is demonstrated in **Figure 1-1 a,b**. As with other CC chemokine receptors, such as CC chemokine receptor 2 (CCR2) with which CCR5 shares a 71% sequence identity, CCR5 binds with chemokines that exhibit two adjacent cysteines at their N termini[37,38]. Chemokine receptors in general undergo post-translational modifications that impact their tertiary structure and subsequently their binding ability. During post-translational modification, CCR5 undergoes palmitoylation of specific cysteine residues on its C-terminal tail (on residues 321, 323 and 324) which is theorised to reduce the tail flexibility via the formation of a fourth intracellular loop[39,40]. The palmitoylation of these three residues has been found to greatly affect the function of CCR5 in both its trafficking to and from the plasma membrane and its ability to mediate signalling[39]. As with other chemokine receptors, the recognition of chemokines by CCR5 happens extracellularly and is thought to be a two-step process involving interaction of the N terminus, extracellular loops and transmembrane domains. The Initial chemokine recognition site is thought to be formed between the chemokine core and the N terminus and 2nd extracellular loop (ECL2) of CCR5[41]. Upon core binding, the chemokine N-terminus can bind the secondary recognition site within the transmembrane helix bundle[42–44]. The stability of the receptor into a conformation conducive with chemokine binding is thought to be influenced by the presence of a disulfide bridge formed between cysteine residues on the N-terminus and the 3rd extracellular loop (ECL3)[37]. Alternative binding partners such as small molecule antagonists may access CCR5 independently of the receptor N terminus through interaction with the major binding pocket, consisting of 3rd, 4th, and 6th transmembrane helices (TM3, TM4, TM5 and TM6), and the minor binding pocket, consisting of 1st, 2nd, 3rd and 7th transmembrane helices (TM1, TM2, TM3 and TM7), thereby allowing allosteric antagonism[45]. Like CCR2, CCR5 is a promiscuous receptor that can bind with multiple different chemokines. In contrast, alternate chemokine receptors, such as CXCR4, display a higher specificity and bind a single primary chemokine. Differences in promiscuity may be partially explained using structural comparisons of the receptors, with previous studies demonstrating a shift in the position of both the N-terminus and ECL2 that result in partial coverage of the binding pocket in CXCR4 when compared with CCR5[46].

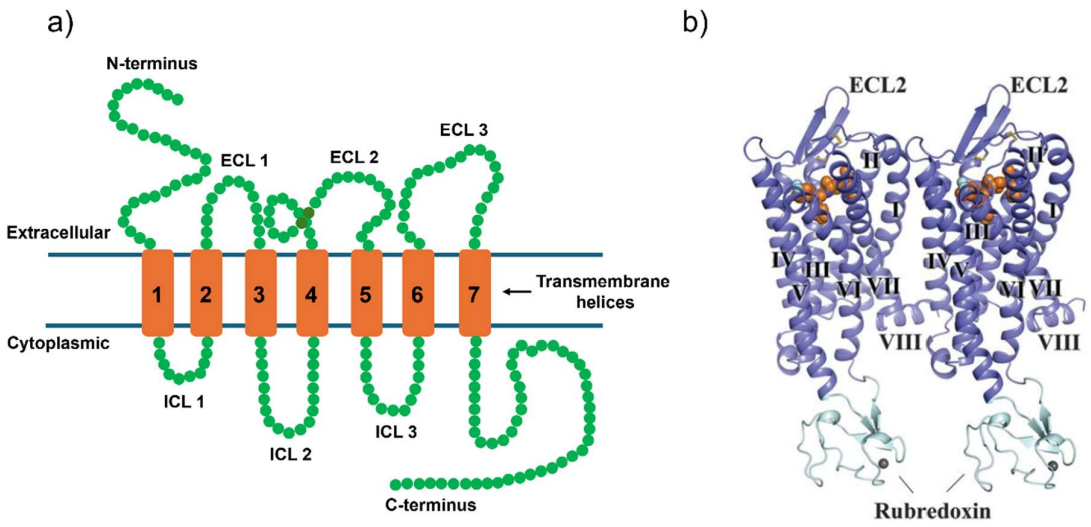

Figure 1-1: Demonstration of the 2D and 3D structure of CCR5. a) Illustration of the 2D structure of CCR5, highlighting the 7 transmembrane helices, N and C termini and all extracellular loops (ECL) and intracellular loops (ICL). In particular, the extracellular N terminus acts as the primary binding site for the fluorescent tags employed in this study. Further, the initial chemokine recognition site is formed between the N-terminus and 2nd extracellular loop (ECL2). This Illustration is based on diagrams and data from previous studies[47,48]. b) 3D structure of two CCR5-rubredoxin fusions, each bound to the small-molecule reversible CCR5 antagonist Maraviroc, determined using X-ray diffraction. CCR5 is coloured blue, rubredoxin is coloured light cyan, Maraviroc is represented as orange spheres, zinc ions are represented as grey spheres and disulfide bonds are represented as yellow sticks. Transmembrane helices are denoted using numerals I-VII (VIII denotes a short α helix observed in the C-terminus of the receptor). The presence of both rubredoxin and Maraviroc aid in the crystallographic determination of receptor structure, with rubredoxin facilitating crystalisation and Maraviroc stabalising receptor conformation. The presence of two CCR5 molecules in this example is the result of crystal packing, with two receptors being observed per asymmetric unit. This 3D structure was reprinted from previous studies[46].

1.3.2. CCR5 signalling

Like other chemokine receptors, CCR5 serves to transduce signals across the plasma membrane via extracellular agonist binding inducing an intracellular response. As a GPCR, CCR5 can carry out G-protein-mediated intracellular signalling in which CCR5-activated G-protein subunits can trigger signalling cascades such as those involving adenylyl cyclase and phospholipase. These mechanisms have far reaching physiological scope, with the ability to induce the formation of intracellular signalling mediators such as inositol-1,4,5-trisphosphate (IP3) and the mobilisation of intracellular calcium. In the case of T-cell function, for which the involvement of CCR5-mediated signalling is well known, CCR5 signalling mediates the activation of the lipid kinase phosphatidylinositol 3-kinase (PI3K) and

protein tyrosine kinases PTK2 and PTK2b all of which are thought to be essential for cell migration[37,49–52]. In addition, CCR5-mediated activation of Ras homolog family member A (RhoA) GTPases facilitates cytoskeletal rearrangement vital for cell polarisation[37,53] and CCR5-mediated activation of members of the mitogen-activated protein kinase (MAPKs) family underpins aspects of T-cell proliferation[40,54].

However, the ability of chemokines to transduce signals across the plasma membrane is not limited to G-protein dependent pathways. In the case of CCR5, G-protein independent signalling can take place in conjunction with β-arrestin acting as a scaffolding protein. Evidence suggests that CCL4-mediated migration of CCR5 expressing cells is enacted through G-protein independent activation of extracellular signal-regulated kinases (ERK 1/2) and a further kinase complex consisting of the lipid kinase P13K and protein kinases Lyn and PTK2b via a β-arrestin scaffold[50].

1.3.3. CCR5 regulation and trafficking

In the event of prolonged activation, CCR5 undergoes internalisation via a process known as downmodulation. In the case of chemokine stimulation, CCR5 typically undergoes internalisation via homologous downmodulation whereby residues on the C-terminal CCR5 tail are phosphorylated by a member of the G-protein receptor kinase (GRK) family, preventing subsequent G-protein binding. These phosphorylated sites facilitate the binding of the β-arrestin scaffolds that, in turn, allow interaction of CCR5 with the adaptor protein complex AP2 that marks the receptor for internalisation[55,56].

The negative regulation of CCR5 can also be carried out by signals not related to the original agonist via heterologous downmodulation involving protein kinase C (PKC), a secondary-messenger-activated protein kinase that is activated downstream of the receptor. Agonist-independent downmodulation is often the result of negative crosstalk between receptors, an example in the case of CCR5 being its negative cross-talk with G-protein coupled chemokine receptor CXCR4[57]. Similarly to GRK-related downmodulation, heterologous downmodulation sees the phosphorylation of CCR5 thereby, inciting β-arrestin binding and subsequent internalisation. Both of these phosphorylation mechanisms can be considered as rapid, however the half-life of PKC-mediated phosphorylation is considered to be an order of magnitude lower than that of GRK mediated phosphorylation[58].

The second and minute time scales over which these mechanisms occur are vital to providing a rapid cellular response to temporally changing signalling environments.

However, long term positive and negative regulation of receptor expression, can be exerted through modification of CCR5 mRNAs expression as well as epigenetic changes such as histone acetylation and methylation[59].

The mechanism by which CCR5 undergoes β-arrestin mediated internalisation leads to resensitisation with return of the active receptors to the plasma membrane in a process known as recycling. Endocytosis of CCR5 is generally facilitated by the coat protein clathrin[56,60–62], with CCR5-bound β-arrestin interacting with the clathrin adaptor molecule AP2. This adaptor allows for the localisation of CCR5 into clathrin rich areas of the plasma membrane known as clathrin coated pits which, upon interaction with the GTPase dynamin, can be cleaved to form vesicles that act to transport the internalised receptors to early endosomes for sorting. Clathrin-independent transportation of CCR5 to early endosomes may also be carried out via the membrane protein caveolin, whereby CCR5 is instead transported to caveolin-rich membrane invaginations known as caveolae[56].

Upon delivery to the early endosomes, CCR5 destined for recycling is transported to the endocytic recycling compartment and is subsequently returned to the plasma membrane via recycling endosomes[63]. A major determinant of the recycling pathway of CCR5 is the existence of a PDZ ligand motif on the C-terminal tail which is thought to allow for the interaction of internalised CCR5 with PDZ domain-expressing sorting machinery. Further, upon sorting of the receptor into the recycling pathway, the PDZ motif of internalised CCR5 allows for interaction with receptor recycling proteins, namely the ezrin-radixin-moesin (ERM)-binding phosphoprotein 50 (EBP50), also known as Na+/H+ Exchanger Regulatory Factor (NHERF-1)[64,65]. Unlike many ligand-receptor interactions, where rapid ligand dissociation occurs as a result of the low pH environment of the endosome, CCR5 ligand dissociation occurs in a slow pH-independent manner that allows for repeated recycling events to occur without dissociation[63,66]. Further, the identity of the instigating CCR5 agonist has been shown to affect the resultant receptor fate, with CCR5 demonstrating an agonist-specific distribution along its recycling pathway. For example, CCR5 activation by the CC chemokine ligand 5 (CCL5/RANTES) results in accumulation of CCR5 in the recycling endosomes and subsequent movement to the plasma membrane[63]. However, CCR5 activation by N-terminally modified analogues of CCL5 such as PSC-RANTES, AOP-RANTES and MET-RANTES result in spatiotemporal alterations in CCR5 behaviour along the recycling pathway[63,67,68].

1.3.4. CCR5 presentation

The investigation of CCR5 in living cells has revealed that CCR5 has the potential to adopt a variety of conformational sub-states that affect its function and membrane presentation. Considering the varying structural domains of CCR5 and their relative roles in CCR5 ligation, activation and internalisation, it is clear that the orientation and subsequent availability of these sites are vital to receptor behaviour.

Interrogation of CCR5 conformational states has been studied through the technique of immunolabeling, whereby fluorescent antibodies specific to distinct receptor domains are used to provide a readout of the intensity, and sometimes location, of the respective binding site availability. These studies utilise extracellular binding sites such as the N-terminal region and the extracellular loops. Previous studies in the Signoret lab sought to elucidate information on the distribution of conformational states by employing a variety of CCR5 specific fluorescent antibodies in the study of both human immune cells and model cell lines. This study provided evidence that two distinct antibodies (MC5 and CTC5) that both recognise an overlapping region of the receptor N-terminus demonstrated differential binding. Further, unlike in the case of MC5, CTC5-bound receptors displayed resistance to downmodulation when exposed to CCL5, suggesting the existence of two independent pools of receptors that exhibit a disparity in their functionality[69].

Additional immunofluorescent studies interrogating the spatial distribution of CCR5 on the plasma membrane similarly revealed a disparity in presentation, dependent on the ligand employed. Investigations employing antibodies specific to ECL2 (2D7 and 45531) revealed distinct ligand-specific presentation of CCR5, with 2D7-bound CCR5 displaying a uniform distribution across the membrane and 45531-bound CCR5 residing in a pattern of puncta across the membrane. Further, investigations employing antibodies specific to the N-terminus and a tyrosine-sulphated version of the N-terminus (MC5 and PA11, respectively) revealed further ligand-dependent variance of receptor presentation into uniform or punctuated distributions, with MC5 binding to uniformly distributed CCR5 and PA11 binding to CCR5 distributed into puncta. These studies also provided evidence that varying conformational pools of receptors may access their available endocytic pathways (clathrin or caveolin mediated) in a conformation specific manner[70].

In addition to variance in the conformational states of individual receptors and the associated changes in function and spatial arrangement, a full understanding of CCR5 presentation requires the consideration of the ability of receptors to oligomerise and the potential effects

this may have on receptor function. GPCRs are known to operate not only as individual monomeric units but also as oligomers[71,72]. Further, chemokine receptors themselves have been shown to operate in both a homo-oligomeric fashion as well as forming hetero-oligomers with distinct receptors[73]. Investigations into the oligomeric state of CCR5 have provided conflicting insights into the ability of CCR5 to form oligomers in the steady state and upon exposure to agonists. Further, the role of oligomerisation in CCR5 functionality and the factors by which this oligomerisation is influenced remain a topic of debate.

Early studies into the oligomeric state of CCR5 suggested that CCR5 can undergo dynamic agonist-modulated dimerisation both in the form of homodimers and in the form of heterodimers with the chemokine receptor CCR2[74–77]. However, more recent studies suggest that CCR5 can exist in a constitutive dimeric state on the plasma membrane without the need for chemokine binding or receptor activation. Our current understanding of CCR5 oligomerisation is backed up by a body of investigations that employ a range of traditional biological and biophysical techniques, each with their respective advantages and disadvantages. Classic biological studies have employed immunoprecipitation assays of cross-linked samples, providing evidence of constitutive CCR5 dimers and implicating N-terminal residues as a potential dimerisation interface[78–80]. However, these studies provide a limited breadth of information, with no information gained regarding the spatiotemporal characteristics of the receptors. Further, bulk ensemble techniques such as these provide only an averaged view of the receptor oligomerisation and offer limited information on the distribution of rare species.

In recent years, more advanced techniques have been employed to evidence the existence of constitutive CCR5 dimers within the cell. Studies employing bimolecular fluorescence complementation (BiFC), which sees the use of two fluorescent sub-units that only emit upon association, support the existence of constitutive dimers[65,81]. However, due to the requirement of successful and irreversible sub-unit association, under-estimation of dimerisation events is possible and the ability of transiently interacting receptors to dissociate may be affected, thereby limiting the ability of this method to probe transient association[82,83]. These results do however, in part, agree with studies employing the alternative technique of bioluminescence resonance energy transfer (BRET) which sees the employment of bioluminescent doner and fluorescent acceptor molecules that engage only when in close proximity (<10nm). These studies support the existence of agonist-independent constitutive dimers and larger oligomers and suggest the potential oligomerisation of CCR5 within the endoplasmic reticulum (ER) during CCR5 biosynthesis[84–86]. However, BRET assays similarly suffer from the inherent restrictions of interrogating a

population of homodimers whilst relying on the interaction of two distinct signalling molecules, rendering the accurate quantification of dimer populations impossible. More advanced methods utilising the proximity-dependent transfer of resonance energy to report on oligomerisation have been employed in the form of time resolved Forster resonance energy transfer (FRET) experiments which see the employment of interacting fluorescent molecules that require excitation but often display a heightened brightness, in contrast to older techniques. Although these investigations similarly suggest the presence of CCR5 dimers and larger oligomers[87], this technique too suffers from similar disadvantages to BRET and BiFC and although principles of resonance energy transfer can be employed within advanced microscopy techniques to probe dimers on an individual level, the investigations outlined above rely on a bulk ensemble readout that lacks single molecule precision.

From this large body of investigations, it can be argued that the existence of constitutive homodimers of CCR5 in the steady state is likely. However, the existence of larger oligomers of CCR5 and the role that chemokine binding has on the existence of these varying reported species is still a matter of debate. It is clear however, considering the range of reported CCR5 conformational and spatiotemporal states as well as the complex and often conflicting readouts of receptor oligomerisation, that CCR5 demonstrates a high level of heterogeneity and represents a clear case study for the employment of cutting-edge biophysical techniques capable of super-resolution determination of CCR5 positioning and single-molecule determination of oligomeric state.

1.4. Disease and therapeutics

1.4.1. Role in immunity

The chemokine receptor CCR5 is known to be involved in a range of aspects of the human immune response, with the most notable of these being its regulation of T-cell activation. T cells exhibit the ability to migrate towards antigen presenting cells within the lymph nodes via CCR5-mediated interaction with CCL3 and CCL4 chemoattractants[88,89]. Further, upon interaction of T cells and antigen presenting cells to form a TCR-MHC mediated immunological synapse, high expression of CCR5 localised at the synaptic cleft indicates CCR5-mediated communication between the interacting cells[90]. Although CCR5 expression is a shared feature of leukocytes, increased levels of CCR5 have been associated with several subtypes of T-cells such as Tregs and T-helper 1 (Th1) T-cells that employ CCR5 mediated signalling for migration to sites of infection to carry out their anti-inflammatory and pro-inflammatory functions respectively[91–93].

The involvement of CCR5 and its ligands within immune cell function is not however limited to T-cells but instead to a range of immune functions related to both lymphocytes and myeloid cells. In the case of B-cells, production of CCL5 has a role in T-cell recruitment and is postulated to serve an autocrine function, with CCL5 being found to encourage both cell proliferation and the production of antibodies within B-cells in vitro[94]. Within myeloid cells such as monocytes and neutrophils, CCR5 is responsible for both the development of cells within the bone marrow as well as the migration of cells towards inflammation sites. Differentiation of monocytes into M1 type macrophages is linked with increased levels of CCR5 at the plasma membrane[95] while upregulation of CCR5 in neutrophils upon activation, alongside changes in the expression of other chemokine receptors, is linked with the induction of phagocytic behaviour[96].

The importance of CCR5, as a mediator of immune cell trafficking, is exemplified in its role in disease prevention. The chemotactic axis formed between CCR5 and CCL5 is believed to play an essential role in the response to a range of bacterial, parasitic and viral infections. In the case of bacterial infections such as chlamydia, T-cell migration to sites of infection, such as the genital mucosa in the case of Chlamydia trachomatis infection, is facilitated through CCR5[97]. The response to parasitic infections such as toxoplasmosis similarly relies on CCR5 for myeloid and lymphocyte recruitment to the intestine[98]. Further, a clear example of the involvement of CCR5 in the response to viral infection can be seen in that of influenza, in which early expression of CCR5 and secretion of CCL5 by lung-resident macrophages facilitates the migration of phagocytic cells to the site of infection. Subsequent recruitment of activated lymphocytes to the site of infection is likewise controlled via the CCR5/CCL5 chemotactic axis[99].

1.4.2. CCR5 in pathology

Despite its function in disease prevention, CCR5 involvement has been implicated in the pathogenesis of a large range of diseases, with both the inappropriate chemotactic function of the receptor and the hijacking of normal chemotactic function by foreign pathogens being thought to play a role[100,101].

Due to the importance of CCR5 in chemotaxis, the receptor is considered to play a large role in a range of non-infectious diseases linked with the inflammatory response. Chronic inflammatory disorders including allergies and autoimmune disorders such as rheumatoid arthritis can be characterised by a dysfunctional recruitment of immune cells leading to a

disproportionate immune response. The inappropriate response that underpins these disorders can often be, in part, attributed to mis-regulation of the receptor and the availability of agonists. Further, the inappropriate response of CCR5-mediated immune cells within infectious diseases can likewise lead to elevated pathology and symptoms. In the case of influenza, excessive levels of CCR5-mediated signalling can lead to disproportionate recruitment and activation of immune cells in the lungs that can facilitate permanent damage to the respiratory system[99]. Dysfunctional CCR5-mediated signalling can also play an immunosuppressant role in diseases through inappropriate recruitment of suppressor immune cells, such as in the case of chronic endometriosis where this dysfunction acts to prevent the proper regulation of endometrial tissue and allows disease proliferation[102].

Normal functionality of CCR5 has also been implicated in the pathology of some diseases. A key example of this, and one of the main motivations behind a large portion of CCR5 investigations, is the vital role that CCR5 plays in human immunodeficiency virus (HIV) infection. Through a large body of investigations, CCR5 has been implicated as a key facilitator of the HIV life cycle, acting as an HIV coreceptor and providing entry of HIV into the cell[36,103]. This mechanism is thought to be carried out by the most common type of the virus (HIV-1) through the targeting of CCR5 expressed on CD4+ cells, such as helper T cells and macrophages. HIV-1 is thought to bind with CD4 on the plasma membrane of these cells using the virus-surface envelope glycoprotein gp120. A CD4 binding-induced conformational change in gp120 allows subsequent binding of CCR5 due to the revelation of an otherwise inaccessible binding site. Upon CCR5 binding and formation of trimolecular complexes with CD4 and gp120, further conformational changes activate HIV-1 to trigger fusion between the viral and host cell membrane and thereby allow viral entry into the host cell[104]. Interestingly, studies investigating the varying conformational states reported for the CCR5 receptor suggested that the CCR5-mediated permissibility of HIV-1 may in fact be conformation dependent, with distinct pools of CCR5 molecules displaying a varying capacity to engage with gp120[87].

1.4.3. CCR5 in tumorigenesis

As a key mediator of immune cell trafficking, the importance of the role that CCR5 plays in cancer suppression is evident. However, despite the immunogenic characteristics of the CCR5-CCL5 axis, recent studies have suggested that CCR5-mediated signalling can also play a pro-tumorigenic role[105,106]. Current research indicates that cancer cells possess the ability to manipulate chemokine networks to support tumour progression through the ‘hijacking’ of chemotactic axes, such as that of CCR5 and CCL5, in order to recruit and re-

educate immune cells. This function is thought to play a key role in the formation of a tumour microenvironment (TME), a pro-tumorigenic buffer region that facilitates immune evasion and promotes cancer proliferation[107–112]. The TME is often, in part, composed of recruited Tregs which perform an immunosuppressive function through the release of anti-inflammatory cytokines. These immunosuppressive signals allow for discouragement of cytotoxic T-cell recruitment and the subsequent evasion of immunosurveillance[110]. In addition, release of CCL5 by cells of the TME is postulated to stimulate CCR5-mediated tumour growth, whereby CCR5 is thought to induce various growth pathways and enhance glucose uptake[113–115].

The formation of the immunosuppressant TME has become a well-studied phenomenon in a range of cancers, examples of which include leukaemia, breast cancer, prostate cancer and pancreatic cancer. However, the role of CCR5 in cancer progression is not considered to be confined to TME formation. In a similar manner to the paracrine CCL5 signalling associated with the TME, CCR5-mediated tumour growth is thought to be facilitated through autocrine signalling of CCL5[116]. Further, CCR5-mediated signalling is considered to play a functional role in cancer cell migration, invasion and dissemination through the body, as observed in prostate cancer that sees the promotion of invasion through CCL5-induced rearrangement of the extracellular matrix[117] and in breast cancer where paracrine CCL5 signalling induces cancer cell motility and recruitment to various areas of the body[118,119]. Beyond TME-associated recruitment and facilitation of metastatic migration, the pro-tumorigenic features of CCR5 extend to the promotion of angiogenesis, metabolic adjustments and therapeutic resistance through both autocrine and paracrine CCL5 signalling[106,113,120–122].

Overexpression of CCR5 and CCL5 in the context of cancer can be a result of both oncogenic transformation of cells and the accumulation of CCR5 expressing and CCL5 secreting cells within the TME[123,124]. Endogenous upregulation of CCR5 within cancer cells is evidenced by the detection of CCR5 and CCL5 overexpression within tumours resulting from a wide range of cancers, including but not limited to breast cancer, hodgkin lymphoma and lymphocytic leukaemia[106,116,123–126]. The determination of the CCR5/CCL5 chemotactic axis as the primary chemotactic actor in the progression of cancer, coupled with the poor prognosis of patients exhibiting upregulation of CCR5 has highlighted the CCR5 receptor as a promising target for the development of cancer therapeutics. However, the role of CCR5 in cancer progression is complicated and our understanding of the function of CCR5 in varying tumour types remains incomplete

1.4.4. CCR5 targeted therapeutics

The revenue associated with the development and sale of pharmaceutical therapeutics is estimated at trillions of US dollars globally[127]. However, approximately one-third of all Food and Drug Administration (FDA) approved therapeutics target G-protein coupled receptors[128], with a large portion of these drugs being designed to target chemokine receptors, due to their importance in the human immune response. In the case of CCR5, many of the investigations into CCR5-targeting therapeutics have been aimed at the development of an effective HIV treatment.

Early inspiration for the development of CCR5-targeting HIV therapeutics came from the observation of individuals displaying a simultaneous defect in CCR5 expression and increased resistance to HIV infection. This mutation, known as the CCR5-Delta-32 mutation (Δ32), sees the removal of 32 nucleotides from the CCR5 gene, resulting in a receptor whose structure is lacking in transmembrane domains and displays ineffective G-protein binding characteristics, thereby effectively disabling the receptor function[103]. Individuals displaying the Δ32 mutation can be homozygous individuals that are unable to express functional CCR5, or heterozygous individuals that, despite expressing some CCR5 functionality, see a large reduction in the number of functional receptors. Additionally, the ability of functional CCR5 to form dysfunctional dimers with CCR5Δ32 leads to further suppression of normal CCR5 function relative to wild type individuals.

Although Individuals displaying the Δ32 mutation experience lower risk of infection relative to the wild type[129], the disruption of normal CCR5 function has far reaching effects on downstream immune function and can leave the individual susceptible to a large range of other viruses, parasites and bacteria. This compromise between the desired alteration of CCR5 function and the minimisation of the potential inflammation and immune suppression that stem from these alterations has become the hallmark of CCR5-targeted therapeutic development. It is clear then that the development of safe and effective CCR5-targeted therapeutics requires the understanding of CCR5 conformation and behaviour and any changes that these therapeutics may affect.

The first, and most notable, successful CCR5-targeting HIV therapeutic is the small-molecule reversible CCR5 antagonist Maraviroc (MVC), which was developed by Pfizer and received FDA approval for treatment of patients with CCR5 tropic HIV-1 in 2007[130]. Evidence suggests that the binding site for MVC exists as a deep binding pocket within the transmembrane bundle, independent of the chemokine and gp120 binding sites. Structural

analysis of the CCR5-MVC complex suggests that this binding site is formed between key residues on the transmembrane domains TM1, 2, 3, 5, 6 and 7. Under this regime of allosteric binding, it is expected that MVC induces a conformational change within the receptor that inhibits its function. The inactive CCR5 state that MVC effectively stabilises is thought to be characterised by several structural changes, such as key tryptophan and tyrosine residues that appear in conformations distinct from those of functional CCR5 and close packing of helices within the transmembrane bundle allowing subsequent stabilisation of the inactive conformation through salt-bridge interactions[46]. The suggestion that MVC and other small nonpeptidic CCR5 ligands, such as TAK-779 (TAK), acts as allosteric modulators is supported by biochemical, structural and mutagenesis studies[45,131,132] and current understanding suggests that the MVC binding pocket, although distinct from the gp120 binding site and the primary chemokine binding site, may overlap with the secondary chemokine binding site described in the two-step model[46]. This would suggest that MVC may inhibit the binding of the chemokine N-terminus to the secondary chemokine binding site but that it may not inhibit the initial binding of the chemokine core to the primary binding site.

Although MVC has seen effective use in the treatment of CCR5 tropic HIV-1, due to mutations in GP120 and outgrowth of CXCR4-tropic variants, strains of HIV which display resistance to MVC treatment have developed[133,134]. This has provided motivation for the discovery of novel CCR5-targeted HIV-1 entry inhibitors. Several of these prospective therapeutics have been analogues of CCL5 formed through the alteration of the CCL5 N terminus. One such analogue is PSC-RANTES, which sees the incorporation of several non-natural structures at the CCL5 N-terminus[135]. Despite displaying high levels of potency as an HIV-1 inhibitor, the super-agonistic behaviour of PSC-RANTES provides an increased risk of mucosal inflammation[136,137]. In addition, the requirements of synthetic structures in PSC-RANTES production results in a high cost of drug treatment[138]. Several CCL5 analogues have been produced subsequently using random mutagenesis of the CCL5 N terminus, namely 6P4-RANTES (6P4), 5P12-RANTES (5P12) and 5P14-RANTES (5P14), with all 3 analogues reported to have anti-HIV potency comparable to that of PSC-RANTES[138]. While 6P4 is reported to have a similar agonistic effect to that of PSC-RANTES, 5P12 and 5P14 are reported to display no G Protein-linked signalling activity, with 5P14 continuing to induce internalisation and 5P12 displaying no induction of internalisation[138–140]. Thus, 5P12 and 5P14 provide lower-cost therapeutic candidates with a lower risk of induced inflammation.

Recent insight into the role of the CCR5/CCL5 chemotactic axis in the pathogenesis of cancer has highlighted CCR5 as a potential target for cancer therapeutics. As in the case of HIV treatment, therapeutics focus on the reduction of CCR5 activation using CCR5

antagonists like MVC, which is currently under re-assessment as a clinical treatment for cancer patients[106,141,142]. The utility of alternative CCR5 ligands such as PSC-RANTES, 5P12 and 5P14 in the treatment of cancer remains to be seen but the continued development of CCR5-targeting therapeutics for the treatment of HIV, cancer and other CCR5-dependent pathologies has clear value. However, knowledge surrounding the effect of these CCR5 ligands on the structure, conformation, cell presentation, internalisation and signalling behaviour of the receptor remains incomplete.

1.5. Microscopy and fluorescence

1.5.1. Light microscopy

The advent of microscopy forms a key pillar in the study of Biology and our understanding of life on the microscopic scale. The ability to visualise subjects under a heightened magnification has allowed scientists a window into otherwise unobservable systems and the advancement of microscopy techniques over time has resulted in the ability to study biology over a remarkable range of length scales at an ever-increasing level of detail. The simplest of techniques that could be considered microscopy employ a singular lens. The history of these lenses is long and uncertain, but it has been speculated that their origins lie in the roman empire at the turn of the 1st century, where their name can be linked with the lentil with which they share a similar double convex shape[143].

A more recognisable interpretation of a microscope can be found in early examples of the compound microscope which employs multiple lenses in series to facilitate proper observation of the magnified image. The earliest compound microscope to be developed is credited to Hans and Zacharias Janssen who, in the turn of the 16th century combined two positionable lenses in a tube to allow variable magnification[144]. Following this development, the polymath Robert Hooke, employing his own compound microscope, achieved the accolade of being the first credited scientist to investigate biology at the microscopic scale and in the mid-17th century released his book ‘Micrographia’ which illustrated biological samples under magnification and forms a key milestone in the history of biological study[145]. One of the first scientists to be considered a microscopist, Antonie van Leewenhoek saw the continued advancement of magnification and, using his single lens microscopes, that offered up to 266x magnification, subsequently described the existence of human, bacterial, plant and yeast cells in the late 17th century[146–149]. Since this time, the light microscope has seen continuous development and has served a role in a vast range of key biological discoveries. They have attained a commonplace role in clinical and scientific settings for the routine

observation of microscopic structures as well as continuing to provide vital visual confirmation and contradiction of theoretical models at the cutting edge of biology.

Modern light microscopy can broadly be broadly split into two categories, those that provide an image using the illuminating light source after the light has interacted with the sample and those that use an illuminating light source to stimulate fluorescence within the sample, the emitted light from which is used to form the image. These two categories have distinct underlying principles and they each display a range of subtypes developed to address distinct requirements in sample analysis, however they often share common optical components and can be used in conjunction on the same microscope[150].

The former of these categories includes techniques such as brightfield microscopy in which a light source and the objective, the core optical element of modern light microscopes that facilitates the initial collection and focusing of light from the sample, are placed on opposite sides of the sample. The sample can then be imaged by its effect on the illumination through absorption, scattering and deflection. When imaging thin or transparent samples, such as in the case of cellular imaging, brightfield is often limited in its capability to resolve details, especially in the absence of cellular staining. Increased detail can be resolved within transparent samples via contrast enhancing forms of microscopy such as phase contrast. This method employs the use of phase rings that serve to convert sample-induced phase differences in the illuminating light into differences in brightness, thereby providing a visual indication of optical density through the sample[151]. While techniques such as brightfield usually employ white illumination, the latter of the aforementioned categories, known in general terms as ‘fluorescence microscopy’, employs illumination in a wavelength band specific to the fluorescent reporter that is being used in the sample. This illumination is often supplied using LEDs, arc lamps and lasers with additional optical filters designed to ensure that only the appropriate band of wavelengths are permitted for both the illumination and collection paths. This form of microscopy offers key enhancements in the specificity and resolution of cellular imaging but requires key consideration in the preparation of experimental set-up[151].

1.5.2. Fluorescence

Fluorescence is a phenomenon whereby a molecule can undergo the nanosecond-scale emission of light upon absorption of electromagnetic radiation, typically light from an external source, where the emitted light displays a longer wavelength than that of the light being absorbed[152]. Electrons display an ability to increase in energy upon absorption of a photon,

thereby facilitating the promotion of the electron into an excited state. Excited states tend to be short-lived with electrons returning to lower energy states through the release of energy in the form of photon emission and non-radiative processes such as vibration. The wavelength of a given photon is inversely proportional to its energy and due to the discrete levels in which excited electrons may exist, the wavelength of photons associated with the relaxation of electrons into lower energy states is similarly discrete. The disparity in wavelength between exciting photons and emitted photons is known as the Stokes shift and is caused by the relaxation of electrons through non-radiative means, which thereby reduces the energy available to photons upon emission. The promotion and relaxation of electrons through singlet excited states, so called due to the constraint of electron pairs to reside with opposite spin states cancelling out their overall magnetic moment, is not the sole mechanism for energy transfer, however. Electrons display an ability to undergo forbidden transitions into triplet excited states, a transition that does not offer a preferable route back to the singlet ground state. In brief, triplet states exist when electrons in separate orbitals display parallel spins, resulting in a magnetic moment that can be parallel, anti-parallel or perpendicular to the magnetic field and thereby offering three forms of differing energy in which the molecule can exist. Triplet states are relatively long lived and effectively disable the fluorescent emission of the molecule while occupied. Further, these states are heavily associated with the photochemical reactions that result in photobleaching, the irreversible loss of the ability of a molecule to fluoresce[152–154].

The Stokes shift of fluorescent light is a key element in the utility of fluorescence-based approaches to the study of biology. The utility of a given investigatory tool can be measured by its ability to distinguish between the desired signal and the non-desired background of your subject. Due to the Stokes shift, fluorescence-based techniques, provided the employment of optical filters, allow for the differentiation of fluorescent emission (signal) from the excitation light and other background light (background). In the case of microscopy, the use of fluorescent molecules known as fluorophores allows for the visualisation of specific constituents of a given biological sample, such as proteins distributed throughout the sample, or entire regions such as the cell nucleus or plasma membrane. The specificity that fluorescence microscopy facilitates, when compared with traditional light microscopy, drives its commonplace use in biological research, with this technique providing vital information regarding the location and proportion of a given biomolecule within a sample. However, the use of fluorophores is not limited to microscopy, with fluorophores being employed in various other techniques such as fluorescence spectroscopy and flow cytometry[155–157]. Regardless of the technique being employed, fluorescence-based assays require the careful complementation of fluorophores with the available light sources and filter sets to maximise

signal, limit fluorophore photobleaching and reduce background from sources such as cellular autofluorescence[152].

1.5.3. Fluorophores and cellular imaging

Since the advent of fluorescence microscopy and other fluorescence-based assays, a wide body of research has been conducted into the development of effective fluorophores for use in biological investigations, resulting in a large range of candidates each displaying certain benefits and applicability to different investigatory pursuits. A notable example of a fluorescent probe that has seen widespread employment in biological investigation is the Green fluorescent protein GFP, which was first isolated from the jellyfish Aequorea Victoria in the 1960s[158–160]. Like other fluorescent proteins, GFP exhibits a β-barrel structure with a central alpha helix that forms a ring structure exhibiting the conjugated double bonds that are a hallmark of fluorescent probes (chromophore). Mutations in the number of conjugated bonds has led to the development of fluorescent proteins that emit light of a differing wavelength to GFP, with the addition of bonds leading to increased emission wavelength, as in the case of the yellow fluorescent protein YFP[161]. Further, GFP saw enhancements through site directed mutagenesis. This mutant, known formally as enhanced GFP (EGFP), displays increased brightness and folding efficiency and has thus become the common form of GFP used in cell biology applications[159].

A given fluorophore's brightness is governed by the product of its quantum yield and extinction coefficient, the former of these values represents the ratio of photons emitted to photons absorbed while the latter is a measure of how much excitation light can be absorbed at a specific wavelength[162]. Due to its relatively high quantum yield, GFP exhibits a brightness that is higher than many other commonplace reporters, such as luciferase[163]. Further, the β-barrel structure of GFP serves to protect the chromophore, thereby limiting the effect of the external environment on the fluorescence, and the auto-catalytic generation of the GFP chromophore limits the existence of free dye contributing to non-specific background, as can be found in alternate labelling techniques[164,165]. The creation of GFP vectors have allowed for the production of GFP-biomolecule fusions that offer high expression within mammalian cells, complete biomolecule specificity and a brightness in biomolecule reporting that can be distinguished above cell autofluorescence. These advancements have rendered GFP ideal for the tracking of biomolecules of interest within cells, with several studies employing GFP as a reporter for the CCR5 receptor[166,167].

The use of GFP fusions is not without its disadvantages and concerns, however. The excitation and emission spectrum of GFP shares overlap with that of autofluorescence stemming from intracellular endogenous fluorophores, such as nicotinamide adenine dinucleotide (NADH)[168], resulting in increased background signal in comparison to assays employing probes of a longer wavelength[169]. Further, within fluorescent microscopy investigations it is often desirable to image samples with multiple fluorophores offering distinct and distinguishable fluorescent wavelengths to decipher the interaction of independent biomolecules or pools of biomolecules. Although fluorescent proteins offering alternative fluorescent wavelengths exist, they often, as in the case of the red fluorescent protein mCherry, offer a reduced brightness[170]. Additionally, the expression of fluorescent protein fusions within cells requires techniques such as transfection to integrate the fusion expressing vector into the host cell[171]. This process applies strain to cellular populations and, in the pursuit of a population of mammalian cells that express the fusion stably, requires the employment of immortalised cell lines[172]. This process can be time intensive and can raise further concerns regarding the impact of the fluorescent protein on the function of the biomolecule and the effect of the expression level on the biomolecule in relation to endogenous levels. However, the employment of immortalised cell lines allows for the selection of overall cell behaviour and shape, allowing for the isolated study of biomolecules in the absence of distinct and otherwise endogenous biomolecules in a conformation that is conducive with advanced microscopy techniques, as in the case of Chinese hamster ovary (CHO) cells which offer a flat basal membrane and ready adhesion to glass coverslips[60,63].

The advent of fluorescent probes that offer an increased brightness and range of fluorescent wavelengths, coupled with the mainstream use of alternative and less-invasive labelling techniques means that there are a wide range of options available to current biological investigations. Within the modern assortment of fluorescent probes exist synthetic dyes that have been developed for their applicability to biological assays[173]. A commonly employed example of these dyes is the Alexa Fluor family of probes developed by Molecular Probes and now provided by Invitrogen[174,175]. The member of this family most comparable with GFP is Alexa Fluor 488 which was developed through the chemical modification of the organic dye fluorescein and was designed to address the issues of photobleaching and pH-dependent intensity apparent in its predecessor. This dye offers roughly twice the brightness of GFP due to advancements in both quantum yield and extinction coefficient and this dye, alongside others from the Alexa Fluor family and alternate families such as DyLight, see commonplace use in modern fluorescent microscopy. In general, organic dyes are employed alongside labelling techniques that rely on specificity gained from biomolecule-specific antibodies or modern self-labelling proteins such as SNAP-tag, and do not rely on the

cellular production of the fluorescent probe. In the case of immunofluorescent assays, dye conjugated antibodies can be designed that offer specificity to the biomolecule of interest and provide a rapid method for the preparation of samples without the requirement of transfection[176]. This method facilitates the imaging of primary and otherwise non-transfected cells, however, antibody labelling offers a reduced level of label specificity in comparison with fluorescent protein fusions due to the non-specific binding of antibody conjugates to the sample and the presence of unbound dye resulting in background signal and an increased uncertainty in the true level of biomolecule expression. The more recent employment of self-labelling proteins, in which cells are transfected to produce a biomolecule of interest fused to a constituent part of a self-labelling protein binding pair, such as SNAP-tag and its corresponding ligand, combine the high-brightness probe compatibility and ease of end-point labelling of immunofluorescence with an increased labelling specificity[177]. However, the requirement of SNAP-tag integration into the cell results in constraints similar to those of fluorescent protein fusion techniques. An additional consideration in the choice of probe is its molecular weight, with an increased probe weight potentially affecting the dynamics and overall function of the target molecule. GFP has a significant molecular weight of 27 kDa[178], whereas small dyes such as Alexa Fluor 488 have a much smaller weight of 0.643 kDa[179]. However, the labelling technique employed to introduce these dyes can contribute significant weight, with SNAP-tag contributing 19.4 kDa[180] and antibody labelling contributing approximately 150 kDa[181]. Therefore, SNAP-tag labelling, when combined with small organic dyes, offers a lower weight alternative to GFP.

Regardless of the technique employed in the labelling of a specific biomolecule, or whether the sample in use is of primary origin or is of an immortalised cell line, fluorescence microscopy can be conducted on live samples or samples that have undergone fixation by formaldehyde[182]. Although the study of live cells provides a heightened level of biological relevance and is necessary for the true study of biomolecule dynamics, fixation provides a method of halting cellular function and effectively immobilising all cellular constituents. This method is vital to a range of fluorescent microscopy techniques that require significant time periods for the acquisition of images, over which non fixed samples may display dynamics that jeopardise localisation. Further, fixation allows for the study of biomolecule presentation at specific timepoints, such as a specified time after an induced change in cellular environment. Finally, fixation allows for the safe storage of samples prior to the execution of microscopy and limits the effects of this execution, such as changes in temperature and CO_2 levels, on cell behaviour.

1.6. Advanced biophysical techniques

1.6.1. Epifluorescence and confocal imaging

The most common form of cellular fluorescence microscopy employs the direct illumination of a large area of a sample in a similar manner to the white light employed in brightfield. This method is known commonly as epifluorescence or widefield microscopy and, in the case of many biological studies, serves its purpose of detecting fluorescently tagged cell constituents rapidly and effectively[151]. However, this method is limited in its ability to resolve fluorophores mainly through the heightened level of background signal contributed by out of focus light. The development of new fluorescence microscopy techniques has often been driven by the desire to reduce the effect this out of focus light has on the techniques ability to resolve. In the case of confocal microscopy this is achieved by reducing the width of the illumination to a small point and detecting via a small pinhole that restricts the detection to emission from the desired focal spot, this illuminating area must then be scanned across the cell to build up a complete image of the desired sample area[183]. Techniques such as this provide a higher spatial resolution than traditional epifluorescence but require a longer period of time over which a single image can be acquired, thereby reducing the ability to accurately image dynamic structures and often necessitating the fixation of samples. This trade-off between spatial and temporal resolution is a hallmark of microscopy technique development, spatial and temporal resolution can be maximised, but often at the expense of one another, with comprehensive biological studies often employing multiple microscopy techniques.

Although the development of fluorescence microscopy techniques has resulted in increased spatial resolution, this resolution has been historically restricted by the diffraction limit of light. Spatial resolution can be defined as the smallest distance over which two points can be distinguished. When imaged in the absence of aberrations, single fluorophores appear as a point spread function (PSF) which exhibits, in the imaging plane, as a pattern of concentric diffraction rings known as an airy disk. When located in close proximity to one another, the PSF of each fluorophore may overlap, resulting in difficulty distinguishing the location of individual fluorophores. Objects can be deemed to be just spatially distinguishable when the airy disk of one object is located over the first minimum of the airy disk of the second object, a rule known as the Rayleigh criterion[184]. The overall resolving power of an objective lens (d) is inversely proportional of its numerical aperture (NA), a measure of the range of angles over which the objective can gather light, and proportional to the wavelength of light being collected (λ) and can be described by the Abbe formula: $d = \lambda/2NA$[185]. However, these

constitute two of several different ways of defining the lateral spatial resolution in a given system. Fluorescence microscopy assays do not typically employ emission wavelengths less than 400-500 nm and the oil immersion objective lenses used typically display a NA roughly equal to 1.4, therefore the resolving power of traditional fluorescence microscopy is usually limited to 140-180nm, and in practice, this resolution is not always achieved. In recent years, techniques have been developed that allow for spatial resolutions that surpass the diffraction limit, with the 2014 Nobel prize in chemistry being awarded for the development of this, so-called, super-resolution microscopy[186].

1.6.2. Structured illumination microscopy

A range of super resolution techniques have seen development in recent years, with each displaying the ability to surpass the diffraction limit, alongside respective advantages and disadvantages in their application to biological questions[187]. One such technique is Structured illumination microscopy (SIM) which sees the resolving power increased by a factor of 2 relative to traditional techniques. This technique is based upon widefield fluorescence microscopy and achieves an increased resolution through the employment of patterned illumination[188]. A sample containing fluorophores that are closely located to one another can be considered to display patterned emission with a high and often unresolvable spatial frequency. Upon the interaction of patterned illumination and the fluorophore distribution, an interference pattern known as moiré fringes is formed, these fringes contain information regarding the two contributing light sources and display a lower and more easily resolvable spatial frequency than the two contributing light sources. As the patterned illumination is defined, computational deconvolution can be performed on the interference pattern to define the normally unresolvable high spatial frequency of the sample emission[189].

The resolution enhancements offered by SIM can be further explained by the consideration of Fourier space[190]. The observable region offered by uniform illumination in Fourier space is represented **Figure 1-2a**, where the radius of this circular region represents the spatial frequencies of emission light that can be captured by the objective, with the diffraction limit of an objective lens acting as a low pass frequency filter and limiting the radius of the observable region. The sinusoidal illumination patterns used in SIM generally have three Fourier components at 0 ± the inverse stripe spacing, where their offset can be optimised such that the outlying components sit close to the frequency limit of the objective lens, as represented by the three red dots in **Figure 1-2b**. Upon interference of the patterned illumination and the sample, the subsequent moiré fringes represent information that has effectively shifted position in Fourier space from a normally unobservable high spatial

frequency position into the passband of the objective lens, as shown in **Figure 1-2c**. Precise knowledge of the frequency and orientation of the illumination pattern allows for the weighting and shift of these mixed frequencies to their proper place in Fourier space, consequently increasing the observable area. To increase the observable region, which is analogous to the resolving power, by a factor of two, three phase-stepped sinusoidal illumination patterns must be employed, with the orientation of each pattern being shifted through 360°, as illustrated in **Figure 1-2d**, thereby resulting in 9 raw images for each SIM reconstruction[191,192].

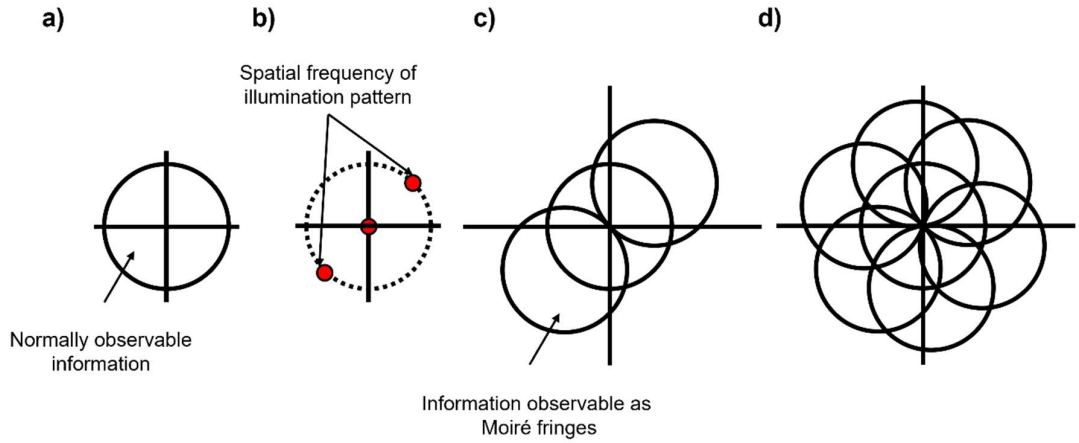

Figure 1-2: Illustration demonstrating key concepts in SIM. a) Observable region offered by uniform illumination in Fourier space. b) The three Fourier components of a sinusoidally striped illumination pattern (red dots). c) Expanded region observable as moiré fringes. d) Observable region increased by a factor of two through the employment of three phase stepped illumination patterns, each shifted through 360°.

The widefield foundations of SIM have facilitated its incorporation into multi-functional microscopes and its ease of use in biological assays that previously relied on more traditional fluorescence microscopy techniques. Unlike alternative super-resolution techniques, such as stochastic optical reconstruction microscopy (STORM), which rely on the photoswitchable characteristics of certain tailored fluorophores, SIM does not require alteration in the preparation of biological samples beyond the use of the bright and photostable fluorophores commonly used in traditional techniques[187,193]. Further, techniques that rely on the selective and temporal excitation of individual fluorophores to induce temporary separation of emitters often require the acquisition of tens of thousands of raw images over tens of minutes[194]. In comparison, the 9 raw images required for each SIM reconstruction provides a much higher usability and applicability to live samples. However,

the application of SIM to highly dynamic structures that display a high diffusion coefficient remains limited.

1.6.3. Single molecule techniques

Among the plethora of biological assays available, relatively few display the ability to interrogate individual biomolecules, with most assays offering an average readout of a desired metric that is instead influenced by the characteristics of the most common form of a given biomolecule. These bulk ensemble techniques offer very little information regarding rare events and are incapable of reporting on the heterogeneity that may exist within the biomolecule population. Recent years have seen the advent of single-molecule techniques which aim to report on individual biomolecules within a sample, thereby unveiling any heterogeneity within the population and allowing the investigation of rare and potentially vital species[195]. In the case of fluorescence microscopy, single molecule techniques aim to define characteristics of single biomolecules through the detection and tracking of individual fluorophores. These techniques benefit by the employment of a one-to-one binding ratio of fluorophores to biomolecules, such as can be found in the aforementioned fluorescent protein fusions, to ensure that an individual fluorophore can effectively be equated to a single biomolecule. This can provide metrics such as overall copy number, diffusion coefficients and localisation on a single molecule level[196].

A major benefit of these techniques is the ability to report on biomolecule stoichiometry through the tracking of the intensity of biomolecular assemblies over time. This relies on the principle of photobleaching, whereby a fluorophore undergoes the irreversible cessation of fluorescence after a certain level of exposure to excitation light. If the intensity of a given fluorescently tagged biomolecular assembly can be tracked accurately as its constituent fluorophores undergo photobleaching then the number of constituent fluorophores, and subsequently the number of biomolecules, provided a one-to-one binding ratio, can be counted[197]. This counting can be conducted either through the division of the initial assembly intensity by the intensity of a single fluorophore, provided that both of these values can be accurately defined, or through the technique of stepwise photobleaching[198]. This technique requires the analysis of the temporal intensity trace of a given assembly for characteristic steps in intensity reduction which correspond to single photobleaching events. By determining the number of photobleaching steps within a given trace, the number of constituent fluorophores and corresponding biomolecules can be inferred[199].

Single molecule techniques require not only the high spatial resolution offered by modern fluorescence microscopy, but also high temporal resolution to ensure that the location and intensity of fluorophores can be tracked with fine scrutiny. In the case of photobleaching-dependent measurements of assembly size, this temporal resolution is key to the determination of initial fluorophore intensity and the accurate counting of photobleaching events, with a reduction in this resolution likely inducing an underestimation of initial intensity and overall fluorophore count. Techniques which see the improvement of spatial resolution through the use of patterned illumination or photoactivatable dyes display a reduction in the temporal resolution that limits their applicability to single molecule assays. In order to benefit from both the high spatial and temporal resolution required by single molecule assays, investigations seek to increase the signal to noise ratio (SNR) of their sample whilst retaining a high frame rate. Previous studies have achieved this through the use of slimfield microscopy, an adapted form of widefield microscopy which employs the use of high-powered laser excitation, reduced fields of view and high frame rate cameras which has seen employment in the investigation of biomolecules in a variety of sample types[200–206].

Slimfield microscopy is particularly suited to the employment of inclined illumination techniques that can facilitate optical sectioning and increased SNR. Techniques such as highly inclined and laminated optical sheet (HILO) microscopy see the introduction of the excitation beam at an angle relative to the coverslip surface[207,208]. Provided a restricted beam width, this can provide selective excitation of a thin section of a sample, thereby reducing the excitation of off-target fluorophores and the subsequent background light stemming from out of focus emission. HILO is particularly useful for the study of biomolecules located within intracellular compartments, especially in cases of high autofluorescence or the presence of off-target fluorophores. The angle of incidence that is employed in highly inclined and laminated optical sheet (HILO) microscopy varies based on the desired focal plane. However, once the angle of incidence reaches the critical angle for a glass water interface, the illumination undergoes total internal reflection, limiting the transmission of illumination and creating an evanescent energy field. This energy field provides an enhanced source of fluorophore excitation that decays exponentially in the axial direction and forms the basis of total internal reflection fluorescence (TIRF) microscopy[196,209]. TIRF illumination effectively provides an enhanced excitation of fluorophores located within approximately 200 nm of the coverslip surface whilst limiting the excitation of fluorophores located deeper in the sample. This excitation enhancement and restriction of penetration depth result in TIRF being particularly useful for in-vitro assays that see the immobilisation of biomolecules to the coverslip surface[199]. However, investigation into biomolecules which reside in the membrane of cells can benefit from the utility of TIRF, provided the membrane

is closely adhered to the coverslip surface. Using these techniques, biomolecules can be imaged with a maximised signal to noise ratio and frame rate, and, provided that the population of fluorophores is not over-crowded, individual biomolecules, or assemblies of biomolecules, can be computationally tracked with a temporal resolution that is conducive with the determination of assembly dynamics and size[1].

1.7. Aims

In summary, the CC chemokine receptor CCR5 plays a key role in immune function and forms a therapeutic target for a range of diseases. CCR5 is known to conduct its role via the recognition of extracellular ligands, inducing conformational change and downstream internalisation of the receptor, with therapeutic binding partners being designed to interfere with this function. However, our understanding of the overall spatial arrangement of CCR5 populations and oligomeric state of constituent receptors, both in the steady state and under ligand-induced activation, remains incomplete. Reported range in the conformational state of CCR5 sub-populations, alongside range in reported oligomeric state of CCR5 suggests a high level of heterogeneity. However, previous investigations of CCR5 behaviour have relied on diffraction-limited and bulk-ensemble readouts. The continued investigation of CCR5 behaviour in the steady state and upon interaction with natural and therapeutic ligands would benefit from the application of cutting-edge biophysical techniques capable of the super-resolved determination of CCR5 spatial arrangement and the single-molecule determination of CCR5 oligomeric make-up. Given the literature, the key unknows we wish to address are the spatial arrangement of CCR5 in mammalian cells on a super-resolved level, the oligomeric make-up of CCR5 on a single-molecule level and the effect that CCR5 agonists and antagonists have on the spatial and oligomeric characteristics of CCR5. For this purpose, this thesis aims to:

- Examine the overall spatial arrangement of steady state CCR5 in an existing adherent mammalian cell model using super-resolution microscopy

- Develop a CCR5-expressing cell model and slimfield-based imaging technique tailored to the single-molecule investigation of CCR5 in adherent mammalian cells

- Examine the behaviour and oligomeric state of steady state CCR5 using single-molecule techniques

- Examine the effect of CCL5, small molecule antagonists and CCL5 analogues on the behaviour of CCR5

- Develop additional CCR5-expressing cell models to boost the breadth and biological relevance of future investigations

2. Materials and methods

2.1 Reagents and consumables

Tissue culture reagents and plastics were purchased from Invitrogen Life Technologies, (Paisley, UK), and chemicals from Sigma-Aldrich Company Ltd (Poole, UK), unless otherwise indicated.

2.2. Cell culture

The CHO-K1 cells employed in this study were gifted by Professor Paul Kaye (The Hull York Medical School). CHO-K1 were cultured in Dulbecco's Modified Eagle Medium (DMEM) (ThermoFisher) supplemented with Fetal calf serum (FCS) (ThermoFisher) at a final concentration of 10%, alongside penicillin (100 U/ml), streptomycin (0.1 mg/ml) and L-glutamine (4 mM) (ThermoFisher). Cells were incubated at 37°C and 5% CO_2.
The CHO-CCR5 cells (Dihydrofolate reductase (DHFR)-deficient CHO cells stably transfected for the expression of $CCR5^{210}$) employed in this study were cultured in 10% (v/v) FCS-MEM eagle, α modification (Sigma-Aldrich) supplemented with FCS at a final concentration of 10%. Cells were incubated at 37°C and 5% CO_2.

The CHO-GFP-CCR5 cells (CHO-K1 cells stably transfected for the expression of GFP-CCR5) employed in this study were cultured in DMEM supplemented with FCS at a final concentration of 10%, alongside penicillin (100 U/ml), streptomycin (0.1 mg/ml), L-glutamine (4 mM) and the selection antibiotic hygromycin-B (400 ug/ml) (Invitrogen). Cells were incubated at 37°C and 5% CO_2.

The Jurkat cells employed in this study were gifted by Professor Dimitris Lagos (The Hull York Medical School). Jurkat were cultured in RPMI 1640 (ThermoFisher) supplemented with FCS at a final concentration of 10%, alongside penicillin (100 U/ml), streptomycin (0.1 mg/ml) and L-glutamine (4 mM). Cells were incubated at 37°C and 5% CO_2.
The CHO-SNAP-CCR5 cells (CHO-K1 cells stably transfected for the expression of SNAP-CCR5) employed in this study were cultured in DMEM (Thermo Fisher) supplemented with FCS at a final concentration of 10%, alongside penicillin (100 U/ml), streptomycin (0.1 mg/ml), L-glutamine (4 mM) and the selection antibiotic G418 (1 mg/ml). Cells were incubated at 37°C and 5% CO_2.

The passage of cells was carried out upon the cells reaching confluence. In the case of adherent cells grown in a 10 cm dish, cell media was aspirated prior to the addition of 2 ml of sterile phosphate-buffered Saline buffer (PBS). This PBS wash was aspirated prior to the addition of 2 ml of Trypsin-Ethylenediaminetetraacetic acid (EDTA) and subsequent 37°C incubation for detachment. Rounding of cells was confirmed using a compound microscope prior to the addition of 8 ml of culture medium. The complete detachment of cells from the dish was encouraged through the pipetting of the culture medium up and down, ensuring the break-down of clumped cells. A portion of this cell solution was added to culture medium at a ratio of 1:5, 1:10 or 1:20 dependent on cell type and desired plating density, this lower concentration cell solution was added to a new 10 cm dish and allowed to rest at 37°C for reattachment and growth. Plating density was informed through the process of cell counting, whereby 50 µl of the original cell solution is added to a haemocytometer alongside 50 µl of Trypan blue solution. The number of live cells within the haemocytometer were counted and used to estimate the overall cell density in the original dish.

In the case of non-adherent cells grown in a T-25 culture flask, cell suspension was agitated through pipetting the suspension up and down to separate clumped cells and allow an even cell distribution throughout the suspension. A portion of this cell solution was added to culture medium at a ratio of 1:5, 1:10 or 1:20 depending on desired plating density, this lower concentration cell suspension was added to a new T25 flask and allowed to rest at 37°C for growth.

2.2.1. Transfection and generation of CHO-GFP-CCR5

CHO-GFP-CCR5 cell lines were generated by transfecting CHO-K1 with a pCDNA3.1 Hygro-GFP-CCR5[167] construct that lacked the presence of a strong pre-promoter amplification region, using the TransIT-X2 transfection reagent from Mirus (MIR 6003), according to manufacturer protocols. CCR5 expression within mixed populations was maintained by culturing cells in the presence of 400 µg/ml hygromycin. The creation of clonal CHO-GFP-CCR5 populations was carried out through the isolation of single cells from the mixed population for expansion. This process was achieved through limited dilution, whereby mixed population cells were detached and seeded in a 96-well plate at an average density of 1 cell per well in the presence of hygromycin. Wells were inspected using brightfield microscopy to identify wells that contained a single cell. Well inspection continued every few days to determine which wells exhibited successful growth of clonal colonies. Initial inspection of GFP-CCR5 expression was carried out using an upright fluorescent microscope. Once confluent, colonies under consideration were expanded in 24 well plates.

Further characterisation of expression was characterised using flow cytometry with CHO-K1 control cells.

2.2.2. Transfection and generation of CHO-SNAP-CCR5

CHO-SNAP-CCR5 cell lines were generated by transfecting CHO-K1 with a SNAP-CCR5 construct[211] using either the TransIT-X2 transfection reagent from Mirus (MIR 6003) or the X-tremeGENE HP reagent from Sigma Aldrich (6366236001). SNAP-CCR5 plasmid (pFLAG-SNAP-CCR5-WT) was originally made by Cisbio[212] and was provided by Dr. Anne Brelot (Institut Pasteur, Paris France). SNAP-CCR5 plasmid underwent bacterial amplification prior to purification using a midiprep and subsequent concentration categorisation using a NanoDrop (Thermofisher). SNAP-CCR5 expression was maintained by culturing cells in the presence of 1 µg/ml G418 and SNAP-CCR5 expressing cells were isolated for single-cell cloning through the process of limited dilution cloning, as described above. Selection of specific populations based on their clonality, and expression levels was aided through the characterisation of Alexa Fluor 647-associated signal using flow cytometry against non-transfected CHO-K1 controls employing both the monoclonal antibody FLAG-M2 and anti-CCR5 primary antibodies 2D7 and MC-5. Further characterisation of both stably and transiently transfected populations employed SNAP-Surface Alexa Fluor 647 from New England Biolabs (S9136S). Transient transfection of CHO-SNAP-CCR5 took place using the same methods as above, however these mixed populations did not receive exposure to selection antibiotics.

2.2.3. Transfection and generation of Jurkat-GFP-CCR5

Jurkat cell lines were transfected with either the pCDNA3.1 Hygro-GFP-CCR5 construct employed in CHO-GFP-CCR5, a construct solely coding for GFP or a an alternate GFP-CCR5 construct that does not code for antibiotic resistance[167]. Cells were transfected using a Nucleofector II device (LONZA) alongside the Cell Line Nucleofector Kit V (LONZA), following the manufacturer protocol. Cell transfection was carried out using Nucleofector modes that either prioritise cell viability post transfection (high viability) and those designed to prioritise protein expression at the cost of cell viability post-transfection (high expression). Determination of GFP expression post-transfection was carried using Flow cytometry against non-transfected Jurkat controls.

2.3. Flow cytometry

2.3.1. Flow cytometry of CHO-GFP-CCR5

Upon reaching confluence, CHO-GFP-CCR5 underwent cell detachment following the steps outlined above. In place of Trypsin-EDTA, the PBS wash was instead replaced using PBS containing 10mM EDTA (PBS-EDTA) prior to incubation at 37°C for detachment. A portion of the detached cell solution was used for the determination of cell density using cell counting, as outlined above. The remaining cell solution was transferred to a 50 ml Falcon tube and underwent a 6-minute centrifugation at 10g to form a cell pellet. The supernatant was aspirated to remove any remaining EDTA and the cell pellet was resuspended at 2 x 10^6cells/ml. 50 µl of this cell solution was added to a single well of a non-tissue culture treated 96-well u-bottom plate. The number of wells which received cell solution corresponded to the number of conditions to be studied using flow cytometry.

The 96-well plate underwent a 3-minute centrifugation at 10g and 4°C to form a cell pellet and the supernatant was removed through flicking the plate. Cell pellets were broken down using a vortex mixer and cells were resuspended in 200 µl of FACS buffer (PBS, 1% FCS, 0.05% sodium azide). In the case of GFP-expression analysis in fixed cells, cells again underwent centrifugation and supernatant flicking to remove this initial FACS buffer wash. Cells were resuspended in FACS buffer containing 3% formaldehyde for the fixation of cells and were stored at 4 °C for 20 mins. In the case of overnight fixation, cells were resuspended in FACS buffer containing 1% formaldehyde and were stored at 4 °C overnight. Fixed cells were washed and resuspended in 200 µl FACS buffer before analysis using flow cytometry.

In the case of immunofluorescent labelling of cells, cells were resuspended in 50 µl FACS buffer containing the respective primary antibody at a concentration of 2.5 µg/ml following the initial FACS buffer wash and were placed on a shaker at 4 °C for 1 hour prior to being centrifuged as before for the removal of supernatant. Unlabelled and secondary only controls underwent the same treatment using FACS-buffer in the absence of primary antibodies. Cell washing was performed as before, with cells being resuspended in 200 µl FACS buffer and undergoing a 3-minute centrifugation at 4 °C, 3 washes were performed following primary antibody staining. Cells underwent fixation as described above prior to being washed and resuspended in 100 µl NH_4Cl free aldehyde quenching solution (10mM NH_4Cl in PBS) for 30 minutes at 4 °C. Following 2 FACS buffer washes, cells were resuspended in 50 µl FACS buffer containing the respective secondary antibody at a concentration of 4 µg/ml and were

placed on a shaker at 4 °C for 1 hour. Unlabelled control cells underwent the same treatment using FACS buffer in the absence of secondary antibodies. Cells underwent an additional 3 washes and were resuspended in 200 µl prior to the analysis of fluorescence intensity using flow cytometry.

2.3.2. CHO-GFP-CCR5 calcium flux assay

CHO-GFP-CCR5 were detached using PBS-EDTA and counted, as described above, prior to receiving two PBS washes and being resuspended in PBS at a concentration 2 x 10^6cells/ml. Quest Fluo-8 AM (AAT Bioquest) was introduced to the cells at a final concentration of 2.5 mM and cells underwent a 30 min incubation at room temperature in the dark. After incubation, cells underwent two further PBS washes for the removal of excess dye and cells were resuspended in HBSS buffer solution (1.26 mM $CaCl^2$) (ThermoFisher) at a concentration of 1 x 10^6cells/ml. Cell solution was portioned into 500 µl aliquots and were kept on ice until analysis by flow cytometry. A portion of aliquots saw the addition of TAK-779 at a final concentration of 400nM to determine the effects of CCR5 antagonist pre-exposure. Cell aliquots underwent aspiration by the cytometer prior to the addition of CCL5 to determine the baseline level of fluorescence. Cells were exposed to CCL5 at a concentration of 10nM, a concentration deemed optimal in previous investigations[213]. Aspiration continued upon the addition of CCL5 and continued for the remainer of the induced-response, acquisition was repeated as required. A blank stimulation control underwent acquisition to account for the mechanical impact of the instrument on the readings. Data was presented as the fluorescent signal (fluo-8-Ca^{2+}-FITC) against time, with successive gates of 5 s intervals for the duration of the response. These results were reported as the fluorescent signal normalised to the baseline signal of each sample before stimulation. Data was plotted using Prism v9.4.1 (GraphPad Software Inc., La Jolla, USA). Experimentation was performed by Dr Nathalie Signoret.

2.3.3. CHO-GFP-CCR5 internalisation assay

CHO-GFP-CCR5 were detached in PBS-EDTA and counted, as described above. Cells were resuspended in binding medium at a concentration of 2 x 10^6cells/ml and underwent incubation at 37°C for up to 60 minutes either in binding medium (RPMI 1640 without bicarbonate, containing 0.2% BSA and 10 mM Hepes, pH 7.0) alone or in the presence of 100 nM PSC-RANTES (gifted by Prof. Oliver Hartley, University of Geneva). Aliquots of cells were taken at each time point (5, 15, 30 and 60 minutes) and were transferred to a non-tissue culture treated u-bottom 96 well plate kept on ice. Each time condition was split between two wells to allow separate primary antibody labelling with 2D7 (BD biosciences) in

FACS buffer or an anti-GFP monoclonal antibody (proteintech) in FACS buffer, respectively. Samples underwent 1% formaldehyde overnight fixation and labelling with the secondary antibody GAM-DyLight 650 (ThermoFisher), as described above, prior to analysis by flow cytometry. The percentage of fluorescent signal for each condition was calculated using the specific mean fluorescence intensity (CCR5-asoociated mean fluorescence intensity subtracted for background signal) Experimentation was performed in triplicate by Dr Nathalie Signoret.

2.3.4. Flow cytometry of Jurkat

Transfected Jurkat cells underwent preparation for flow cytometry 64 hours after being transfected. Transfected cells were observed using a compound microscope to confirm the presence of healthy cells. Cells were transferred to a round bottom polypropylene centrifugation tube and underwent a 6-minute centrifugation at 10g and 4 ^{o}C to form a cell pellet. Cells underwent a wash through the resuspension of cells in 250 µl of FACS buffer following a 3-minute centrifugation at 10g and 4 ^{o}C. Supernatant was aspirated and cells were resuspended in 250 µl of FACS buffer prior to analysis using flow cytometry.

2.3.5. Flow cytometry of CHO-SNAP-CCR5

In the case of stably transfected CHO-SNAP-CCR5 clones and mixed populations, confluent cells were prepared for labelling in a non-tissue culture treated 96-well u-bottom plate using the steps outlined above for CHO-GFP-CCR5. In the case of immunofluorescent staining, cells likewise underwent labelling using the steps outlined above for CHO-GFP-CCR5. The protocol for the immunofluorescent staining of CHO-SNAP-CCR5 saw alteration, as outlined in the final results chapter of this thesis. This adapted protocol saw the extension of primary antibody labelling to a 2-hour period at 4 ^{o}C and the fixation of cells taking place after both primary and secondary antibody labelling.

In the case of labelling using SNAP-surface Alexa Fluor 647, cells were detached and transferred to a non-tissue culture treated 96-well u-bottom plate as outlined above. Cells were washed, as above, but using 200 µl of binding medium and a 3-minute centrifugation at 10g and 37 ^{o}C. Cells were resuspended in 50 µl of binding medium containing SNAP-surface Alexa Fluor 647 at a concentration of 5 µM and underwent a 30-minute incubation at 37 ^{o}C. Cells underwent three additional washes in binding medium to remove unbound SNAP-surface Alexa Fluor 647. Cells underwent a further wash using 200 µl of FACS buffer prior to a 20-minute incubation in 200 µl of FACS buffer containing 3% formaldehyde for the fixation of cells. Fixation solution was removed using a final FACS buffer wash and cells were

resuspended in 200 µl of FACS buffer for analysis by flow cytometry. The protocol for SNAP-surface Alexa Fluor 647 labelling saw alteration, as outlined in the final results chapter of this thesis. This adapted protocol saw the reduction of the concentration of SNAP-surface Alexa Fluor 647 employed from 5 µM down to 62 nM and the absence of fixation prior to analysis. The choice of adapted SNAP-surface Alexa Fluor 647 concentration was informed through flow cytometry analysis of non-transfected CHO-K1 cells that underwent labelling as outlined above using a range of SNAP-surface Alexa Fluor 647 concentrations created through serial dilution.

In the case of transiently transfected CHO-SNAP-CCR5, cells were prepared for labelling using the steps outlined above for stably-transfected cell lines. Cells underwent preparation 48-hours after the transfection of cell populations that displayed either a high or low level of cell confluence. Once prepared, these cells underwent either immunofluorescent staining or SNAP-surface Alexa Fluor 647 labelling using the adapted protocols outlined above.

2.3.6. Flow cytometry analysis

Flow cytometry of cells was performed on a CytoFLEX S (Beckman Coulter) system in the Technology Facility (University of York). Analysis of flow cytometry data was performed using CytExpert (Beckman Coulter).

2.4. SIM imaging

2.4.1. Preparation of CHO-CCR5 for SIM imaging

CHO-CCR5 were grown in a 10 cm dish to confluency prior to being detached using Trypsin-EDTA following the detachment protocol outlined above. Cells were seeded onto #1.5 grade round coverslips (standardised thickness of approximately 0.17 mm) seated in a 24-well tissue culture plate at a concentration of 1:20 in 250 µl of culture medium. Seeded coverslips were incubated at 37 ^{o}C and 5% CO^2 for 48 hours to allow cell reattachment and growth to a confluence of approximately 30%.

Prepared coverslips were inspected using a compound microscope to ensure cell health and attachment. Culture medium was aspirated and replaced with 400 µl of PBS which was in turn aspirated, forming a PBS washing step. PBS washing was carried out 3 times prior to the addition of 250 µl of PBS containing 3% formaldehyde for 20 minutes for the fixation of

cells. In the case of CHO-CCR5 exposed to CCL5, initial culture medium was replaced with 250 µl of binding medium containing CCL5 (Peprotech) at a concentration of 100 nM and cells were incubated at 37 ºC for the desired perturbation time. When several CCL5 perturbation times were required in one sample preparation, 250 µl of binding medium was added to each well prior to the addition of 50 µl of binding medium containing CCL5 at 6 times the desired concentration to the well corresponding to the longest CCL5 exposure. All wells underwent incubation at 37 ºC and binding medium containing CCL5 was added to the remaining wells corresponding to their respective exposure times, such that all wells received fixation at the same time point. Cells underwent a 20-minute fixation through the addition of 300 µl of PBS containing 6% formaldehyde, providing a final concentration of 3% in 600 µl. In studies employing a labelled form of CCL5, CHO-CCR5 were exposed to either 10nM Alexa Fluor 647-CCL5 (R&D Systems) or a 1:100 ratio of Rhodamine-CCL5 to unlabelled CCL5 at a concentration of 100nM, following the steps described above.

In the case of CHO-CCR5 exposed to CCL5 alongside pre-treatment of cells using antagonists and CCL5-analogues, initial culture media was replaced with 250 µl of binding medium containing the corresponding pre-treatment, with MVC, TAK, 5P12 and 5P14 being present at a concentration of 10 µM, 800 nM, 100 nM and 100 nM respectively (5P12 and 5P14 were gifted by Prof. Oliver Hartley, University of Geneva). Cells underwent a 30-minute incubation at 37 ºC. Non-pre-treated samples were handled in the same way using binding medium in the absence of pre-treatment. Subsequent CCL5 exposure was carried out as described above, with 50 µl of binding medium containing CCL5 at 6 times the desired concentration being added to each well at the corresponding timepoint and cells undergoing fixation, as described above.

After fixation, cells underwent 3 PBS washes and a single extended PBS wash in which the PBS was left for 5 minutes prior to aspiration. Cells received 250 µl of NH4Cl free aldehyde quenching solution for 30 minutes. Quenching solution was replaced with 250 µl of PBS containing 1% FCS for 30 minutes to minimise non-specific binding of antibodies. This solution was replaced with 250 µl of PBS containing 1% FCS alongside DyLight 650-MC5 or Alexa Fluor 488-MC5 at concentration of 2 µg/ml and cells were stored on a shaker for 60 minutes. Cells underwent 3 extended PBS washes whilst remaining on the shaker. Coverslips were mounted on glass slides using mowial mounting medium, as employed in previous studies[214], and were allowed to dry at 37 ºC. MC5 is an anti-CCR5 monoclonal antibody produced from a hybridoma and purified by Prof. Matthias Mack[63]. Non-interference of this antibody with CCL5 binding, as well as CCR5 conformation, activation and internalisation, has been validated by previous studies[60,63,166]. In previous in-house

development, MC5 was directly coupled with DyLight 650 and Alexa Fluor 488 at a dye to protein ratio of 1.57:1 and 0.8:1 respectively, using the Dylight-650 NHS ester coupling kit (Thermofisher) and Alexa Fluor 488 antibody labelling kit (Invitrogen).

2.4.2. CHO-CCR5 imaging by SIM

SIM imaging was performed on a custom system located in The National Physical Laboratory. This SIM system is built on an Olympus IX71 inverted widefield epifluorescence microscope, as described in previous studies[1,191,192]. This system employs the projection of illumination patterns onto samples, generated using the spatially filtered image of a binary phase grating displayed on a liquid-crystal-on-silicon spatial light modulator (SXGA-3DM, Forth Dimension Displays). Images of CHO-CCR5 were acquired using a 60x/1.3 silicone immersion objective lens (UPLSAPO, Olympus) alongside a quad-band fluorescence filter cube (TRF89901-EM, Chroma) and excitation provided by either a 488 nm, 515 nm or 638 nm diode laser (Luxx, Omicron Laserage), with an effective (Abbe) resolution of ~ 170 nm under 638 nm excitation.

Images of CHO-CCR5 were recorded using a scientific CMOS camera (ORCA Flash 4.0, Hamamatsu Photonics) with the global exposure period of the camera being synchronised with the spatial light modulator. Nine raw images were captured using a series of sinusoidal illumination patterns to allow the final reconstruction of a super resolution image. These 9 patterns comprised of three orientations, each separated by 120°, and three pattern phases, separated by $2\pi/3$ per orientation. High-pass filtering was used to suppress out-of-focus information close to the centre of each separated Fourier space information passband[191] prior to passbands being shifted and combined as described in previously studies[215]. Images were acquired across several planes of the cell in order to form a z-stack of images demonstrating expression throughout the cell. Image z-stacks were acquired starting from the basal membrane and moving up towards the apical membrane. Images were acquired with 200-500 nm step sizes between each acquisition.

2.4.3. Intensity analysis of CHO-CCR5

Image stacks of CHO-CCR5 obtained using SIM underwent maximum z-axis intensity projection using ImageJ with the Fiji platform (ImageJ/Fiji) to give representation of overall cell expression. Cell boundaries were determined using ImageJ/Fiji to segment cells from the extracellular environment and bordering cells. Cell segments were created using global Otsu thresholding to determine the cell circumference. ImageJ *measure* function was employed to record the average intensity of the cell normalised to the area of the cell.

Estimation of background signal was determined using the average intensity of a circular area of 100-pixel radius set within the extracellular space over several images. Estimations of background signal were used to quantify the mean cell intensity above a baseline background level. Within a given condition, the overall intensity of each cell was used to calculate the mean average intensity for this condition, with the error associated with this mean average being reported as the standard error of the mean. In the case of the determination of CCL5-associated intensity, analysis was carried out in an identical manner, employing the cell boundary determined using the CCR5-associated signal of the same cell. In the case of cell projections displayed using a photobleaching correction, images captured at different focal offsets were corrected for photobleaching by scaling using an exponential decay curve measured by repeated imaging of the same region of a cell under identical conditions. All images displayed within the same figure are contrast matched unless otherwise stated.

2.4.4. Cluster analysis in SIM images

CHO-CCR5 images of the basal membrane underwent cell boundary segmentation, as described above. Images then underwent binarisation using a combination (in parallel, followed by an AND operation) of global Otsu thresholding and local Otsu thresholding with a rolling ball radius of 25 pixels using ImageJ/FIJI. The binary images revealed objects corresponding to local enrichment of CCR5. The 'Analyse Objects' function of ImageJ/Fiji was used to determine the number of objects, alongside the area, centroid and circularity of each object. The number density of objects was calculated using a 2D kernel density estimate of the object centroid coordinates, with kernel width of the widefield lateral resolution, ~180 nm, as described previously[1].

Centroid coordinates of foci were analysed using ClusDoc software[216]. The relative clustering or dispersal of objects was assessed for each individual cell using the Ripley H function. The Ripley H function is equal to the Ripley L function less the radius, H(r) = L(r)-r, where L(r) is the radius of a circle in which the experimentally counted points inside would otherwise be uniformly distributed[217]. Thus, Ripley H is a measure of the deviation from uniform distribution, H(r) = 0, with positive deviations corresponding to ''attractive'' clustering of objects. The clustering results were validated against simulated negative and positive controls, which were point clouds generated respectively from random 2D coordinates or points on a square lattice with rms noise of half the lattice spacing (MATLAB). Nearest neighbour distances were calculated using the minimum value of H(r) associated with the initial negative H(r) values, values were averaged over all cells to provide a mean value ±

standard error of the mean. Clustering gradients were determined as the peak of a kernel density estimate of gradient values calculated pairwise between adjacent H(r), with a kernel width of 0.001. Cluster analysis was performed in collaboration with Dr Alex Payne-Dwyer.

2.5. Confocal and traditional fluorescence imaging

2.5.1. Confocal imaging of CHO-CCR5

Samples of CHO-CCR5 labelled with Alexa Fluor 488-MC5 and exposed to Alexa Fluor 647-CCL5, both with and without pre-treatment with MVC and TAK, were prepared using the steps outlined above (2.3.1 Preparation of CHO-CCR5 for SIM imaging).

Cells were imaged using an LSM 980 laser scanning confocal microscope (Zeiss) in the Technology facility (University of York) employing Zen imaging software (Zeiss). Optically sectioned images were taken from the basal membrane through to the apical membrane of the cell. Images underwent LSM plus deconvolution (Zeiss) to improve signal-to-noise ratio and resolution. Image stacks of CHO-CCR5 obtained using confocal underwent maximum z-axis intensity projection using ImageJ/Fiji to give representation of overall cell expression. Maximum z-axis intensity projections corresponding to CCR5 signal and those corresponding to CCL5 signal were overlaid for each cell to create dual-colour images.

2.5.2 Traditional fluorescence imaging of CHO-SNAP-CCR5

Transiently transfected CHO-SNAP-CCR5 labelled with SNAP-Surface Alexa Fluor 647 were prepared using the steps outlined above (2.3.1 Preparation of CHO-CCR5 for SIM imaging). Cells were imaged using an Axiovert inverted widefield epifluorescence microscope (Zeiss) combined with a Retiga E7 CMOS camera (Teledyne). Images underwent contrast matching using ImageJ/Fiji.

2.6. PaTCH imaging

2.6.1. Preparation of CHO-GFP-CCR5 for PaTCH imaging

CHO-GFP-CCR5 were grown in a 10 cm dish to confluency prior to being detached using Trypsin-EDTA following the detachment protocol outlined above. Cells were seeded onto 1.5 mm thick round coverslips seated in a 24-well tissue culture plate at a concentration of 1:20

in 250 µl of culture medium. Seeded coverslips were incubated at 37 ºC and 5% CO^2 for 48 hours to allow cell reattachment and growth to a confluence of approximately 30%.

Prepared coverslips were inspected using a compound microscope to ensure cell health and attachment. Culture medium was aspirated and replaced with 400 µl of PBS which was in turn aspirated, forming a PBS washing step. PBS washing was carried out 3 times prior to the addition of 250 µl of PBS containing 3% formaldehyde for 20 minutes for the fixation of cells. After fixation, cells underwent 3 PBS washes and coverslips were mounted on glass slides as outlined above (2.3.1 Preparation of CHO-CCR5 for SIM imaging).

2.6.2. Preparation of CHO-SNAP-CCR5 for PaTCH imaging

Transiently transfected CHO-SNAP-CCR5 labelled with SNAP-Surface Alexa Fluor 647 were prepared using the steps outlined above (2.3.1 Preparation of CHO-CCR5 for SIM imaging).

2.6.3. imaging of cells using PaTCH microscopy

Imaging was performed on a custom-built single-molecule Slimfield microscope developed in the lab of Professor Mark Leake (University of York), as previously described[1,200,201,206]. Alteration of this microscope for Partially TIRF-coupled HILO (PaTCH) microscopy acquisition saw the optimisation of the angle of excitation beam delivery for the imaging of the basal membrane of mammalian cells[218], thereby distinguishing this mode from the traditionally used TIRF and HILO modes. The angle of incidence of the excitation beam in the PaTCH imaging mode was set to a sub-critical angle of 55° by translation of a telescope lens, as calibrated using the lateral displacement of the beam downstream of the focal plane[199]. At this angle, it was estimated that approximately 30% of the incident light is coupled into a reflected TIRF mode, with the associated enhancement of the excitation field at the surface. The remaining light couples into transmitted HILO modes, which extend the excitation field into regions of the basal membrane not directly contacting the coverslip, but not the interior of the cell.

The samples were illuminated using either brightfield illumination or using a 488 nm wavelength laser (Coherent OBIS LX) that was spatially filtered to the TEM00 transverse mode. The objective lens utilised was a 100x, NA 1.49 oil-immersion lens (Nikon ApoTIRF,). The illumination area was approximately 60 µm wide in the sample plane as characterised using a sample of immobilised standard fluorescent microbeads (Promega), this width corresponds to the distance from the beam axis over which the intensity of the illumination

drops to $1/e^2$ of the peak intensity. The laser power at the source was 30 mW, corresponding to an excitation intensity of approximately 0.5 kW/cm^2 at the sample plane.

The approximate focal plane corresponding to the basal membrane of mammalian cells was determined using brightfield illumination. The focal plane was fine-tuned using a sacrificial cell under 488 nm illumination. Field of view was shifted to a neighbouring cell using brightfield illumination prior to 488 nm imaging of this cell, thereby minimising any undesired photobleaching within the cell prior to image capture. A single sequence of images was captured for each field of view in OME TIFF format using a Prime 95b camera (Teledyne Photometrics). The exposure time was 10 ms per frame, during which the laser was digitally triggered, and a total framerate of 77 fps over 1000 - 3000 frames at 53 nm/pixel magnification. The estimated lateral resolution is 180 nm, while the localisation precision of each focus is approximately 40 nm[219]. The detection performance was characterised using in vitro recombinant GFP (abcam) immobilised to a coverslip[220–222].

2.6.4. Stoichiometry analysis of PaTCH images

PaTCH images underwent processing using the custom in-house software suite ADEMScode (MATLAB, MathWorks) (GitHub)[1,223]. Within each frame of a given image sequence, foci were identified as local maxima in fluorescent intensity inside a circular region of interest (ROI) with an 8-pixel radius above the local background signal, averaged over a surrounding square ROI with an area of 17 x 17 pixels. The super-resolved centroid, width and integrated intensity (sum of pixel values with background subtraction) of each focus was established through the fitment of a gaussian intensity mask and all foci underwent thresholding using signal-to-noise ratio (SNR). The SNR of a given focus was defined as the background-subtracted integrated intensity of the circular ROI divided by the standard deviation of pixel values displayed by the respective square ROI, with the minimum SNR for foci to be accepted being 0.4[201,224]. Foci identified in consecutive frames were linked into tracks if they displayed both a persistent overlap of 75-100% and an intensity ratio of 50–200%. Once tracks were identified, the initial intensity of each track was determined through backwards linear extrapolation across the first 5 frames of the image sequence to the time point of initial laser exposure.

The characteristic intensity associated with a single GFP (iSingle value) was estimated as the modal brightness of foci after a period of sufficient photobleaching, thereby ensuring the presence of single molecules[222]. This value was sense-checked through comparison with values of single-molecule brightness obtained through the imaging of immobilised recombinant GFP and values obtained via the determination of monomeric intensity intervals

of tracks undergoing stepwise photobleaching, identified by a Chung–Kennedy edge-preserving filter[206,225–227]. In order to determine the number of GFP-CCR5 fusions present within each tracked focus, the initial intensity of the track was divided by the characteristic intensity of a single GFP, as determined above[228]. Analysis of track stoichiometry was limited to tracks determined in the first 10 frames of the image sequence in order to avoid the underestimation of track stoichiometry due to photobleaching.

The representation of the collated stoichiometries of all tracks for a given condition used kernel density estimate (KDE) plots. The employment of KDE plots served to reduce subjective bias in the determination of heterogeneity, relative to histograms, where an excess of bins can lead to the suggestion of increased heterogeneity, while too few bins can mask heterogeneity[229]. The kernel width associated with these plots was set as 0.6 molecules, a value which corresponds to the root mean squared (rms) detection sensitivity of the integrated intensity of a single GFP molecule in a focus. Alternatively, collated values of stoichiometry were represented, alongside number of tracks per cell, as violin distributions with overlaid jitter distributions, alongside bars boxes and whiskers denoting the median, interquartile range (IQR) and 2.5 x interquartile range respectively (MATLAB). Collated values of stoichiometry were also represented using a jitter distribution, overlaid with the mean intensity of the respective condition (Origin). Jitter distributions displayed dots spread horizontally to allow individual visualisation.

The periodicity associated with the collated stoichiometries of a given condition was calculated by sorting the stoichiometry values[230] and taking the nearest neighbour differences[224]. Stoichiometry intervals were likewise represented using a KDE plot with a kernel width of 0.6 molecules. The resultant periodicity was determined as the modal peak value within this plot. The error in the periodicity estimate was determined as the product of 0.6 molecules and the square root of the ratio of the mean stoichiometry and the number of extrapolation points, divided by the number of tracks contained in the modal peak.

2.6.5. Intensity analysis of PaTCH images

Image sequences of CHO-GFP-CCR5 and CHO-SNAP-CCR5 cells were represented as maximum intensity projections. Projections were taken after an initial period of photobleaching (100^{th} frame to the final frame) to facilitate the determination of cell boundaries and subsequent segmentation of cells. Segmentation and intensity measurements were carried out as described above (2.3.3 Intensity analysis of CHO-CCR5). Collated values of intensity across all cells were displayed as Jitter plots to facilitate the determination of cell sub-populations.

2.6.6. Comparison of PaTCH, TIRF and HILO imaging modes

CHO-GFP-CCR5 were imaged using Slimfield microscopy given a varied angle of incidence of the excitation beam, corresponding to HILO (45°), PaTCH (55°) and TIRF (62°) imaging modes, as described[1]. In order to minimise the effect of photobleaching in the comparison of imaging modes, cells underwent a 10 s (750 frame) pre-bleach under epifluorescence illumination. Image sequences comprising 100 frames were acquired under HILO, PaTCH and TIRF imaging modes sequentially. Image stacks were represented as maximum intensity projections under each condition. GFP-CCR5 puncta were localised and segmented using intensity thresholding, with the resultant spatial distribution of puncta being overlaid between conditions and thereby allowing the identification of puncta present across imaging modes. The signal of puncta was determined as the raw integrated density captured within a circular window 6-pixels in diameter. The associated background was determined as the raw integrated density under the same circular window shifted to the adjacent area surrounding the puncta. Both signal and background measurements underwent global background subtraction, with global background being determined as the average raw integrated density present in the extracellular area across all three imaging modes. Mean values for the signal to background ratio of puncta were determined using 10 puncta for each imaging mode. Error associated with these averages is the standard error of the mean.

2.7. Figures and graphs

Figures were created using MATLAB, Origin, CytExpert, Zen or ImageJ/FIJI, unless otherwise stated. Illustrative figures were created using Microsoft PowerPoint or Biorender.com.

2.8. Statistics

For statistical tests reported in **Figure 4-11**, MATLAB was used to perform the nonparametric Brunner-Munzel test, as reported[1]. A conservative Bonferroni-adjusted significance level was employed to account for multiple comparisons within samples ($\alpha = 0.05/5 = 0.01$). Values for N and p are reported alongside the figure, with N representing either the number of cells or the number of foci in the sample. Significant stochastic inequality of the populations under

comparison is denoted using an asterisk (*) indicating that $p < 0.01$. Brunner-Munzel statistical tests were performed by Dr Alex Payne-Dwyer. Due to the underlying distributions and variances not being known a priori, a target sample size of $n \leq 5$ cells (and $n \leq 24$ tracks) per condition was estimated. These targets were based on a minimum detection level of 1 sd at 80% power under normal statistics for a one-tailed or two-tailed Z-test respectively. Cell cultures were assigned randomly for ligand ± groups, as described[1].

Statistical evaluation of variance amongst overall cellular intensities in populations of CHO-CCR5 and CHO-GFP-CCR5 was carried out in Origin (OriginLab) using the nonparametric Kruskal–Wallis one-way analysis of variance (KW-ANOVA) test alongside subsequent Dunn's testing, results were determined relative to a significance level of 0.05 (ns - $P > 0.05$, * - $P \leq 0.05$, ** - $P \leq 0.01$, *** - $P \leq 0.001$, **** - $P \leq 0.0001$).

3. Revealing the super-resolved spatial distribution of CCR5 and the effect of agonists and antagonists on CCR5 behaviour

3.1 Introduction

Previous investigations of the chemokine receptor CCR5 have employed immortalised cell lines modified for the over-expression of CCR5. In the case of fluorescence microscopy-based experiments, these cell lines have been studied using immunofluorescence staining to enable receptor detection. Using these techniques, previous studies have aimed to determine characteristics of CCR5, such as its expression levels and overall cellular distribution[60,63,66]. However, these investigations have relied upon traditional fluorescence and confocal microscopy techniques which offer a resolution that is limited by the optical diffraction limit of light. The restricted spatial resolution that traditional techniques offer can provide basic information regarding overall CCR5 characteristics but is unable to resolve finer details in the arrangement of receptor assemblies.

The advent of super-resolution techniques, which can surpass the optical diffraction limit of light, has provided a clear advancement opportunity in the determination of CCR5 characteristics. Utilising a CHO cell line stably expressing CCR5 at a high level (CHO-CCR5), coupled with fluorescent antibodies specific to the CCR5 receptor, this project aims to provide hitherto unseen super resolution detail of CCR5 behaviour. Utilising structured illumination microscopy (SIM), we aim to unveil the super-resolved spatial distribution of CCR5 in mammalian cells, thereby revealing characteristics of the CCR5 receptor that are inaccessible using traditional techniques. Previous studies comparing receptor conformation and internalisation in both CHO-CCR5 and a variety of human immune cells indicate cell-type specific regulation of CCR5[69]. As the difference in behaviour between CCR5 expressed within human immune cells and CCR5 expressed in non-immune cell models are not fully understood, extensive investigation of the receptor would benefit from the use of a range of human immune cells. However, the lack of endogenous CCR5 and related chemokine receptors within the CHO cell line[63], coupled with the flat adherent cell morphology and amplified receptor expression offered, highlights CHO-CCR5 as an ideal model for the isolated study of CCR5 using super-resolution techniques.

These techniques also afford the ability to investigate ligand-mediated changes in the spatial distribution of CCR5. In the case of the CCR5 agonist CCL5, it is expected that CCL5-

mediated activation leads to CCR5 endocytosis. However, the changes in CCR5 distribution and overall surface levels upon exposure to CCL5 have yet to be studied in super-resolution. In addition, super-resolution investigations of CCR5 antagonists, such as the FDA approved HIV therapeutic Maraviroc (MVC)[130], would allow for insight as to how MVC impacts on CCR5 to inhibit CCL5-mediated activation. The small molecule MVC is thought to bind deep within the CCR5 transmembrane bundle, inducing a conformational change that inhibits receptor function. The identification of MVC, alongside the alternative small-molecule TAK-779 (TAK), as allosteric modulators of receptor function are supported through biochemical, structural and mutagenesis studies, although it remains unclear whether MVC inhibits the initial binding of the chemokine-core to the primary binding site[45,46,131,132]. This study also aims to extend super resolution investigation to the study of the prospective therapeutics 5P12 and 5P14 on CCR5-CCL5 interactions. 5P12 and 5P14 are N-terminally altered analogues of CCL5 initially developed as HIV therapeutic candidates, with both being reported not to induce G protein-linked signalling activity. However, they vary in their ability to mediate CCR5 internalisation, with 5P14 being reported to induce CCR5 internalisation and 5P12 being reported to display no induction of CCR5 internalisation[137,139,140]. The use of fluorescently labelled CCL5 will allow the determination of CCL5-cell association, alongside the determination of CCR5 spatial distribution, in the presence of these small molecule antagonists and CCL5-analogues, thereby helping to interpret and confirm their respective modes of action.

3.2. Structured illumination microscopy reveals CCR5 expressed evenly across the basal membrane of CHO-CCR5

Super-resolution investigations into mammalian cells benefit from the maximisation of signal while retaining a high level of specificity to the target biomolecule, thereby increasing the achievable signal to background ratio. For this purpose, SIM studies investigating CCR5 employed CHO-CCR5 cells, for which previous bulk ensemble and diffraction-limited studies had been performed[60,63,66,210]. Fluorescent emission intensity and biomolecule specificity was ensured through the employment of CCR5-specific surface immunolabelling using the CCR5 Monoclonal antibody MC-5, itself labelled with the fluorophore DyLight 650 (see methods 2.4.1). The employment of CHO cells above other immortalised cell lines was informed by characteristic traits of CHO cells, such as ready adherence to glass surfaces and flat uniform morphologies when fixed, that highlight them as an ideal candidate for microscope-based studies of membrane proteins. As illustrated in **Figure 3-1a**, in preparation of the microscopy studies detailed in this chapter, larger cultures of CHO-CCR5 are divided and cultured directly onto circular glass coverslips that are housed within isolated wells of a multi-well

plate. The direct growth of cells onto coverslips allows for the optimisation of cell density and flatness of the basal membrane. Additionally, the placement of coverslips into individual wells of the same 24-well plate allows for selective treatment of individual samples whilst minimising extraneous variables between samples. Once the cells have undergone treatment, they are fixed and immune-stained (see methods section 2.4.1), coverslips are mounted on glass slides for microscopy.

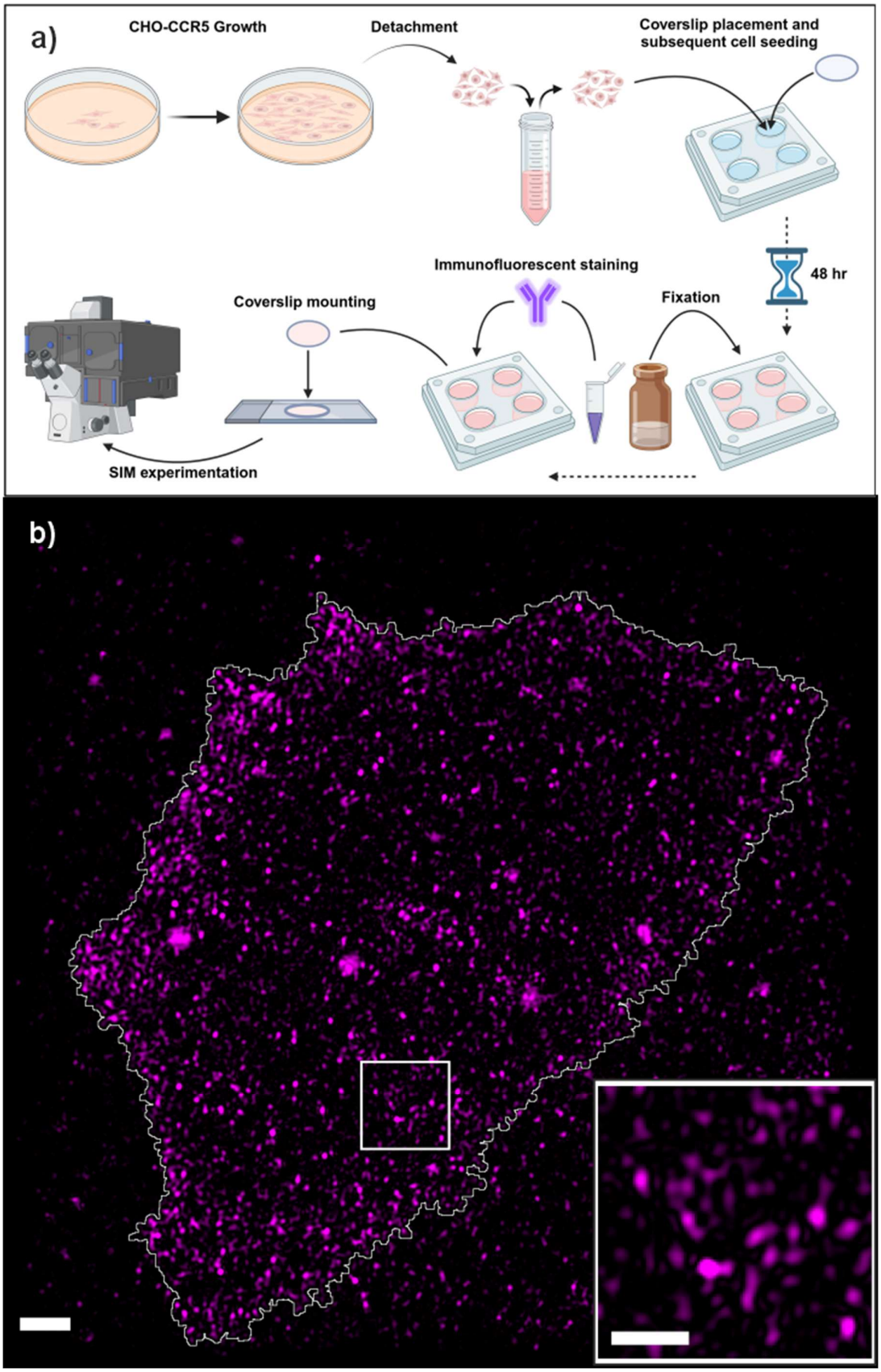
a)
CHO-CCR5 Growth
Detachment
Coverslip placement and subsequent cell seeding
48 hr
Immunofluorescent staining
Fixation
Coverslip mounting
SIM experimentation
b)

Figure 3-1: Experimental outline underpinning mammalian cell SIM imaging. a) Illustration demonstrating the preparation of CHO-CCR5 for fixed cell imaging. (Illustration created with BioRender.com). b) SIM image of a representative CHO-CCR5 cell labelled with DyLight 650-MC5. Image acquired at the basal membrane of the CHO-CCR5 cell with a bordering cell located below and to the right. Image demonstrates white cell boundary segmentation that aids in downstream analysis and includes a magnified inset of the basal membrane demonstrating the spatial distribution of CCR5. (Scale bar 2 μm, (magnified insets 1 μm)).

Initial study of the basal membrane of CHO-CCR5 using SIM revealed a distinct expression of CCR5 throughout the basal membrane, as demonstrated in the representative image shown in **Figure 3-1b**. The expression of CCR5 populations within defined puncta can be seen across the basal membrane, with the number of these puncta being spread across the membrane and the size and proximity of puncta showing variance. Further, this image demonstrates the flat and adherent nature of the basal membrane of CHO-CCR5, allowing for the segmentation of individual cells. The cell highlighted in **Figure 3-1b** neighbours a bordering cell to its right and open coverslip to its left, demonstrating the isolation of fluorescence to CCR5-expressing membrane. Further, the inclusion of a magnified inset of the basal membrane highlights the shape and proximity of CCR5 puncta.

Certain cells sampled presented variance in their morphologies, including the presence of membrane protrusions. Although these filopodia are not of high biological relevance to this investigation, the extensions of the representative cell shown in **Figure 3-2** serve to illustrate the higher spatial resolution and image contrast of SIM over traditional widefield microscopy. Employing traditional widefield techniques for the study of CHO-CCR5 allows for the approximate investigation of cell morphology and general CCR5 distribution, as shown in **Figure 3-2a**. However, the employment of SIM reconstruction reveals the finer structure of CCR5 expression within the membrane, as shown in **Figure 3-2b**. This improved image quality, coupled with the optical sectioning property of SIM, aid quantitative analysis of image data and enable puncta of CCR5 assemblies to be isolated from the cellular background through intensity thresholding.

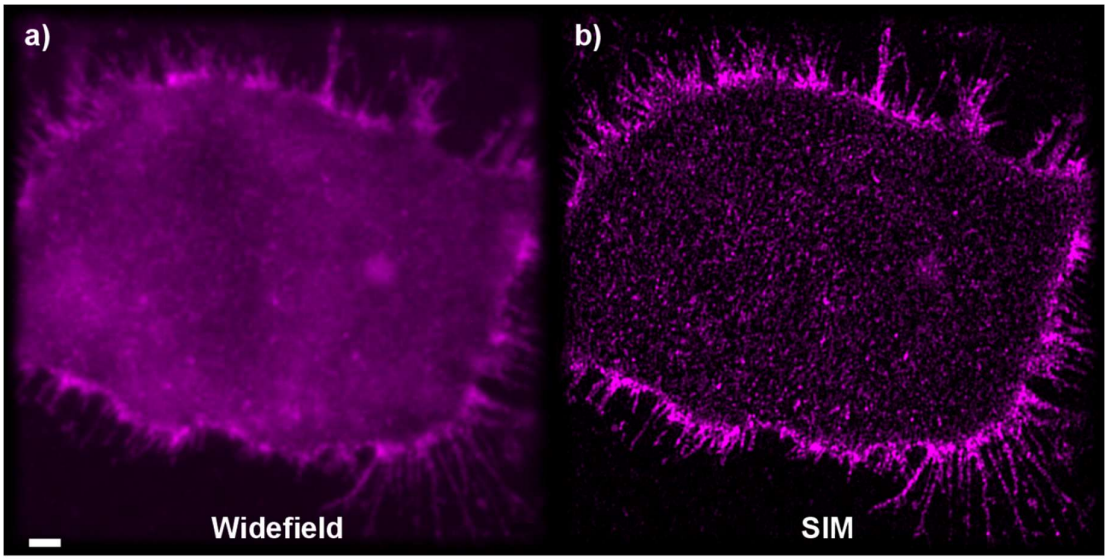

Figure 3-2: Comparison of spatial resolution between widefield and super resolution techniques. a) Widefield image of a representative CHO-CCR5 cell labelled with DyLight 650-MC5. Image was acquired at the basal membrane of the CHO-CCR5 cell and was selected for demonstration due to the fine filopodia structure displayed by this cell. b) SIM reconstruction of the cell shown in a), demonstrating the improvement in spatial resolution upon reconstruction. (scale bar 2 µm).

3.3. 3D visualisation of the membrane reveals that CCR5 is evenly dispersed across the entire cell membrane

The optical sectioning capabilities of SIM allows for super resolution images to be acquired in distinct planes along the Z-axis. By imaging from the basal membrane through to the apical membrane, CCR5 expression on CHO-CCR5 was visualised across the whole cell using 3D representations, as shown in **Figure 3-3**. Similar to the single plane SIM images shown in the previous figures of this chapter, the cell shown in **Figure 3-3** is a representative example of CHO-CCR5 labelled with the DyLight-650-MC5. This time, the extension of analysis to multi-plane images requires the correction of photobleaching effects on the fluorescence intensity between planes to accurately represent the 3D distribution. Further representation of these images included the exclusion of background fluorescence located outside the cell.

From the images displayed in **Figure 3-3**, we see further demonstration that membrane-bound CCR5 assemblies appear as distinct puncta uniformly distributed along the basal membrane. However, these images also demonstrate the expression of CCR5 assemblies as puncta across the entire plasma membrane. Due to the external labelling of CCR5, in

cross-sectional images corresponding to planes above the basal membrane puncta are only visible within annulus-shaped regions of the cell surface. Despite the increase in intracellular background signal seen in **Figure 3-3g** due to photobleaching correction, the annular distribution of fluorescent foci is clearly retained. Finally, acquisition of optically sectioned slices allowed the reconstruction of colour depth projections and 3D images, as shown in **Figure 3-3h,i**. These reconstructions enabled the visualisation of this annular distribution of cell surface CCR5, thereby revealing the topology of the cellular exterior while further highlighting the uniformity of the CCR5 distribution.

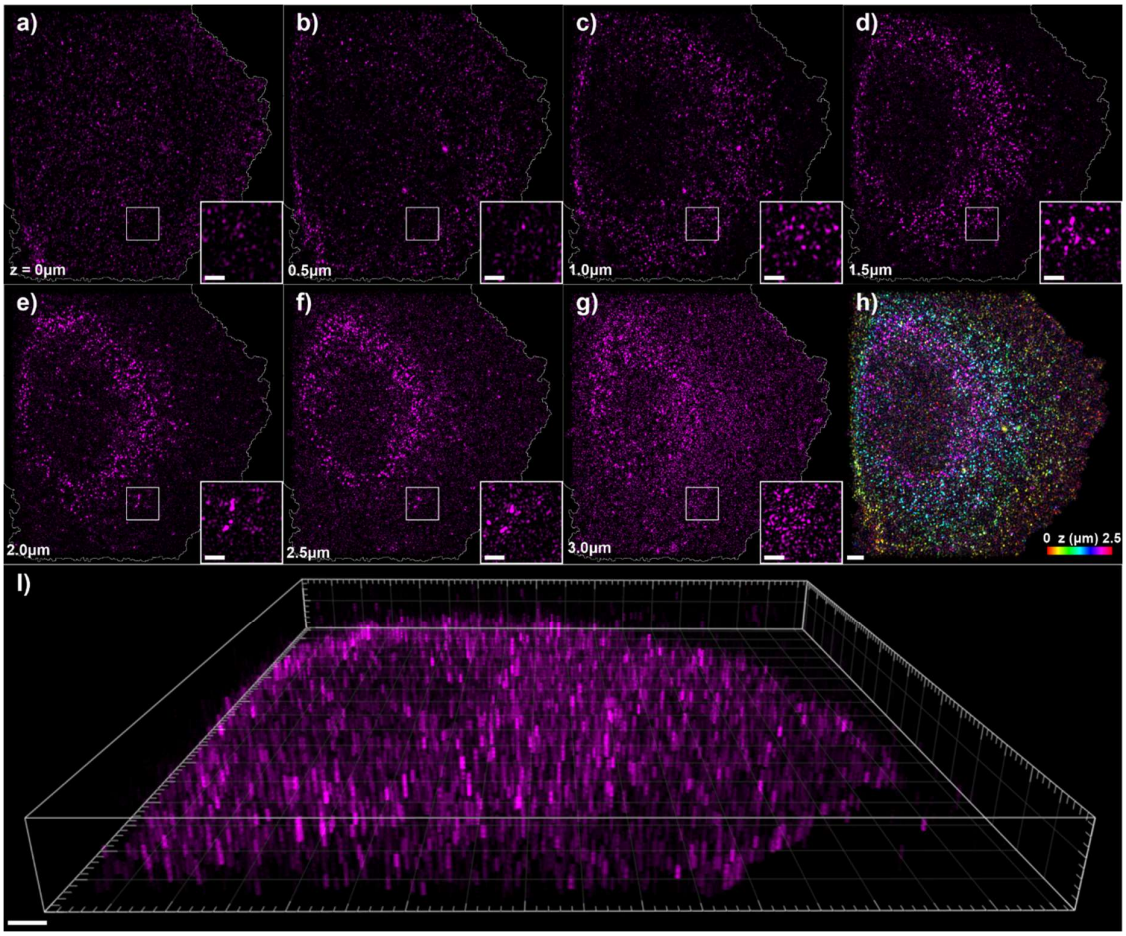

Figure 3-3: SIM images of CHO-CCR5 cells labelled with DyLight 650-MC5 across several focal planes. a - g) Individual SIM image planes of a representative CHO-CCR5 cell, from the basal membrane through to the apical membrane in 500 nm steps (ranging from 0 - 3.0 µm above the basal membrane), displaying cell boundary segmentation (white) and magnified insets. h) Colour depth projection over the images shown in a-f). i) 3D reconstruction of cell images shown in a-g). (Scale bar 2 µm, (magnified insets 1 µm)).

3.4. Ripley's clustering analysis of the basal membrane reveals a non-random spatial distribution

As demonstrated in **Figure 3-2**, the utilisation of SIM allows for clear improvement in our ability to resolve localised clusters of CCR5 assemblies. This improved image quality allows for the quantitative analysis of image data and enables puncta of CCR5 assemblies to be isolated from the cellular background through intensity thresholding (see methods 2.4.4), as shown in **Figure 3-4b**. The investigation of isolated puncta revealed distinct 'hot spots' in the overall spatial distribution of puncta (**Figure 3-4c**), indicating the existence of spatial clustering in the distribution of individual puncta. To examine the spatial arrangement of puncta, clustering analysis was performed using Ripley's H function[217] on centroids determined for individual puncta. As represented in **Figure 3-4d**, analysis is based on the counting of objects at an increasing distance averaged over all possible origin points inside the cell and can be used to describe the level of clustering, uniformity or dispersion of points within a distribution. Visualising the Ripley's H values as a function of radius over the diameter of the cell membrane, we see that a net clustering of objects is characterised by the accumulation of positive Ripley's H values across this diameter, as shown in **Figure 3-4e,f**. The modal clustering gradient thereby provides an estimation of the spatial correlation of CCR5 puncta throughout the basal membrane. Within the basal membrane of CHO-CCR5, this analysis revealed a positive modal average gradient of $dH(r)/dr = 0.004 \pm 0.001$. Additionally, the initial minima displayed in the Ripley's H value distribution provides an estimate for the nearest neighbour distance between CCR5 puncta, with the average for CHO-CCR5 being measured at 290 ± 10 nm across 10 cells.

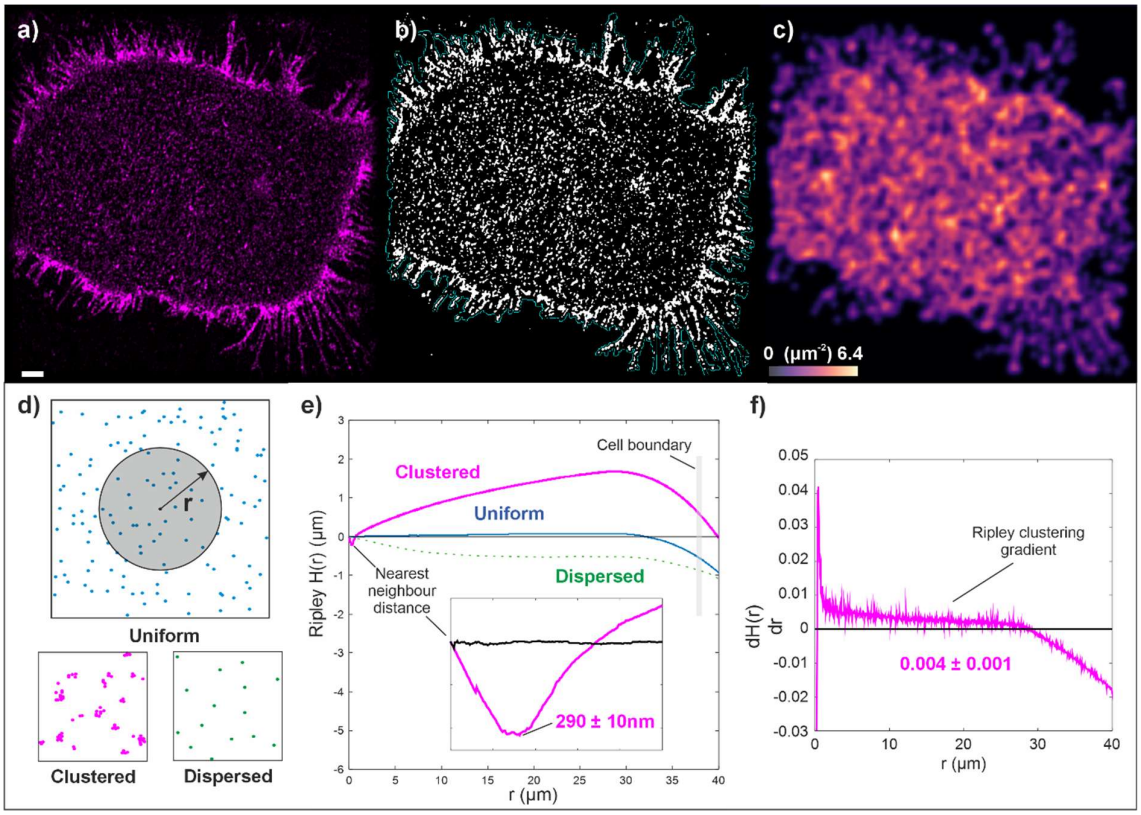

Figure 3-4: Images and quantitative clustering metrics of CCR5 in the basal membrane of CHO-CCR5 cells labelled with DyLight 650-MC5. a) SIM image of the basal membrane of a representative CHO-CCR5 cell (scale bar 2 μm). b) Binarised mask of the SIM image displaying CCR5 puncta isolated through intensity thresholding. c) Number density distribution of individual puncta centroids, ranging from 0 - 6.4 μm-2. d) Illustration demonstrating the function of Ripley's H analysis in the investigation of uniform, clustered and dispersed point distributions. e) Distribution of Ripley's H values for a real representative CHO-CCR5 cell (magenta) and a generated 2D map of points whose displacement separations are sampled from a random Poisson distribution (blue). Also shown is an illustrative curve depicting the expected results of a generic dispersed point distribution (green dotted). Inset shows the same distribution of Ripley's H values for the CHO-CCR5 cell (magenta) and random point distribution (blue) over a range of 0 - 1 μm and provides an average nearest-neighbour distance for binarised CHO-CCR5 puncta (N=10 cells). f) The gradient of the distribution of Ripley's H values for the CHO-CCR5 cell represented in f) which provides a modal average clustering gradient for CHO-CCR5 (N=10 cells). As this gradient is the derivative of H(r) with respect to the radius, this value is unitless.

3.5. Intensity analysis of CCR5 expression confirms agonistic effects of CCL5 and the antagonistic effects of MVC and TAK

The investigation of CCR5 spatial distribution was extend to the study of CCL5-induced effects on the behaviour of the receptor. This study saw the application of SIM to reveal the expression of cell-surface CCR5 both in the steady state and upon exposure to CCL5 over a range of exposure times. Additionally, through the provision of exposure to the small molecule antagonists MVC or TAK within sample-subsets prior to CCL5 exposure, this study aimed to directly visualise the antagonistic effects of these ligands. As shown in **Figure 3-5a,e** a qualitative decrease in the fluorescence intensity of representative CHO-CCR5 cells can be seen corresponding to the extent of CCL5 exposure. Additionally, as shown in **Figure 3-5f,g**, the pre-treatment of CHO-CCR5 with either MVC or TAK before 30-minute exposure to CCL5 interferes with the CCL5-associated reduction in cell surface CCR5. These results are quantified by measuring the mean fluorescence intensity of cell surface CCR5 within each condition after cells have undergone segmentation, as shown in **Figure 3-5h**. **Figure 3-5i** thereby shows a quantifiable reduction in the presence of cell surface CCR5 as a function of CCL5 exposure time, with the mean fluorescence intensity of cell surface CCR5 showing a 42% reduction after 30 minutes of CCL5 exposure. In contrast, cells pre-exposed to MVC and TAK, prior to 30 minutes of CCL5 exposure, showed a 10% and 5% reduction in intensity.

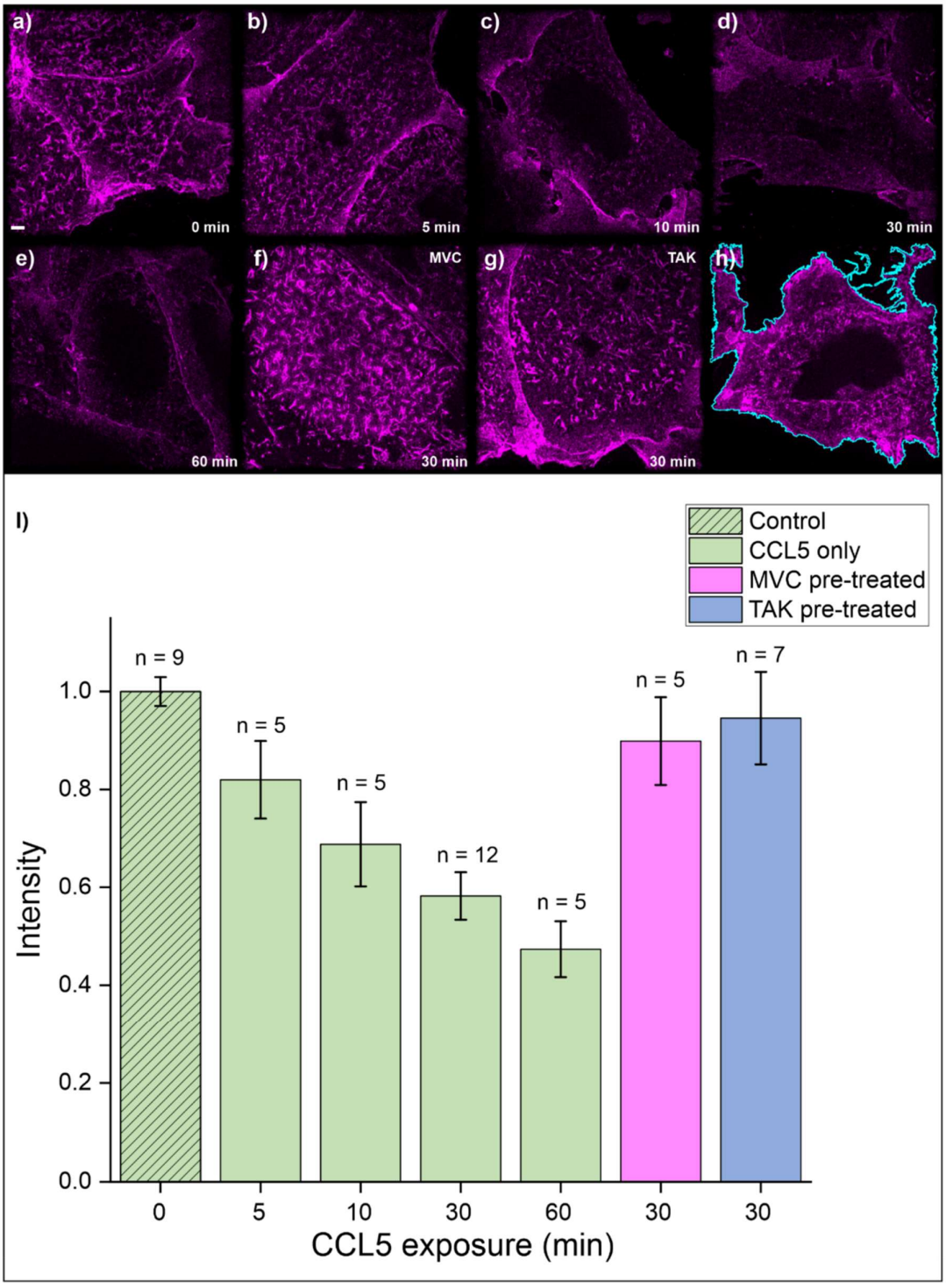

Figure 3-5: Investigating the perturbation of CCR5 with agonist CCL5 and antagonists MVC and TAK using SIM. a) SIM image of a representative fixed CHO-CCR5 cell labelled with DyLight 650-MC5, shown as a maximum intensity z-axis projection of optically sectioned slices acquired from the basal through to the apical membrane (scale bar 2 μm). b-e) SIM images of representative cells from CHO-CCR5 samples exposed to 100nM CCL5 for discrete lengths of time ranging between 5 and 60 minutes. f-g) SIM images of representative cells from CHO-CCR5 samples exposed to CCL5

for 30 minutes after a 30-minute pre-exposure to antagonists maraviroc (MVC) and TAK-779 (TAK) respectively. h) SIM image of a representative cell from a CHO-CCR5 sample exposed to CCL5 for 30 minutes after a 60-minute pre-exposure to maraviroc demonstrating a cell segmentation overlay. i) Bar chart representing the mean fluorescence intensity of DyLight 650-MC5 labelled CHO-CCR5 cells from the samples represented in a-g) across multiple cells from up to 2 separate experiments. (n represents number of cells, error bars represent SEM and intensity values are normalised with respect to the control sample (0 min)).

3.6. Intensity analysis of rhodamine-labelled CCL5 tracer demonstrates antagonist induced inhibition of CCL5-cell association

SIM investigations were further extended to allow the direct visualisation of the cell-association characteristics of CCL5 through the employment of fluorescently labelled CCL5. Through the DyLight 650-MC5 surface labelling of CHO-CCR5 cells after a 30-minute perturbation with CCL5 and a rhodamine-labelled CCL5 tracer, simultaneous measurements of the spatial distribution of CCR5 and CCL5 were possible. Similar to the experiment outlined above, CCL5 perturbation was conducted at a 100 nM concentration but with the employment of a 1:100 ratio of rhodamine-labelled to non-labelled CCL5, as informed by optimisation tests employing higher ratios which resulted in a high extracellular binding of rhodamine-CCL5 to the coverslip. The excess extracellular binding seen in the use of higher concentrations of rhodamine-CCL5 may be the result of CCL5 aggregation and binding to glycosaminoglycans (GAGs) present in the extracellular matrix, with both the oligomerisation and GAG-binding of chemokines providing roles in the formation of chemokine gradients[231]. As shown in **Figure 3-6a,b**, the spatial distribution of DyLight 650-MC5-CCR5 was used to create cellular segmentations. As shown in **Figure 3-6c**, these segmentations allowed the isolation of cell-associated rhodamine signal, thereby allowing the quantification of cell-associated CCL5. Further, through the provision of exposure to antagonists MVC and TAK within sample-subsets prior to rhodamine-CCL5 exposure, this study aims to investigate CCR5-antagonist binding. As shown in **Figure 3-6-d**, a quantifiable reduction in cell-associated rhodmaine-CCL5 can be seen after 30 minutes of agonist exposure, provided antagonist pre-treatments. MVC and TAK pre-treatment can be seen to cause a 13% and 19% reduction in cell-associated rhodamine-CCL5 respectively, thereby suggesting a potential MVC and TAK induced reduction in CCL5 binding.

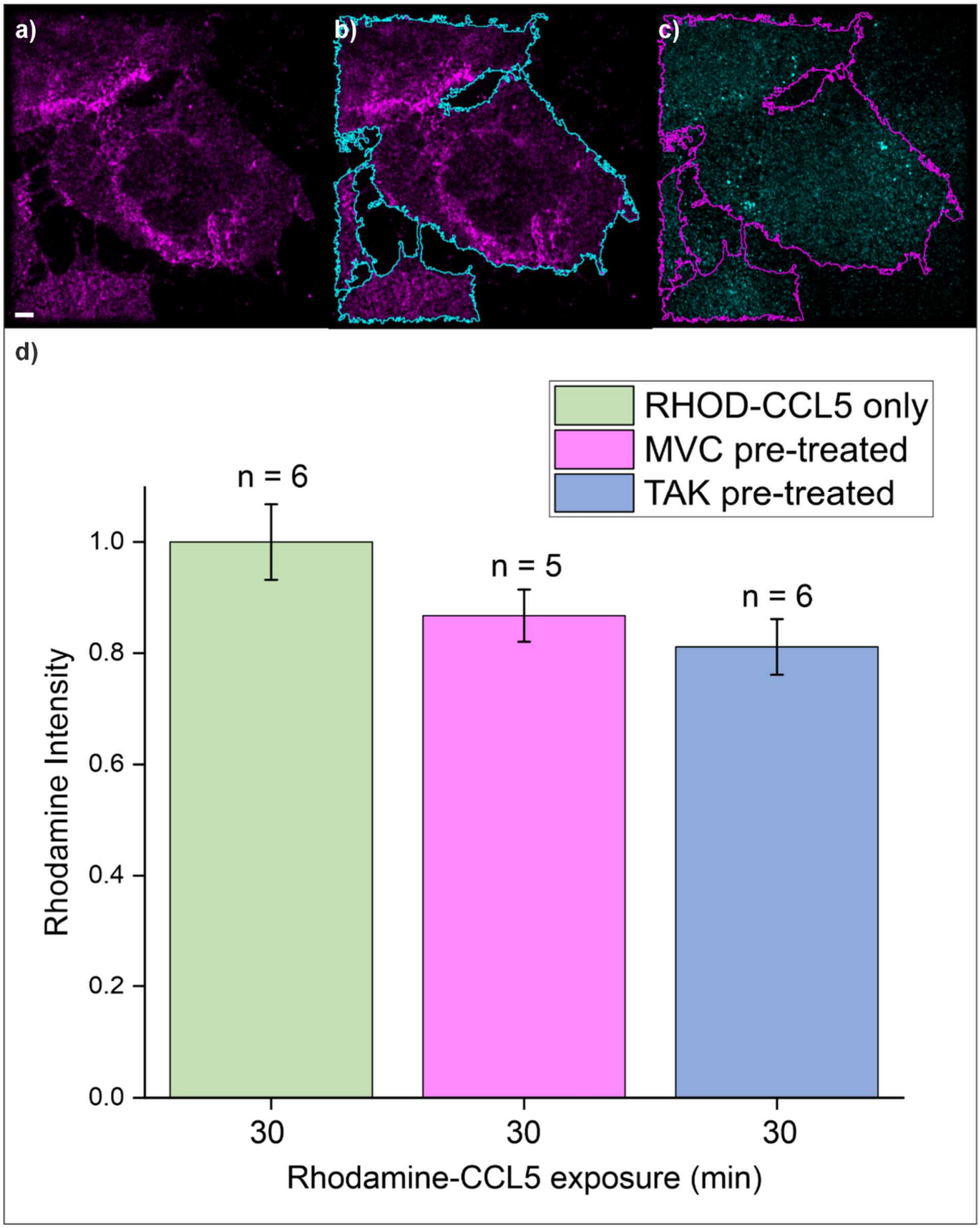

Figure 3-6 Investigating the cell-association of labelled CCL5 using SIM. a) SIM image of a representative fixed CHO-CCR5 cell labelled with DyLight 650-MC5, shown as a maximum intensity z-axis projection of optically sectioned slices acquired from the basal through to the apical membrane (scale bar 2 μm). b) demonstration of cell segmentation over which CCR5-associated fluorescence can be qualitatively seen, overlaid onto the cell seen in a). c) SIM image of rhodamine-CCL5 present on the cell shown in a) after 30 minutes exposure, demonstrating the segmentation over which CCL5-associated fluorescence is quantified. d) Bar chart representing the mean fluorescence intensity of

cell-associated rhodamine-CCL5 on DyLight 650-MC5 labelled CHO-CCR5 cells after 30 minutes of agonist exposure, with or without pre-exposure to antagonists MVC and TAK. Data acquired across multiple cells from up to 2 separate experiments. (n represents number of cells, error bars represent SEM and intensity values are normalised with respect to the control sample (No antagonist pre-treatment)).

3.7. Intensity analysis of CCR5 expression confirms the agonistic effects of CCL5 and the effects of an extended range of CCR5 antagonists and CCL5 analogues

Extension of dual colour studies benefitted from the optimisation of fluorescently labelled perturbations to address the low signal and high background seen in previous results employing rhodamine-CCL5. This was achieved through employment of a commercially available CCL5 that is coupled with the bright Alexa Fluor 647 dye. Initial experimentation employing this dye aimed to determine the optimal concentration of Alexa Fluor 647-CCL5 to visualise CCL5-dependent changes in CCR5 presentation while reducing background signal. These experiments were performed on a confocal microscope, a system that provides a lower resolution than SIM but facilitates the rapid course screening of CCR5 and CCL5 associated fluorescence within sample sets. **Figure 3-7** shows representative examples of the CCR5 and CCL5 distribution in CHO-CCR5 cells with or without 30 min exposure to 10nM CCL5 and with or without pre-exposure to the CCR5 antagonists MVC and TAK, with all images shown as dual-colour maximum intensity z-axis projections of optically sectioned slices throughout the cell.

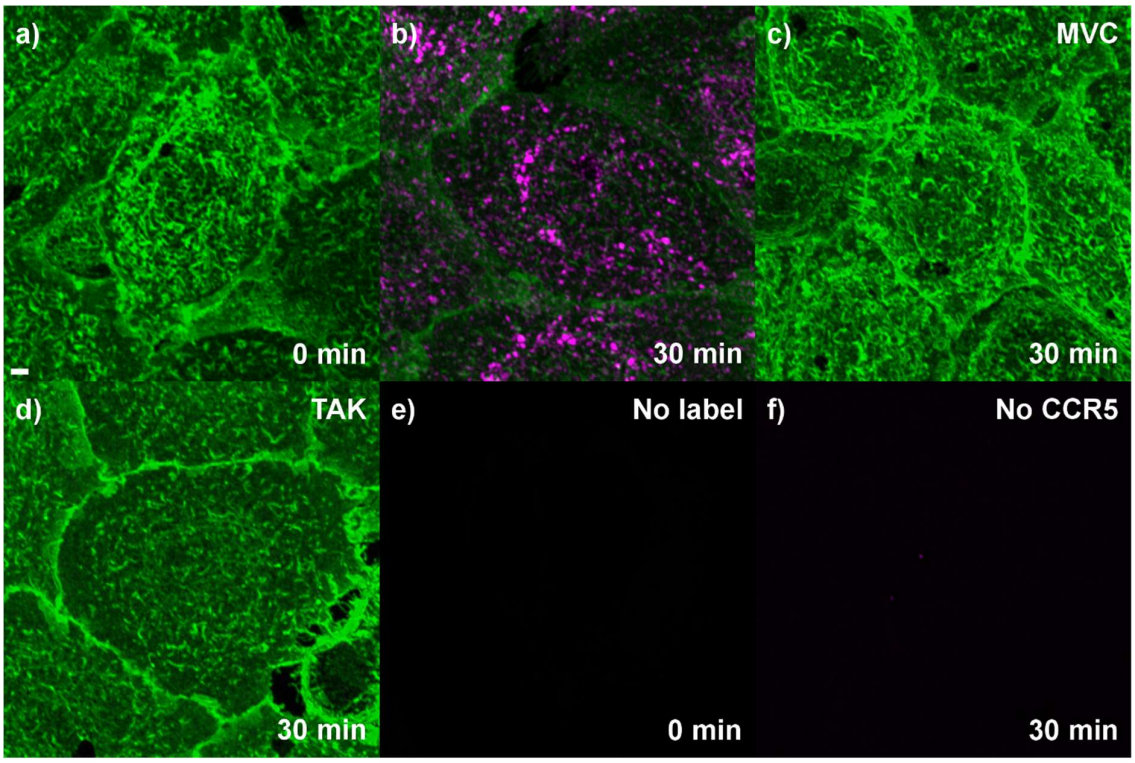

Figure 3-7: Confocal-based screening of Alexa Fluor 647-CCL5 concentration on CHO-CCR5. a) Confocal image of a representative fixed CHO-CCR5 cell labelled with Alexa Fluor 488-MC-5 (scale bar 2 μm). b) Confocal image of a representative cell from a CHO-CCR5 sample exposed to 10 nM Alexa Fluor 647-CCL5 for 30 minutes. c-d) Confocal images of representative cells from CHO-CCR5 samples exposed to Alexa Fluor 647-CCL5 for 30 minutes after a 30-minute pre-exposure to antagonists maraviroc (MVC) and TAK-779 (TAK) respectively. e) Confocal image of a representative cell from a CHO-CCR5 sample that did not receive antibody staining. f) Confocal image of a non-CCR5-expressing CHO cell labelled with Alexa Fluor 488-MC-5 and exposed to Alexa Fluor 647-CCL5 for 30 minutes. All images are shown as maximum intensity z-axis projections of optically sectioned slices acquired from the basal through to the apical membrane with both 488 and 647 associated fluorescence displayed. All images are contrast matched with respect to one another in both 488 (green) and 647 (magenta) channels.

As can be seen in **Figure 3-7a**, confocal-based images of CHO-CCR5 reveal a similar CCR5 (green) distribution to those found using SIM but at a lower resolution. Further, the absence of 647-associated fluorescence (magenta) in this dual-colour image indicates a negligible level of cellular autofluorescence captured in the 647 channel. Upon exposure to CCL5, a decrease in the intensity of CCR5 can be seen alongside strong binding of CCL5, with bound CCL5 distributed in distinct puncta throughout the cell, indicating CCL5-mediated internalisation of CCR5, as shown in **Figure 3-7b**. In contrast, cells that received pre-

exposure to the CCR5 antagonists MVC and TAK display a negligible signal in the 647 channel and retain a high level of CCR5 expression, with cells exposed to MVC displaying a slightly higher expression, as shown in **Figure 3-7c,d**, thereby indicating the ability of these antagonists to interfere with CCL5 binding and subsequently inhibit effective CCR5-CCL5 binding and associated downstream internalisation. The inclusion of non-labelled control cells reveals that CHO-CCR5 displays negligible 488-associated autofluorescence in the absence of CCR5-labelling and the inclusion of labelled and CCL5-perturbed non-CCR5 expressing CHO cells reveal a negligible level of non-specific Alexa Fluor 647-CCL5 binding, as shown in **Figure 3-7e,f**. Comparison of this data with those obtained using a low ratio rhodamine-CCL5 tracer in the previous figure presents a much stronger indication of CCL5-CCR5 interaction. This disparity may indicate the effect of a higher total concentration of CCL5 on the strength of aggregation and GAG-association.

The employment of the improved protocol for dual colour CCR5-CCL5 imaging was extended to SIM in order to provide an increased spatial resolution and quantifiable metrics on CCL5 binding alongside CCR5 surface expression, with the addition of samples pre-exposed to a wider range of CCR5 antagonists providing further insight into their function. The range of CCR5 antagonists employed in this study was extended to include the CCL5-analogues 5P12-RANTES (5P12) and 5P14-RANTES (5P14), which were initially developed as candidates for an effective CCR5-targeted HIV therapeutic[138]. **Figure 3-8** shows representative SIM images of the CCR5 distribution in CHO-CCR5 provided varying exposure to CCL5 and with or without pre-exposure to the CCR5 antagonists MVC and TAK, 5P12 and 5P14, with all images shown as single-channel maximum intensity z-axis projections of optically sectioned slices throughout the cell. As shown in **Figure 3-8a**, non-perturbed CHO-CCR5 cells display high expression of CCR5 with minimal extracellular background fluorescence. Upon exposure to CCL5, the overall surface expression of CCR5 can be seen to reduce proportionally to the extent of CCL5 exposure (**Figure 3-8b,e**), thereby supporting our previous results obtained in SIM studies employing non-labelled CCL5 and confocal studies employing labelled CCL5. Samples exposed to CCL5 for 30 minutes following pre-exposure to antagonists MVC and TAK provide support to previously shown SIM and confocal studies, with both antagonists effectively preventing CCL5-induced internalisation of CCR5, and likewise suggest a MVC-induced enhancement of CCR5 expression, as shown in **Figure 3-8f,g.**

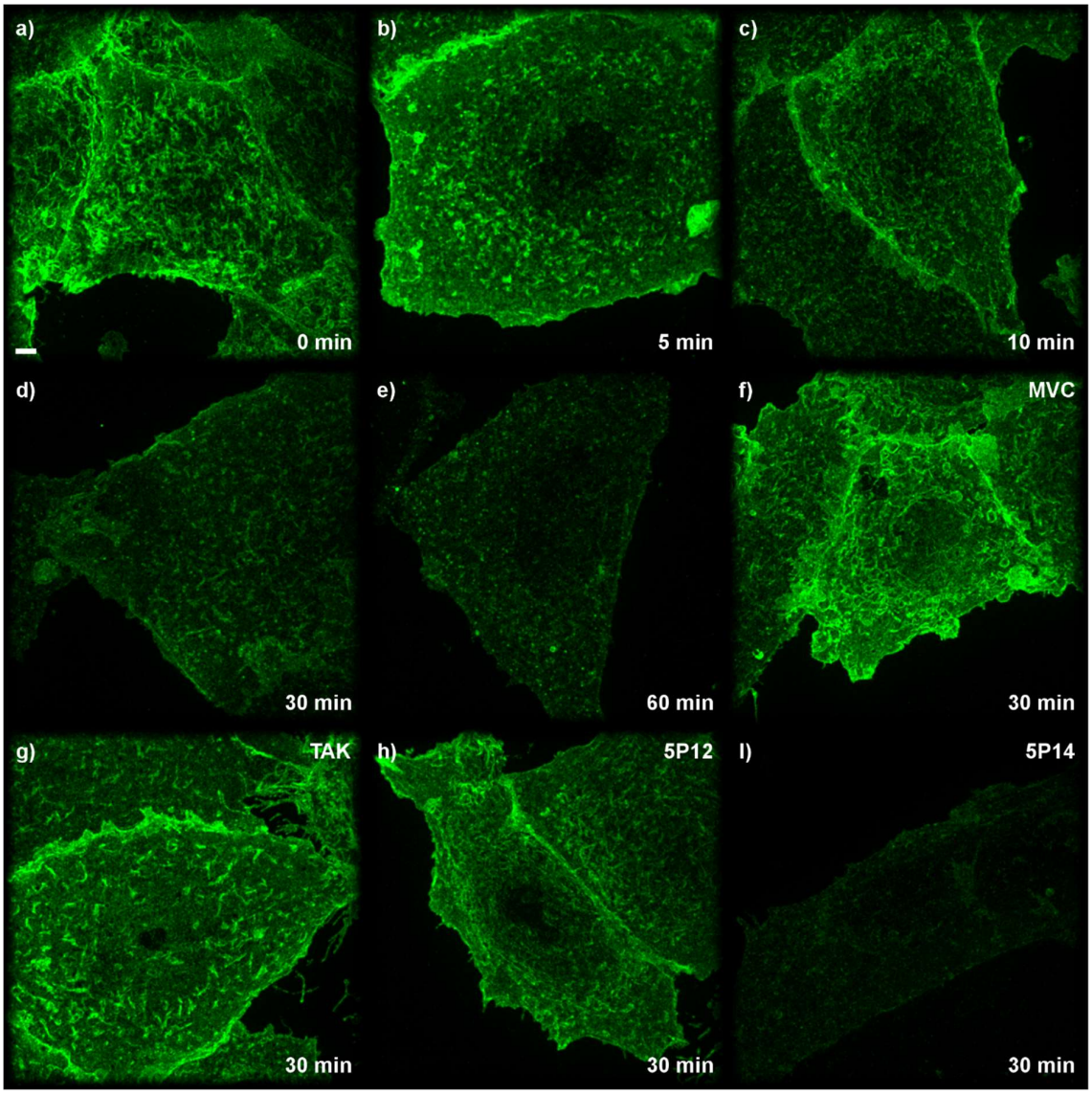

Figure 3-8: 488-based SIM imaging of CHO-CCR5 exposed to labelled CCL5 and a range of CCR5 antagonists and other CCL5 analogues. a) SIM image of a representative fixed CHO-CCR5 cell labelled with Alexa Fluor 488-MC-5 (scale bar 2 μm). b-e) SIM images of representative cells from CHO-CCR5 samples exposed to 10 nM Alexa Fluor 647-CCL5 for discrete lengths of time ranging between 5 and 60 minutes. f-i) SIM images of representative cells from CHO-CCR5 samples exposed to Alexa Fluor 647-CCL5 for 30 minutes after a 30-minute pre-exposure to small molecule antagonists maraviroc (MVC) and TAK-779 (TAK), as well as CCL5 analogues 5P12 and 5P14 respectively. All images are shown as maximum intensity z-axis projections of optically sectioned slices acquired from the basal through to the apical membrane. All images are contrast matched with respect to one another.

Studies of the extended range of CCR5 antagonists confirm that 5P12 operates as an efficient inhibitor of CCL5-induced internalisation, with resultant CCR5 expression at a similar level to cells pre-exposed to TAK, as shown in **Figure 3-8h**. However, as seen in

Figure 3-8i, cells that received pre-exposure to 5P14 prior to CCL5 exposure display a drastic reduction in CCR5 surface expression that surpasses that of 30 min of lone CCL5 exposure, confirming that 5P14 induces significant CCR5 internalisation as previously reported[138].

Quantification of this study was achieved through the measure of total cellular CCR5 expression, with many cells imaged per sample allowing for an average to be calculated in each condition. As in previous experiments, overall CCR5 intensity was calculated in each optically sectioned image by measuring the average intensity within a segmented maximum intensity z-axis projection. As shown in **Figure 3-9** a quantitative decrease in the fluorescence intensity of CHO-CCR5 cells can be seen corresponding to the extent of CCL5 exposure, a result that supports previous SIM findings employing DyLight 650 labelled CCR5 and non-labelled CCL5. Additionally, these results show a large reduction in CCR5 expression after 10 minutes of CCL5 exposure, with a 27% reduction in CCR5-associated fluorescence when compared with the non-perturbed sample. In comparison, there is a 32% and 36% reduction in CCR5-associated fluorescence after 30 and 60 minutes of CCL5 exposure, respectively, indicating 10 minutes as the time interval over which the majority of CCL5-induced internalisation takes place, beyond which rate of internalisation reduces. As in previous experiments, the pre-treatment of CHO-CCR5 with either MVC or TAK can be seen to induce the effective inhibition of CCL5-induced internalisation. However, pre-treatment with MVC is shown to induce a 17% increase in the surface expression of CCR5 relative to the non-perturbed control, with TAK inducing no change. Study of the CCL5-analogue 5P12 reveals it as an effective inhibitor of CCL5-induced internalisation, albeit with an efficiency lower than that of both MVC and TAK, allowing for a 17% reduction in CCR5-associated fluorescence when compared with the non-perturbed control. Finally, these results confirm that the alternate CCL5-analogue 5P14 acts as a potent driver of CCR5 internalisation, with cells exposed to both 5P14 and CCL5 displaying an average CCR5 intensity that is greatly lower than cells exposed to CCL5 alone, showing an average reduction of 71% with respect to the non-perturbed control

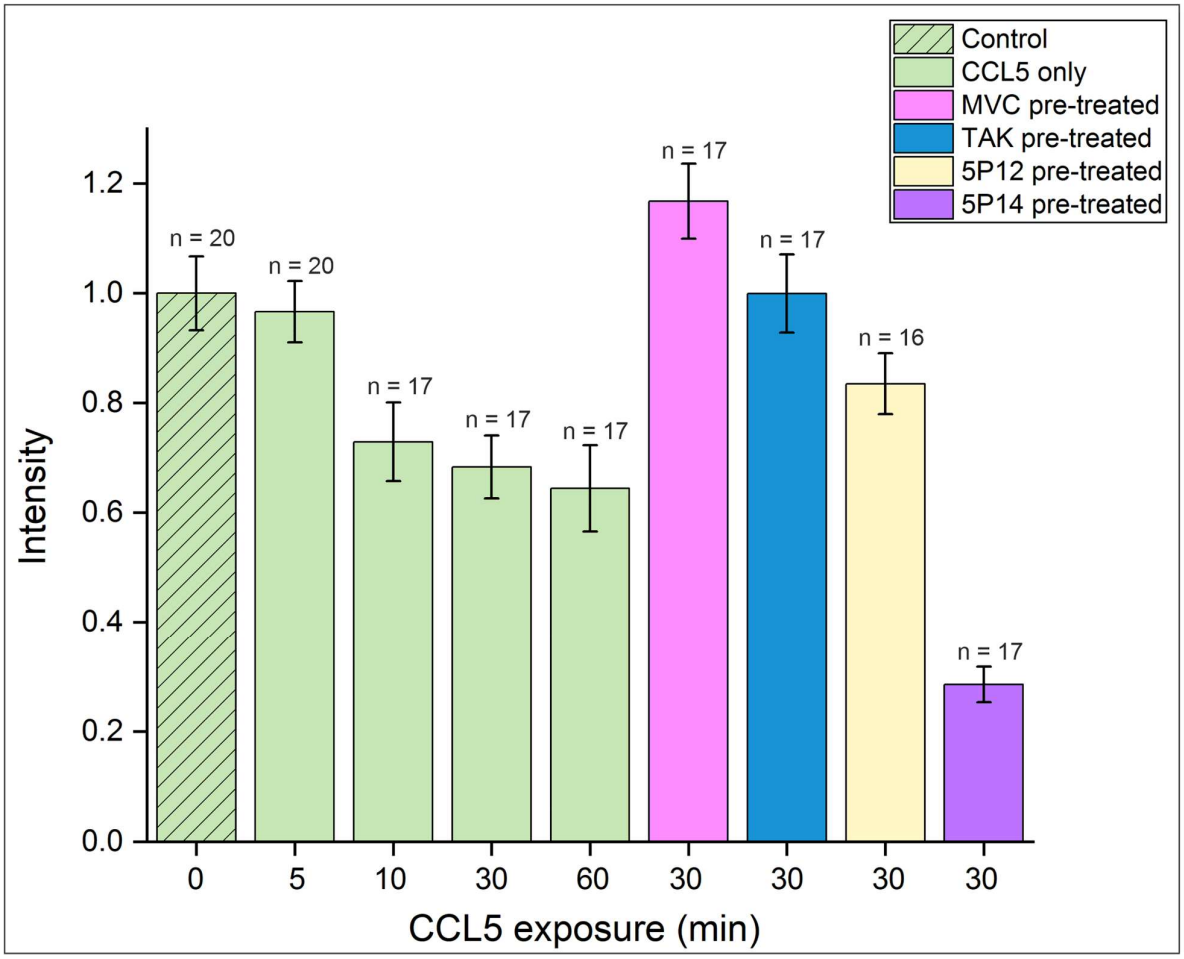

Figure 3-9: Quantitative analysis of 488-based SIM images of CHO-CCR5 exposed to labelled CCL5 and a range of CCR5 antagonists and other CCL5 analogues. Bar chart representing the mean fluorescence intensity of segmented Alexa Fluor 488-MC-5 labelled CHO-CCR5 cells from the samples represented in Figure 3-8 across multiple cells ranging from 16 to 20 cells per sample. Symbol n represents the number of cells sampled for the corresponding condition, error bars represent SEM and intensity values are normalised with respect to the control sample (0 min CCL5 exposure (green cross-hatched)).

3.8. Intensity analysis of Alexa Fluor 647 labelled CCL5 reveals CCL5 binding landscape in CHO-CCR5 and confirms the effects of a range of antagonists on CCL5 binding

The employment of fluorescently labelled CCL5 in the study of CCR5 perturbation allows for the determination of changes in the binding behaviour and distribution of CCL5, provided a varying extent of CCL5 exposure and the presence of, or lack thereof, alternate CCR5 binding partners. This study therefore sees the extension of SIM-based intensity analysis to the CCL5 binding landscape, using Alexa Fluor 647-CCL5. As shown in **Figure 3-10a**,

control CHO-CCR5 cells that have undergone CCR5-specific 488 staining but have not been exposed to CCL5 show a minimal intensity in the 647 channel, demonstrating a negligible level of autofluorescence and negligible detection of Alexa Fluor 488-associated fluorescence in the 647 channel. Upon exposure to CCL5, we see an increase in intensity proportional to the extent of CCL5 exposure (**Figure 3-10b,e**). This CCL5-associated emission appears confined to the cell boundary with minimal non-specific binding to the extracellular space. The binding landscape displayed in these images suggests that CCL5 is distributed throughout the cell in the form of distinct puncta, in a similar structure to that seen in the CCR5 surface distribution. The study of CHO-CCR5 that have received pre-treatment with CCR5 antagonists prior to being exposed to CCL5 suggest that all tested antagonists and other CCL5 analogues are effective in inhibiting the binding of CCL5, with each condition demonstrating CCL5-associated intensity that is comparable with the control, as can be seen in **Figure 3-10f,i**.

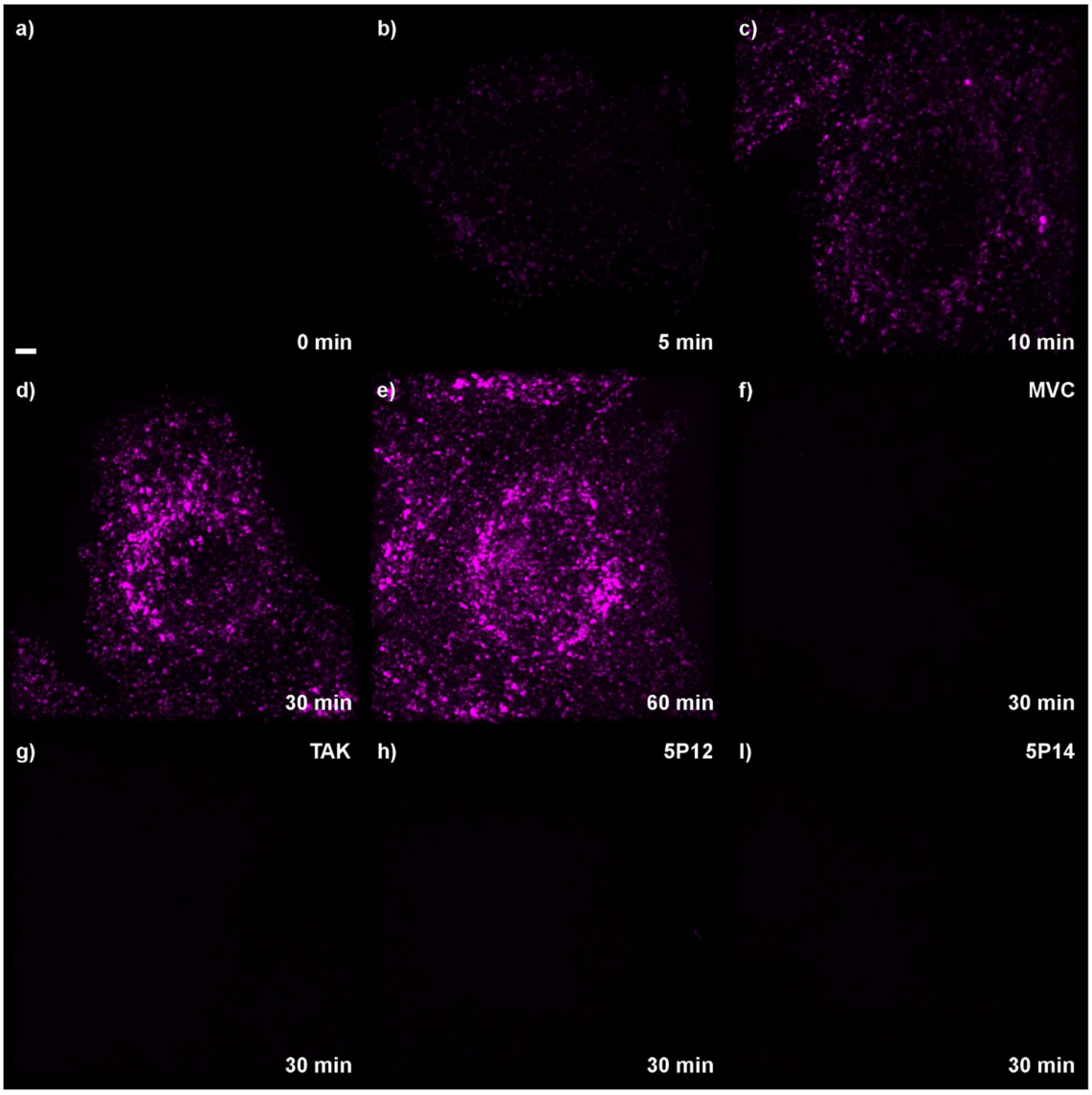

Figure 3-10: 647-based SIM imaging of CHO-CCR5 exposed to labelled CCL5 and a range of CCR5 antagonists and other CCL5 analogues. a) SIM image of a representative fixed CHO-CCR5 cell labelled with Alexa Fluor 488-MC-5 (scale bar 2 μm). b-e) SIM images of representative cells from CHO-CCR5 samples exposed to 10 nM Alexa Fluor 647-CCL5 for discrete lengths of time ranging between 5 and 60 minutes. f-i) SIM images of representative cells from CHO-CCR5 samples exposed to Alexa Fluor 647-CCL5 for 30 minutes after a 30-minute pre-exposure to small molecule antagonists maraviroc (MVC) and TAK-779 (TAK), as well as CCL5 analogues 5P12 and 5P14 respectively. All images are shown as maximum intensity z-axis projections of optically sectioned slices acquired from the basal through to the apical membrane. All images are contrast matched with respect to one another.

The quantification of the extent of CCL5-cell association, reflecting both the binding and endocytosis of labelled CCL5, within each condition was achieved using the same method previously applied to CCR5 quantification, with overall CCL5 intensity being calculated in

each optically section image by measuring the average intensity within a segmented maximum intensity z-axis projection, utilising the segmentation defined using the CCR5-associated 488 emission. As shown in **Figure 3-11** a quantitative increase in the CCL5-associated fluorescence intensity can be seen corresponding to the extent of CCL5 exposure, a result that is in contrast to the corresponding decrease in CCR5-associated fluorescence found in prior results analysing Alexa Fluor 488 labelled CCR5. Additionally, these results show a sustained increase in intensity from 5 minutes through to 60 min, indicating the continued increase of CCL5-cell association despite a previously determined deceleration of CCR5 internalisation. As in previous experiments employing rhodamine-labelled CCL5, the pre-treatment of CHO-CCR5 with either MVC or TAK can be seen to interfere with the binding of CCL5, with an 86% and 85% reduction in CCL5-associated fluorescence when compared with cells that were exposed to only CCL5 for 30 minutes. Similarly, the study of the CCL5-analogues 5P12 and 5P14 are shown to interfere with CCL5 binding, with a comparable reduction in CCL5-associated fluorescence of 88% and 89%, respectively, despite the greatly differing effects of 5P12 and 5P14 on the internalisation of CCR5. These results suggest that the large reduction in CCR5 surface expression upon exposure to both 5P14 and CCL5 is affected solely by 5P14, implicating it as an effective CCL5 competitor.

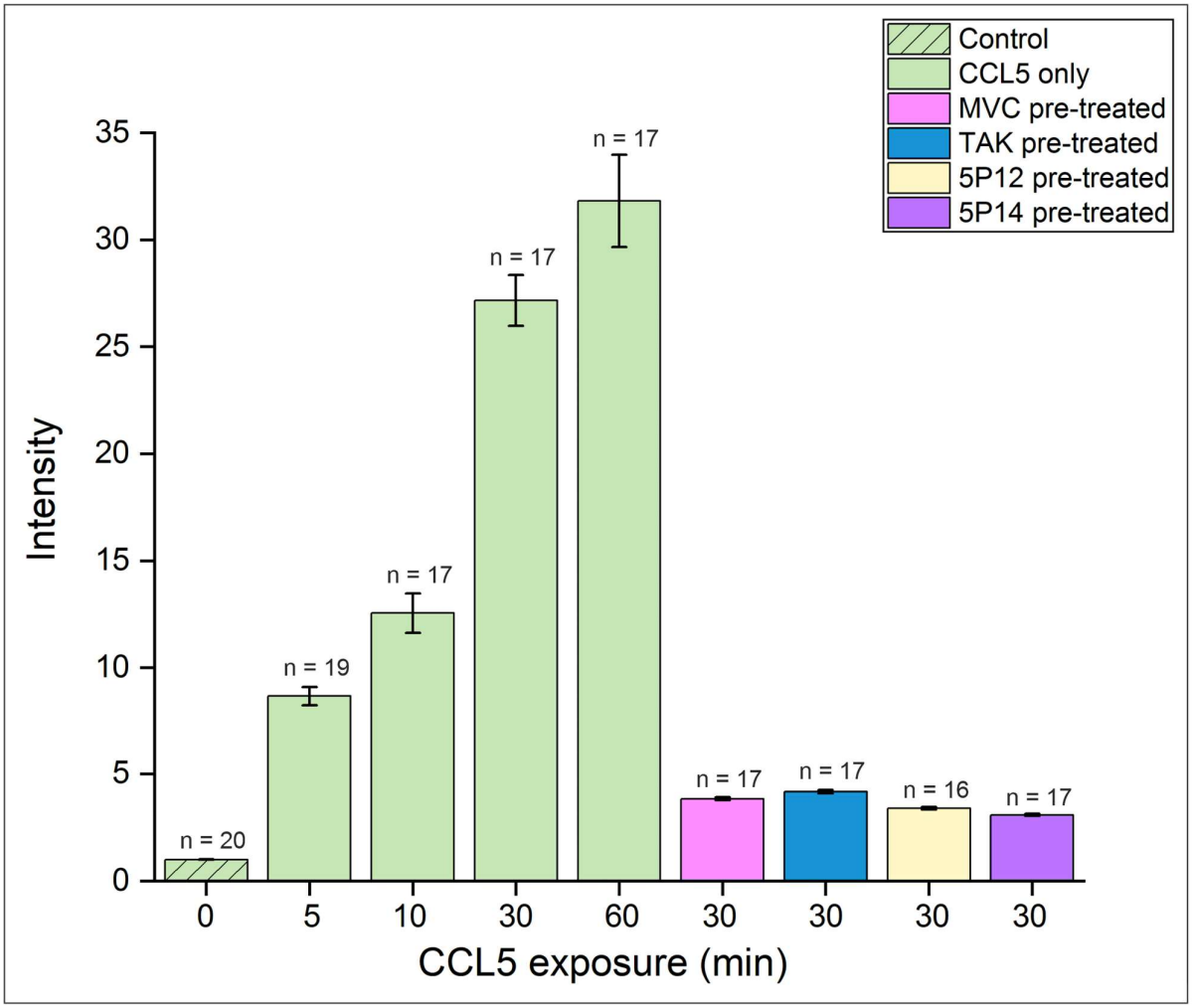

Figure 3-11: Quantitative analysis of 647-based SIM images of CHO-CCR5 exposed to labelled CCL5 and a range of CCR5 antagonists. Bar chart representing the CCL5-associated mean fluorescence intensity of segmented Alexa Fluor 488-MC-5 labelled CHO-CCR5 cells from the samples represented in Figure 3-10 across multiple cells ranging from 16 to 20 cells per sample. Symbol n represents the number of cells sampled for the corresponding condition, error bars represent SEM and intensity values are normalised with respect to the control sample (0 min CCL5 exposure (green cross-hatched))

3.9. Discussion

Investigations into the spatial distribution of the CCR5 receptor on mammalian cells were carried out using an established line of CCR5 expressing CHO cells that had been utilised in preceding studies[60,63,66,210]. Our study aimed to unveil the distribution of CCR5 using super resolution SIM microscopy, thereby allowing the precise quantification of CCR5-associated fluorescence and determination of ligand-induced changes in CCR5 behaviour. The resulting 3D image data, which captured DyLight 650-MC5 labelled CCR5 assemblies from the basal

to the apical membrane, revealed that CCR5 is expressed in distinct puncta throughout the entire plasma membrane. Through the localisation of the intensity centroids of these puncta we were able to quantify the level of clustering in the CCR5-puncta distribution using Ripley's H-function. Comparing these results with that of a randomly generated distribution of points, we found that CHO-CCR5 exhibits a clustered distribution with a modal clustering gradient of 0.004 ± 0.001. These results indicate that the puncta in which CCR5 appear to collect are in a non-random spatial distribution over the plasma membrane. Additional investigations are needed to determine whether the location of CCR5 puncta is correlated to a biological process and whether this organisation serves specific cellular roles. Finally, analysis of Ripley's H values over a short range facilitated the determination of the nearest neighbour separation of CCR5 puncta with the mean distance being 290 ± 10 nm, a result that further guides the characterisation of CCR5 expression.

These investigations were extended through the super resolution study of CCR5 behaviour provided temporally varying perturbation with the CCR5-agonist CCL5. This study reveals the time dependant CCL5-induced reduction in CCR5 associated fluorescence at the cell surface, thereby indicating CCR5 internalisation corresponding to the extent of CCL5 exposure. Further, through the investigation of 30-minute pre-exposures of samples to the CCR5 antagonists Maraviroc and TAK-779, prior to subsequent exposure to CCL5, this study reveals antagonist-induced inhibition of CCR5 internalisation, with the mean fluorescence intensity of cell surface CCR5 showing a 42% reduction after 30 minutes of CCL5 exposure, whilst showing only a 10% and 5% reduction in intensity in samples that were pre-treated with MVC and TAK respectively, results that corroborate the expected action of CCL5, maraviroc and TAK on CCR5 internalisation. This study was further extended through the investigation of the CCL5 binding landscape both with and without pre-treatment with antagonists. By employing rhodamine labelled CCL5, these results exhibited the quantification of the fluorescent intensity of cell associated CCL5, with a quantifiable reduction in fluorescence being seen after 30 minutes of CCL5 exposure, provided antagonist pre-treatments. MVC and TAK pre-treatment can be seen to cause a 13% and 19% reduction in cell associated CCL5 respectively, thereby indicating the binding of antagonists to CCR5, in place of CCL5. Although these results corroborate the expected antagonistic effects of MVC and TAK, low binding efficiency and significant non-specific binding of rhodamine CCL5 forms a clear limitation.

The investigation of CCR5 surface expression and CCL5 binding characteristics using SIM was concluded through the employment of the alternate fluorescently labelled CCL5 Alexa Fluor 647-CCL5 and the complimentary CCR5 label Alexa Fluor 488-MC-5. This study

provided further confirmation of the time-dependent nature of CCL5-induced internalisation of CCR5 under an increased magnitude of cell sampling, with the average CCR5-associated fluorescence intensity dropping 27%, 32% and 36% after 10, 30 and 60 minutes respectively. These results correspond to a time dependent increase in the population of cell bound CCL5, with bound CCL5 being seen to collect in distinct puncta in a similar structure to those previously outlined for CCR5. The inclusion of MVC and TAK pre-exposures within these experiments provided further evidence of their efficacy as CCR5 antagonists, with results showing a 17% increase in CCR5 surface expression provided pre-exposure to MVC and no significant change in expression provided pre-exposure to TAK. These results respectively correspond to an 86% and 85% reduction in CCL5-associated fluorescence confirming their function as inhibitors of CCL5 binding. In the case of the allosteric binding of MVC, these results suggest that, although the MVC binding pocket is thought to solely overlap with the secondary chemokine binding site of the two-step model, MVC is able to inhibit the initial binding of the chemokine core to the primary binding site. As the pre-exposure of cells to MVC occurs over a significant timescale of 30 minutes, it is possible that while MVC-bound CCR5 are unable to internalise, CCR5 within recycling pathways may continue to be turned over to the membrane surface. Therefore, observations of MVC-induced increases in CCR5-associated signal may be due to an accumulation of CCR5 at the cell surface. In addition to MVC and TAK, this study allowed for the investigation of the alternate CCR5 antagonists and CCL5 analogues 5P12 and 5P14. Although pre-exposure to 5P12 resulted in an outcome more similar to those of MVC and TAK, allowing for a 17% reduction in CCR5 expression after 30 minutes of CCL5 exposure but resulting in an 88% reduction in CCL5 binding, pre-exposure to the alternate CCL5-analogue 5P14 resulted in a 71% reduction in CCR5 expression alongside an 89% reduction in CCL5 binding. These results agree with previous findings outlining the behaviour of 5P14 in which it was found to induce significant internalisation at an intermediate level between that of CCL5 and the known super-agonist PSC-RANTES, albeit with no associated downstream signalling[138–140].

4. Revealing the characteristics of CCR5 presentation on the single molecule level

4.1 Introduction

Advancement in experimental technique has seen the development of assays that are capable of interrogating biomolecules on an individual basis. These single molecule techniques offer key advantages in the characterisation of biomolecules due to their ability to detect rare species and events. In the study of biomolecules that display heterogeneity, the employment of these techniques allows for a more accurate characterisation of receptor presentation, in contrast to traditional bulk-ensemble techniques which provide insight into the average characteristics of the biomolecule with limited ability to distinguish between heterogeneous species.

Investigations outlined in the previous chapter revealed the overall presentation of CCR5 across the membrane, with CCR5 being found to exist in distinct assemblies throughout the cell and treatment dependent changes in presentation being demonstrated. However, these investigations reported solely on the cell-wise spatial distribution of CCR5 and did not interrogate the make-up of individual CCR5 assemblies. To better understand this distinctive presentation of CCR5, we seek to characterise these CCR5 assemblies on an individual basis. Through the employment of single molecule biophysical techniques, we aim to determine the oligomeric composition of individual receptor assemblies, the distribution of assembly sizes across the cell and potential changes in cell-wise assembly distributions that may accompany the ligand-dependent shifts in CCR5 presentation that were demonstrated in the previous chapter. This is achieved through microscopy techniques that utilise the photobleaching effect of fluorophores and rely on a high signal to noise ratio and temporal resolution in order to accurately track individual biomolecule assemblies and estimate the number of constituent biomolecules within a given assembly. These techniques provide clear utility in the accurate characterisation of assembly organisation but possess unique experimental requirements. As the techniques outlined here are objective-based, in a similar fashion to the microscopy techniques outlined in Chapter 3, the use of adherent cells expressing CCR5 is ideal. However, the optimal use of these techniques requires the creation of a tailored cell line that fulfil three essential characteristics: i) having a low level of CCR5 expression, ii) a one-to-one receptor-to fluorophore ratio and iii) a broadly consistent level of expression across cells in a given population in order to detect individual receptors, minimise background fluorescence and obtain consistent observations.

Single molecule microscopy techniques, such as those employed here, often involve the selected excitation of a thin depth of a biological sample in order to reduce out of focus fluorescence and thereby raising the achievable SNR. In the case of investigations into intracellular structures, studies are often based on HILO, where a distinct intracellular plane can be selectively excited. However, investigations into biomolecules located close to the coverslip surface benefit from the employment of TIRF, an inclined excitation microscopy that provides an excitation field enhancement but is limited in the selectivity of the excitation plane, with this technique being ideal for the in-vitro study of coverslip-bound biomolecules. In the study of membrane-bound biomolecules, such as CCR5, TIRF is capable of providing excitation to the basal membrane of flat and adherent cells. However, despite the characteristic flatness of adherent cells, such as CHO, they can be seen to display a ruffled basal membrane topology whose extremities can extend beyond the TIRF depth of field (~100-200 nm)[199]. This study therefore introduces an adapted form of inclined excitation microscopy that aims to benefit from the basal membrane excitation of TIRF while increasing the depth of excitation to include all foci contained in the basal membrane of adherent mammalian cells. Using this new imaging mode, coupled with established single molecule tracking techniques we aim to reveal key insights into the finer structure of CCR5 assemblies.

4.2. Generation of model cell line for the expression of GFP-CCR5

Chapter 3 saw the investigation of the CCR5 receptor using a non-clonal CHO cells stably expressing CCR5 at a high expression level (CHO-CCR5). Although this model has proven extremely useful in the characterisation of CCR5 using super resolution microscopy techniques, the extension of studies to alternate techniques requires improvements and adaptations to the suite of CCR5 expressing cell models available. In the case of single molecule microscopy assays employing techniques such as TIRF and HILO, the maximisation of signal to noise ratio is vital for the tracking of individual receptor assemblies. However, the ability to isolate individual receptor assemblies within images captured using these techniques relies on the total copy number of the fluorescently tagged receptor lying below a certain limit, beyond which individual assemblies would be so crowded as to not allow accurate tracking. Further, the receptor counting techniques employed in this study rely on a consistent receptor to fluorophore binding ratio, without which, estimates of stoichiometry may be vastly over or underestimated. For these purposes, this study saw the development of a clonal cell line which expresses a one-to-one N-terminally tagged GFP-

CCR5 fusion to a level that is suitable for single-molecule studies. Due to the optimal characteristics of CHO cells within microscopy applications, this cell line was chosen for transfection for GFP-CCR5 prior to undergoing single-cell cloning for the creation of several populations with consistent expression that vary relative to one another (see methods 2.2.1). **Figure 4-1** shows analysis of one such clonal population of CHO-GFP-CCR5, chosen due to its optimal GFP-CCR5 expression for single molecule applications. As shown in **Figure 4-1a,d**, despite being developed for a relatively low level of GFP-CCR5 expression, this clonal population can be seen to display GFP-associated fluorescence that is significantly higher than that of a non-labelled CHO control sample, as determined using flow cytometry. Further, extension of the characterisation of CHO-GFP-CCR5 to fluorescence microscopy reveals detectable GFP expression within CHO-GFP-CCR5 that cannot be seen in control samples, as shown qualitatively in **Figure 4-1b**.

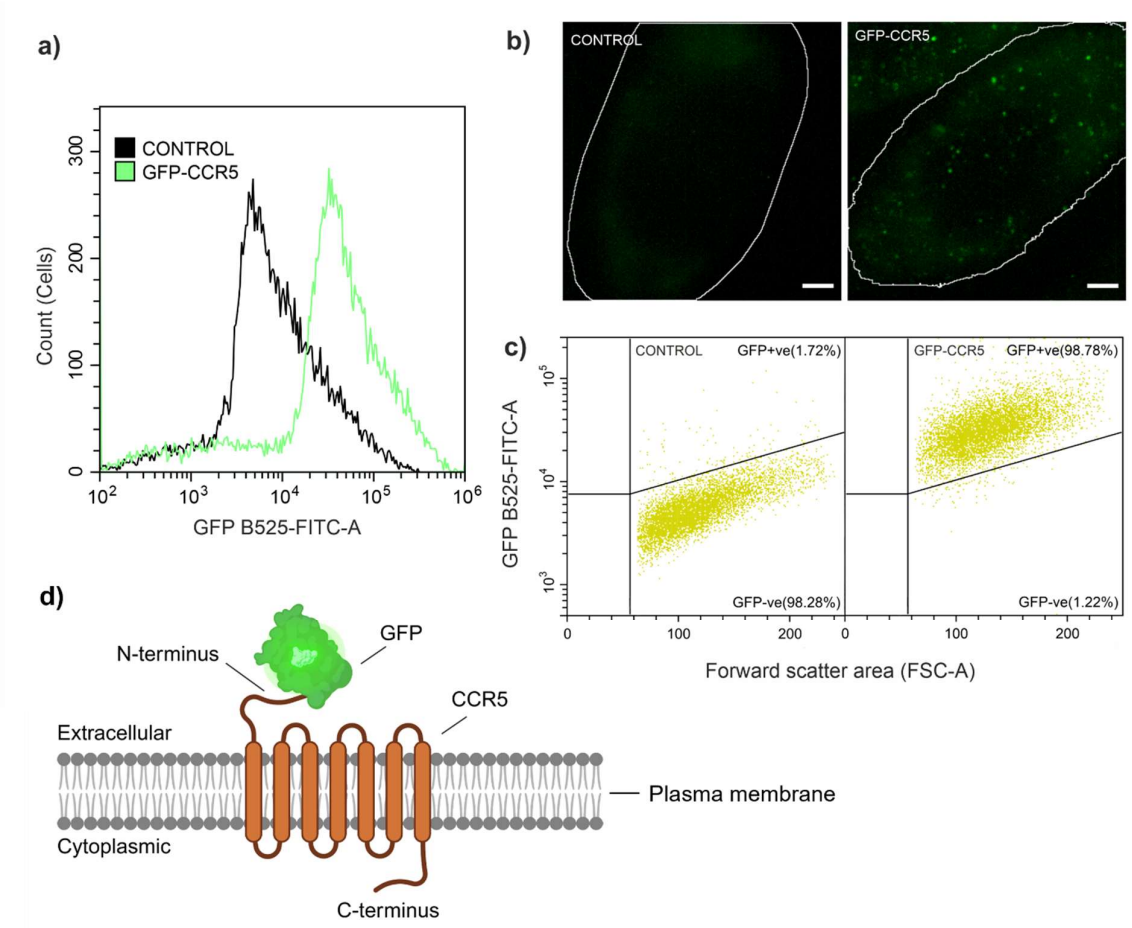

Figure 4-1: Characterisation of GFP-CCR5 expression in transfected CHO cells using flow cytometry and fluorescence microscopy confirms increased fluorescence above control samples. a) Distribution of GFP emission intensity over several thousand cells for both control and

GFP-CCR5 positive samples. b) Fluorescence microscopy images of the basal membrane of both control and GFP-CCR5 positive cells. Cell boundary segmentation shown in white. (Scale bar 2 μm). c) Scatterplot of GFP-range emission intensity against the forward scatter area of both control and GFP-CCR5 positive cells. a) and c) show cell populations after gating to remove debris and doublets. Fluorescent intensity is recorded in the FIT-C channel corresponding to the fluorescent protein (GFP). d) Illustration of GFP located on the N-terminus of CCR5. (Illustration created in https://BioRender.com)

Although the expression of GFP within CHO-GFP-CCR5 has been determined using flow cytometry and microscopy, the employment of this cell line in the study of CCR5 characterisation requires the confirmation of CCR5 presence. Further, confirmation is needed of the effect, if any, of GFP on the accessibility of key binding sites on the CCR5 receptor. In particular, the presence of GFP on the extracellular N-terminus of CCR5, as illustrated in **Figure 4-1d**, necessitates confirmation of the accessibility of the N-terminus and chemokine binding site. For this purpose, CHO-GFP-CCR5 were analysed using flow cytometry after immunolabelling with primary antibodies specific to the CCR5 N-terminus (MC-5) and chemokine binding site (2D7). Experimental controls included the analysis of cells exposed solely to the secondary fluorescent antibody (Alexa Fluor 647) in the absence of primary antibody, as well as cells exposed only to media. Additionally, a third non-anti-CCR5 primary antibody (FLAG-M2) was employed as an isotype control. As shown in **Figure 4-2**, a large shift in Alexa Fluor 647-associated fluorescence can be seen in populations of cells exposed to MC-5 when compared to populations that were exposed solely to Alexa Fluor 647, thereby indicating a strong specificity of MC-5 to CHO-GFP-CCR5 and indicating the presence and accessibility of the CCR5 N-terminus. Similarly, a large shift can be seen in populations of cells exposed to 2D7 when compared to populations that were exposed solely to Alexa Fluor 647, thereby indicating a strong specificity of 2D7 to CHO-GFP-CCR5 and indicating the presence and accessibility of the CCR5 chemokine binding site. In contrast, populations that were exposed to the isotype control show no such shift relative to the other controls, providing validation of the CCR5-specificity of MC-5 and 2D7. Lastly, minimal shift can be seen when comparing cell populations that were exposed solely to Alexa Fluor 647 and populations that received no labelling, indicating an insignificant level of background labelling in this experiment.

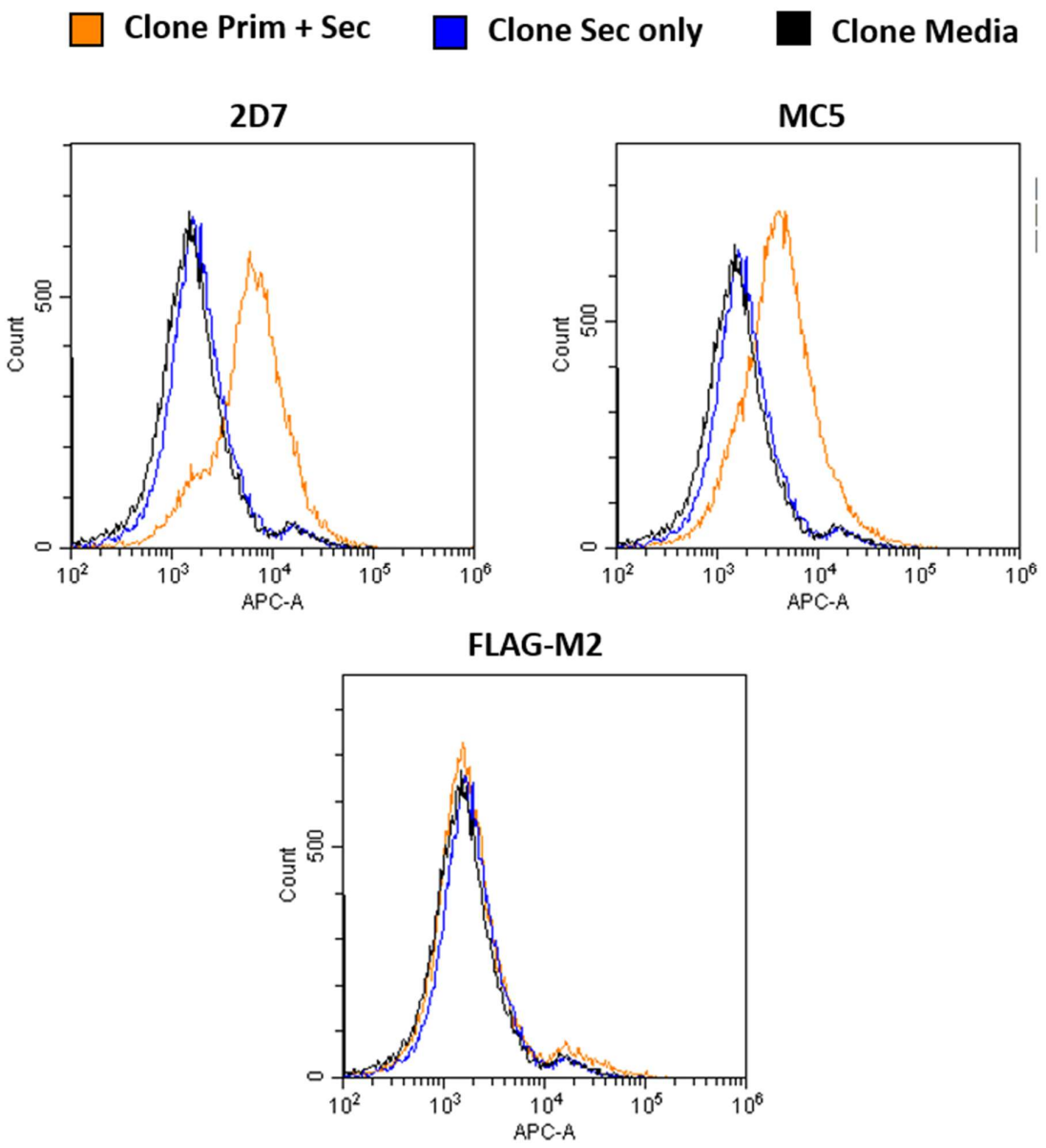

Figure 4-2: Characterisation of GFP-CCR5 expression in transfected CHO cells using flow cytometry and anti-CCR5 fluorescent antibodies confirms CCR5 expression and binding site availability. Distribution of Alexa Fluor 647 emission intensity over several hundred cells for CHO-GFP-CCR5 samples labelled with Goat anti-Mouse Alexa Fluor 647 secondary antibodies, with and without pre-labelling with primary antibodies 2D7, MC-5 and FLAG M2, compared with non-labelled control samples. Figures show cell populations after gating to remove debris and doublets. Fluorescent intensity is recorded in the APC channel corresponding to the secondary fluorescent antibody employed (Alexa Fluor 647). Orange – cells exposed to both primary antibody and secondary fluorescent antibody. Blue – cells exposed to secondary fluorescent antibody in the absence of a primary antibody. Black – cells exposed to neither primary or secondary antibodies.

Further characterisation of the newly created CHO-GFP-CCR5 cell line sought the conformation of CCR5 functionality. For this purpose, a flow-cytometry based calcium flux assay was carried out in which changes in calcium associated fluorescent signal were monitored in CHO-GFP-CCR5 during live exposure to the CCR5 ligand CCL5, with any such changes being likely to be associated with CCL5-mediated activation of CCR5 and thereby inferring CCR5 functionality. In order to confirm any changes were due to CCL5 mediated activation, cell populations with and without pre-exposure to the CCR5 antagonist TAK-779 were studied. As shown in **Figure 4-3**, this study revealed an increase in calcium signalling-associated fluorescence upon exposure to CCL5 in the absence of antagonist. In contrast, populations that received pre-exposure to TAK-779 did not display an increase in calcium-associated fluorescence upon exposure to CCL5. These results suggest a functional response of GFP-CCR5 to CCL5 in agreement with results found in previous studies[167]. The extent of calcium flux observed in this study is low in comparison to that of previous studies, however this result is representative of the relatively low GFP-CCR5 expression for which this cell line was developed.

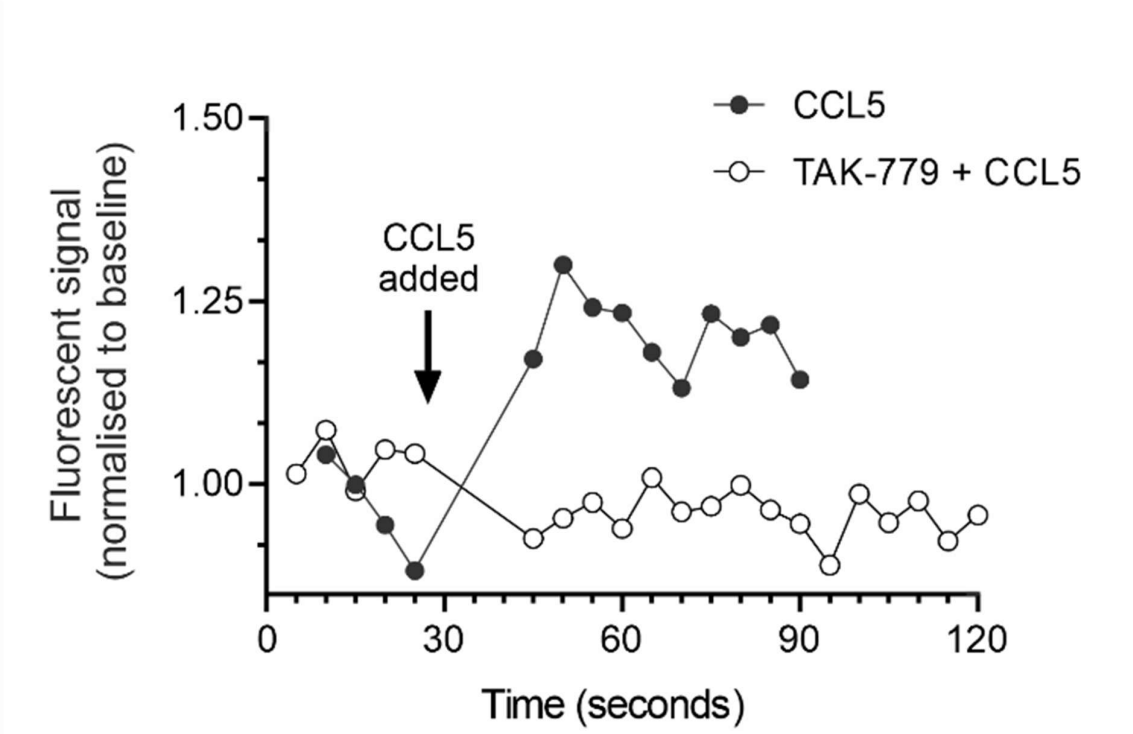

Figure 4-3: GFP-CCR5 functionality determined through changes in calcium flux upon ligand stimulation. Flow cytometry-based calcium flux assay in which the change in calcium associated fluorescent signal is monitored within samples of CHO-GFP-CCR5 during live exposure to 10 nM CCL5, with and without pre-exposure to the CCR5 antagonist TAK-779. Values of fluorescent signal are reported normalised to the average baseline fluorescence prior to CCL5 exposure. Figure shows data from a single experiment n =1.

Although confirmation of agonist-mediated activation of CCR5 provides an indication of CCR5 functionality within the GFP-CCR5 fusion, further characterisation of this functionality is necessary to determine the ability of GFP-CCR5 to undergo the internalisation that is expected upon agonist stimulation. This was carried out using a flow cytometry-based assay in which the accessibility of both GFP and CCR5 to respective specific antibodies was determined after distinct periods of exposure to the super-agonist PSC-RANTES, thereby indicating the extent of agonist-induced GFP-CCR5 internalisation, if any. Although GFP fluorescence is detectable using flow cytometry, it does not allow discrimination between cell surface and internalised GFP-CCR5. The employment of post-agonist anti-GFP labelling allows the isolated determination of cell surface GFP at a given time point. As shown in **Figure 4-4**, fluorescent signals associated with antibodies bound to GFP (anti-GFP) and the CCR5 chemokine binding site (2D7) were measured within CHO-GFP-CCR5 cells that underwent fixation after varying levels of exposure to the PSC-RANTES. A decrease in both the accessibility of the GFP epitope and the availability of the chemokine binding site can be seen over the course of 60

minutes. These results indicate the successful binding of PSC-RANTES to the chemokine binding site and the subsequent internalisation of GFP-CCR5. However, the rate at which GFP-CCR5 undergoes PSC-RANTES-induced internalisation is low relative to previous studies employing non-tagged CCR5[66], thereby indicating that, although the presence of N-terminal GFP may not inhibit CCR5 internalisation, GFP may reduce the speed at which CCR5 internalisation can take place.

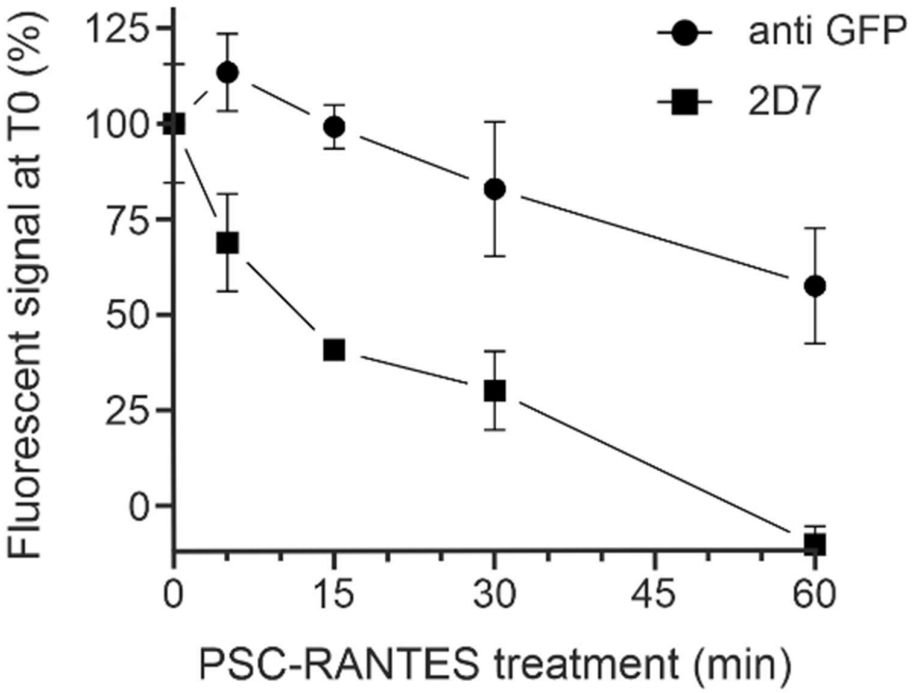

Figure 4-4: GFP-CCR5 ability to internalise determined through changes in GFP and CCR5 accessibility upon ligand stimulation. Flow cytometry-based downmodulation assay monitoring fluorescent signals associated with anti-CCR5 and anti-GFP antibodies within CHO-GFP-CCR5 cells fixed after varying levels of exposure to the super-agonist PSC-RANTES at a concentration of 100 nM. Experiment was performed in triplicate and data are expressed as the mean values ± SEM.

4.3. Slimfield microscopy reveals CCR5 expressed evenly across the basal membrane of CHO-GFP-CCR5

Initial investigation of the newly developed and characterised CHO-GFP-CCR5 cell line aimed to determine the spatial distribution of CCR5 in comparison to the established CHO-CCR5 cell

line. For this purpose, CHO-GFP-CCR5 were imaged using a slimfield-based approach concurrent with the single-molecule techniques to be applied within this study. Due to the low level of CCR5 expression within CHO-GFP-CCR5, any such investigation employing SIM would yield a signal to noise ratio that is not conducive with accurate reconstruction. A comparison between the two cell lines is therefore best made using the independent microscopy techniques for which the two lines are respectively best suited. As shown in **Figure 4-5a**, CHO-GFP-CCR5 displays CCR5 expressed in distinct puncta across the basal membrane in a qualitatively similar distribution to that of the DyLight 650-MC5 labelled CHO-CCR5 cell shown in **Figure 4-5b**. Further comparison reveals that the overall expression of CCR5 assemblies in CHO-GFP-CCR5 is lower than that of CHO-CCR5, providing the increased average separation of CCR5 assemblies that is required for single molecule investigations. Although further studies are required into the accurate determination of puncta diameter in both respective cell lines, the general uniformity in the size of CCR5 puncta between both cell models provides confidence that any spatial dependence in CCR5 expression between these two lines is related.

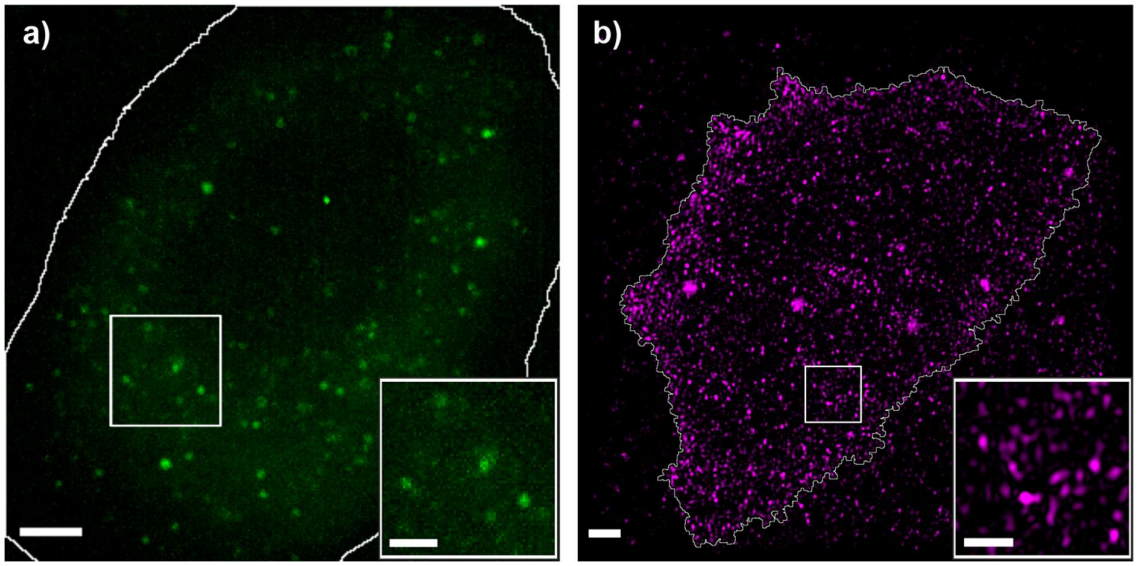

Figure 4-5:Comparison of CCR5 expression in CHO-GFP-CCR5 cell line against established CHO-CCR5 cell line. Qualitative images showing the basal membrane spatial distribution of fluorescently labelled CCR5 in a a) CHO-GFP-CCR5 cell imaged using slimfield-based microscopy and b) DyLight 650 labelled CHO-CCR5 cell imaged using SIM. Cell boundary segmentation shown in white. Magnified insets (bottom right) originate from the areas indicated by white boxes located on the respective cell membrane. (Scale bar 2 μm, (magnified insets 1 μm)).

4.4. Development of novel microscopy technique PaTCH

Although the increased spatial resolution of SIM imaging provides a more detailed insight into CCR5 spatial characteristics and allows for improved segmentation of individual CCR5 puncta for the determination of cluster arrangement, investigations into the make-up of individual clusters requires the employment of single-molecule microscopy techniques. These methods rely on microscopy techniques that prioritise temporal resolution whilst retaining a high signal to noise ratio, often necessitating optical sectioning to reduce out of focus background light. This can be achieved through the inclination of the excitation beam in methods such as HILO and TIRF. As illustrated in **Figure 4-6**, microscopes developed for use in TIRF applications can commonly be used in three distinct modes. Epifluorescence microscopy allows for the direct excitation of the sample but can result in extraneous background fluorescence stemming from excited fluorophores lying above or below the focal plane. Inclining the excitation beam allows for HILO microscopy, in which excitation is more efficiently restricted to the focal plane and sees successful employment in the investigation of intracellular molecules. Inclination of the excitation beam beyond the critical angle of the glass-water interface results in total internal reflection of the excitation path and the creation of an evanescent energy field that extends a short distance into the sample, thereby resulting in TIRF microscopy. TIRF finds successful application in the investigation of molecules located in close proximity to the coverslip surface.

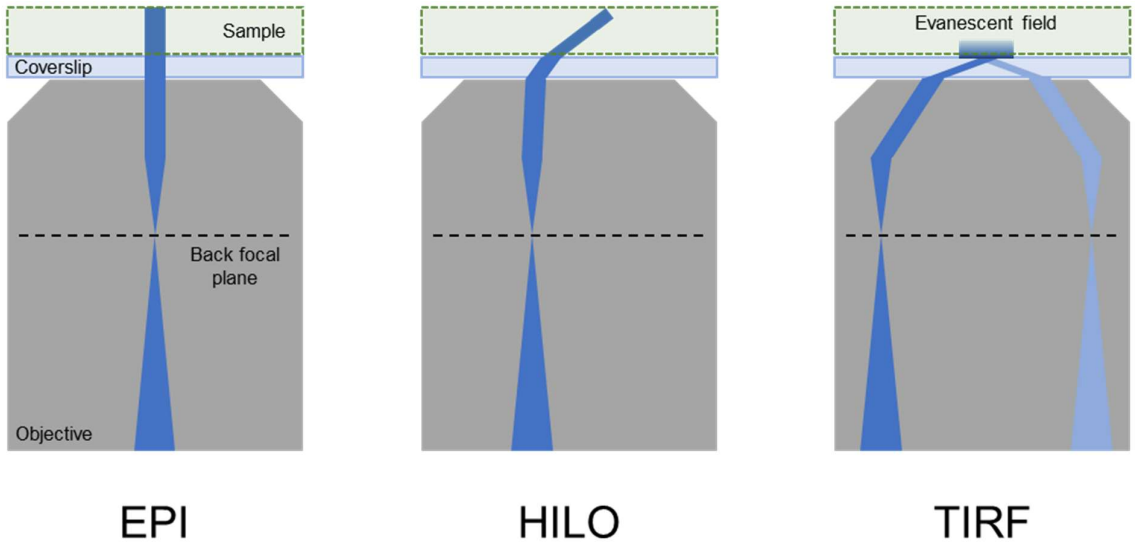

Figure 4-6: Demonstration of key differences in epifluorescence, HILO and TIRF imaging modes. Illustration demonstrating the excitation path of light (blue) through the objective, coverslip and sample in three distinct imaging modes (epifluorescence (EPI), HILO and TIRF).

Although TIRF provides the necessary SNR and temporal resolution to perform single molecule studies, the restricted distance over which the evanescent field can extend into the sample provides a limitation of this technique. In the case of adherent mammalian cells such as CHO, the basal membrane topology can result in a large part of the membrane being retracted from the evanescent field, with only the strongest adhered footprint of the cell being excited. In order to retain the optical sectioning required for single molecule techniques, whilst ensuring the excitation of the entire basal membrane, this study sought the development of a novel imaging mode tailored to the study of basal membrane-bound molecules on adherent cells. This technique, known as Partially TIRF-coupled HILO (PaTCH) microscopy, utilises an intermediate angle of incidence lying between that of traditional HILO and TIRF modes, with a portion of the excitation coupled into a TIRF mode and a portion coupled into a HILO mode, thereby benefiting from the evanescent energy field associated with TIRF and the increased penetration depth achievable in HILO. In order to quantify the improvements seen in PaTCH over its contemporary imaging modes, images of CHO-GFP-CCR5 were analysed to provide a readout of the signal of individual GFP-CCR5 assemblies relative to their adjacent background. As shown in **Figure 4-7a,b**, a representative CHO-GFP-CCR5 was imaged using TIRF, PaTCH and HILO modes. Qualitatively, an increase in GFP-CCR5 signal can be seen in puncta excited by PaTCH when compared with HILO. Additionally, the overall excitation of the basal membrane using PaTCH is seen to be more uniform when compared with TIRF. **Figure 4-7c** sees the quantitative comparison of signal and background between puncta that are excited by both HILO and PaTCH imaging modes (puncta 1-3), and between puncta that are excited by both TIRF and PaTCH imaging modes (puncta 4-6). These results demonstrate that puncta imaged using PaTCH benefit from a signal enhancement relative to HILO, alongside a reduction in background fluorescence. Further, although TIRF is capable of providing enhanced signal relative to PaTCH, as seen in punctum 4, this restricted illumination mode can result in a higher background fluorescence, likely originating from fluorescent material bound to the coverslip surface. Additionally, TIRF provides a lower signal from puncta located further from the coverslip surface, such as in puncta 5 and 6. These results, combined with the average signal to background ratio of 1.8 ± 0.1, 3.6 ± 0.6 and 2.4 ± 0.4 for puncta imaged using HILO, PaTCH and TIRF respectively, demonstrate the general increase in fluorescent signal and reduction in fluorescent background offered by PaTCH in the imaging of the basal membrane. Mean values for the signal to background ratio of puncta were determined using 10 puncta for each imaging mode (see methods 2.6.6). Error associated with these averages is the standard error of the mean.

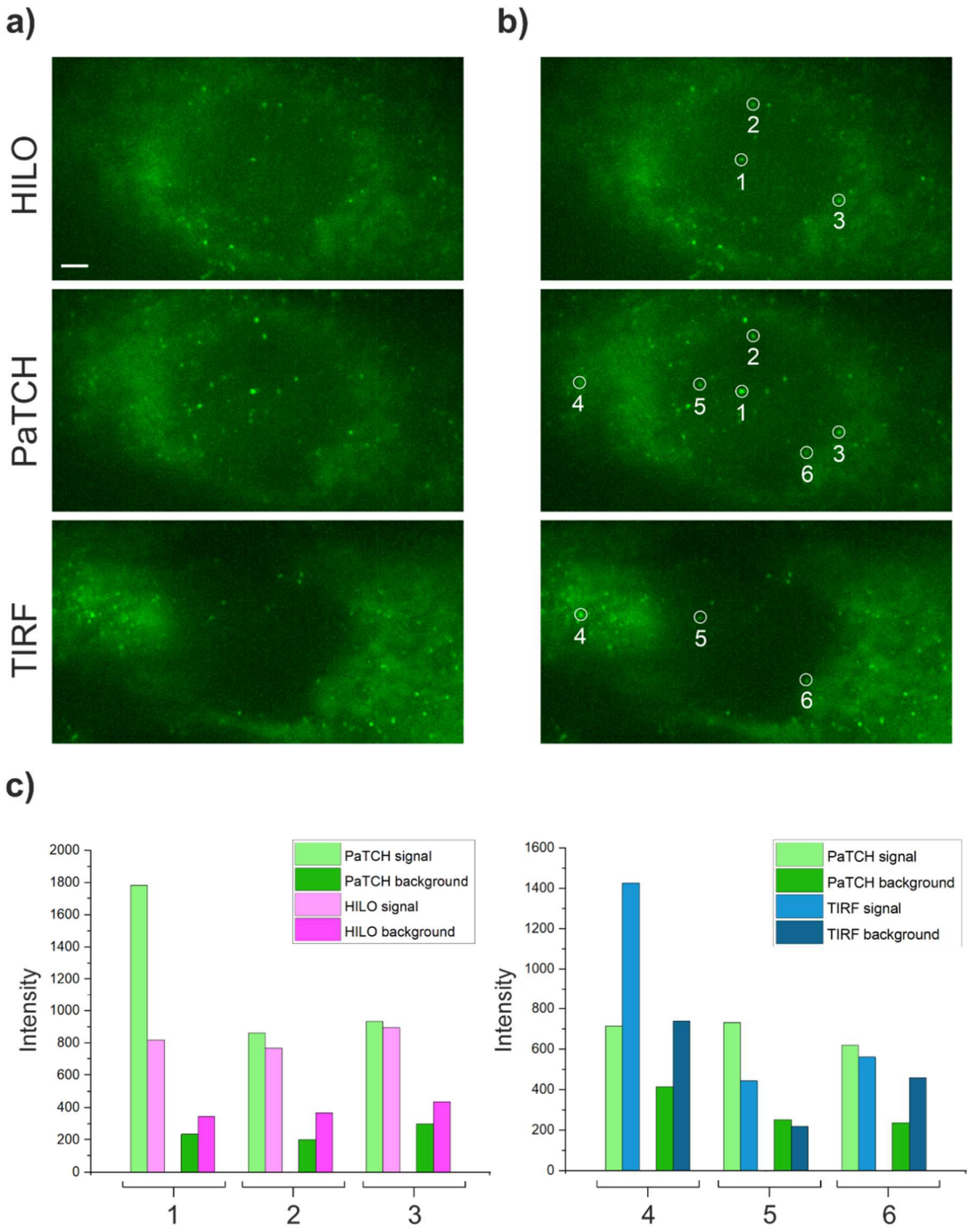

Figure 4-7: Comparison of HILO, PaTCH and TIRF imaging modes for the single molecule detection of GFP-CCR5 in CHO-GFP-CCR5. a) CHO-GFP-CCR5 cell imaged using HILO, PaTCH and TIRF microscopy. (Scale bar 2 μm). b) Circular overlays highlighting CCR5 assemblies present in both HILO/PaTCH images and in both TIRF/PaTCH images. Overlays are numbered to facilitate further analysis. c) Comparison of signal and background between HILO and PaTCH imaging modes, in puncta labelled 1-3, and between TIRF and PaTCH imaging modes, in puncta labelled 4-6. Intensity represents the raw integrated density, captured using a 6-pixel diameter circle, above a

mean global background calculated using the extracellular space. Measurements of signal were taken directly over the puncta, while measurements of local background were taken adjacent to puncta.

4.5. Tracking of individual receptor assemblies imaged using PaTCH

Through the employment of high temporal techniques such as PaTCH, it is possible to track the intensity of individual clusters of a given fluorescently tagged molecule over time with an accuracy that allows for the approximation of initial cluster intensity and the observation of discrete photobleaching events. These metrics underpin techniques developed for the determination of cluster size and molecular stoichiometry. As illustrated in **Figure 4-8**, a given fluorescent complex of an unknown size can be characterised through observation of the cluster intensity over time. In this illustration, the complex is shown to undergo three distinct reductions in its intensity over time, corresponding to three independent photobleaching events and inferring the presence of three fluorophores within the complex. Additionally, this trimeric complex can be characterised by dividing the initial complex intensity by the characteristic intensity of a single fluorophore, provided an accurate approximation of the initial complex intensity prior to excitation and an accurate determination of the intensity of a single fluorophore.

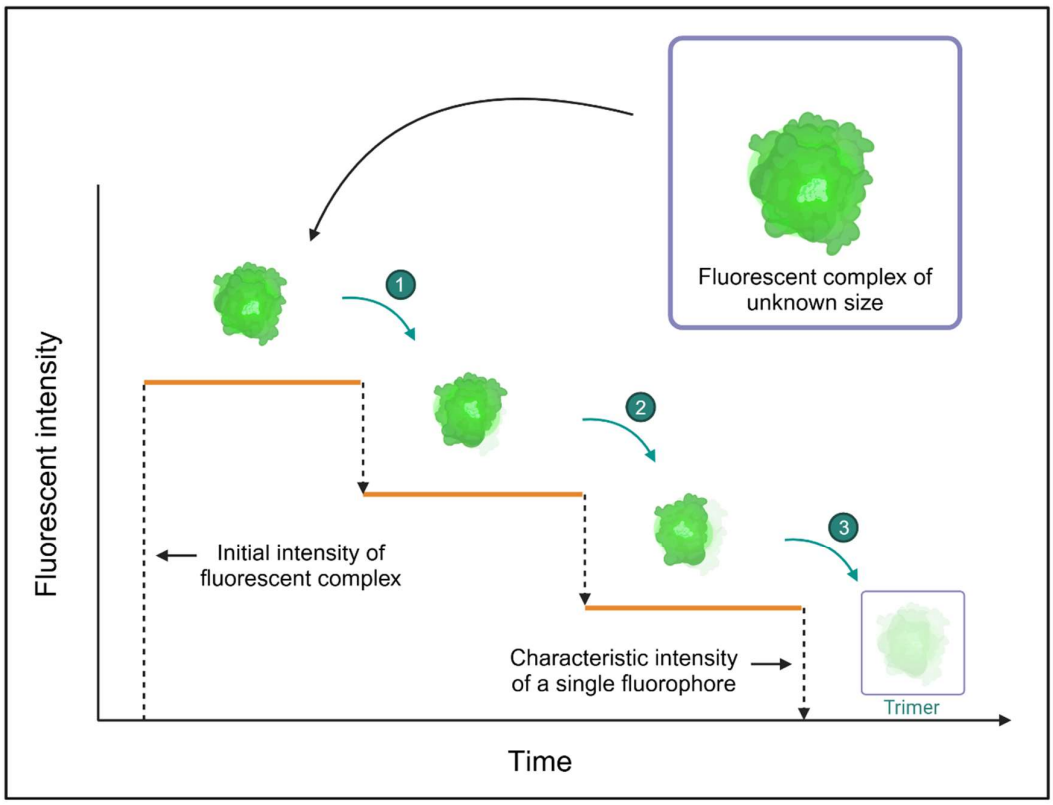

Figure 4-8: Demonstration of the utility of stepwise photobleaching for estimates of cluster sizes. Illustration demonstrating the concept of stepwise photobleaching, in which knowledge of the initial intensity of a fluorescent complex, combined with the counting of individual photobleaching events can be used to determine the number of fluorophores are that contained within the fluorescent complex. (Illustration created with BioRender.com)

In order to determine the initial intensity of a given fluorescent complex, the characteristic intensity of a single fluorophore and the time-dependent reductions in fluorescent intensity, PaTCH-based imaging employs the use of tracking software that is capable of isolating individual fluorescent complexes and recording their intensity over time. As can be seen in **Figure 4-9a**, the tracking ability of ADEMScode is demonstrated through overlaying foci isolated by ADEMScode (white) onto an image of the corresponding CHO-GFP-CCR5 cell imaged using PaTCH. Each focus is tracked frame by frame with the position and fluorescent intensity of the focus being recorded. As shown in **Figure 4-9b**, the temporal changes in intensity can be plotted to demonstrate the stepwise changes corresponding to photobleaching events. The representative traces shown here exhibit fluctuations in intensity, however this effect is accounted for in the determination of stoichiometry through the approximation of initial foci intensity and determination of the fluorescent intensity of a single GFP in these imaging conditions. One such trace, highlighted in green, shows an

example of a GFP-CCR5 assembly whose intensity underwent decay with minimal fluctuation. The intensity of this trace can be seen to drop in a stepwise fashion from an apparent stoichiometry of 7 to 2, with the reduction in intensity between each step supporting the accuracy of the estimated brightness of a single GFP molecule through which the stoichiometry was calculated.

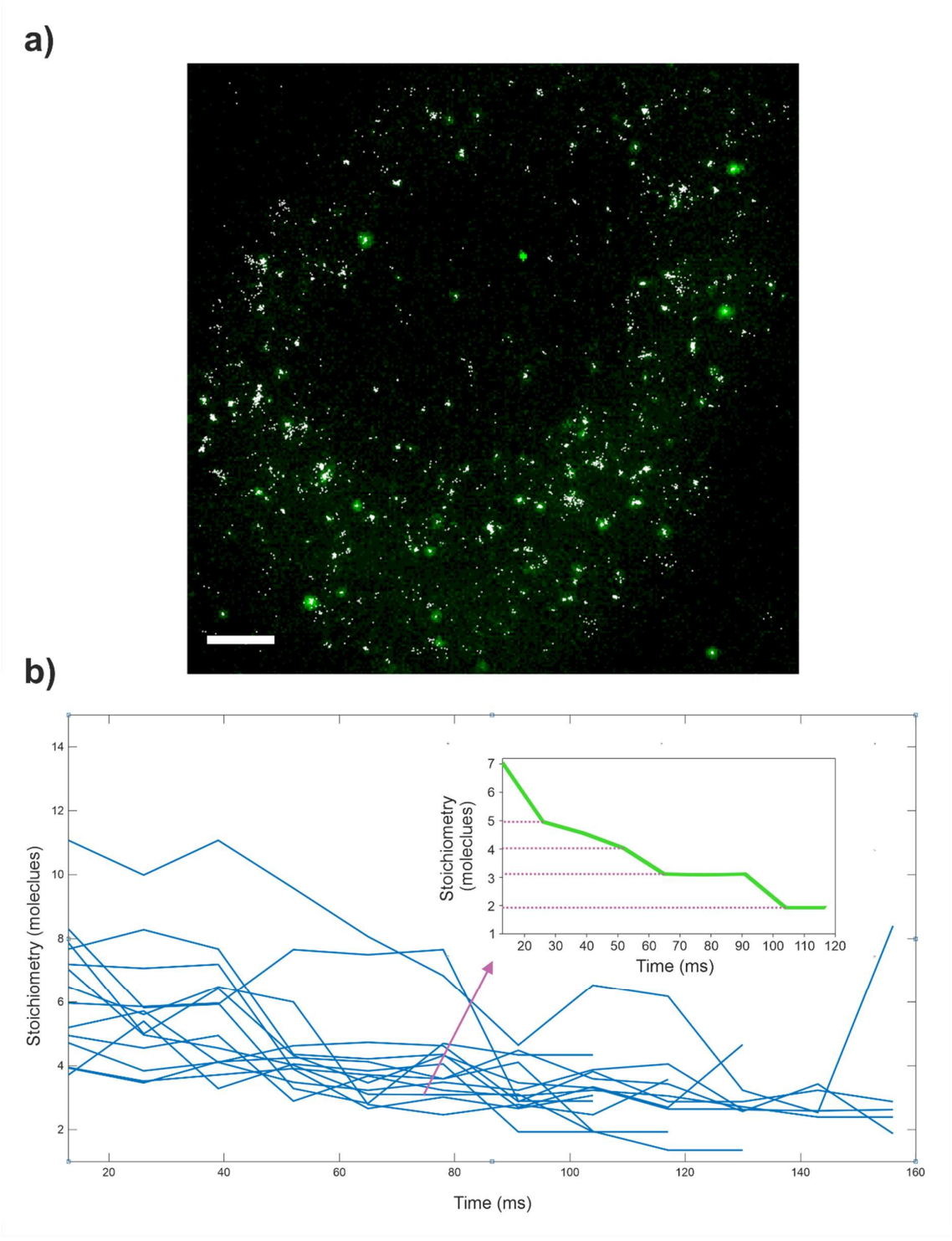

Figure 4-9: ADEMScode tracking of CHO-GFP-CCR5 reveals photobleaching steps. a) CHO-GFP-CCR5 cell imaged using PaTCH micrscopy with an overlay (white) showing tracks determined by ADEMScode tracking (MATLAB). (Scale bar 2 μm). b) Chung–Kennedy edge-preserving filtered Intensity time traces revealing the photobleaching-induced intensity decay of tracked foci towards the

end of the photobleaching process. Inset trace (green) shows an example of a tracked GFP-CCR5 assembly.

4.6. Intensity analysis of tracked assemblies allows determination of assembly sizes and estimation of CCR5 stoichiometry

Utilising the single-molecule sensitivity of PaTCH microscopy, we are able to identify the characteristic brightness of a single GFP as the modal intensity of single GFP-CCR5 molecules following sufficient photobleaching, further confirmed through the quantification of single-molecule photobleaching steps in fluorescence intensity and the control imaging of recombinant GFP in vitro. This global value is used to normalise the initial intensity of GFP-CCR5 foci in order to acquire estimates of stoichiometry. Further controls for each PaTCH experiment included the imaging of immobilised fluorescent microbeads to characterise the illumination and the imaging of non-transfected CHO cells to characterise the level of autofluorescence detectable and ensure false-positive foci are not present. Employing these techniques in the study of fixed CHO-GFP-CCR5 cells reveals a wide distribution of assembly stoichiometries over many cells and hundreds of tracked assemblies, as shown in **Figure 4-10**. These results are represented as kernel density estimates with the kernel width corresponding to the total uncertainty in the single molecule stoichiometry. This population of independent track-derived stoichiometries shows characteristic peaks, with the average nearest-neighbour interval between independent stoichiometry measurements revealing the typical periodicity inside oligomeric assemblies. Although the accurate measurement of small differences between two large stoichiometries is difficult, it is possible to successfully average those differences over many pairs. Thereby, for GFP-CCR5, we find the modal average periodicity to be 2.3 ± 0.5 CCR5 molecules. This periodicity value Indicates a strong tendency for CCR5 molecules to occur in dimeric subunits inside CCR5 assemblies.

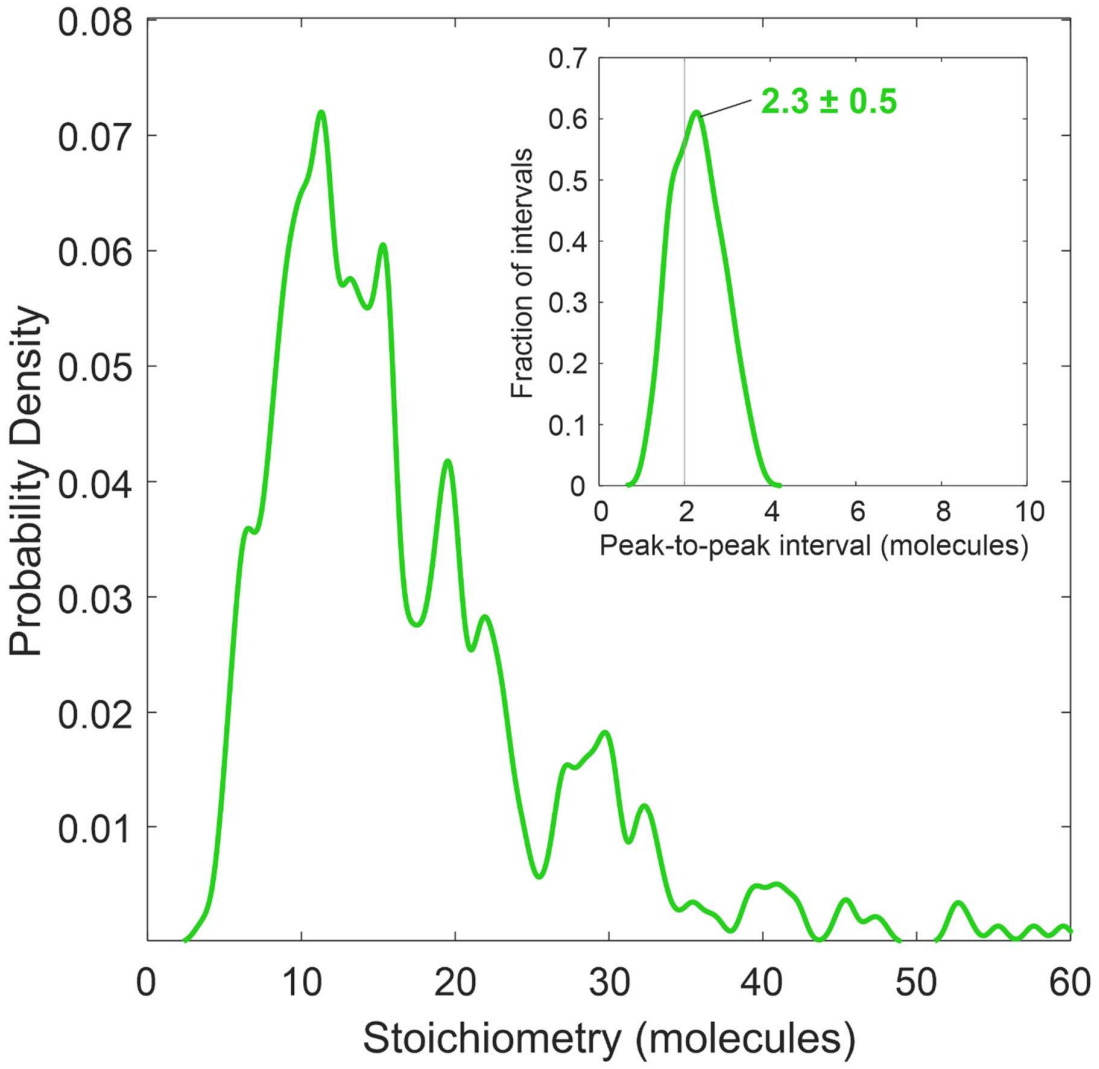

Figure 4-10: Estimating number of GFP-CCR5 molecules within individual GFP-CCR5 assemblies reveals homodimeric sub-units. Kernel density estimates of stoichiometry and (inset) periodic stoichiometry intervals of GFP-CCR5 associated foci (N = 460 tracks) detected by PaTCH microscopy in fixed CHO-GFP-CCR5 cells (N = 9 cells). Kernel width = 0.6 molecules, corresponding to the total uncertainty in the single molecule stoichiometry, rather than statistical fluctuations. Measured intervals in probability density or stoichiometry are therefore more reliable at lower stoichiometry.

4.7. PaTCH based investigations of CCR5 assembly stoichiometry reveals ligand induced effects

Extending the PaTCH-based investigation of CCR5 assemblies, this project sought to study the effects of CCR5 ligands on the behaviour of CCR5 in this context. Initial ligand investigations aimed to study CCL5-induced effects on GFP-CCR5 over a short perturbation time. The interaction between CCR5 and CCL5 is a process reported to induce internalisation, with CCL5 perturbed cells being expected to exhibit a reduction in cell surface CCR5. By limiting CCL5 exposure to 5 minutes, this study aims to determine any pre-internalisation reorganisation of CCR5. As shown in **Figure 4-11a**, the determination of the GFP-CCR5 stoichiometry distribution, provided 5 minutes exposure to CCL5, was carried out using the same method outlined in the previous section. Upon comparison with the non-perturbed control data, we see that assemblies of GFP-CCR5 retain a similarly wide distribution of sizes. Further, pair-wise periodicity analysis suggests that GFP-CCR5 retains dimeric sub-units, with the modal average periodicity to be 2.2 ± 0.3 CCR5 molecules, thereby indicating no change in the dimeric composition of CCR5 upon CCL5 exposure.

Additional analysis of these distributions reveals that the presence of CCL5 does not tend to change the average number of CCR5 assemblies, with the mean number of tracks detected not significantly differing before and after CCL5 addition, as shown in **Figure 4-11b** ((46.1 ± 4.8 and 51.1 ± 6.8 tracks per cell respectively) under the Brunner-Munzel (BM) test (n = 18, p = 0.429 | not significant at adjusted p < 0.01 level, NS)). Further, the mean stoichiometry of these assemblies lies in the vicinity of ~20 molecules regardless of CCL5 addition, as shown in **Figure 4-11c** (BM test: 17.1 ± 0.4 and 18.6 ± 0.5 molecules before and after CCL5 addition respectively, n = 920, p = 0.145 |NS). Taken together, these results suggest that the total amount of CCR5 present on the cell surface is approximately conserved under our experimental conditions.

However, CCL5 appears to affect large and small assemblies of CCR5 differently, with a larger spread of stoichiometry of assemblies in perturbed cells than can be accounted for by any difference in sampling variance. At the lower end, assemblies are more commonly comprised of approximately 8 CCR5 molecules, while at the higher end CCR5 contributes toward the growth of larger assemblies of greater than approximately 36 molecules. These two sub-groups are populated at the expense of intermediate assemblies near the mean stoichiometry. This is confirmed by the difference in the means of each, before and after CCL5 addition (BM test at stoichiometry <15 molecules, n = 436, p = 0.0085|∗; at

stoichiometry >15 molecules, n = 480, p = 0.0053|∗), despite almost identical numbers of assemblies in each group.

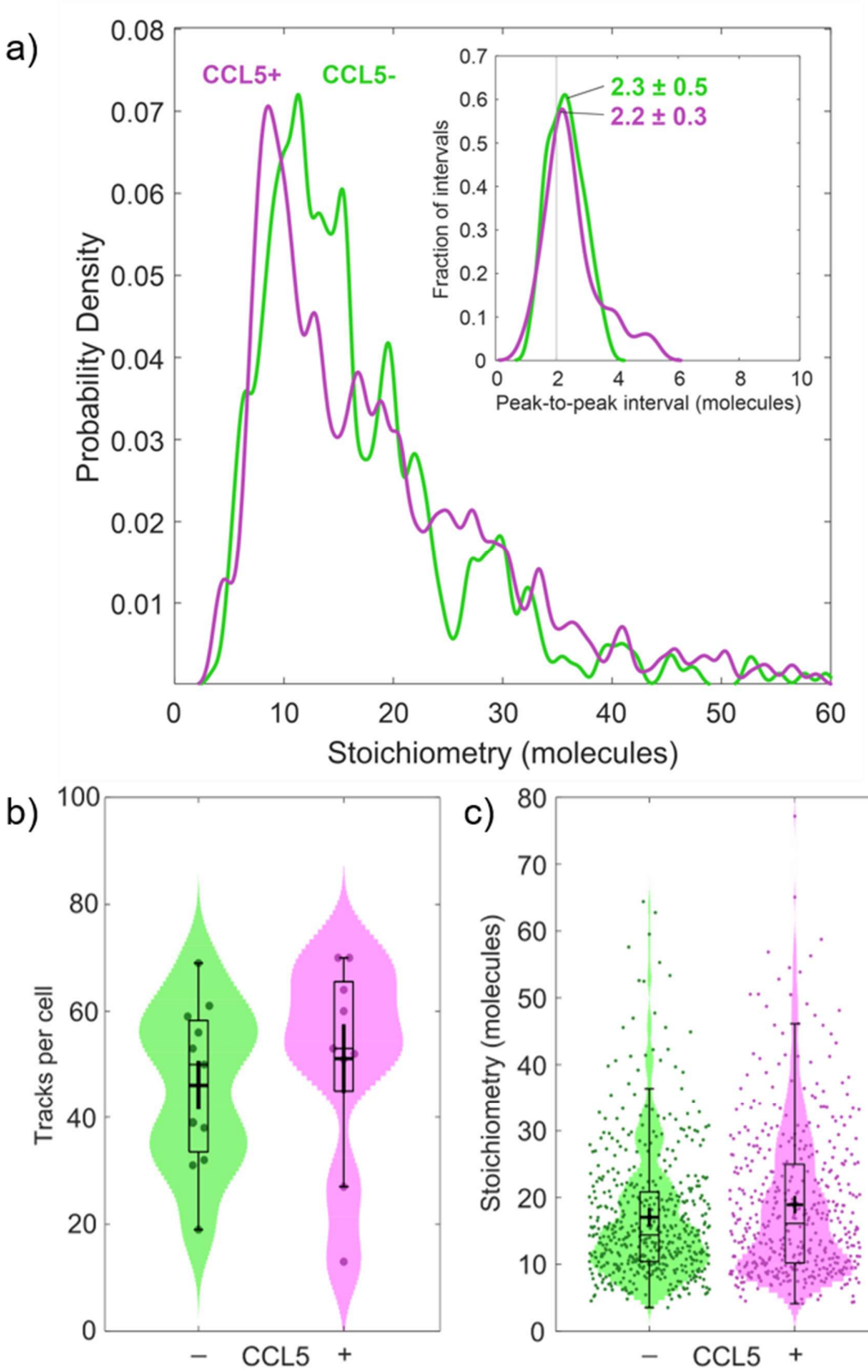
a)
CCL5+
CCL5-
Probability Density
Stoichiometry (molecules)
Fraction of intervals
Peak-to-peak interval (molecules)
2.3 ± 0.5
2.2 ± 0.3
b)
Tracks per cell
CCL5
c)
Stoichiometry (molecules)
CCL5

Figure 4-11: Investigating the effect of limited CCL5 exposure on the stoichiometry of GFP-CCR5. a) Kernel density estimates of stoichiometry and (inset) periodic stoichiometry intervals of GFP-CCR5 associated foci before (green) and after (magenta) the addition of 100nM CCL5 for 5 minutes (N=460 or 507 tracks respectively) detected by PaTCH microscopy in GFP-CCR5 transfected CHO cells (N=9 and 11 cells respectively). Kernel width = 0.6 molecules, corresponding to the total uncertainty in the single molecule stoichiometry, rather than statistical fluctuations. Measured intervals in probability density or stoichiometry are therefore more reliable at lower stoichiometry. (BM test for difference in periodicity, p=0.479|* NS). b) Numbers of GFP-CCR5 tracks detected per cell, with and without CCL5 perturbation, represented as dots spread horizontally to allow individual visualisation (N = 9 or 11 cells, respectively). c) Violin distributions of the stoichiometry of GFP-CCR5 assemblies, with and without CCL5 perturbation, represented as dots spread horizontally to allow individual visualisation (N = 460 or 507 tracks respectively). Bars, boxes, and whiskers denote median, interquartile range (IQR), and 2.5× IQR respectively and the cross denotes the mean ± SEM for both b) and c).

In order to further investigate the effect of CCR5 ligands on the behaviour of CCR5, this study aimed to investigate the extended exposure of CCR5 to the ligand CCL5, alongside the CCR5 antagonist MVC, using PaTCH. Initial studies focused on the determination of overall CCR5 expression through the quantification of total CCR5-associated fluorescent intensity, provided varying ligand exposure, over approximately 50 cells per condition. As shown in **Figure 4-12a**, the total CCR5-associated fluorescent intensity of non-perturbed CHO-GFP-CCR5 cells exhibit a broad range, however these can be seen to be grouped in three distinct bands. These bands may be indicated as low, mid and high levels of expression amongst the whole cellular population, relating to both the cells basal level of expression and the active state of the cell. Upon exposure to CCL5 for 30 minutes, the distribution of intensities can be seen to shift towards lower intensities, with the mean intensity dropping significantly, thereby indicating CCL5-induced internalisation of CCR5, in agreement with previous SIM studies employing CHO-CCR5.

Upon exposure to CCL5 after pre-treatment with MVC, the intensity distribution can be seen to shift towards higher intensities, with the mean intensity increasing significantly above that of the non-perturbed sample, a result likewise in agreement with previous SIM studies employing CHO-CCR5. Upon exposure to MVC in isolation however, the distribution of intensities does not appear to shift, with the mean intensity not changing significantly, thereby indicating minimal effect of MVC on GFP-CCR5 expression. These results indicate that CCL5 and MVC may exhibit a combined effect on the intensity of GFP-CCR5 only when both are present in the sample. As shown in **Figure 4-12b**, with individual data points being grouped into high, mid and low intensity levels, it is possible to quantify changes in the

proportion of cells contain within these boundaries between each condition. These results show a similar distribution of cells between the non-perturbed condition and cells perturbed with MVC in isolation. However, a complete depletion in the population of highly expressing cells can be seen upon exposure to CCL5. Further, we see an 82% increase in the population of highly expressing cells, coupled with a 104% decrease in the population of low expressing cells, upon exposure to CCL5 provided pre-exposure to MVC. These results further exemplify the change in the distribution of cellular expression upon exposure to MVC and CCL5.

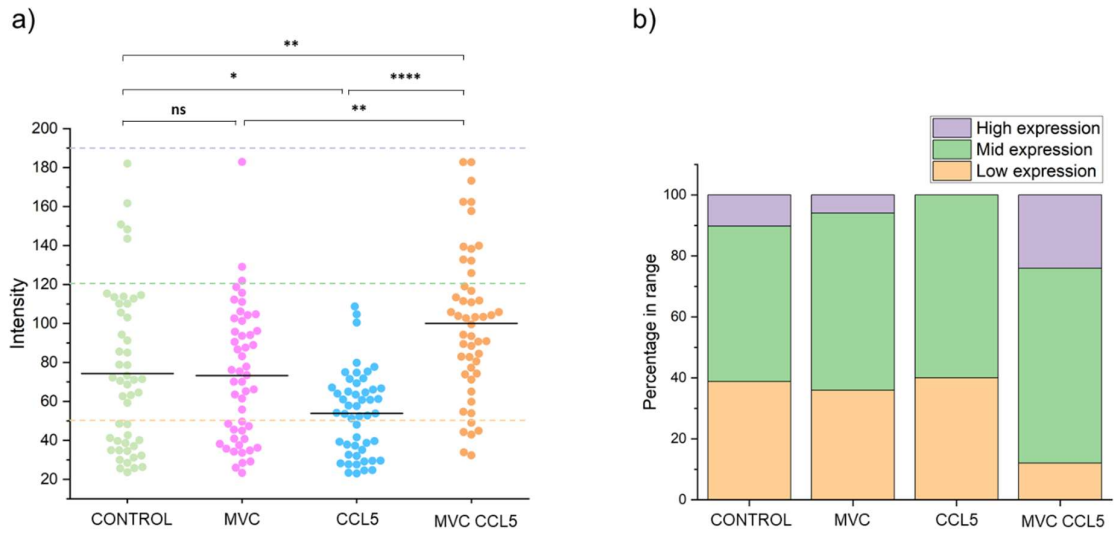

Figure 4-12: Investigating the basal membrane fluorescent signal of fixed CHO-GFP-CCR5 cells perturbed with various ligands using PaTCH microscopy. a) Jitter plots representing the fluorescence intensity of CHO-GFP-CCR5 with and without perturbations with various ligands. Intensity of CHO-GFP-CCR5 both with (Blue) and without (Green) exposure to CCL5, as well as Intensity of CHO-GFP-CCR5 given exposure to Maraviroc (MVC) both with (Orange) and without (Pink) subsequent exposure to CCL5 are represented by coloured points. Pre-treatment using MVC took place over 30 minutes. Subsequent exposure to CCL5 took place over 30 minutes. ~50 cells were analysed for each condition. Intensity measurements were taken within the cell as informed by cell segmentation masks. Intensity values are background subtracted. Bars represent the mean fluorescent intensity for a given plot. Dashed lines represent threshold boundaries between points deemed to represent low, mid and high expression. Points are spread horizontally to allow individual visualisation. Statistical analysis was carried out using a Kruskal–Wallis one-way analysis of variance (KW-ANOVA) test, ns - $P > 0.05$, * - $P \leq 0.05$, ** - $P \leq 0.01$, *** - $P \leq 0.001$, **** - $P \leq 0.0001$. b) stacked bar chart representing the percentage of points within each condition that fall into the expression thresholds indicated in a).

PaTCH based investigations continued with the imaging of ligand perturbed CHO-GFP-CCR5 samples for the estimation of assembly stoichiometry. Through cluster size analysis we aimed to extend our study of ligand induced changes from overall CCR5 expression to the make-up of individual assemblies through single molecule techniques. By determining the stoichiometry of individual assemblies expressed on CHO-GFP-CCR5 cells from varying conditions, this study aimed to determine the effects of extended CCL5 and MVC exposure on the makeup of CCR5 assemblies. As shown in **Figure 4-13**, the size of CCR5 assemblies were determined over many cells within each condition. A wide range in stoichiometry values can be seen within each condition and each condition can be seen to display a similar overall distribution, with the majority of assemblies displaying a size of 5 to 20 CCR5 receptors and each condition displaying much larger assemblies. Upon comparison of the mean stoichiometry of each condition we see that upon 30 minutes of exposure to CCL5, the average stoichiometry reduces significantly, indicating the potential breakdown of larger assemblies. In contrast, we see that upon exposure to the antagonist MVC, no significant change can be seen when compared to the non-perturbed control. Finally, we see that upon exposure to CCL5, provided pre-exposure to MVC, the average stoichiometry reduces significantly relative to the non-perturbed control. However, this distribution shift shows no significant difference from the shift induced by CCL5 in isolation, thereby indicating that although MVC is capable of inhibiting CCL5-induced internalisation of CCR5, MVC has no significant effect on the CCL5 induced changes in the stoichiometry of CCR5 assemblies.

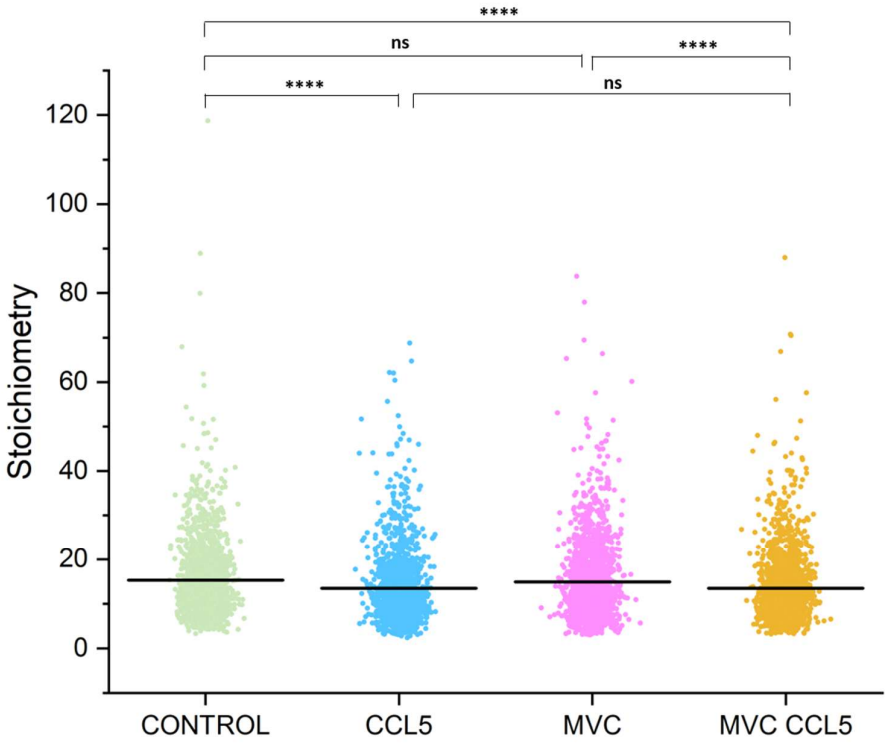

Figure 4-13: Investigating the stoichiometry of GFP-CCR5 assemblies in fixed CHO-GFP-CCR5 cells perturbed with various ligands using PaTCH microscopy. Jitter plots representing the stoichiometry of GFP-CCR5 assemblies in fixed CHO-GFP-CCR5 with and without perturbations with various ligands. GFP-CCR5 stoichiometry with (Blue) and without (Green) exposure to CCL5, as well as cells given exposure to Maraviroc (MVC) both with (Orange) and without (Pink) subsequent exposure to CCL5 are represented by coloured points. Pre-treatment using MVC took place over 30 minutes. Subsequent exposure to CCL5 took place over 30 minutes. ~40 cells were analysed for each condition. Bars represent the mean stoichiometry for a given condition. Points are spread horizontally to allow individual visualisation. Statistical analysis was carried out using a Kruskal–Wallis one-way analysis of variance (KW-ANOVA) test, ns - $P > 0.05$, * - $P \leq 0.05$, ** - $P \leq 0.01$, *** - $P \leq 0.001$, **** - $P \leq 0.0001$.

4.8. Discussion

This study sought the continued investigation of the CCR5 assemblies detected in the previous chapter through the employment of single-molecule biophysical techniques. In order to achieve these aims, development in both sample creation and microscopy

techniques was necessary. The detection of single molecules presents distinct requirements in sample preparation, with molecules under investigation ideally presenting a fluorescent tag at a consistent one-to-one ratio and being expressed at a low level in line with single molecule detection. For this purpose, this study saw the successful creation of a CHO-cell line stably expressing a GFP-CCR5 fusion at a low level. Further, this cell line was successfully characterised for GFP-expression, CCR5 expression and CCR5 functionality through flow-cytometry-based assays. Although established microscopy techniques such as TIRF can facilitate effective single-molecule investigations of molecules located in close proximity to the coverslip surface, this study sought the development of a novel microscopy technique tailored to the basal membrane imaging of adherent mammalian cells with a capacity to limit excitation to the basal membrane whilst ensuring the extension of the excitation to account for uneven membrane topology. The increased ability of this novel technique to resolve fluorescent assemblies in the basal membrane, as well as the associated increase in signal and reduction in background fluorescence, with respect to the established techniques of TIRF and HILO were successfully quantified using the new CHO-GFP-CCR5 line. This novel mode of imaging, coupled with a newly developed CCR5 expressing cell line tailored for single-molecule applications, facilitated the successful single-molecule investigation of CCR5 and provides an ideal model for future studies.

Using PaTCH microscopy for the study of CHO-GFP-CCR5 allowed for the initial characterisation of the spatial distribution of GFP-CCR5, highlighting the similarity in GFP-CCR5 presentation to the previously established CCR5-expressing cell line CHO-CCR5, with CCR5 retaining a punctated distribution across the basal membrane. This study saw the successful tracking of CCR5 assembly intensity over time with a high temporal resolution facilitating the estimation of assembly stoichiometry. GFP-CCR5 stoichiometry was found to vary across a wide distribution displaying characteristic peaks with an average periodic interval of 2.3 ± 0.5 molecules. The existence of this periodicity suggests that CCR5 assemblies likely consist of homodimeric sub-units, a result that is in agreement with previous studies which report the existence of dimeric CCR5[212,232]. Recent studies have been conducted that similarly employ CCR5 fused with GFP expressed within CHO cells, providing validity to this method of reporting[233], however these studies employ GFP coupled to the C-terminus of CCR5, as distinct from the N-terminus coupling employed in this study. Due to the existence of a PDZ binding domain on the C-terminus of CCR5, C-terminal coupling raises potential concerns regarding the downstream effect of PDZ masking on the behaviour of CCR5[64,65].

These single-molecule investigations were extended to study the behaviour of CCR5 upon exposure to the CCR5 agonist CCL5 and the CCR5 antagonist Maraviroc, both with and without subsequent exposure to CCL5. Initial studies aimed to investigate any pre-internalisation changes in the structure of CCR5 assemblies induced by CCL5 over a short time frame of 5 minutes. Application of PaTCH based stoichiometry estimation revealed a similar distribution in assembly stoichiometry between cells exposed to CCL5 and non-perturbed samples, with a pair-wise periodicity in stoichiometry values of 2.2 ± 0.3, thereby indicating the retention of the dimeric composition of CCR5 upon CCL5 exposure over this time frame. However, despite the total expression of CCR5 on the cell surface both with and without CCL5 exposure being approximately conserved, further analysis of the distribution of stoichiometry between the two conditions suggests a CCL5-induced shift, with both smaller and larger assembly populations increasing at the expense of intermediate assemblies. This shift may indicate the breakdown of intermediate assemblies present in the non-perturbed condition into smaller assemblies for relocation to sites of internalisation.

Further studies were conducted to investigate the effects of extended ligand exposure on the behaviour of GFP-CCR5. Initial studies focused on the mean fluorescence intensity of GFP-CCR5 at the basal membrane, provided a 30-minute exposure to CCL5 both with and without a 30-minute pre-treatment with MVC, alongside investigation of the lone effects of MVC, revealing that despite a broad range of cellular intensities exhibited in samples of CHO-GFP-CCR5 within each condition, cellular intensities may be associated with three distinct bands of intensity ranging from high to low expression. The distribution of cellular intensities can be seen to significantly reduce upon exposure to CCL5, with a complete depletion in the population of highly expressing cells, thereby indicating CCL5-induced internalisation as seen in previous SIM studies. Upon exposure to MVC in isolation, the distribution of intensities does not appear to shift significantly, thereby indicating minimal effect of MVC on GFP-CCR5 expression. However, upon exposure to CCL5 after pre-treatment with MVC, the distribution can be seen to shift towards higher intensities, with the mean intensity increasing significantly above that of the non-perturbed sample, the population of highly expressing cells increasing by 82% and the population of low expressing cells reducing by 104%. These results indicate that CCL5 and MVC may exhibit a combined effect on the intensity of GFP-CCR5 when both are present in the sample, a result that is in agreement with previous SIM studies of CHO-CCR5.

Finally, this study sought the quantification of assembly stoichiometry given extended exposure to CCL5 and MVC, with any resultant shift in the stoichiometry distributions indicating a ligand-induced reorganisation of assemblies. This study revealed a significant

reduction in the mean stoichiometry upon 30-minutes exposure to CCL5, indicating the CCL5-induced breakdown of larger assemblies. Further, despite the increase in basal membrane expression of CCR5 upon exposure to CCL5, provided pre-treatment with MVC, as reported in both PaTCH and SIM studies, this condition revealed a significant reduction in the mean stoichiometry, with this shift showing no significant difference from that induced by CCL5 in isolation. These results, coupled with the non-significant shift induced by MVC in isolation, suggest that MVC has no significant effect on the CCL5-induced reorganisation of CCR5 assemblies.

5. Development of new CCR5 expressing cell models for the advancement of CCR5 investigation

5.1 Introduction

Previous investigations saw the employment of an established line of CCR5-expressing adherent cells suited to the analysis of CCR5 spatial distribution using super resolution microscopy. Investigations into the makeup of CCR5 structures revealed using this model required the development of a new adherent cell line that expressed a GFP-CCR5 fusion at a level that facilitated single-molecule investigation. To facilitate further investigation of CCR5, this project sought the creation of additional bespoke cell models tailored to a range of biological assays. Although adherent cell-lines such as CHO offer an ideal morphology for fluorescent microscopy, CCR5 is endogenously expressed in non-adherent cells. The extension of available cell models to include a non-adherent CCR5-expressing cell line would provide opportunities for the validation of conclusions reached on CCR5 behaviour using an assay of increased biological relevance. Further, through the employment of an immortalised T-cell line in the creation of this new model, investigations could be extended to the study of CCR5 behaviour in the context of T-cell activation and in the interaction between cells. For this purpose, this study sought the creation of a Jurkat cell line which stably expressed the GFP-CCR5 construct employed in the previous chapter for the study of T-cell-expressed CCR5 using single molecule techniques.

In order to advance both the super resolution and single-molecule based investigations demonstrated in the previous chapters, this study additionally sought the creation of an adherent cell line which expresses CCR5 fused to a SNAP-tag self-labelling protein tag. Previous super resolution investigations relied on immunofluorescent staining for the localisation of CCR5. Although this technique has allowed the determination of the CCR5 spatial distribution in adherent cells using SIM, immunofluorescent staining demonstrates limitations. These limitations are primarily concerned with label specificity, with immunofluorescent staining generally offering a lower specificity in comparison with fluorescent protein fusions due to non-specific binding of antibodies, the retention of unbound dye contributing to background signal, incomplete saturation of all receptors with the label and the potential inability of primary antibodies to recognise all forms of the receptor. Although the employment of fluorescent protein fusions, such as the GFP-CCR5 studied in the previous chapter, provide an increased label specificity, the brightness of

fluorescent proteins is generally lower in comparison to modern organic dyes, thereby rendering cell models such as CHO-GFP-CCR5 sub-optimal for super resolution imaging. The advent of self-labelling protein tags such as SNAP-tag have allowed for the creation of cell models that benefit from both the high-brightness probes available from immunofluorescent staining and the higher labelling specificity associated with fluorescent protein fusions, thereby offering an adaptable suite of fluorophores while retaining a relatively low level of non-specific binding and a higher assurance of receptor recognition at a one to one binding ratio. Once more employing CHO cells, this study sought the creation of a CHO-SNAP-CCR5 cell line tailored for use in both PaTCH-based single molecule investigations and SIM-based super resolution investigations in order to facilitate correlative microscopy experiments and allow access to the wide range of fluorescent probes available in the SNAP-tag suite.

5.2. Characterisation of Jurkat T-cell line transfected for the expression of GFP-CCR5

In order to facilitate the extension of both future super resolution and single molecule investigations to the study of CCR5 in the context of a T-cell model, this project sought the creation of a non-adherent Jurkat cell line which expresses the GFP-CCR5 fusion employed in previous investigations (GFP-CCR5-PCDNA3.1). Initial attempts to create a Jurkat-GFP-CCR5 line saw the employment of the chemical transfection techniques that allowed the successful creation of CHO-GFP-CCR5, however several attempts employing these techniques resulted in a lack of cell recovery post-transfection. Further attempts to develop Jurkat-GFP-CCR5 saw the employment of an electroporation-based transfection method known as nucleofection. As shown in **Figure 5-1**, Jurkat were analysed using flow cytometry 64 hours after nucleofection to determine the GFP-associated fluorescence exhibited by the cells. Jurkat that underwent nucleofection for the production of GFP-CCR5-PCDNA3.1 were compared with several controls, including non-nucleofected Jurkat alongside Jurkat that had undergone nucleofection with H_2O, a plasmid coding for GFP and an alternate plasmid coding for high-expression of GFP-CCR5 with the absence of antibiotic resistance. Further, analysis of Jurkat nucleofected to produce GFP-CCR5-PCDNA3.1 included samples which were nucleofected under conditions designed to prioritise cell viability post transfection (high viability) and those designed to prioritise protein expression at the cost of cell viability post-transfection (high expression). As shown in **Figure 5-1a**, cells having undergone nucleofection using H_2O in place of plasmid display a similar distribution to cells that have not undergone nucleofection. However, as shown in **Figure 5-1b**, cells having undergone

nucleofection for the production of GFP display positive GFP expression when compared with the H_2O control. Despite this, as shown in **Figure 5-1c-e**, cells nucleofected using the alternate GFP-CCR5 plasmid, as well as cells nucleofected using the GFP-CCR5-PCDNA3.1 plasmid, showed no GFP positivity when compared with H_2O controls, regardless of nucleofection conditions.

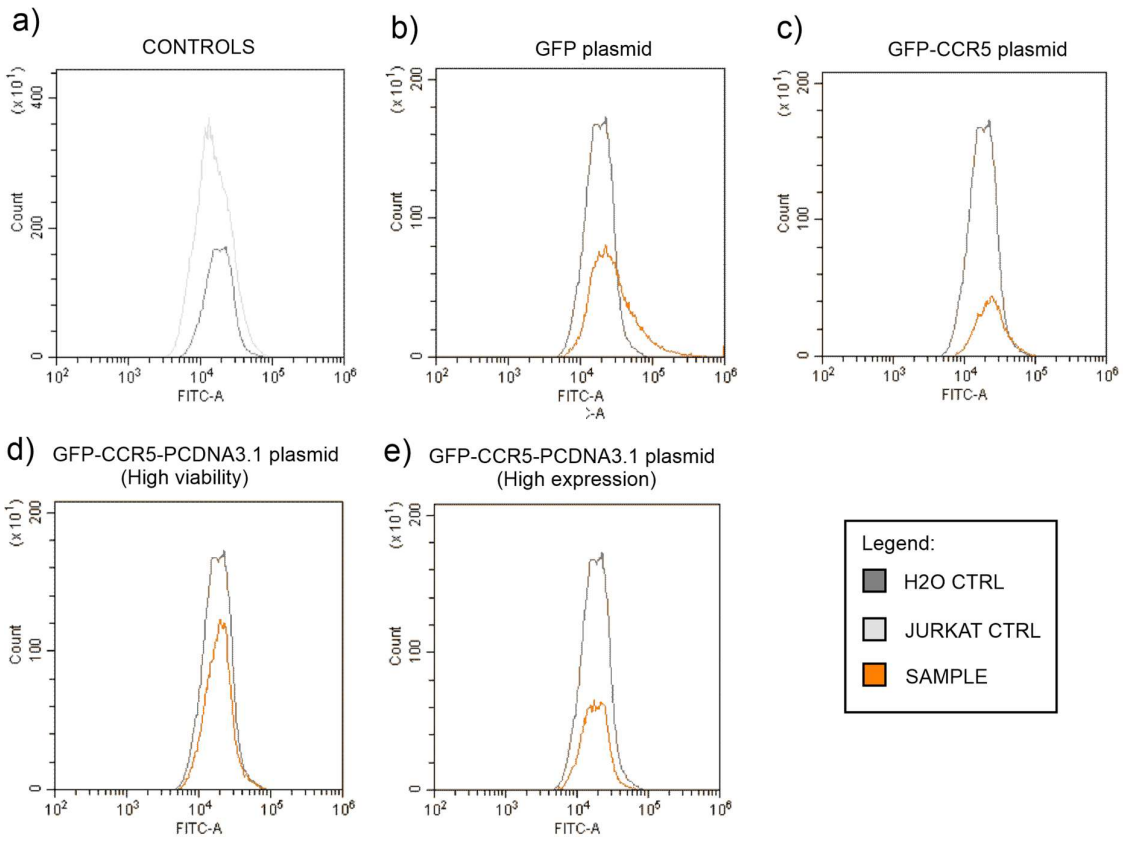

Figure 5-1: Determining the GFP-associated fluorescence of Jurkat that have undergone transfection for the expression of GFP-CCR5 using flow cytometry. a) Distribution of GFP associated emission intensity of non-transfected Jurkat and Jurkat transfected using H_2O in place of any plasmid. b) Distribution of GFP associated emission intensity of Jurkat transfected for the production of GFP, compared with H_2O control. c) Distribution of GFP associated emission intensity of Jurkat transfected for the production of GFP-CCR5 using a high-expression plasmid not coding for antibiotic resistance, compared with H_2O control. d) Distribution of GFP associated emission intensity of Jurkat transfected for the production of GFP-CCR5-PCDNA3.1, a low-expression plasmid which codes for antibiotic resistance, compared with H_2O control. This sample, alongside samples in a), b) and c), was transfected under conditions designed to prioritise cell viability post-transfection. e) Distribution of GFP associated emission intensity of Jurkat transfected for the production of GFP-CCR5-PCDNA3.1, compared with H_2O control. This sample was transfected under conditions

designed to prioritise protein expression at the cost of cell viability post-transfection. Dark grey indicates H_2O control sample, Light grey indicates non-transfected Jurkat control sample and Orange indicates Jurkat sample which has undergone transfection with the respective plasmid. Figures show cell populations after gating to remove debris and doublets.

5.3. Characterisation of CHO transfected for the expression of SNAP-CCR5 at the mixed population level

In order to facilitate correlative microscopy experiments benefiting from both super resolution and single molecule techniques, this project aimed to create a line of CHO cells which express CCR5 fused to a SNAP-tag self-labelling protein. For this purpose, a plasmid coding for the expression of SNAP-CCR5 was acquired prior to expansion and isolation using midi-prep. After confirmation of protein concentration using a NanoDrop spectrophotometer, CHO cells were transfected using the chemical transfection methods employed in the successful transfection of CHO-GFP-CCR5. Upon expansion of mixed population CHO-SNAP-CCR5 cells held under antibiotic selection, single CHO-SNAP-CCR5 cells were isolated and expanded to form clonal populations, each expressing a uniform intensity. Initial characterisation of CHO-SNAP-CCR5 aimed to determine the expression of SNAP-CCR5 within the mixed population using flow cytometry. Determining the fluorescent intensity of samples exposed to fluorescent antibodies specific to both CCR5 (MC-5 and 2D7) and the SNAP-CCR5 plasmid (FLAG-M2) would indicate the average expression of SNAP-CCR5 amongst the mixed population when compared with a range of controls. As shown in **Figure 5-2a,b**, a threshold may be applied to intensity distributions of each condition to indicate the shift in SNAP-CCR5-associated fluorescence. This threshold was calibrated to include the majority of cells within a non-transfected CHO control sample and is demonstrated using the shift in fluorescent intensity seen between samples labelled using 2D7 and a non-labelled CHO-SNAP-CCR5 control. As shown in **Figure 5-3c**, minimal shift in fluorescent intensity is seen between both transfected and non-transfected control samples, demonstrating minimal background binding of Alexa Fluor 647 and a minimal effect of transfection on autofluorescence. Further, although an increase in intensity can be seen in cells exposed to Alexa Fluor 647-MC5 and Alexa Fluor 647-FLAG-M2, a similar increase can be seen in CHO exposed to Alexa Fluor 647-MC5 and Alexa Fluor 647-FLAG-M2. Finally, the largest increase in intensity is seen in cells exposed to Alexa Fluor 647-2D7, however, results relating to the intensity of CHO exposed to Alexa Fluor 647-2D7 are not available. These results therefore indicate the potential expression of SNAP-CCR5 within mixed population CHO-SNAP-CCR5, albeit accessible by only the 2D7 antibody.

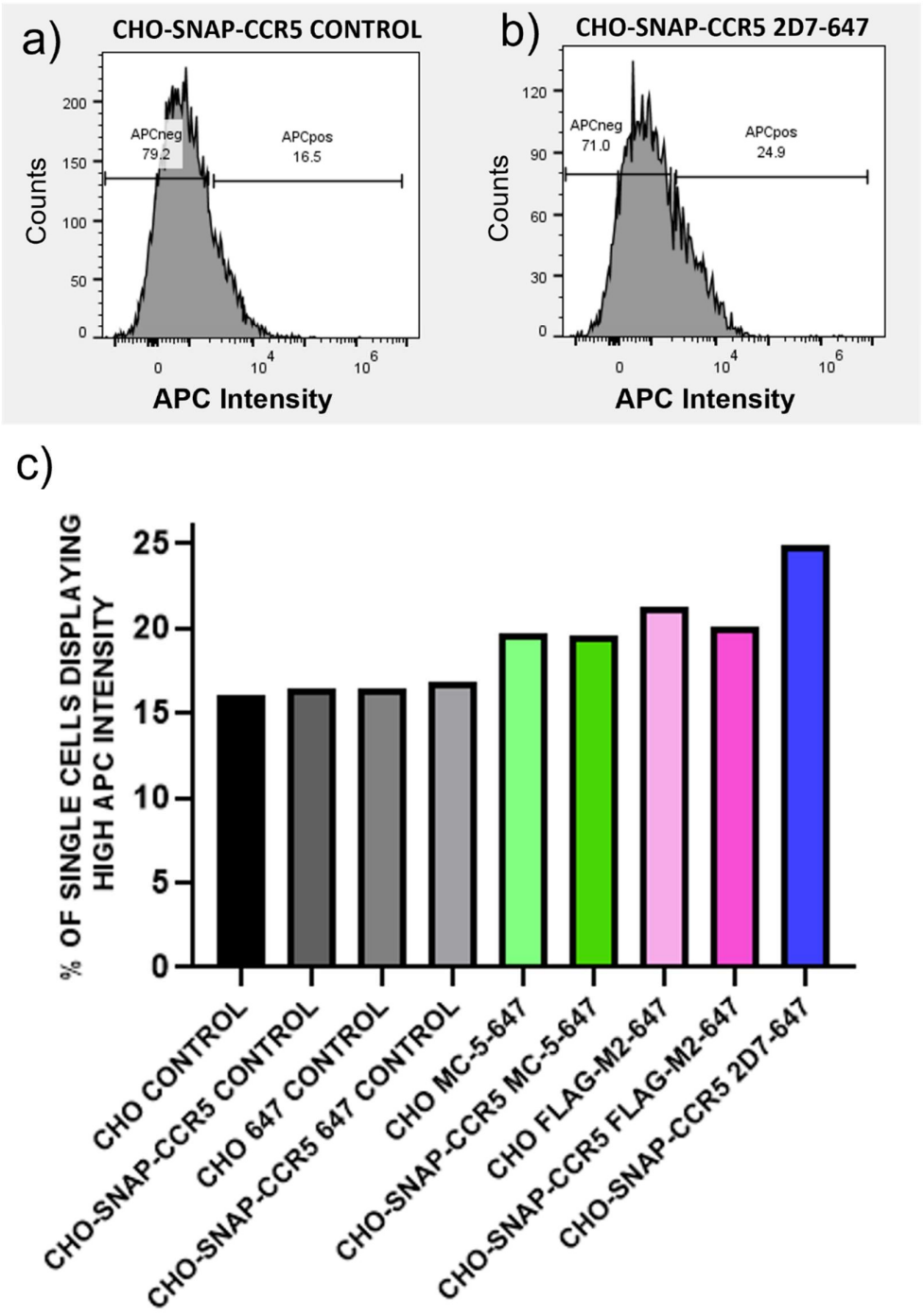

Figure 5-2: Determining the CCR5 expression of mixed population CHO-SNAP-CCR5 using flow cytometry. a-b) Demonstration of arbitrary positive and negative thresholding of APC intensity in samples of CHO-SNAP-CCR5, calibrated to include the majority of cells within a non-transfected CHO control sample. c) Bar chart representing the percentage of single cells that display a fluorescent intensity above the threshold shown in a-b). Fluorescent intensity is recorded in the APC channel corresponding to the secondary fluorescent antibody used (Alexa Fluor 647). Samples shown include CHO-SNAP-CCR5 cells and CHO cells, each with secondary only controls to show non-specific

binding of Alexa Fluor 647 and each with a double negative control to show the autofluorescence of the samples. CHO-SNAP-CCR5 are shown using primary antibodies specific to CCR5 (MC-5 and 2D7) as well as primary antibodies specific to the FLAG sequence included in the SNAP-CCR5 plasmid (FLAG-M2). CHO samples are shown using primary antibodies MC-5 and FLAG-M2, 2D7 was not included in the CHO controls due to the high value and scarcity of this molecule. All primary antibodies were coupled with Alexa Fluor 647 as their corresponding secondary. Figures show cell populations after gating to remove debris and doublets.

5.4. Characterisation of SNAP-CCR5 expression in clonal populations of CHO-SNAP-CCR5 using immunofluorescent labelling

In order to continue the development of a stable CHO-SNAP-CCR5 line, this study sought the determination of SNAP-CCR5 expression within clonal populations. To maximise the likelihood of isolating a population that displayed a sufficient SNAP-CCR5 expression, approximately 50 individual clonal populations were analysed for Alexa Fluor 647-2D7 associated fluorescence using flow cytometry with comparison to control samples including CHO-GFP-CCR5, CHO-SNAP-CCR5 and CHO cells exposed to Alexa Fluor 647-2D7 and Alexa Fluor 647 only. Of the ~ 50 clonal populations of CHO-SNAP-CCR5, several displayed varying levels of cells deemed positive when compared with CHO controls and secondary only controls. Of these positive populations, 6 were chosen for further cultivation that displayed high, medium and low expression levels relative to CHO-GFP-CCR5. As shown in **Figure 5-3a,b**, the previously developed CHO-GFP-CCR5 line displays positivity for both GFP-associated and Alexa Fluor 647-2D7-associated fluorescence. Further, **Figure 5-3c** demonstrates similar distributions for CHO exposed to Alexa Fluor 647-2D7 and Alexa Fluor 647 only, suggesting minimal non-specific binding of 2D7. As shown in **Figure 5-3d**, all clonal CHO-SNAP-CCR5 populations chosen for further cultivation display positivity for CCR5, with the distribution of each population exposed to Alexa Fluor 647-2D7 showing a positive shift with respect to the samples exposed to Alexa Fluor 647 only and CHO controls. Populations deemed to display a medium level of expression show a similar distribution to the previously cultivated CHO-GFP-CCR5, while the high and low populations display a relative shift in expression. The final distribution displays an example of an isolated population that exhibits dual sub-populations, with one sub-population appearing negative and one sub-population appearing high in SNAP-CCR5 expression. Each clone chosen for further cultivation was named corresponding to its respective origin well, with the two high expression clones being named AE3 and AB9, the two medium expression clones being

named BF2 and AF9, the low expression clone being named BE10 and the dual expression population being named BF1.

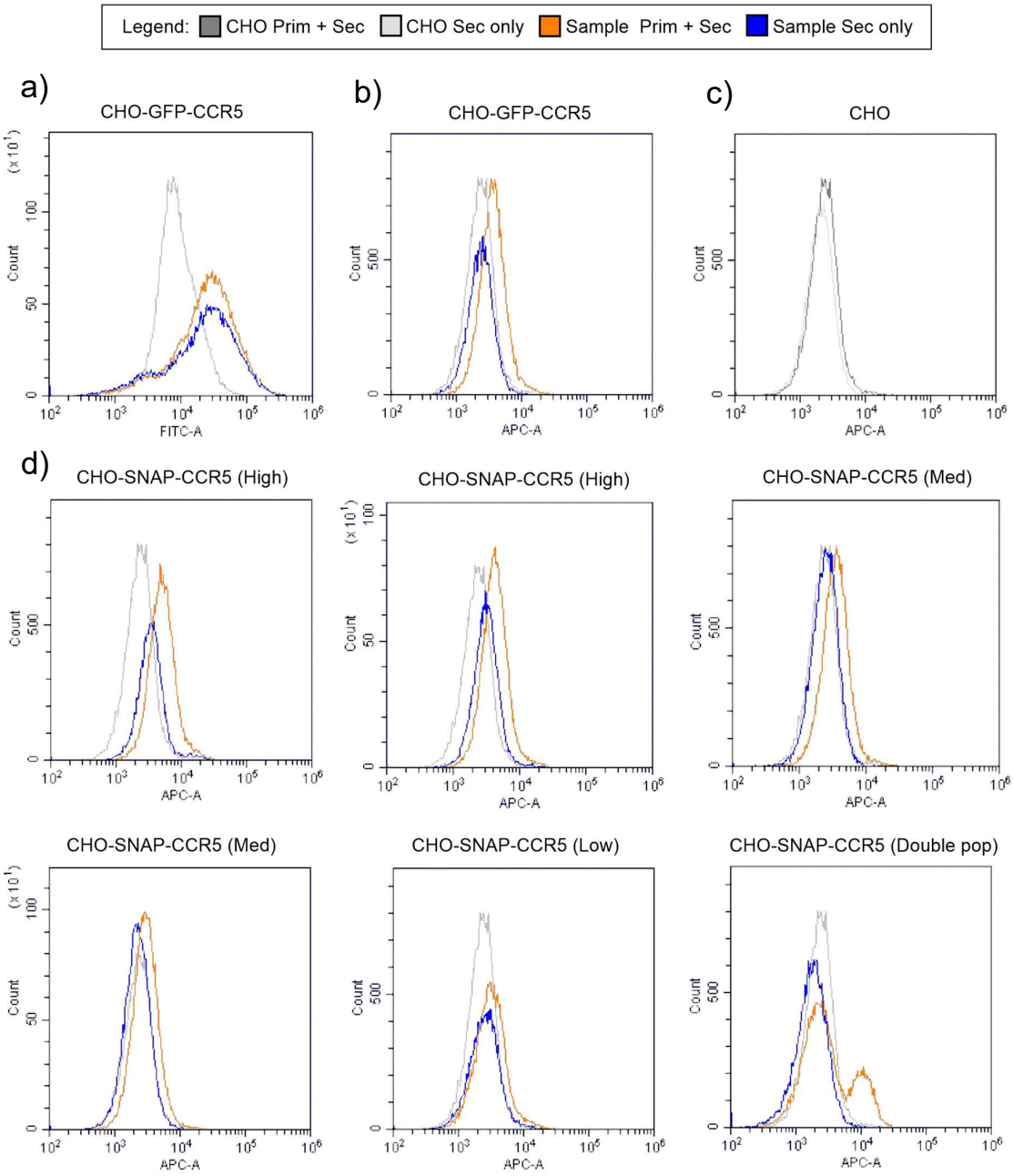

Figure 5-3: Determining the CCR5 expression of clonal populations of CHO-SNAP-CCR5 using flow cytometry. a) Distribution of GFP associated emission intensity for CHO-GFP-CCR5 exposed to Alexa Fluor 647-2D7, CHO-GFP-CCR5 exposed to Alexa Fluor 647 only and CHO exposed to Alexa Fluor 647-2D7. Recorded in the FITC channel. b) Distribution of Alexa Fluor 647 associated emission intensity for CHO-GFP-CCR5 exposed to Alexa Fluor 647-2D7, CHO-GFP-CCR5 exposed to Alexa Fluor 647 only and CHO exposed to Alexa Fluor 647-2D7. Recorded in the APC channel. c) Distribution of Alexa Fluor 647 associated emission intensity for both CHO exposed to Alexa Fluor 647-2D7, and CHO exposed to Alexa Fluor 647 only. Recorded in the APC channel. d) Distribution of

Alexa Fluor 647 associated emission intensity for various clonal populations of CHO-SNAP-CCR5 which have been exposed to either Alexa Fluor 647-2D7 or Alexa Fluor 647 only. These are shown alongside distributions for CHO cells exposed to Alexa Fluor 647-2D7. Clones are determined to have High, medium or low expression relative to the control. One clonal population displays characteristics of a dual population. Recorded in the APC channel. Dark grey indicates Alexa Fluor 647-2D7-CHO, Light grey indicates Alexa Fluor 647-CHO, Orange indicates Alexa Fluor 647-2D7-CHO-GFP-CCR5 or Alexa Fluor 647-2D7-CHO-SNAP-CCR5 respectively and Blue indicates Alexa Fluor 647-CHO-GFP-CCR5 or Alexa Fluor 647-CHO-SNAP-CCR5 respectively. Figures show cell populations after gating to remove debris and doublets.

In order to verify the expression of SNAP-CCR5 within clonal samples of CHO-SNAP-CCR5, as well as ensuring the accessibility of the CCR5 N-terminus, flow cytometry investigations were repeated using not only 2D7, but the additional primary antibodies MC-5 and FLAG-M2. Clonal populations were exposed to Alexa Fluor 647-2D7, Alexa Fluor 647-MC5 and Alexa Fluor 647-FLAG-M2 and were compared with a series of control samples including secondary only clonal controls and non-transfected CHO exposed to both primary and secondary antibodies. As shown in **Figure 5-4**, shifts in 2D7-associated signal appear reduced when compared to previous flow cytometry experiments, a result that is especially pronounced in populations AE3 and AB9, which had previously been categorised as highly expressing. Further, shifts in MC-5 and FLAG-M2 associated fluorescence above control samples are minimal in each clonal sample. Low levels of MC-5-associated fluorescence may be due to SNAP-associated masking of the CCR5 N-terminus, thereby restricting the accessibility of the MC-5 binding site. However, when combined with a low level of both FLAG-M2 and 2D7-associated fluorescent signal, these results suggest the loss of SNAP-CCR5 expression in all clonal populations over time.

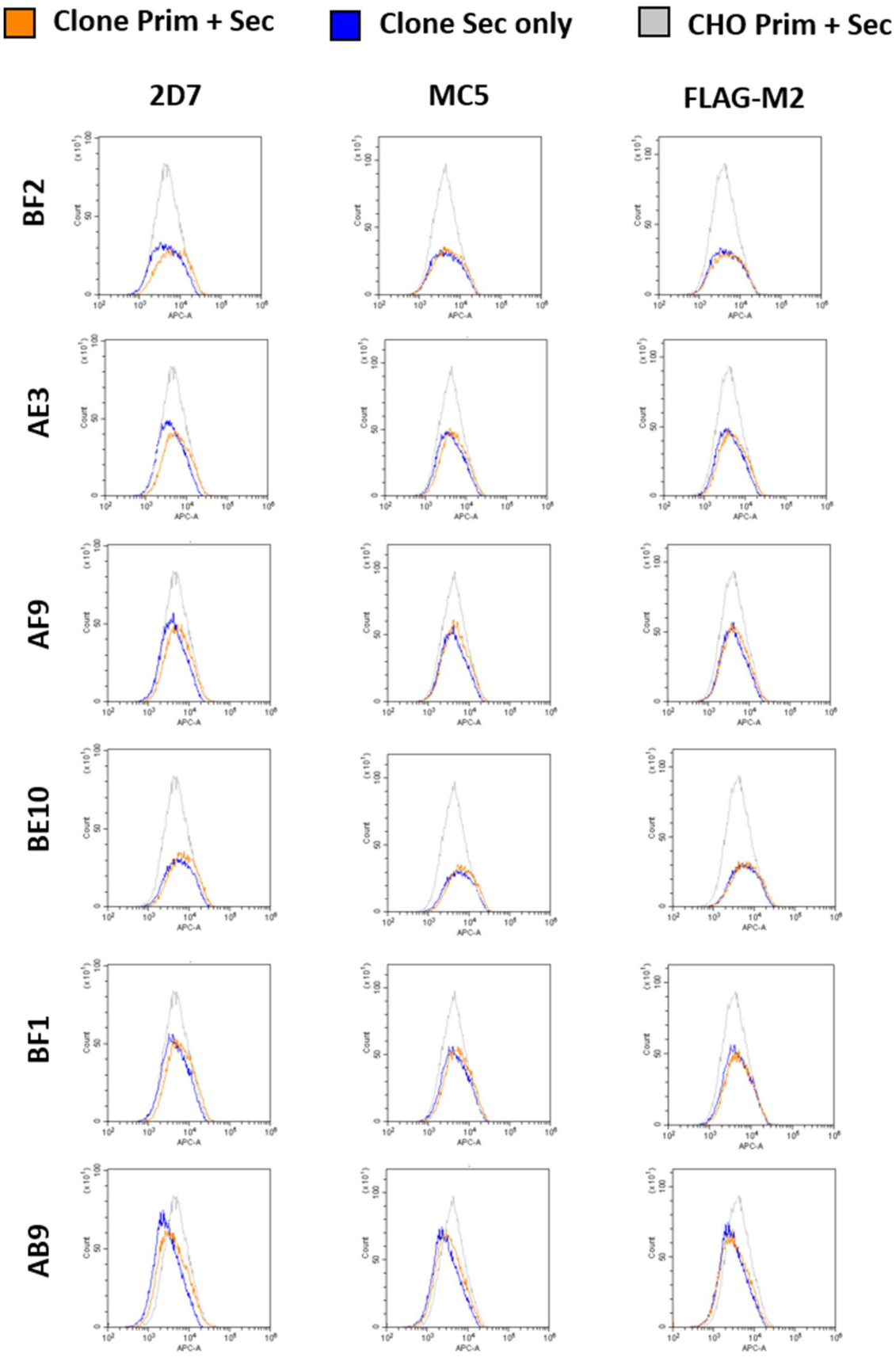
Clone Prim + Sec
Clone Sec only
CHO Prim + Sec
2D7
MC5
FLAG-M2
BF2
AE3
AF9
BE10
BF1
AB9
Count
APC-A

Figure 5-4: Determining the CCR5 expression of clonal populations of CHO-SNAP-CCR5 using flow cytometry-based analysis of 2D7, MC-5 and FLAG-M2 associated fluorescence. Distribution of Alexa Fluor 647 associated emission intensity for various clonal populations of CHO-SNAP-CCR5 which have been exposed to either Alexa Fluor 647-2D7, Alexa Fluor 647-MC5, Alexa Fluor 647-FLAG-M2 (Orange) or Alexa Fluor 647 only (Blue). These are shown alongside distributions of CHO cells exposed to Alexa Fluor 647-2D7, Alexa Fluor 647-MC5 and Alexa Fluor 647-FLAG-M2 respectively (Grey). Recorded in the APC channel. Samples were fixed after exposure to primary antibodies and stored overnight. Samples were exposed to secondary antibodies the following day prior to analysis. Figures show cell populations after gating to remove debris and doublets.

In order to maximise the specific binding of immunofluorescent labels while minimising any associated non-specific binding, flow cytometry investigations of clonal populations were repeated using an improved protocol. This new protocol saw the delay of sample fixation until exposure to the fluorescent secondary antibody had been carried out, thereby removing any effects of the fixation solution on the non-specific binding of dyes. Further this new protocol saw an increase in the amount of time that samples were exposed to their respective primary antibody up to two hours. By increasing this timeframe, it allows for any additional binding of the primary antibody that may not have been achievable after a shorter time scale. Additionally, this new protocol benefitted from the analysis of samples on the same day as sample preparation to minimise any transient loss of specific binding. As in previous experiments, clonal populations were prepared with primary and secondary antibodies prior to fixation and were compared with clonal samples with and without exposure to secondary in the absence of primary antibodies. Samples were analysed directly after sample preparation. As shown in **Figure 5-5**, small shifts can be seen in the intensity distribution of some clones, with the tail of higher expressing cells shifting slightly to the right in certain clones with certain primary antibodies. For example, BE10 displays a small peak shift in samples exposed to each primary antibody when compared with controls, whereas AE3 displays a small peak shift only upon exposure to 2D7. However, this does not constitute compelling evidence of the expression of SNAP-CCR5 within CHO-SNAP-CCR5 clonal samples. These results suggest that, although clonal populations display antibiotic resistance associated with successful transfection, the populations have undergone the transient loss of SNAP-CCR5 expression to a level that is not reliably detectable using immunofluorescent staining.

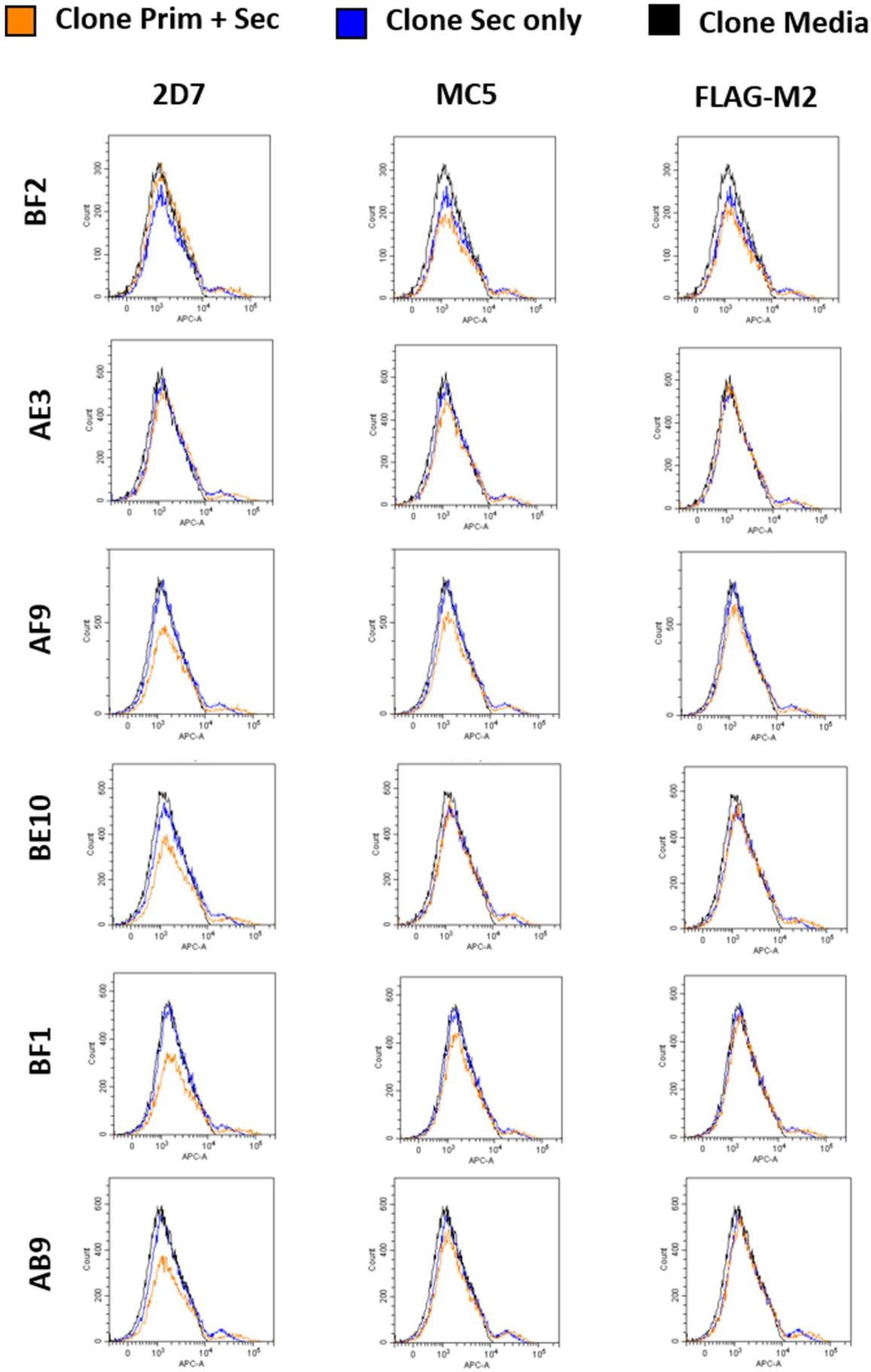
Clone Prim + Sec
Clone Sec only
Clone Media
2D7
MC5
FLAG-M2
BF2
AE3
AF9
BE10
BF1
AB9
Count
APC-A

Figure 5-5: Determining the CCR5 expression of clonal populations of CHO-SNAP-CCR5 using flow cytometry-based analysis of 2D7, MC-5 and FLAG-M2 associated fluorescence, with extended exposure to primary antibodies. Distribution of Alexa Fluor 647-associated emission intensity for various clonal populations of CHO-SNAP-CCR5 which have been exposed to either Alexa Fluor 647-2D7, Alexa Fluor 647-MC5, Alexa Fluor 647-FLAG-M2 (Orange), Alexa Fluor 647 only (Blue) or no antibodies (Black). Recorded in the APC channel. Exposure of samples to their respective primary antibodies was increased to 2 hours. Samples fixed after exposure to both primary and secondary antibodies and analysed directly after preparation. Figures show cell populations after gating to remove debris and doublets.

5.5. Characterisation of SNAP-CCR5 expression in clonal populations of CHO-SNAP-CCR5 using SNAP labelling

Immunofluorescent staining-based investigations of clonal CHO-SNAP-CCR5 populations revealed an inability to reliably detect SNAP-CCR5. In order to ensure that this is not due to the SNAP-induced masking of antibody binding sites, this study sought to determine SNAP-CCR5 expression using SNAP-Surface-Alexa Fluor 647, a fluorescent label specific to the SNAP-Tag. For this purpose, flow cytometry was carried out on clonal populations with cells being exposed to the label for 30 min at 37C prior to fixation, following the manufacturers recommended protocol. Further, clonal populations labelled with SNAP-Surface-Alexa Fluor 647 were compared with unlabelled controls and labelled non-transfected CHO cells. As shown in **Figure 5-6**, despite a large increase in the Alexa Fluor 647-associated fluorescence in labelled clonal samples when compared with non-labelled samples, a similar increase can be seen in non-transfected CHO control samples that were exposed to the label. These results indicate a high level of non-specific binding of the SNAP-Surface-Alexa Fluor 647 label. Further, the small number of cells available for analysis indicates a sub-optimal SNAP-Surface-Alexa Fluor 647 labelling protocol.

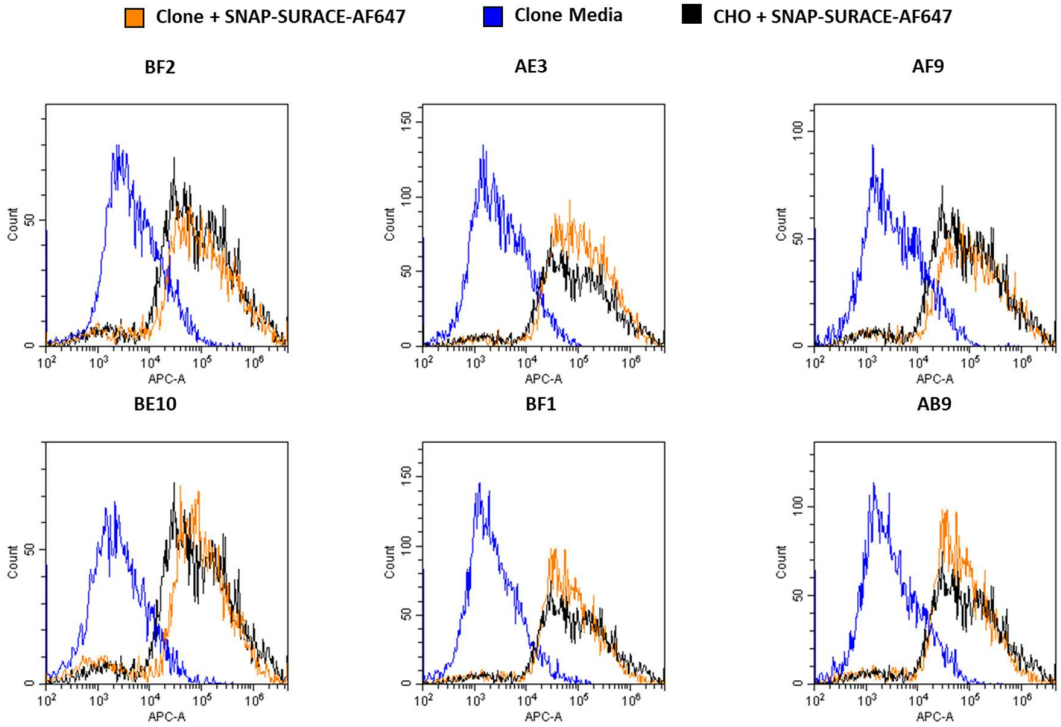

Figure 5-6: Determining the SNAP-CCR5 expression of clonal populations CHO-SNAP-CCR5 using flow cytometry-based analysis of SNAP-Surface-Alexa Fluor 647 associated fluorescence. Distribution of Alexa Fluor 647 associated emission intensity for various clonal populations of CHO-SNAP-CCR5 which have been exposed to either SNAP-Surface-Alexa Fluor 647 (Orange) or media only (Blue). These are shown alongside distributions of CHO cells exposed to SNAP-Surface-Alexa Fluor 647 (Black). Recorded in the APC channel. Samples were labelled with 5 µM SNAP-Surface-Alexa Fluor 647 for 30 min at 37C prior to fixation. Samples were analysed directly after preparation. Figures show cell populations after gating to remove debris and doublets.

Due to the large level of non-specific binding and low level of cells viable for analysis resulting from the SNAP-Surface-Alexa Fluor 647 labelling protocol, this study sought the characterisation of the optimal labelling conditions in order to facilitate future investigations of SNAP-CCR5. This was achieved through flow cytometry-based analysis of non-transfected CHO samples that had undergone labelling at varying concentrations of SNAP-Surface-Alexa Fluor 647. Further, this experiment was conducted in both fixed cells and live cells to investigate the effect of fixation on cell count. As shown in **Figure 5-7a,b**, samples that have undergone fixation result in a much lower number of cells available for analysis when compared with cells that were analysed live. Further, as can be seen in **Figure 5-7b**, SNAP-Surface-Alexa Fluor 647-associated fluorescence reduces proportionally to the concentration of SNAP-Surface-Alexa Fluor 647, with a 1/81 reduction (62 nM) resulting in the lowest level of background binding when compared with non-labelled controls. These results indicate the possibility for the reduction of background binding to a level that is useful

in future investigations. It can be concluded therefore, that the labelling protocol for SNAP-Surface-Alexa Fluor 647 may be improved through both the use of a lower concentration and the analysis of cells in the absence of fixation.

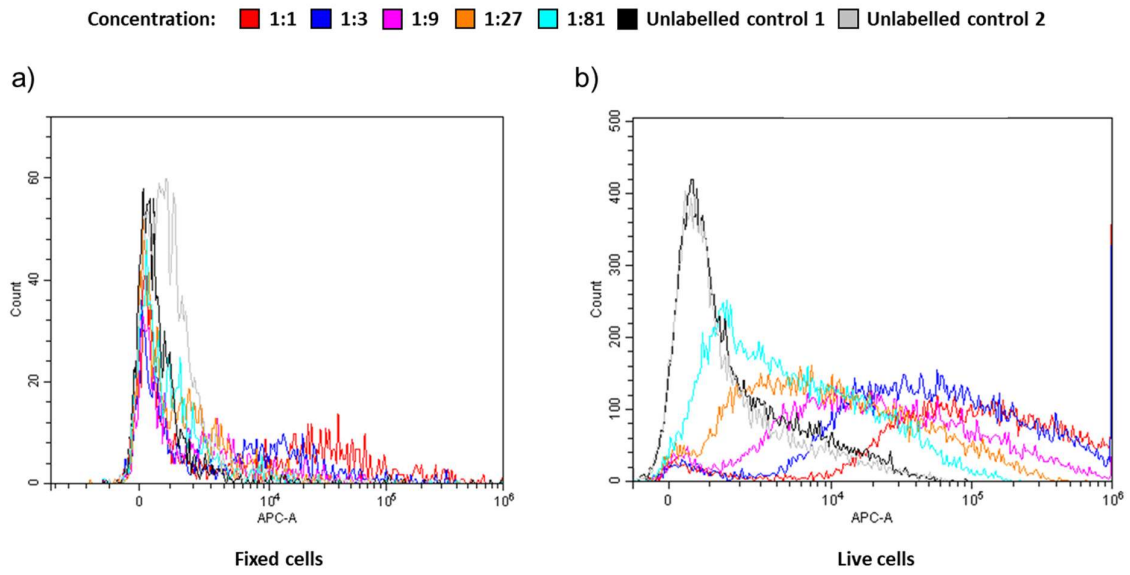

Figure 5-7: Determining the minimal background binding of SNAP-Surface-Alexa Fluor 647 using flow cytometry-based analysis of non-transfected CHO cells with varying labelling conditions. Distribution of Alexa Fluor 647 associated emission intensity for non-transfected CHO cells labelled using varying concentration levels ranging from 0 - 5 µM. Samples were analysed either after fixation a) or live without fixation b). Recorded in the APC channel. Samples were labelled with SNAP-Surface-Alexa Fluor 647 for 30 min at 37C prior to fixation or live analysis. Samples were analysed directly after preparation. Figures show cell populations after gating to remove debris and doublets.

5.6. Characterisation of SNAP-CCR5 expression in transiently transfected populations of CHO-SNAP-CCR5

Previous results demonstrated the transient loss of SNAP-CCR5 expression in stably transfected clonal populations. Continued development of CHO-SNAP-CCR5 samples suitable for correlative microscopy experiments sought the characterisation of transiently transfected cells that had undergone transfection to produce SNAP-CCR5 but did not receive selection antibiotics, samples were instead harvested for analysis by flow cytometry 48 hours after transfection. Samples were transfected whilst exhibiting varying levels of cell confluence, with samples following manufacturers recommended guidelines of high confluence being shown in **Figure 5-8a** and samples following an adapted protocol of low confluence being

shown in **Figure 5-8b**. Samples were labelled following the improved labelling protocol determined previously. As shown in **Figure 5-8a** a large shift in intensity can be seen in labelled transiently transfected samples when compared with non-labelled transiently transfected samples and both labelled and nonlabelled non-transfected controls. These results exemplify the ability of SNAP-Surface-Alexa Fluor 647 to access and report the SNAP-CCR5 construct and indicate the increased expression of SNAP-CCR5 in transiently transfected samples. As shown in **Figure 5-8a**, although a similar peak shift can be seen in cells that displayed high confluence upon transfection, this shift is weak in comparison with the equivalent low confluence sample. These results suggest a higher transfection efficiency in samples when following the adapted protocol.

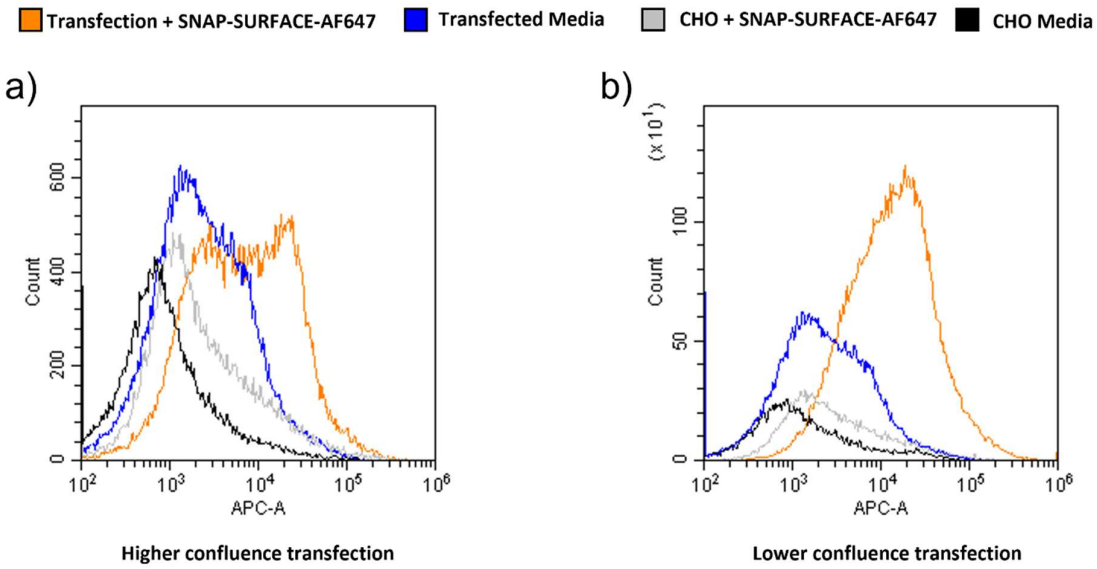

Figure 5-8: Determining the SNAP-CCR5 expression of transiently transfected CHO-SNAP-CCR5 using flow cytometry-based analysis of SNAP-Surface-Alexa Fluor 647 associated fluorescence. Distribution of Alexa Fluor 647 associated emission intensity for CHO cells transiently transfected to produce SNAP-CCR5 which have been exposed to either SNAP-Surface-Alexa Fluor 647 (Orange) or media only (Blue). These are shown alongside distributions for CHO cells exposed to SNAP-Surface-Alexa Fluor 647 (Grey) or media only (Black). Samples underwent transfection under conditions of High confluence (a) or Low confluence (b). Recorded in the APC channel. Samples were labelled with 62 nM SNAP-Surface-Alexa Fluor 647 for 30 min at 37C with no fixation, optimal conditions as determined previously. Samples were analysed directly after preparation. Figures show cell populations after gating to remove debris and doublets.

Further confirmation of the expression of the SNAP-CCR5 construct within transiently transfected samples of CHO-SNAP-CCR5 was carried out through the repeated analysis of

CHO-SNAP-CCR5 samples alongside control samples that had undergone transient transfection using H_2O in place of the SNAP-CCR5 plasmid, thereby indicating any effect of the transfection reagent on SNAP-Surface-Alexa Fluor 647-associated fluorescence. As shown in **Figure 5-9a,b**, a shift in the H_2O control relative to the Media only control indicates an increased level of background binding associated with the transfection reagent. Despite this, as shown in **Figure 5-9b**, a large shift can still be seen relative to the H_2O control in CHO-SNAP-CCR5 that underwent transfection under low confluence, thereby confirming the ability of transiently transfected samples to express the SNAP-CCR5 construct. However, as shown in **Figure 5-9a**, no such shift can be seen in CHO-SNAP-CCR5 that underwent transfection under high confluence, further indicating a higher transfection efficiency in samples when following the adapted protocol.

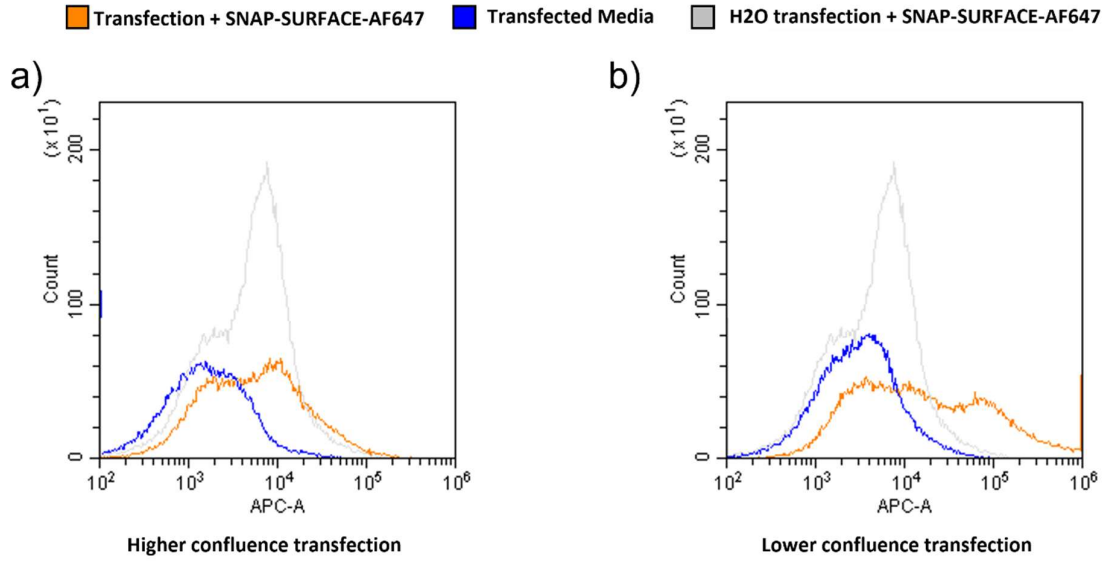

Figure 5-9: Confirming the SNAP-CCR5 expression of transiently transfected CHO-SNAP-CCR5 using flow cytometry-based analysis of SNAP-Surface-Alexa Fluor 647 associated fluorescence. Distribution of Alexa Fluor 647 associated emission intensity for CHO cells transiently transfected for the production of SNAP-CCR5 which have been exposed to either SNAP-Surface-Alexa Fluor 647 (Orange) or media only (Blue). These are shown alongside distributions for CHO cells that have undergone transfection using H_2O and have been exposed to SNAP-Surface-Alexa Fluor 647 (Grey). Samples underwent transfection under conditions of high confluence (a) or low confluence (b). Recorded in the APC channel. Samples were labelled with 62 nM SNAP-Surface-Alexa Fluor 647 for 30 min at 37C with no fixation, optimal conditions as determined in previously. Samples were analysed directly after preparation. Figures show cell populations after gating to remove debris and doublets.

Upon confirmation of the accessibility of the SNAP construct within transiently transfected CHO-SNAP-CCR5, this study sought the confirmation of CCR5 accessibility and FLAG motif accessibility through the use of immunofluorescent staining employing the previously used primary antibodies 2D7, MC-5, and FLAG-M2. For this purpose, transiently transfected CHO-SNAP-CCR5 cells were analysed after labelling with respective primary and secondary antibodies prior to fixation. These samples were compared with transiently transfected CHO-SNAP-CCR5 cells that were exposed to secondary antibodies in the absence of primary antibodies, and H_2O transfected samples that were exposed to both primary and secondary antibodies. As shown in **Figure 5-10**, large shifts can be seen in SNAP-Surface-Alexa Fluor 647 associated fluorescence in labelled transiently transfected samples when compared with controls, regardless of the primary antibody employed. This result clearly indicates the presence of SNAP-CCR5 within transiently transfected samples and confirms the accessibility of the CCR5 chemokine binding site, CCR5 N-terminus and FLAG motif contained within the SNAP-CCR5 construct.

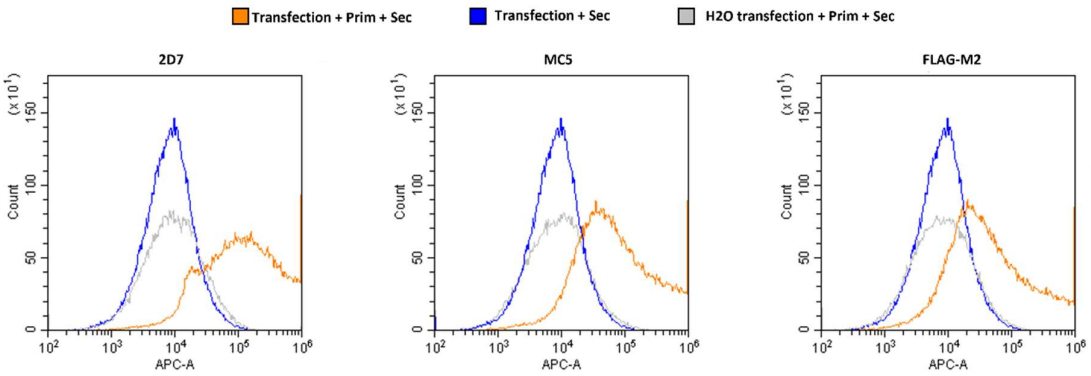

Figure 5-10: Determining the CCR5 expression of transiently transfected CHO-SNAP-CCR5 using flow cytometry-based analysis of 2D7, MC-5 and FLAG-M2 associated fluorescence. Distribution of Alexa Fluor 647 associated emission intensity for CHO cells transiently transfected for the production of SNAP-CCR5 which have been exposed to either Alexa Fluor 647-2D7, Alexa Fluor 647-MC5, Alexa Fluor 647-FLAG-M2 (Orange) or Alexa Fluor 647 only (Blue). These are shown alongside distributions for CHO cells that have undergone transfection using H_2O and have been exposed to either Alexa Fluor 647-2D7, Alexa Fluor 647-MC5, Alexa Fluor 647-FLAG-M2 (Grey). Samples underwent transfection under conditions of Low confluence, optimal conditions as determined previously. Recorded in the APC channel. Exposure of samples to their respective primary antibodies took place over 2 hours. Samples were fixed after exposure to both primary and secondary antibodies and analysed directly after preparation. Figures show cell populations after gating to remove debris and doublets.

Initial fluorescent microscopy studies into the presentation of CHO-SNAP-CCR5 utilised traditional fluorescent microscopy to confirm detectability of SNAP-CCR5. As shown in **Figure 5-11a**, despite fluorescent emission being detected using a channel well suited to Alexa Fluor 647 spectra (Cy5), a large level of fluorescence can also be seen in the Cy3 channel (emission peak at 568nm), indicating background fluorescence that is not specific to Alexa Fluor 647. Further, a large number of fluorescent intercellular puncta can be seen on the coverslip, with an emission most strongly captured in the Cy3 channel. As shown in **Figure 5-11b**, a comparable level of fluorescent emission can be seen in both labelled and unlabelled CHO-SNAP-CCR5 as well as labelled H_2O transfected cells, whereas non-transfected cells exhibit a much lower fluorescent emission regardless of the presence of Alexa Fluor 647. These results indicate that the background fluorescence observed is associated with the transfection reagent. Finally, as shown in **Figure 5-11c**, a small number of cells that express highly in the Cy5 channel are present in labelled CHO-SNAP-CCR5 samples. Although these highly expressing cells display signal in the Cy3 channel, the emission in each channel does not necessarily appear co-localised. These results suggest that the transient transfection of CHO-SNAP-CCR5 produces samples that contain a low number of highly expressing cells.

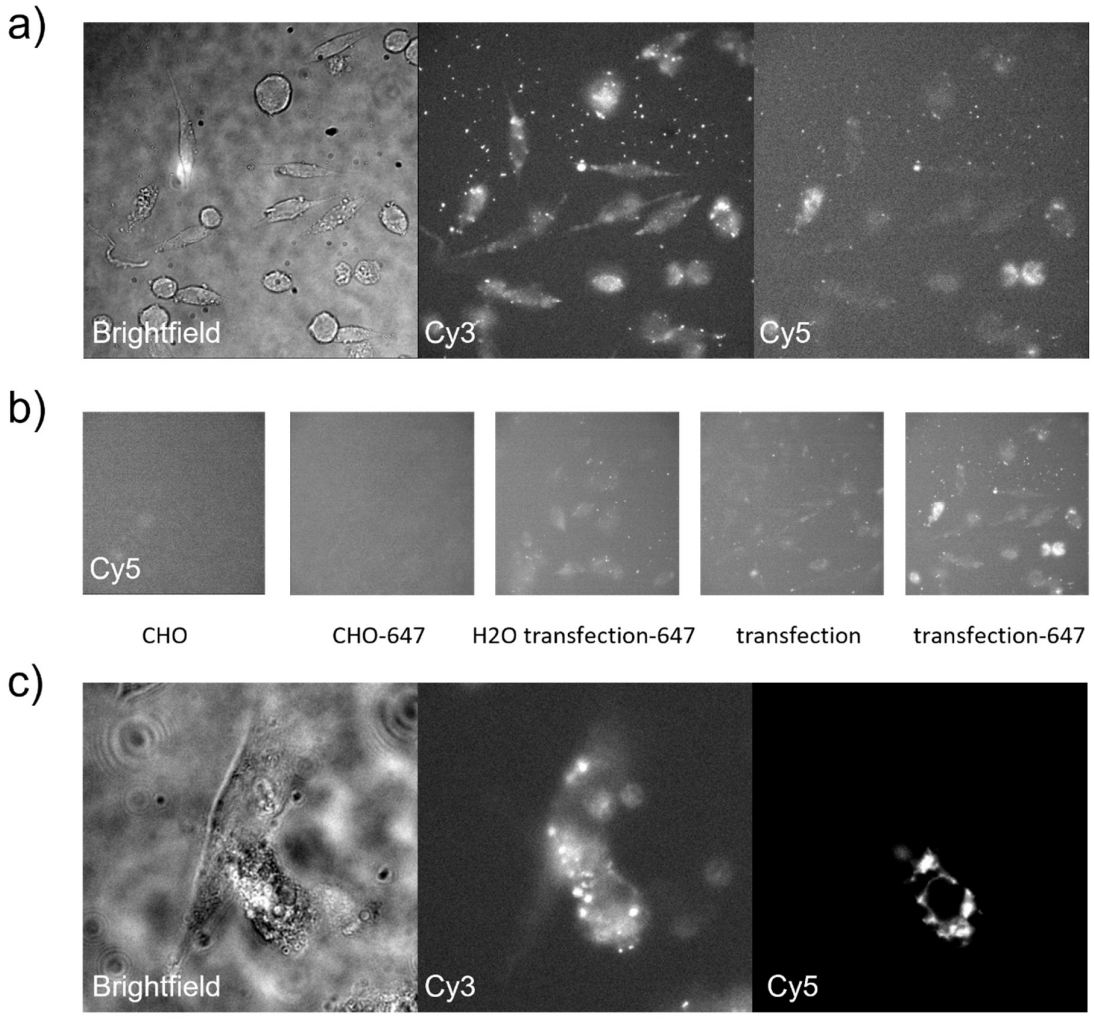

Figure 5-11: Representative images of the SNAP-CCR5 expression of transiently transfected CHO-SNAP-CCR5, acquired using traditional fluorescence microscopy of SNAP-Surface-Alexa Fluor 647 associated fluorescence. Fluorescent images of fixed CHO-SNAP-CCR5 cells labelled with SNAP-Surface-Alexa Fluor 647, compared with control samples of unlabelled CHO-SNAP-CCR5, labelled CHO that have undergone transient transfection using H_2O and both labelled and unlabelled non-transfected CHO. Fluorescence was acquired using a standard upright fluorescent microscope with a 63X objective. Fluorescence was captured in both the Cy3 and Cy5 channels (the latter being suitable for Alexa Fluor 647 imaging). Brightfield images were captured to aid cell localisation. a) single field of CHO-SNAP-CCR5 shown using brightfield, as well as Cy3 and Cy5 fluorescent channels (not contrast matched). b) individual fields of unlabelled CHO, labelled CHO, labelled H_2O transfection, unlabelled CHO-SNAP-CCR5 and labelled CHO-SNAP-CCR5 captured in Cy5 (contrast matched). c) single field of CHO-SNAP-CCR5 shown in brightfield, Cy3 and Cy5 displaying a high expression cell (contrast matched).

Due to the large level of transfection reagent-associated background fluorescence found previously, this study sought the analysis of CHO-SNAP-CCR5 that had undergone transient transfection using the alternate transfection reagent X-tremeGENE HP. As shown in **Figure 5-12a**, flow cytometry investigations demonstrate a peak shift within labelled CHO-SNAP-CCR5 when compared with unlabelled CHO-SNAP-CCR5 transfected cells and labelled H_2O transfected cells. These results indicate a successful transfection of cells for the production of SNAP-CCR5 to a level comparable with that of the previously utilised transfection reagent TransIT-X2. As shown in **Figure 5-12b**, traditional fluorescent imaging of a field of CHO-SNAP-CCR5 reveals Cy3 associated background fluorescence to a level comparable with that previously determined for TransIT-X2 transfected samples. Further, transiently transfected CHO-SNAP-CCR5 likewise demonstrate a small population of cells that express highly in the Cy5 channel. These results indicate that the alternate transfection reagent produces CHO-SNAP-CCR5 populations with a similar transfection efficiency and level of reagent-associated background fluorescence to the previously utilised reagent.

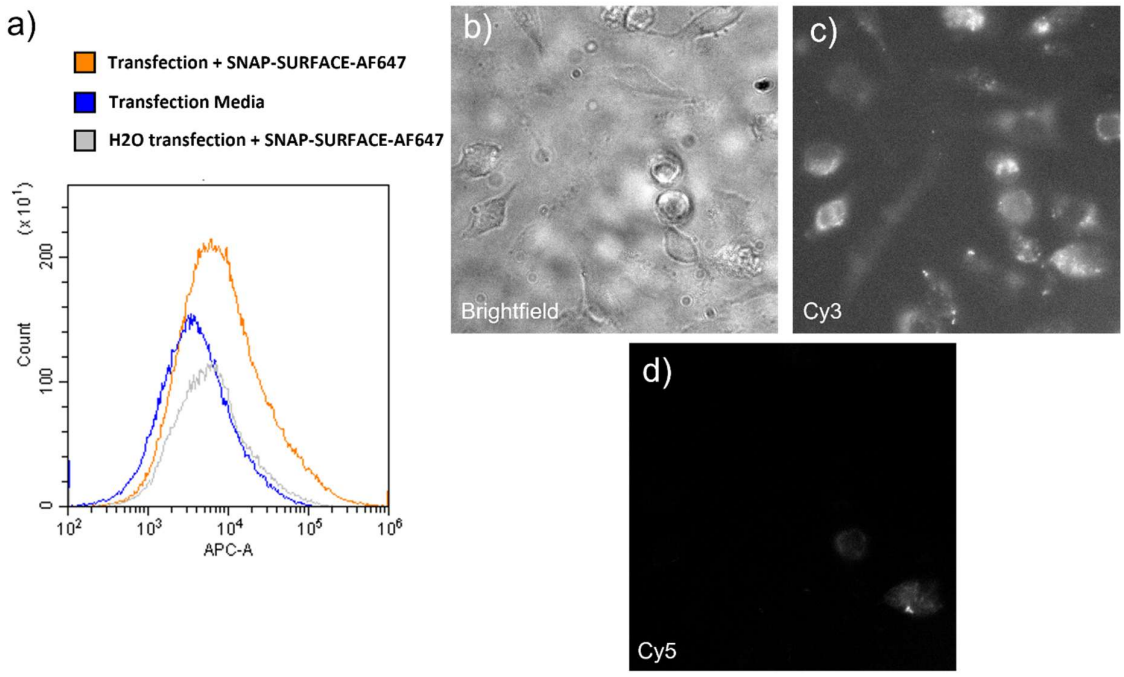

Figure 5-12: Flow cytometry analysis and representative images of the SNAP-CCR5 expression of transiently transfected CHO-SNAP-CCR5, using an alternate transfection reagent. a) flow cytometry-based analysis of transiently transfected CHO-SNAP-CCR5 labelled with SNAP-Surface-Alexa Fluor 647 alongside unlabelled CHO-SNAP-CCR5 and labelled H_2O transfection controls. Figure shows cell populations after gating to remove debris and doublets. b-d) single field of a fixed

transiently transfected CHO-SNAP-CCR5 sample labelled with SNAP-Surface-Alexa Fluor 647. Fluorescence was acquired using a standard upright fluorescent microscope with a 63X objective. Fluorescence was captured in both the Cy3 and Cy5 channels (the latter more suited for Alexa Fluor 647 imaging). Brightfield images were captured for cellular location purposes. (contrast matched). Cells were transfected using an alternate transfection reagent (X-tremeGENE HP).

5.7. Determination of SNAP-CCR5 presentation in transiently transfected populations of CHO-SNAP-CCR5 using PaTCH microscopy

The study of transiently transfected CHO-SNAP-CCR5 was extended through the investigation of SNAP-CCR5 expression using PaTCH-based intensity analysis. As shown in **Figure 5-13a**, expression within labelled CHO-SNAP-CCR5 exhibits a similarly punctated fluorescence to those seen using traditional fluorescence microscopy. Further, these representative images show a similar distribution of fluorescent signal amongst samples regardless of the presence of SNAP-CCR5 plasmid upon transfection. As shown in **Figure 5-13b**, although a small shift in the distribution of cell expression levels can be seen when comparing CHO-SNAP-CCR5 transfected cells with H_2O transfected cells, the mean intensity of each condition does not vary significantly. These results indicate that the transfection of samples causes an increase in non-specific transfection-associated background signal, in agreement with previous qualitative results.

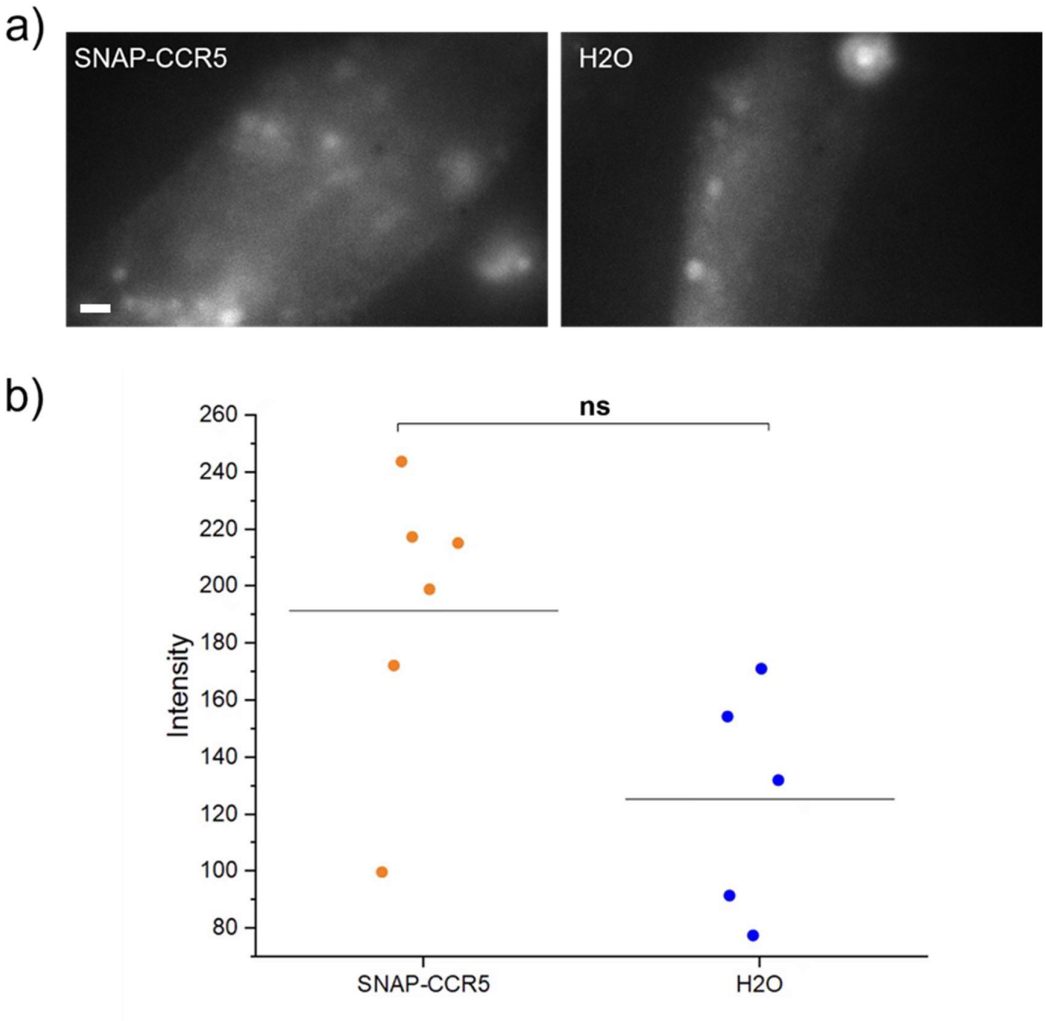

Figure 5-13: Investigating the basal membrane fluorescent signal of fixed CHO-SNAP-CCR5 cells exposed to SNAP-Surface-Alexa Fluor 647 using PaTCH microscopy. a) representative images of labelled transiently transfected CHO-SNAP-CCR5 alongside labelled CHO transiently transfected using H_2O in place of plasmid. (scale bar 2 μm). b) jitter plots representing the fluorescence intensity of labelled transiently transfected CHO-SNAP-CCR5 (orange) alongside labelled CHO transiently transfected using H_2O in place of plasmid (blue). SNAP-Surface-Alexa Fluor 647 labelling took place over 30 minutes at 37C. Intensity measurements were taken within the cell as informed by cell segmentation masks. Intensity values are background subtracted. Bars represent the mean fluorescent intensity for a given plot. Each condition saw the analysis of ~6 cells. Statistical analysis was carried out using a Kruskal–Wallis one-way analysis of variance (KW-ANOVA) test, ns - $P > 0.05$, * - $P \leq 0.05$, ** - $P \leq 0.01$, *** - $P \leq 0.001$, **** - $P \leq 0.0001$.

Further investigation into the suitability of transiently transfected CHO-SNAP-CCR5 for PaTCH-based analysis of CCR5 saw the intensity analysis of samples transfected using the alternate transfection reagent X-tremeGENE HP. This investigation aims to reveal any changes in the previously detected transfection-associated background signal upon use of an alternate transfection reagent. As shown in **Figure 5-14a**, expression within labelled CHO-SNAP-CCR5 exhibits a similarly punctated fluorescence to previous samples employing the transfection reagent TransIT-X2. Further, these representative images show a similar distribution of fluorescent signal amongst samples regardless of the presence of Alexa Fluor 647 or the presence of SNAP-CCR5 plasmid upon transfection. As shown in **Figure 5-14b**, although a small number of highly fluorescent cells can be seen in labelled CHO-SNAP-CCR5, a similar number can be found in unlabelled CHO-SNAP-CCR5. Further, the mean intensity can be seen to remain consistent in all transfected samples, regardless of the presence of Alexa Fluor 647 or the presence of SNAP-CCR5 plasmid upon transfection. Non-transfected samples however display a lower intensity distribution and a significantly lower mean intensity that is unchanged in labelled and unlabelled samples. These results indicate that, although cells display a low level of background binding of SNAP-Surface Alexa Fluor 647, employment of the alternate transfection reagent led to non-specific transfection-associated background fluorescence in a similar manner to the original transfection reagent and highlight the unsuitability of transiently transfected CHO-SNAP-CCR5 for microscopy-based CCR5 investigations.

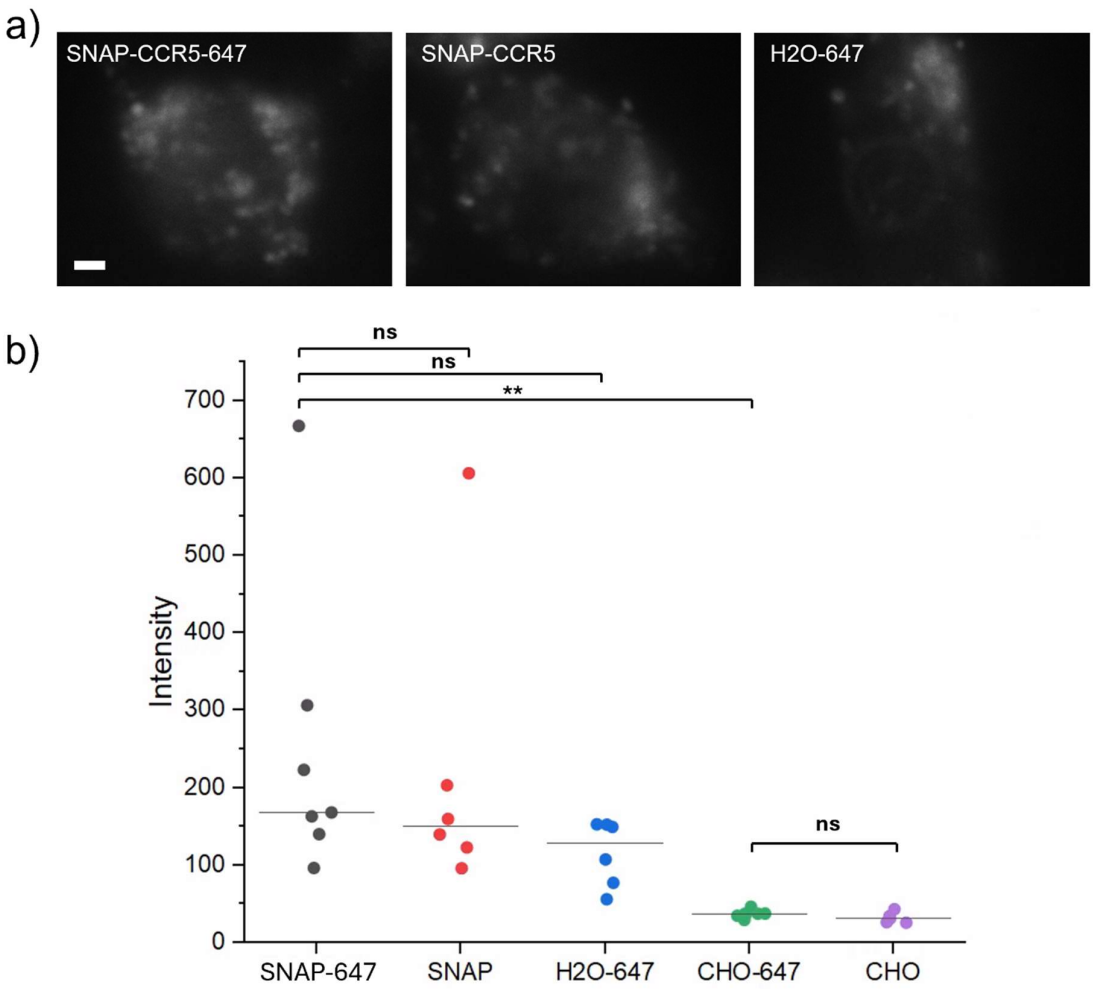

Figure 5-14: Investigating the basal membrane fluorescent signal of fixed CHO-SNAP-CCR5 cells exposed to SNAP-Surface-Alexa Fluor 647 using PaTCH microscopy, employing an alternate transfection method. a) representative images of labelled and non-labelled transiently transfected CHO-SNAP-CCR5 alongside labelled CHO transiently transfected using H_2O in place of plasmid. (scale bar 2 μm). b) jitter plots representing the fluorescence intensity of labelled (black) and non-labelled (red) transiently transfected CHO-SNAP-CCR5 alongside labelled CHO transiently transfected using H_2O in place of plasmid (blue) and both labelled (green) and unlabelled (purple) non-transfected CHO. SNAP-Surface-Alexa Fluor 647 labelling took place over 30 minutes at 37C. Intensity measurements were taken within the cell as informed by cell segmentation masks. Intensity values are background subtracted. Bars represent the mean fluorescent intensity for a given plot. Each condition saw the analysis of ~7 cells. Cells were transfected using an alternate transfection reagent (X-tremeGENE HP). Statistical analysis was carried out using a Kruskal–Wallis one-way analysis of variance (KW-ANOVA) test, ns - $P > 0.05$, * - $P \leq 0.05$, ** - $P \leq 0.01$, *** - $P \leq 0.001$, **** - $P \leq 0.0001$.

5.8. Discussion

This study saw the attempted development of alternate CCR5-expressing cell lines to facilitate the extended study of CCR5 behaviour under a range of microscopy techniques. The extension of the suite of CCR5-expressing models available was initially focused on the development of a non-adherent t-cell line that stably expressed the GFP-CCR5 fusion previously employed in CHO-GFP-CCR5. This development aimed to facilitate future investigations which would focus on the observation of CCR5 behaviour in the context of non-adherent cells, thereby allowing comparison of previously obtained results in adherent cells with those of a model displaying an increased biological relevance. Further, these studies aimed to observe the effect of T-cell activation on the behaviour of CCR5 at the membrane, with these studies seeing potential advancement to the observation of interacting cells in the context of immunological synapse formation. Transfection of Jurkat cells for the production of GFP-CCR5 using the chemical transfection methods employed in the creation of CHO-GFP-CCR5 resulted in no cell recovery post-transfection over several trials. This result necessitated the adoption of alternate transfection techniques, namely the use of nucleofection, a method that uses electroporation to deliver DNA to the nucleus. Flow cytometry-based analysis of transfected Jurkat cells revealed that this method was unable to successfully integrate either the GFP-CCR5 construct utilised in CHO-GFP-CCR5 or an alternate GFP-CCR5 construct which does not induce antibiotic resistance into Jurkat cells. However, the successful transfection of Jurkat for the production of GFP in isolation demonstrated the effectiveness of this method for the production of simpler molecules. The transfection of Jurkat for the production of complex biomolecules has previously been reported as notably difficult[234]. Therefore, extensions to the development of a stable Jurkat-GFP-CCR5 line would require the employment of alternate techniques such as lentiviral transduction and spinoculation[235].

The extension of the suite of CCR5-expressing models available was continued through the development of an adherent CHO cell line which expresses CCR5 fused to a SNAP-tag self-labelling protein tag. This development aimed to facilitate extended super resolution investigations that utilise the improved labelling specificity offered by the SNAP construct over traditional immunofluorescent techniques. Further, the successful creation of CHO-SNAP-CCR5 would allow for the use of a range of bright labels whilst retaining the high level of receptor recognition and one-to one receptor-label binding ratio necessary for single-molecule investigations, thereby allowing for correlative microscopy studies that benefit from both high spatial and temporal resolution microscopy techniques. Initial development of a CHO-SNAP-CCR5 model saw the creation of a mixed population of transfected cells

displaying antibiotic resistance and the isolation of individual clonal populations from this mixed population. Immunofluorescence-based flow cytometry was conducted on both mixed populations and clonal populations of CHO-SNAP-CCR5, with the former results providing early evidence of the presence of CCR5 through the binding of the CCR5 antibody 2D7. Analysis of clonal populations revealed a relatively high level of 2D7 binding in certain clonal populations allowing for the selection of a range of populations for further propagation. However, subsequent investigations of these populations using both 2D7 and alternate primary antibodies, MC-5 and FLAG-M2, suggested the rapid loss of CCR5 expression in clonal samples, despite the demonstration of continued antibiotic resistance, a result that was confirmed through repeated experimentation employing adapted protocols developed to maximise the specific binding and minimise the non-specific binding of fluorescent antibodies. Additionally, this loss of SNAP-CCR5 expression was confirmed through flow cytometry experiments employing SNAP-Surface-Alexa Fluor 647.

The transient loss of SNAP-CCR5 expression in stably transfected cells necessitated the consideration of transiently transfected mixed populations of CHO-SNAP-CCR5 as a model for further investigation. However, future employment of any such model first required the optimisation of the SNAP labelling protocol, which was quantifiably shown to induce a high level of non-specific binding and reduce cell count during flow cytometry. An adapted protocol was developed that saw the recommended concentration of SNAP-Surface-Alexa Fluor 647 being reduced by a factor of 81 and the exclusion of fixation on samples due for investigation in flow cytometry experiments, thereby drastically reducing non-specific binding and increasing available cell counts. Using this adapted protocol, transiently transfected CHO-SNAP-CCR5 were shown to display a high level of specific SNAP-Surface-Alexa Fluor 647 binding. Further, immunofluorescence-based flow cytometry demonstrated a high level of 2D7, MC-5 and FLAG-M2 binding in transiently transfected CHO-SNAP-CCR5. Taken together, these results suggest the accessibility of both the SNAP and FLAG motifs, alongside the N-terminus and chemokine binding site of CCR5, providing compelling evidence for the expression of SNAP-CCR5.

Despite a high level of SNAP-CCR5 expression within samples, both traditional fluorescence and PaTCH-based microscopy of transient CHO-SNAP-CCR5 revealed a high level of transfection reagent-associated background signal that rendered this model incompatible with microscopy-based investigations. Further, the extension of these studies to investigate transient CHO-SNAP-CCR5 that underwent transfection with an alternate reagent demonstrated a similarly high expression of SNAP-CCR5 alongside a similarly high level of reagent-associated signal, detectable using both traditional fluorescence and PaTCH-based

microscopy. The successful creation of a SNAP-CCR5 expressing model compatible with advanced microscopy techniques would therefore require the continued development of a stable line that retains SNAP-CCR5 expression through the employment of alternate transfection techniques, such as nucleofection, or the reduction of reagent-associated fluorescence in transiently transfected cells through the use of alternate reagents.

6. General discussion

6.1 Summary and major findings

The first results chapter of this thesis saw the employment of an established line of CCR5-expressing CHO cells for the determination of the super-resolved spatial distribution of CCR5 using SIM. These investigations demonstrated the collection of CCR5 into distinct large assemblies located across the cell membrane in three dimensions. Spatial analysis of these assemblies revealed a non-random orientation of assembly sites with respect to one another and allowed the determination of the average distance between assembly sites. Investigation into the effect of the CCR5 ligand CCL5 on this distribution demonstrated a significant reduction in cell surface CCR5 proportional to the extent of CCL5 exposure. Investigation into the effect of the small molecule CCR5 antagonist MVC demonstrated a large antagonistic effect that inhibited CCL5-induced reduction of cell surface CCR5 alongside an amplification of CCR5-associated signal. Further, dual-colour investigations revealed an MVC-induced interference of CCL5 binding. Investigation of the alternate small molecule antagonist TAK-779 and the CCL5 analogue 5P12-RANTES demonstrated a similar antagonistic effect with each displaying a clear capacity to interfere with CCL5 binding and to inhibit CCL5-associated reduction of cell surface CCR5. Finally, investigation of the additional CCL5-analogue 5P14-RANTES demonstrated a similar capacity for the interference of CCL5 binding but induced a loss of cell surface CCR5 greater than seen for CCL5, a result in line with previous characterisation of this ligand which established agonist activity with no associated downstream signalling[138].

The second results chapter of this thesis sought the creation of a new cell line designed for use in single-molecule applications and the development of a novel single-molecule fluorescent microscopy technique known as PaTCH, tailored to the investigation of biomolecules expressed on the basal membrane of adherent cells. Extensive characterisation of the new CHO-GFP-CCR5 model confirmed the expression of GFP-CCR5 alongside both CCR5 functionality and accessibility of key CCR5 binding sites. Further, an improvement in the detection of GFP-CCR5 foci was determined using the new PaTCH imaging mode in comparison with established TIRF and HILO modes. PaTCH investigations of CHO-GFP-CCR5 revealed a similar spatial distribution to CHO-CCR5, with CCR5 being revealed to collect into distinct large assemblies located across the basal membrane. The high temporal resolution offered by PaTCH facilitated the tracking of GFP-CCR5 assemblies under conditions inducing photobleaching, thereby allowing the estimation of CCR5 assembly size distributions across many cells. These investigations revealed a wide range of

assembly sizes, with the average assembly comprising approximately 10 to 20 GFP-CCR5 fusions. Further, the distribution of assembly sizes was seen to display characteristic peaks with an average periodic interval of 2.3 ± 0.5 molecules. A result which suggests that CCR5 assemblies likely consist of homodimeric sub-units.

PaTCH-based investigation of CCL5-induced effects revealed a shift in the distribution CCR5 of assembly sizes over a short perturbation time tailored for the investigation of the pre-internalisation activation window. Although CCR5 assemblies were seen to retain a homodimeric sub-unit composition upon exposure to CCL5, the presence of both large and small subpopulations of CCR5 assemblies were seen to increase at the cost of assemblies of an intermediate size. Investigations of extended CCL5 exposure revealed a negative shift in the distribution of cellular CCR5 expression, alongside a significant reduction in the average assembly size, amongst populations exposed to CCL5 for 30 minutes. The study of MVC-associated effects on CCR5 presentation were extended through PaTCH-based investigation of MVC in isolation and in combination with CCL5. MVC in isolation was found to have no significant impact on the average cellular CCR5 expression or the distribution of assembly sizes within this population. However, MVC was further demonstrated as an effective inhibitor of CCL5-induced internalisation, with the average cellular CCR5 expression increasing upon 30 minutes exposure to CCL5 provided MVC pre-treatment. Despite this, MVC was demonstrated to not restrict the CCL5-induced shift in assembly sizes, with the combined exposure of MVC and CCL5 inducing a negative shift in the distribution of assembly sizes that did not significantly differ from the shift induced by CCL5 in isolation.

The final results chapter of this thesis focused on the production of alternate CCR5 expressing cell lines for the advancement of CCR5 investigation. The attempted development of a non-adherent model T-cell line expressing the GFP-CCR5 fusion employed in results chapter 2 aimed to facilitate the CCR5 investigation in the absence of adherence-associated effects and the investigation of CCR5 under the context of T-cell activation. Although the nucleofection of Jurkat cells for the production of GFP in isolation, successful integration of the GFP-CCR5 plasmid was not successful despite attempted optimisation of nucleofection parameters. The attempted development of an adherent cell line expressing CCR5 fused with the SNAP-tag self-labelling protein aimed to facilitate corelative microscopy studies in which super-resolved CCR5 spatial distributions and single-molecule stoichiometry estimates could be determined within a single cell model. Despite the successful generation clonal populations of CHO-SNAP-CCR5 that displayed sustained resistance to selection antibiotics, the expression of SNAP-CCR5 within these clones was

determined to undergo rapid reduction. Optimisation of both the protocol underpinning both SNAP labelling and CCR5 immunofluorescent labelling allowed the successful determination of SNAP-CCR5 expression within transiently transfected cells, with flow cytometry-based assays revealing a high expression and availability of both key CCR5 and SNAP binding sites, thereby providing proof of concept for the employment of CHO-SNAP-CCR5 within future assays. However, a high level of transfection reagent-associated background signal was found within microscopy assays of these cells, suggesting the necessity of continued optimisation of CHO-SNAP-CCR5 transfection prior to the execution of correlative microscopy studies.

In conclusion, this thesis has provided a super-resolved and single-molecule study into the presentation of CCR5 in mammalian cells, allowing the direct visualisation of the spatial distribution of CCR5, demonstrating the collection of CCR5 into distinct assemblies and quantifying the spatial organisation, size and oligomeric make-up of these assemblies. Additionally, this thesis has provided the direct visualisation of the effect of the CCR5 agonist CCL5 alongside the small molecule antagonists MVC and TAK-779 and CCL5 analogues 5P12-RANTES and 5P14-RANTES on the spatial distribution and assembly size distribution of CCR5. Finally, this thesis presents a newly developed single-molecule fluorescent microscopy technique tailored for the investigation of molecules located on the basal membrane of adherent cells and a new CCR5-expressing cell line tailored for use in single molecule assays, alongside efforts in the extension of available lines for the study of CCR5 in systems of increase complexity and biological relevance.

6.2. Results in the context of CCR5 in the steady state

Super resolution investigations revealed cell populations that exhibit a punctated expression of CCR5, with the receptor found to collect into large assemblies across the entire cell membrane. Although the demonstration of CCR5 puncta varied across cell populations, this is to be expected given the varying level of CCR5 expression demonstrated by the CHO-CCR5 cell line employed in this study, with highly expressing cell populations seen to demonstrate a less punctated distribution. PaTCH-based investigation revealed a similarly punctated distribution of CCR5 that remained consistent across all cell populations, a result in line with the low and consistent expression of this clonal cell line. The punctated expression of CCR5 has additionally been demonstrated in alternative studies, with TIRF-based investigations revealing a similar presentation of CCR5 across the basal membrane of adherent cells[236].

The function of the spatial confinement of CCR5 into distinct puncta across the membrane remains unclear. However, the non-random orientation of puncta, as determined in chapter 3, suggests the potential existence of a biological function for which this spatial organisation plays a role. One such potential function is the facilitation of successful ligand binding, with the spatial confinement of the receptor raising the probability of the co-localisation of the receptor with its given binding partner[237]. However, punctated expression may also be influenced by local variations in membrane topology, with recent single-molecule-localisation-microscopy studies revealing a correlation between the variance in the local amount of membrane and the clustered-expression of a randomly distributed membrane molecule[238]. The confirmation of genuine CCR5 clustering would therefore benefit from additional dual-colour investigations which employ membrane markers to account for variations in the membrane topology.

An additional aim of this study was the determination of the stoichiometry of CCR5 assemblies. This study determined that CCR5 assemblies exist in a wide range of sizes and that these assemblies likely comprise dimeric sub-units of CCR5. The oligomeric state of CCR5 remains a topic of debate, however these results are supported by previous bulk ensemble studies that suggest the existence of CCR5 homodimers using a range of techniques[65,81,84,86,87]. However, the results presented here are limited by the employment of cell-fixation, thereby restricting the characterisation of CCR5 assemblies to their size and oligomeric make-up. The extension of this study to the investigation of live cells using PaTCH would allow for the determination of assembly dynamics. Any apparent trend in the relation between assembly size and mobility would provide insight into the existence of heterogeneous assembly sub-populations that may serve distinct roles.

6.3. Results in the context of CCR5 and CCL5

This study aimed to determine the effects of the CCR5 ligand CCL5 on receptor presentation through both super resolution and single-molecule investigations. CCR5 is expected to undergo activation upon interaction with CCL5, with this interaction inducing downstream β-arrestin mediated internalisation of the receptor[55,56]. Single molecule PaTCH-based investigations of the pre-internalisation behaviour of CCR5 revealed a shift in the distribution of CCR5 assemblies over short timescale CCL5 exposure. These results suggested a breakdown of intermediate sized assemblies with a potential recruitment towards larger sites. CCR5 endocytosis is generally facilitated by the coat protein clathrin, with CCR5-bound β–arrestin interacting with the clathrin adaptor molecule AP2. This complex is then

expected to recruit towards areas of the plasma membrane coated by clathrin flat lattices, from which the receptor is removed by the formation of clathrin coated pits[56,60–62]. The demonstration of larger CCR5 puncta along the membrane could be, in part, due to the localisation of CCR5 within these sites of internalisation. In such a case, these results may suggest the CCL5-induced breakdown of otherwise steady state CCR5 assemblies with subsequent recruitment to sites of internalisation. The extension of this investigation to the study of live cells would facilitate the determination of assembly dynamics, providing insight into the potential recruitment of mobile assemblies towards larger stationary sites. Further, the application of dual-colour studies employing a clathrin reporter would allow the co-localisation of clathrin lattices relative to CCR5 assemblies that form suspected sites of internalisation

Super resolution investigation of extended CCL5 exposure demonstrated a clear reduction in the presence of CCR5, with this reduction being proportional to the extent of CCL5 exposure. Further, studies employing labelled CCL5 facilitated the quantification of CCL5-cell association with respect to the extent of treatment, demonstrating an increase in CCL5 presence concurrent with the observed reduction in CCR5 presence. These results thereby demonstrate the binding of CCL5 over time and the resultant internalisation of CCR5. Additionally, these studies provide an indication of the likely time scale over which CCL5-induced internalisation takes place in this model, with the majority of internalisation taking place after ten minutes and a plateau being formed after continued exposure, despite the continued increase of cell-associated CCL5 signal.. CCR5 labelling took place after exposure to CCL5 and therefore reports only membrane-bound CCR5 and not the presence of endocytosed receptors in the cell. In contrast, CCL5-associated signal stems from both CCL5 located at the membrane and CCL5 up taken through endocytosis, the continued increase in CCL5-signal post internalisation therefore likely stems from the combination of endocytosed CCL5 and the binding of CCL5 to receptors that have undergone recycling to the membrane[63]. Studies employing the newly developed CHO-GFP-CCR5 cell line demonstrated CCL5-induced internalisation through flow cytometry studies, however a slower rate of internalisation was seen in comparison to previous studies of CHO-CCR5[66] indicating the potential effect of GFP presence on the CCR5 N-terminus. Despite this, CCL5-induced reduction in cell surface GFP-CCR5 was quantified using single-molecule PaTCH microscopy, with the average GFP-CCR5 expression being seen to reduce after 30 minutes exposure to CCL5. The quantification of overall cell intensity revealed a range of GFP-CCR5 expression amongst cell populations, with three distinct bands of expression being defined in the steady state population and CCL5 being seen to induce the loss of the highly expressing cell population. Extension of PaTCH investigations to the quantification of assembly

stoichiometry revealed a similar range of assembly sizes amongst cells exposed to CCL5 in comparison with the steady state. However, the distribution was seen to undergo a negative shift, with the average assembly size being significantly lower than that of the steady state. This result suggests that the overall loss of CCR5 presence induced by CCL5 is accompanied with an overall reduction in the average size of CCR5 assemblies. Further investigation employing clathrin reporters would provide insight as to the proportion of CCR5 assemblies that may be identified as sites of internalisation upon extended CCL5 exposure.

6.4. Results in the context of CCR5 and small molecule CCR5 antagonists

This study aimed to determine the effects of CCR5 antagonists on the CCL5-induced activation of CCR5. One such antagonist under investigation was the small molecule Maraviroc (MVC) which has seen success as a therapeutic for the treatment of CCR5 tropic HIV-1[130]. The expected function of MVC is the allosteric inhibition of CCL5-induced internalisation, with MVC believed to bind within a deep pocket of the CCR5 transmembrane bundle and induce a conformational change in the receptor that inhibits the binding of CCL5 to its secondary binding site[46]. Super resolution investigation of MVC pre-treatment prior to CCL5 exposure revealed a clear inhibition of CCL5-induced internalisation, demonstrating MVC as an effective CCR5 antagonist in this study. Further, the level of CCR5 associated fluorescence intensity was seen to increase beyond that of the steady state. This result was similarly seen in PaTCH-based investigation of GFP-CCR5 expression, with MVC pre-treatment being found to increase the average CCR5-associated fluorescence intensity relative to the steady state.

The MVC-induced increase of CCR5-associated signal has been demonstrated in previous studies. Investigations that similarly employed an adherent cell line transfected for the production of CCR5 demonstrated an increase in binding of the CCR5 N-terminus antibody CTC8 upon 30 minutes exposure to MVC when compared to the steady state, alongside a reduction in binding of a range of ECL-specific MAbs using flow cytometry[239]. Additionally, investigations of primary T-cells demonstrated an MVC-induced increase in CCR5 density, albeit over a time scale of many hours[240]. These studies, combined with results shown here, demonstrate the potential MVC-induced upregulation of surface CCR5. However, given the conformational change associated with MVC binding, the increase in N-terminal label-associated signal may also be due to an MVC-induced increase in the exposition of the CCR5 N-terminus enacted through this conformational change.

PaTCH-based investigation of CCR5-associated signal given exposure to MVC in isolation and in combination with CCL5 suggest that the MVC-induced increase in signal is only present in samples exposed to both MVC and CCL5. These results suggest the potential binding of CCL5 despite pre-exposure to MVC. Although MVC is expected to induce a conformational change that inhibits the internalisation of CCR5, the ability of CCL5 to bind to the primary chemokine binding site remains unclear[46]. Further evidence of continued CCL5 binding was found through the investigation of assembly reorganisation in which CCL5 was observed to induce a negative shift in the overall distribution of assembly stoichiometries with respect to the non-perturbed sample. Likewise, a negative distribution shift was seen in samples exposed to CCL5, after pre-exposure to MVC, that did not differ significantly from the shift induce by CCL5 in isolation. These results are however in contrast with dual colour super resolution investigations which revealed a large reduction in CCL5-associated signal in cells pre-treated with MVC, suggesting an MVC-induced interference of CCL5-binding. These studies would be advanced through the extension of super resolution investigations to the lone effects of MVC to confirm whether the observed increase in CCR5 signal is present in the absence of CCL5. Further, extension of dual colour CCR5-CCL5 co-localisation within PaTCH-based assembly analysis would provide further insight regarding the ability of CCL5 to bind CCR5 in the presence of MVC and the relation of bound assemblies to their size. In contrast, super resolution studies of the alternate small molecule antagonist TAK-779 (TAK) demonstrated a TAK-induced reduction of CCL5-induced CCR5 internalisation with no increase of CCR5 signal relative to the steady state. In addition, dual colour investigations demonstrated the effective TAK-induced interference of CCL5 binding at a level in line with MVC. Although TAK was confirmed to be an effective inhibitor of CCL5-induced CCR5 activation using flow-cytometry based calcium flux assays in CHO-GFP-CCR5, continued investigation would benefit from PaTCH-based single molecule studies in CHO-GFP-CCR5 to reveal the effect of TAK on CCL5-induced changes in assembly size for a more comparative study of the two small molecule antagonists.

6.5. Results in the context of CCR5 and CCL5 analogues

The development of HIV strains that display MVC resistance has motivated the study of novel CCR5-targeted HIV-1 entry inhibitors[133,134] . One branch of potential therapeutics is formed of CCL5 derivatives differing through the alteration of the chemokine N terminus[138]. These CCL5 analogues present a potential advantage over small molecule antagonists due to their ability to fully engage the CCR5 active cleft and thereby limit potential HIV-1 gp120

mutation and the resultant development of resistant strains[241]. This study aimed to determine the effect of CCL5 analogues 5P12-RANTES (5P12) and 5P14-RANTES (5P14) on CCL5-induced CCR5 internalisation using super resolution microscopy. Both 5P12 and 5P14 are reported to display anti-HIV potency and inhibition of G protein-linked signalling activity, however both displaying differing effects on CCR5 internalisation[138–140]. Investigation of 5P12 demonstrated a clear reduction in CCL5-induced internalisation given 5P12 pre-exposure, albeit at a level lower than that of MVC and TAK. Further, dual colour investigations demonstrated the ability of 5P12 to interfere with CCL5 binding at a level in line with MVC and TAK. These results confirm 5P12 as an effective competitor of CCL5 binding and inhibitor of CCR5 internalisation, in line with previous investigations[138–140].

In contrast, investigation of 5P14 pre-treatment revealed a large reduction in the presence of CCR5 signal that greatly surpassed that of CCL5 in isolation. Further, dual-colour investigations demonstrated the interference of CCL5 binding at a level in line with 5P12 and small molecule antagonists. These results demonstrate 5P14 as an effective competitor of CCL5 binding and a potent driver of CCR5 internalisation in agreement with the previous characterisation of 5P14 that established agonistic activity without inducing downstream signalling of CCR5, with the level of 5P14-induced internalisation lying at an intermediate level between that of CCL5 and the known super-agonist PSC-RANTES[138–140]. The investigation of CCL5 analogues shown here were limited to super resolution intensity analysis. The extension of these studies to PaTCH-based analysis of CCR5 assembly redistribution would allow for more extensive insight into the effect of these ligands on CCL5-induced assembly redistribution and a more comparative study of these prospective therapeutics relative to the established drug MVC.

6.6. Development of biophysical tools and models

In order to determine CCR5 characteristics on the single-molecule level, this study aimed to develop both cell models suitable for single-molecule investigation alongside a novel imaging mode tailored to the single molecule investigation of adherent cell lines that display uneven membrane topology. This aim was achieved through the successful development and characterisation of CHO-GFP-CCR5, alongside the development of PaTCH microscopy, with this technique being shown to provide an increase in recognition of GFP-CCR5 puncta, alongside an increase in signal to background ratio, within our system when compared with the established techniques of HILO and TIRF.

Employing these two developments, this study provided single molecule level insight into the behaviour of CCR5 both in the steady state and under exposure to a range of ligands. Alternative studies have recently been conducted that similarly employ CCR5 fused with GFP expressed within adherent cells, providing scope to this method of reporting[233], however these studies employ a C-terminally tagged CCR5-GFP fusion. Due to the existence of a PDZ binding domain on the C-terminus of CCR5, C-terminal coupling raises potential concerns regarding the downstream effect of PDZ masking on the behaviour of CCR5[64,65]. The slimfield microscope system, on which the PaTCH imaging mode was established, has seen employment in both TIRF and HILO based investigations of a range of biological subjects[199,201,206], however the development of this new imaging mode may facilitate future investigations of membrane-bound biomolecules expressed in adherent mammalian cell lines.

A limitation of this study lies in the sole employment of adherent cell lines for the expression of CCR5, with CCR5 being endogenously expressed in a range of cell types that may display type-specific variance in CCR5 behaviour. In order to facilitate the extension of this investigation to the study of CCR5 in a non-adherent membrane environment, this study sought the creation of a Jurkat T-cell line that expresses the GFP-CCR5 fusion. The non-adherent nature of Jurkat would provide information regarding the characteristics of CCR5 in the absence of adherence-associated effects, such as increased membrane tension, and allow the extension of CCR5 characterisation to a more diverse cellular context. Further, the T-cell origin of Jurkat would aid future investigations concerned with the effect of cellular activation on the characteristics of CCR5 distributions. Upon failure to achieve a successful transfection using the chemical transfection techniques previously utilised in CHO-GFP-CCR5 development, alternative techniques were employed in the form of nucleofection. Cells having undergone transfection were screened for GFP-CCR5 expression 64 hours later using flow cytometry. These results revealed that despite the successful transfection of Jurkat for the production of GFP, transfections for the production of GFP-CCR5 were not successful.

The ease by which Jurkat integrate GFP when compared with the integration of GFP-CCR5 is not surprising given the complex transmembrane structure of CCR5. However, by allowing the transfected cells longer time periods prior to analysis may reveal a higher level of GFP-CCR5 expression. In contrast however, previous studies employing Jurkat transiently transfected for the production of GFP-CCR5[90] reported maximum expression after only 24 hours. It is clear then that further investigations are needed into the expression of GFP-CCR5 after varying timescales post-transfection. Additionally, given the reported difficulty of

the transfection of Jurkat for the production of complex biomolecules[234], extensions to the development of Jurkat-GFP-CCR5 would benefit from the consideration of alternative techniques such as lentiviral transduction and spinoculation[235].

A further limitation of this study lies in the employment of two independent CCR5 expressing cell lines tailored for their use in separate microscopy conditions. In order to perform correlative microscopy experiments that allow for the determination of super-resolved spatial distributions and single molecule determination of receptor stoichiometry within the same cell model, this study sought the development of an adherent cell line expressing the SNAP-tag labelling protein fused to CCR5, as employed by other groups in the study of CCR5[236]. Previous studies investigating SNAP-tag fused cell membrane receptors[242,243] exemplify the value of this labelling technique, with SNAP-tag being used to characterise the spatial distribution and stoichiometry of GPCRs such as beta-2-adergenic receptor[244,245]. Cells transfected to stably produce SNAP-CCR5 were successfully sorted into clonal populations but displayed a rapid reduction in expression over time. Further studies saw the successful characterisation of SNAP-CCR5 expression amongst transiently transfected samples via flow cytometry employing both anti-CCR5 and SNAP-Surface labelling. Although requiring a large amount of optimisation in labelling protocols, these investigations provided a proof of concept for the use of transiently transfected samples for future studies and the prospect of stable cell line development upon execution of improved sorting techniques. Further investigations into the expression of SNAP-CCR5 in transiently transfected cells, using both traditional and single molecule microscopy techniques, revealed a large level of transfection-associated background fluorescence in samples transfected with two independent transfection reagents. Although these investigations suggest the limitations of transiently transfected samples for further analysis, the presence of a small number of cells displaying a high level of SNAP-CCR5 specific fluorescence further indicate the possibility of the future development of a stably expressing cell line through the employment of several rounds of consecutive clonal isolation of highly expressing cells using Fluorescence-activated cell sorting (FACS)[246].

In the absence of the successful creation of a stable line of CHO-SNAP-CCR5, studies may be successfully carried out using transiently transfected cells that have employed a transfection reagent that does not display an increase in non-specific fluorescence or using enriched populations of highly expressing transiently transfected cells isolated using FACS. Alternatively, correlative studies may be achievable through the use of CHO-GFP-CCR5 in combination with immunofluorescent staining with a high labelling ratio and bright organic dyes, thereby providing the photon budget required for super resolution microscopy.

6.7. Future direction of study

The extension of this body of work would aim to address limitations demonstrated within this study and see the application and continued development of the tools shown here for the investigation of CCR5 in systems of increased complexity. As outlined above, the extension of PaTCH-based analysis of CCR5 assemblies in the context of an extended range of CCR5 ligands would provide further clarity on the effect of potential therapeutics relative to MVC. Further, the extension of PaTCH investigations to the study of live cells would allow for the determination of CCR5 assembly dynamics, facilitating the characterisation of assembly sub populations and the spatial tracking of assemblies as they undergo CCL5-induced reorganisation. In addition, the extension of dual colour investigation to the determination of CCR5-CCL5 co-localisation within PaTCH-based investigations would provide insight into any existent correlation between CCL5 binding and CCR5 assembly sub-populations that display a distinct size or mobility. Moreover, the extension of these studies to the investigation of directed chemokine exposure through the employment of a chemokine gradient would allow the study of the spatiotemporal reorganisation of CCR5 assemblies at the leading edge of the cell.

In addition, this investigation would be advanced through the employment of computational modelling. The advent of artificial intelligence modelling tools, such as AlphaFold, has formed a breakthrough in predicting the 3D structure of proteins. Studies using the 2nd iteration of AlphaFold have predicted the structure of CCR5, with results consistent with previously determined crystal structures[247]. The toolset has since evolved with AlphaFold 3, which can now predict the structure of multi-molecule complexes[248]. Extensions of this investigation would thereby benefit from the employment of AlphaFold 3 alongside classic modelling approaches, such as molecular dynamics simulation. Incorporating these methods into our biophysical toolset would allow further insight into the presentation and dynamics of steady-state CCR5, the effect of fluorescent labelling on receptor behaviour, the binding characteristics of CCR5 ligands and the structural changes that these ligands may affect in the receptor.

The successful extension of available CCR5-expressing cell lines would allow for correlative microscopy studies that would provide a more robust characterisation of the spatial distribution and assembly make-up of CCR5 using a single cell displaying a consistent expression level. Further, the availability of a CCR5-expressing non-adherent cell line would facilitate the study of CCR5 in a model displaying a higher level of biological relevance in the absence of adherence-associated effects. However, the non-adherent nature of these cells

would require continued development of the microscopy toolset employed in this study. The spatial confinement of non-adherent cells for the purposes of imaging would require the immobilisation of cells through the use of slide coatings such as Poly-L-lysine[199]. Additionally, due to the lack of a flat membrane region, any such investigation would benefit from imaging in three dimensions with a high axial resolution.

Finally, the development of Jurkat-GFP-CCR5 would facilitate the study of CCR5 in the context of T-cell activation and the formation of an immunological synapse, the stable interface between interacting immune cells which provides the spatial organisation and timescale for cytokine transfer between cells[12,213,249]. Initial studies within this context would aim to induce slide-based synapses by introducing CCR5-expressing cell lines to surfaces coated in antibodies specific to CD3 and CD28, the primary and secondary signalling components for T-cell activation[250,251]. The extension of these investigations would aim to study CCR5 behaviour within the synaptic cleft of interacting cells. However, this investigation would raise challenges in experimental technique, with the synaptic planes of interacting cells being unlikely to run parallel with the focal plane. This challenge may be addressed through the employment of a 3D microscopy technique that offers a high spatiotemporal resolution, such as lattice light sheet microscopy[252]. The application of PaTCH based investigation for the determination of receptor stoichiometry would be restricted to the basal membrane of interacting cells, however correlative study of basal membrane CCR5 reorganisation using PaTCH and the subsequent study of CCR5 reorganisation within the synaptic cleft of the same cells using 3D super resolution microscopy may be achievable, provided cell identification through confinement or the use of marked coverslips.

6.8. Conclusion

The key role that CCR5 plays within the immune response, alongside its involvement within HIV pathology, highlights the importance of the continued characterisation of this receptor and its response to binding partners. Further, despite the immunogenic characteristics of the CCR5-CCL5 axis, recent studies have shown CCR5 to act as a double-edged sword in the progression of cancer, with CCR5-mediated signalling being found to play a pro-tumorigenic role[105,253], thereby highlighting CCR5 as a promising target for future cancer therapeutics and the potential repurpose of CCR5-tagetting HIV therapeutics for the treatment of cancer. The identification of CCR5 as a potential target for cancer therapeutics, alongside the development of CCR5 tropic HIV-1 strains that display resistance to the established drug Maraviroc[133,134] further highlight the importance of the continued development of our

understanding of the interaction of CCR5 with its binding partners. Additionally, the continued development of cutting-edge biophysical microscopy techniques has allowed for the determination of biomolecule characterisation at a level of detail previously unseen and the accessibility of these techniques to biological models of increasing complexity.

This study has therefore taken place in an exciting time for the investigation of CCR5 characteristics, as well as the use and development of biophysical toolsets. Application of these toolsets has allowed the direct visualisation of CCR5, both in the steady state and upon interaction with established and prospective CCR5-targeting therapeutics, with super-resolved and single-molecule detail. Further, this study has facilitated the continued development of biophysical techniques for the investigation of membrane-located biomolecules within mammalian cells.

Abbreviations

5P12: 5P12-RANTES

5P14: 5P14-RANTES

∆32: CCR5-Delta-32 mutation

APC: Antigen presenting cell

BCR: B-cell receptor

BiFC: Bimolecular fluorescence complementation

BM: Brunner-Munzel test

BRET: Bioluminescence resonance energy transfer

CCL3: Chemokine (CC motif) ligand 3

CCL4: Chemokine (CC motif) ligand 4

CCL5: Chemokine (CC motif) ligand 5

CCR2: CC chemokine receptor 2

CCR5: CC chemokine receptor 5

CCR7: CC chemokine receptor 7

CCR9: CC chemokine receptor 9

CHO: Chinese hamster ovary

CXCL16: Chemokine (CXC motif) ligand 16

CXCL2: Chemokine (CXC motif) ligand 2

CXCR4: CXC chemokine receptor 4

DHFR: Dihydrofolate reductase

DMEM: Dulbecco's Modified Eagle Medium

EBP50: Ezrin-radixin-moesin-binding phosphoprotein 50

ECL2: 2nd extracellular loop

ECL3: 3rd extracellular loop

EGFP: Enhanced GFP

ER: Endoplasmic reticulum

ERK: Extracellular signal-regulated kinase

ERM: Ezrin-radixin-moesin

EDTA: Ethylenediaminetetraacetic acid

FACS: Fluorescence-activated cell sorting

FCS: Foetal calf serum

FDA: Food and Drug Administration

FRET: Forster resonance energy transfer

GAG: Glycosaminoglycan

GAP: GTPase-activating protein

GDP: Guanosine diphosphate

GFP: Green fluorescent protein

GPCR: G-protein coupled receptor

GRK: G protein-coupled receptor kinase

GTP: Guanosine triphosphate

HILO: highly inclined and laminated optical sheet

HIV: Human immunodeficiency virus

KDE: Kernel density estimate

KW-ANOVA: Kruskal–Wallis one-way analysis of variance

MAPK: mitogen-activated protein

MHC: Major histocompatibility complex

MVC: Maraviroc

NA: Numerical aperture

NHERF-1: Na+/H+ Exchanger Regulatory Factor

PAMP: Pathogen-associated molecular pattern

PaTCH: Partially TIRF-coupled HILO

PBS: Phosphate-buffered saline

PI3K: Phosphatidylinositol 3-kinase

PKC: Protein kinase C

PRR: Patter-recognition receptor

PSF: Point spread function

PTK: Protein tyrosine kinase

RhoA: Ras homolog family member A

SIM: Structured illumination microscopy

SNR: Signal to noise ratio

STORM: Stochastic optical reconstruction microscopy

TAK: TAK-779

TCR: T-cell receptor

Th cell: T-helper cell

TIRF: total internal reflection fluorescence

TM1: 1st transmembrane helix

TM2: 2nd transmembrane helix

TM3: 3rd transmembrane helix

TM4: 4th transmembrane helix

TM5: 5th transmembrane helix (none of these have been defined at first use)

TM6: 6th transmembrane helix

TM7: 7th transmembrane helix

TME: Tumour microenvironment

Treg: Regulatory T cell

YFP: Yellow fluorescent protein

References

1. Hunter, P., Payne-Dwyer, A.L., Shaw, M., Signoret, N., and Leake, M.C. (2022). Single-molecule and super-resolved imaging deciphers membrane behavior of onco-immunogenic CCR5. iScience *25*, 105675. https://doi.org/10.1016/j.isci.2022.105675.
2. Marshall, J.S., Warrington, R., Watson, W., and Kim, H.L. (2018). An introduction to immunology and immunopathology. Allergy, Asthma & Clinical Immunology *14*, 49. https://doi.org/10.1186/s13223-018-0278-1.
3. Moser, M., and Leo, O. (2010). Key concepts in immunology. Vaccine *28*, C2–C13. https://doi.org/10.1016/j.vaccine.2010.07.022.
4. Turvey, S.E., and Broide, D.H. (2010). Innate immunity. Journal of Allergy and Clinical Immunology *125*, S24–S32. https://doi.org/10.1016/j.jaci.2009.07.016.
5. Stuart, L.M., and Ezekowitz, R.A.B. (2005). Phagocytosis. Immunity *22*, 539–550. https://doi.org/10.1016/j.immuni.2005.05.002.
6. Akira, S., Uematsu, S., and Takeuchi, O. (2006). Pathogen Recognition and Innate Immunity. Cell *124*, 783–801. https://doi.org/10.1016/j.cell.2006.02.015.
7. Bowie, A.G., and Unterholzner, L. (2008). Viral evasion and subversion of pattern-recognition receptor signalling. Nat Rev Immunol *8*, 911–922. https://doi.org/10.1038/nri2436.
8. Bonilla, F.A., and Oettgen, H.C. (2010). Adaptive immunity. Journal of Allergy and Clinical Immunology *125*, S33–S40. https://doi.org/10.1016/j.jaci.2009.09.017.
9. Rajewsky, K. (1996). Clonal selection and learning in the antibody system. Nature *381*, 751–758. https://doi.org/10.1038/381751a0.
10. Kurosaki, T., Kometani, K., and Ise, W. (2015). Memory B cells. Nat Rev Immunol *15*, 149–159. https://doi.org/10.1038/nri3802.
11. Dustin, M.L. (2014). The Immunological Synapse. Cancer Immunol Res *2*, 1023–1033. https://doi.org/10.1158/2326-6066.CIR-14-0161.
12. Davis, D.M., and Dustin, M.L. (2004). What is the importance of the immunological synapse? Trends Immunol *25*, 323–327. https://doi.org/10.1016/j.it.2004.03.007.
13. Beissert, S., Schwarz, A., and Schwarz, T. (2006). Regulatory T Cells. Journal of Investigative Dermatology *126*, 15–24. https://doi.org/10.1038/sj.jid.5700004.
14. Laing, K. (2004). Chemokines. Dev Comp Immunol *28*, 443–460. https://doi.org/10.1016/j.dci.2003.09.006.
15. Horuk, R. (2001). Chemokine receptors. Cytokine Growth Factor Rev *12*, 313–335. https://doi.org/10.1016/S1359-6101(01)00014-4.
16. Ulvmar, M.H., Hub, E., and Rot, A. (2011). Atypical chemokine receptors. Exp Cell Res *317*, 556–568. https://doi.org/10.1016/j.yexcr.2011.01.012.
17. Latorraca, N.R., Venkatakrishnan, A.J., and Dror, R.O. (2017). GPCR Dynamics: Structures in Motion. Chem Rev *117*, 139–155. https://doi.org/10.1021/acs.chemrev.6b00177.
18. Hilger, D., Masureel, M., and Kobilka, B.K. (2018). Structure and dynamics of GPCR signaling complexes. Nat Struct Mol Biol *25*, 4–12. https://doi.org/10.1038/s41594-017-0011-7.
19. Ye, L., Van Eps, N., Zimmer, M., Ernst, O.P., and Scott Prosser, R. (2016). Activation of the A2A adenosine G-protein-coupled receptor by conformational selection. Nature *533*, 265–268. https://doi.org/10.1038/nature17668.

20. Rosenbaum, D.M., Rasmussen, S.G.F., and Kobilka, B.K. (2009). The structure and function of G-protein-coupled receptors. Nature *459*, 356–363. https://doi.org/10.1038/nature08144.
21. Kristiansen, K. (2004). Molecular mechanisms of ligand binding, signaling, and regulation within the superfamily of G-protein-coupled receptors: molecular modeling and mutagenesis approaches to receptor structure and function. Pharmacol Ther *103*, 21–80. https://doi.org/10.1016/j.pharmthera.2004.05.002.
22. Khan, S.M., Sleno, R., Gora, S., Zylbergold, P., Laverdure, J.-P., Labbé, J.-C., Miller, G.J., and Hébert, T.E. (2013). The Expanding Roles of G *βγ* Subunits in G Protein–Coupled Receptor Signaling and Drug Action. Pharmacol Rev *65*, 545–577. https://doi.org/10.1124/pr.111.005603.
23. Smrcka, A. V. (2008). G protein βγ subunits: Central mediators of G protein-coupled receptor signaling. Cellular and Molecular Life Sciences *65*, 2191–2214. https://doi.org/10.1007/s00018-008-8006-5.
24. Ross, E.M., and Wilkie, T.M. (2000). GTPase-Activating Proteins for Heterotrimeric G Proteins: Regulators of G Protein Signaling (RGS) and RGS-Like Proteins. Annu Rev Biochem *69*, 795–827. https://doi.org/10.1146/annurev.biochem.69.1.795.
25. Mundell, S.J., Luo, J., Benovic, J.L., Conley, P.B., and Poole, A.W. (2006). Distinct Clathrin-Coated Pits Sort Different G Protein-Coupled Receptor Cargo. Traffic *7*, 1420–1431. https://doi.org/10.1111/j.1600-0854.2006.00469.x.
26. Gurevich, V. V., and Gurevich, E. V. (2019). GPCR Signaling Regulation: The Role of GRKs and Arrestins. Front Pharmacol *10*. https://doi.org/10.3389/fphar.2019.00125.
27. Zhu, J., Taniguchi, T., Takauji, R., Suzuki, F., Tanaka, T., and Muramatsu, I. (2000). Inverse agonism and neutral antagonism at a constitutively active alpha-1a adrenoceptor. Br J Pharmacol *131*, 546–552. https://doi.org/10.1038/sj.bjp.0703584.
28. Kurose, H., and Kim, S.G. (2022). Pharmacology of Antagonism of GPCR. Biol Pharm Bull *45*, b22-00143. https://doi.org/10.1248/bpb.b22-00143.
29. Rossi, D., and Zlotnik, A. (2000). The Biology of Chemokines and their Receptors. Annu Rev Immunol *18*, 217–242. https://doi.org/10.1146/annurev.immunol.18.1.217.
30. Schall, T.J., and Proudfoot, A.E.I. (2011). Overcoming hurdles in developing successful drugs targeting chemokine receptors. Nat Rev Immunol *11*, 355–363. https://doi.org/10.1038/nri2972.
31. Chemokine/chemokine receptor nomenclature (2003). Cytokine *21*, 48–49. https://doi.org/10.1016/S1043-4666(02)00493-3.
32. Shi, C., and Pamer, E.G. (2011). Monocyte recruitment during infection and inflammation. Nat Rev Immunol *11*, 762–774. https://doi.org/10.1038/nri3070.
33. Tiberio, L., Del Prete, A., Schioppa, T., Sozio, F., Bosisio, D., and Sozzani, S. (2018). Chemokine and chemotactic signals in dendritic cell migration. Cell Mol Immunol *15*, 346–352. https://doi.org/10.1038/s41423-018-0005-3.
34. Broxmeyer, H.E. (2008). Chemokines in hematopoiesis. Curr Opin Hematol *15*, 49–58. https://doi.org/10.1097/MOH.0b013e3282f29012.
35. Hughes, C.E., and Nibbs, R.J.B. (2018). A guide to chemokines and their receptors. FEBS J *285*, 2944–2971. https://doi.org/10.1111/febs.14466.
36. Blanpain, C., Libert, F., Vassart, G., and Parmentier, M. (2002). CCR5 and HIV Infection. Recept Channels *8*, 19–31. https://doi.org/10.3109/10606820212135.
37. Oppermann, M. (2004). Chemokine receptor CCR5: insights into structure, function, and regulation. Cell Signal *16*, 1201–1210. https://doi.org/10.1016/j.cellsig.2004.04.007.

38. Raport, C.J., Gosling, J., Schweickart, V.L., Gray, P.W., and Charo, I.F. (1996). Molecular Cloning and Functional Characterization of a Novel Human CC Chemokine Receptor (CCR5) for RANTES, MIP-1β, and MIP-1α. Journal of Biological Chemistry *271*, 17161–17166. https://doi.org/10.1074/jbc.271.29.17161.
39. Blanpain, C., Wittamer, V., Vanderwinden, J.-M., Boom, A., Renneboog, B., Lee, B., Le Poul, E., El Asmar, L., Govaerts, C., Vassart, G., et al. (2001). Palmitoylation of CCR5 Is Critical for Receptor Trafficking and Efficient Activation of Intracellular Signaling Pathways. Journal of Biological Chemistry *276*, 23795–23804. https://doi.org/10.1074/jbc.M100583200.
40. Kraft, K., Olbrich, H., Majoul, I., Mack, M., Proudfoot, A., and Oppermann, M. (2001). Characterization of Sequence Determinants within the Carboxyl-terminal Domain of Chemokine Receptor CCR5 That Regulate Signaling and Receptor Internalization. Journal of Biological Chemistry *276*, 34408–34418. https://doi.org/10.1074/jbc.M102782200.
41. Samson, M., LaRosa, G., Libert, F., Paindavoine, P., Detheux, M., Vassart, G., and Parmentier, M. (1997). The Second Extracellular Loop of CCR5 Is the Major Determinant of Ligand Specificity. Journal of Biological Chemistry *272*, 24934–24941. https://doi.org/10.1074/jbc.272.40.24934.
42. Govaerts, C., Blanpain, C., Deupi, X., Ballet, S., Ballesteros, J.A., Wodak, S.J., Vassart, G., Pardo, L., and Parmentier, M. (2001). The TXP Motif in the Second Transmembrane Helix of CCR5. Journal of Biological Chemistry *276*, 13217–13225. https://doi.org/10.1074/jbc.M011670200.
43. Blanpain, C., Doranz, B.J., Bondue, A., Govaerts, C., De Leener, A., Vassart, G., Doms, R.W., Proudfoot, A., and Parmentier, M. (2003). The Core Domain of Chemokines Binds CCR5 Extracellular Domains while Their Amino Terminus Interacts with the Transmembrane Helix Bundle. Journal of Biological Chemistry *278*, 5179–5187. https://doi.org/10.1074/jbc.M205684200.
44. Govaerts, C., Bondue, A., Springael, J.-Y., Olivella, M., Deupi, X., Le Poul, E., Wodak, S.J., Parmentier, M., Pardo, L., and Blanpain, C. (2003). Activation of CCR5 by Chemokines Involves an Aromatic Cluster between Transmembrane Helices 2 and 3. Journal of Biological Chemistry *278*, 1892–1903. https://doi.org/10.1074/jbc.M205685200.
45. Scholten, D., Canals, M., Maussang, D., Roumen, L., Smit, M., Wijtmans, M., de Graaf, C., Vischer, H., and Leurs, R. (2012). Pharmacological modulation of chemokine receptor function. Br J Pharmacol *165*, 1617–1643. https://doi.org/10.1111/j.1476-5381.2011.01551.x.
46. Tan, Q., Zhu, Y., Li, J., Chen, Z., Han, G.W., Kufareva, I., Li, T., Ma, L., Fenalti, G., Li, J., et al. (2013). Structure of the CCR5 Chemokine Receptor–HIV Entry Inhibitor Maraviroc Complex. Science (1979) *341*, 1387–1390. https://doi.org/10.1126/science.1241475.
47. Kasprowicz, R.M. (2014). A study of chemokine receptors and the immunological synapse.
48. Alkhatib, G. (2009). The biology of CCR5 and CXCR4. Curr Opin HIV AIDS *4*, 96–103. https://doi.org/10.1097/COH.0b013e328324bbec.
49. Turner, L., Ward, S.G., and Westwick, J. (1995). RANTES-activated human T lymphocytes. A role for phosphoinositide 3-kinase. J Immunol *155*, 2437–2444.
50. Cheung, R., Malik, M., Ravyn, V., Tomkowicz, B., Ptasznik, A., and Collman, R.G. (2009). An arrestin-dependent multi-kinase signaling complex mediates MIP-1β/CCL4

signaling and chemotaxis of primary human macrophages. J Leukoc Biol *86*, 833–845. https://doi.org/10.1189/jlb.0908551.

51. Cicala, C., Arthos, J., Ruiz, M., Vaccarezza, M., Rubbert, A., Riva, A., Wildt, K., Cohen, O., and Fauci, A.S. (1999). Induction of Phosphorylation and Intracellular Association of CC Chemokine Receptor 5 and Focal Adhesion Kinase in Primary Human CD4+ T Cells by Macrophage-Tropic HIV Envelope. The Journal of Immunology *163*, 420–426. https://doi.org/10.4049/jimmunol.163.1.420.
52. Ganju, R.K., Dutt, P., Wu, L., Newman, W., Avraham, H., Avraham, S., and Groopman, J.E. (1998). β-Chemokine Receptor CCR5 Signals Via the Novel Tyrosine Kinase RAFTK. Blood *91*, 791–797. https://doi.org/10.1182/blood.V91.3.791.
53. Bacon, K.B., Schall, T.J., and Dairaghi, D.J. (1998). RANTES Activation of Phospholipase D in Jurkat T Cells: Requirement of GTP-Binding Proteins ARF and RhoA. The Journal of Immunology *160*, 1894–1900. https://doi.org/10.4049/jimmunol.160.4.1894.
54. Wong, M., Uddin, S., Majchrzak, B., Huynh, T., Proudfoot, A.E.I., Platanias, L.C., and Fish, E.N. (2001). RANTES Activates Jak2 and Jak3 to Regulate Engagement of Multiple Signaling Pathways in T Cells. Journal of Biological Chemistry *276*, 11427–11431. https://doi.org/10.1074/jbc.M010750200.
55. Kelly, E., Bailey, C.P., and Henderson, G. (2008). Agonist-selective mechanisms of GPCR desensitization. Br J Pharmacol *153*. https://doi.org/10.1038/sj.bjp.0707604.
56. Borroni, E.M., Mantovani, A., Locati, M., and Bonecchi, R. (2010). Chemokine receptors intracellular trafficking. Pharmacol Ther *127*, 1–8. https://doi.org/10.1016/j.pharmthera.2010.04.006.
57. Hecht, I. (2003). Heterologous desensitization of T cell functions by CCR5 and CXCR4 ligands: inhibition of cellular signaling, adhesion and chemotaxis. Int Immunol *15*, 29–38. https://doi.org/10.1093/intimm/dxg002.
58. Pollok-Kopp, B., Schwarze, K., Baradari, V.K., and Oppermann, M. (2003). Analysis of Ligand-stimulated CC Chemokine Receptor 5 (CCR5) Phosphorylation in Intact Cells Using Phosphosite-specific Antibodies. Journal of Biological Chemistry *278*, 2190–2198. https://doi.org/10.1074/jbc.M209844200.
59. Tausendschön, M., Dehne, N., and Brüne, B. (2011). Hypoxia causes epigenetic gene regulation in macrophages by attenuating Jumonji histone demethylase activity. Cytokine *53*, 256–262. https://doi.org/10.1016/j.cyto.2010.11.002.
60. Signoret, N., Hewlett, L., Wavre, S., Pelchen-Matthews, A., Oppermann, M., and Marsh, M. (2005). Agonist-induced endocytosis of CC chemokine receptor 5 is clathrin dependent. Mol Biol Cell *16*, 902–917. https://doi.org/10.1091/MBC.E04-08-0687.
61. Mueller, A., Kelly, E., and Strange, P.G. (2002). Pathways for internalization and recycling of the chemokine receptor CCR5. Blood *99*, 785–791. https://doi.org/10.1182/BLOOD.V99.3.785.
62. Grove, J., Metcalf, D.J., Knight, A.E., Wavre-Shapton, S.T., Sun, T., Protonotarios, E.D., Griffin, L.D., Lippincott-Schwartz, J., and Marsh, M. (2014). Flat clathrin lattices: stable features of the plasma membrane. Mol Biol Cell *25*, 3581–3594. https://doi.org/10.1091/mbc.e14-06-1154.
63. Signoret, N., Pelchen-Matthews, A., Mack, M., Proudfoot, A.E.I., and Marsh, M. (2000). Endocytosis and Recycling of the HIV Coreceptor Ccr5. Journal of Cell Biology *151*, 1281–1294. https://doi.org/10.1083/jcb.151.6.1281.

64. Delhaye, M., Gravot, A., Ayinde, D., Niedergang, F., Alizon, M., and Brelot, A. (2007). Identification of a Postendocytic Sorting Sequence in CCR5. Mol Pharmacol *72*, 1497–1507. https://doi.org/10.1124/MOL.107.038422.
65. Hammad, M.M., Kuang, Y.Q., Yan, R., Allen, H., and Dupre, D.J. (2010). Na+/H+ Exchanger Regulatory Factor-1 Is Involved in Chemokine Receptor Homodimer CCR5 Internalization and Signal Transduction but Does Not Affect CXCR4 Homodimer or CXCR4-CCR5 Heterodimer. Journal of Biological Chemistry *285*, 34653–34664. https://doi.org/10.1074/JBC.M110.106591.
66. Signoret, N., Christophe, T., Oppermann, M., and Marsh, M. (2004). pH-Independent Endocytic Cycling of the Chemokine Receptor CCR5. Traffic *5*, 529–543. https://doi.org/10.1111/J.1600-0854.2004.00200.X.
67. Escola, J.-M., Kuenzi, G., Gaertner, H., Foti, M., and Hartley, O. (2010). CC Chemokine Receptor 5 (CCR5) Desensitization. Journal of Biological Chemistry *285*, 41772–41780. https://doi.org/10.1074/jbc.M110.153460.
68. Kiss, D., Longden, J., Fechner, G., and Avery, V. (2009). The functional antagonist Met-RANTES: A modified agonist that induces differential CCR5 trafficking. Cell Mol Biol Lett *14*. https://doi.org/10.2478/s11658-009-0017-1.
69. Fox, J.M., Kasprowicz, R., Hartley, O., and Signoret, N. (2015). CCR5 susceptibility to ligand-mediated down-modulation differs between human T lymphocytes and myeloid cells. J Leukoc Biol *98*, 59–71. https://doi.org/10.1189/JLB.2A0414-193RR.
70. Flegler, A.J., Cianci, G.C., and Hope, T.J. (2014). CCR5 Conformations Are Dynamic and Modulated by Localization, Trafficking and G Protein Association. PLoS One *9*, e89056. https://doi.org/10.1371/journal.pone.0089056.
71. Angers, S., Salahpour, A., and Bouvier, M. (2002). Dimerization: An Emerging Concept for G Protein–Coupled Receptor Ontogeny and Function. Annu Rev Pharmacol Toxicol *42*, 409–435. https://doi.org/10.1146/annurev.pharmtox.42.091701.082314.
72. Smith, N.J., and Milligan, G. (2010). Allostery at G Protein-Coupled Receptor Homo- and Heteromers: Uncharted Pharmacological Landscapes. Pharmacol Rev *62*, 701–725. https://doi.org/10.1124/pr.110.002667.
73. Miller, M., and Mayo, K. (2017). Chemokines from a Structural Perspective. Int J Mol Sci *18*, 2088. https://doi.org/10.3390/ijms18102088.
74. Rodríguez-Frade, J.M., Mellado, M., and Martínez-A, C. (2001). Chemokine receptor dimerization: two are better than one. Trends Immunol *22*, 612–617. https://doi.org/10.1016/S1471-4906(01)02036-1.
75. Mellado, M. (2001). Chemokine receptor homo- or heterodimerization activates distinct signaling pathways. EMBO J *20*, 2497–2507. https://doi.org/10.1093/emboj/20.10.2497.
76. Vila-Coro, A.J. (2000). HIV-1 infection through the CCR5 receptor is blocked by receptor dimerization. Proceedings of the National Academy of Sciences *97*, 3388–3393. https://doi.org/10.1073/pnas.050457797.
77. Rodríguez-Frade, J.M., Vila-Coro, A.J., Martín de Ana, A., Albar, J.P., Martínez-A., C., and Mellado, M. (1999). The chemokine monocyte chemoattractant protein-1 induces functional responses through dimerization of its receptor CCR2. Proceedings of the National Academy of Sciences *96*, 3628–3633. https://doi.org/10.1073/pnas.96.7.3628.
78. Benkirane, M., Jin, D.-Y., Chun, R.F., Koup, R.A., and Jeang, K.-T. (1997). Mechanism of Transdominant Inhibition of CCR5-mediated HIV-1 Infection by

ccr5Δ32. Journal of Biological Chemistry *272*, 30603–30606. https://doi.org/10.1074/jbc.272.49.30603.
79. Chelli, M., and Alizon, M. (2002). Rescue of HIV-1 Receptor Function through Cooperation between Different Forms of the CCR5 Chemokine Receptor. Journal of Biological Chemistry *277*, 39388–39396. https://doi.org/10.1074/jbc.M205394200.
80. Charette, N., Holland, P., Frazer, J., Allen, H., and Dupré, D.J. (2011). Dependence on different Rab GTPases for the trafficking of CXCR4 and CCR5 homo or heterodimers between the endoplasmic reticulum and plasma membrane in Jurkat cells. Cell Signal *23*, 1738–1749. https://doi.org/10.1016/j.cellsig.2011.06.008.
81. Nakano, Y., Monde, K., Terasawa, H., Yuan, Y., Yusa, K., Harada, S., and Maeda, Y. (2014). Preferential recognition of monomeric CCR5 expressed in cultured cells by the HIV-1 envelope glycoprotein gp120 for the entry of R5 HIV-1. Virology *452–453*, 117–124. https://doi.org/10.1016/j.virol.2013.12.034.
82. Wong, K.A., and O'Bryan, J.P. (2011). Bimolecular Fluorescence Complementation. Journal of Visualized Experiments. https://doi.org/10.3791/2643.
83. Rose, R.H., Briddon, S.J., and Holliday, N.D. (2010). Bimolecular fluorescence complementation: lighting up seven transmembrane domain receptor signalling networks. Br J Pharmacol *159*, 738–750. https://doi.org/10.1111/j.1476-5381.2009.00480.x.
84. Issafras, H., Angers, S., Bulenger, S., Blanpain, C., Parmentier, M., Labbé-Jullié, C., Bouvier, M., and Marullo, S. (2002). Constitutive Agonist-independent CCR5 Oligomerization and Antibody-mediated Clustering Occurring at Physiological Levels of Receptors. Journal of Biological Chemistry *277*, 34666–34673. https://doi.org/10.1074/jbc.M202386200.
85. Hüttenrauch, F., Pollok-Kopp, B., and Oppermann, M. (2005). G Protein-coupled Receptor Kinases Promote Phosphorylation and β-Arrestin-mediated Internalization of CCR5 Homo- and Hetero-oligomers. Journal of Biological Chemistry *280*, 37503–37515. https://doi.org/10.1074/jbc.M500535200.
86. Springael, J.-Y., Le Minh, P.N., Urizar, E., Costagliola, S., Vassart, G., and Parmentier, M. (2006). Allosteric Modulation of Binding Properties between Units of Chemokine Receptor Homo- and Hetero-Oligomers. Mol Pharmacol *69*, 1652–1661. https://doi.org/10.1124/mol.105.019414.
87. Colin, P., Zhou, Z., Staropoli, I., Garcia-Perez, J., Gasser, R., Armani-Tourret, M., Benureau, Y., Gonzalez, N., Jin, J., Connell, B.J., et al. (2018). CCR5 structural plasticity shapes HIV-1 phenotypic properties. PLoS Pathog *14*, e1007432. https://doi.org/10.1371/JOURNAL.PPAT.1007432.
88. Masopust, D., and Schenkel, J.M. (2013). The integration of T cell migration, differentiation and function. Nat Rev Immunol *13*, 309–320. https://doi.org/10.1038/nri3442.
89. Hickman, H.D., Li, L., Reynoso, G. V., Rubin, E.J., Skon, C.N., Mays, J.W., Gibbs, J., Schwartz, O., Bennink, J.R., and Yewdell, J.W. (2011). Chemokines control naive CD8+ T cell selection of optimal lymph node antigen presenting cells. Journal of Experimental Medicine *208*, 2511–2524. https://doi.org/10.1084/jem.20102545.
90. Contento, R.L., Molon, B., Boularan, C., Pozzan, T., Manes, S., Marullo, S., and Viola, A. (2008). CXCR4–CCR5: A couple modulating T cell functions. Proceedings of the National Academy of Sciences *105*, 10101–10106. https://doi.org/10.1073/pnas.0804286105.

91. Lynch, E.A., Heijens, C.A.W., Horst, N.F., Center, D.M., and Cruikshank, W.W. (2003). Cutting Edge: IL-16/CD4 Preferentially Induces Th1 Cell Migration: Requirement of CCR5. The Journal of Immunology *171*, 4965–4968. https://doi.org/10.4049/jimmunol.171.10.4965.
92. Patterson, S.J., Pesenacker, A.M., Wang, A.Y., Gillies, J., Mojibian, M., Morishita, K., Tan, R., Kieffer, T.J., Verchere, C.B., Panagiotopoulos, C., et al. (2016). T regulatory cell chemokine production mediates pathogenic T cell attraction and suppression. Journal of Clinical Investigation *126*, 1039–1051. https://doi.org/10.1172/JCI83987.
93. Woodward Davis, A.S., Roozen, H.N., Dufort, M.J., DeBerg, H.A., Delaney, M.A., Mair, F., Erickson, J.R., Slichter, C.K., Berkson, J.D., Klock, A.M., et al. (2019). The human tissue-resident CCR5 $^{+}$ T cell compartment maintains protective and functional properties during inflammation. Sci Transl Med *11*. https://doi.org/10.1126/scitranslmed.aaw8718.
94. Sullivan, N.L., Eickhoff, C.S., Zhang, X., Giddings, O.K., Lane, T.E., and Hoft, D.F. (2011). Importance of the CCR5–CCL5 Axis for Mucosal *Trypanosoma cruzi* Protection and B Cell Activation. The Journal of Immunology *187*, 1358–1368. https://doi.org/10.4049/jimmunol.1100033.
95. MANTOVANI, A., SICA, A., SOZZANI, S., ALLAVENA, P., VECCHI, A., and LOCATI, M. (2004). The chemokine system in diverse forms of macrophage activation and polarization. Trends Immunol *25*, 677–686. https://doi.org/10.1016/j.it.2004.09.015.
96. Capucetti, A., Albano, F., and Bonecchi, R. (2020). Multiple Roles for Chemokines in Neutrophil Biology. Front Immunol *11*. https://doi.org/10.3389/fimmu.2020.01259.
97. Olive, A.J., Gondek, D.C., and Starnbach, M.N. (2011). CXCR3 and CCR5 are both required for T cell-mediated protection against C. trachomatis infection in the murine genital mucosa. Mucosal Immunol *4*, 208–216. https://doi.org/10.1038/mi.2010.58.
98. Bonfá, G., Benevides, L., Souza, M. do C., Fonseca, D.M., Mineo, T.W.P., Rossi, M.A., Silva, N.M., Silva, J.S., and de Barros Cardoso, C.R. (2014). CCR5 Controls Immune and Metabolic Functions during Toxoplasma gondii Infection. PLoS One *9*, e104736. https://doi.org/10.1371/journal.pone.0104736.
99. Ferrero, M.R., Tavares, L.P., and Garcia, C.C. (2022). The Dual Role of CCR5 in the Course of Influenza Infection: Exploring Treatment Opportunities. Front Immunol *12*. https://doi.org/10.3389/fimmu.2021.826621.
100. Zeng, Z., Lan, T., Wei, Y., and Wei, X. (2022). CCL5/CCR5 axis in human diseases and related treatments. Genes Dis *9*, 12–27. https://doi.org/10.1016/j.gendis.2021.08.004.
101. Ellwanger, J.H., Kulmann-Leal, B., Kaminski, V. de L., Rodrigues, A.G., Bragatte, M.A. de S., and Chies, J.A.B. (2020). Beyond HIV infection: Neglected and varied impacts of CCR5 and CCR5Δ32 on viral diseases. Virus Res *286*, 198040. https://doi.org/10.1016/j.virusres.2020.198040.
102. Guo, P., Bi, K., Lu, Z., Wang, K., Xu, Y., Wu, H., Cao, Y., and Jiang, H. (2019). CCR5/CCR5 ligand-induced myeloid-derived suppressor cells are related to the progression of endometriosis. Reprod Biomed Online *39*, 704–711. https://doi.org/10.1016/j.rbmo.2019.05.014.
103. Lederman, M.M., Penn-Nicholson, A., Cho, M., and Mosier, D. (2006). Biology of CCR5 and Its Role in HIV Infection and Treatment. JAMA *296*, 815. https://doi.org/10.1001/jama.296.7.815.

104. Brelot, A., and Chakrabarti, L.A. (2018). CCR5 Revisited: How Mechanisms of HIV Entry Govern AIDS Pathogenesis. J Mol Biol *430*, 2557–2589. https://doi.org/10.1016/j.jmb.2018.06.027.
105. Tan, M.C.B., Goedegebuure, P.S., Belt, B.A., Flaherty, B., Sankpal, N., Gillanders, W.E., Eberlein, T.J., Hsieh, C.-S., and Linehan, D.C. (2009). Disruption of CCR5-Dependent Homing of Regulatory T Cells Inhibits Tumor Growth in a Murine Model of Pancreatic Cancer. The Journal of Immunology *182*, 1746–1755. https://doi.org/10.4049/JIMMUNOL.182.3.1746.
106. Aldinucci, D., Borghese, C., and Casagrande, N. (2020). The CCL5/CCR5 Axis in Cancer Progression. Cancers (Basel) *12*, 1765. https://doi.org/10.3390/cancers12071765.
107. Aldinucci, D., and Casagrande, N. (2018). Inhibition of the CCL5/CCR5 Axis against the Progression of Gastric Cancer. International Journal of Molecular Sciences 2018, Vol. 19, Page 1477 *19*, 1477. https://doi.org/10.3390/IJMS19051477.
108. Aldinucci, D., and Colombatti, A. (2014). The inflammatory chemokine CCL5 and cancer progression. Mediators Inflamm *2014*. https://doi.org/10.1155/2014/292376.
109. Aldinucci, D., Borghese, C., and Casagrande, N. (2019). Formation of the Immunosuppressive Microenvironment of Classic Hodgkin Lymphoma and Therapeutic Approaches to Counter It. International Journal of Molecular Sciences 2019, Vol. 20, Page 2416 *20*, 2416. https://doi.org/10.3390/IJMS20102416.
110. Chang, L.Y., Lin, Y.C., Mahalingam, J., Huang, C.T., Chen, T.W., Kang, C.W., Peng, H.M., Chu, Y.Y., Chiang, J.M., Dutta, A., et al. (2012). Tumor-derived chemokine CCL5 enhances TGF-β-mediated killing of CD8 + T cells in colon cancer by T-regulatory cells. Cancer Res *72*, 1092–1102. https://doi.org/10.1158/0008-5472.CAN-11-2493.
111. Upadhyaya, C., Jiao, X., Ashton, A., Patel, K., Kossenkov, A. V., and Pestell, R.G. (2020). The G protein coupled receptor CCR5 in cancer. In, pp. 29–47. https://doi.org/10.1016/bs.acr.2019.11.001.
112. Jiao, X., Nawab, O., Patel, T., Kossenkov, A. V., Halama, N., Jaeger, D., and Pestell, R.G. (2019). Recent advances targeting CCR5 for cancer and its role in immuno-oncology. Cancer Res *79*, 4801–4807. https://doi.org/10.1158/0008-5472.CAN-19-1167.
113. Gao, D., and Fish, E.N. (2018). Chemokines in breast cancer: Regulating metabolism. Cytokine *109*, 57–64. https://doi.org/10.1016/j.cyto.2018.02.010.
114. Ding, H., Zhao, L., Dai, S., Li, L., Wang, F., and Shan, B. (2016). CCL5 secreted by tumor associated macrophages may be a new target in treatment of gastric cancer. Biomedicine & Pharmacotherapy *77*, 142–149. https://doi.org/10.1016/j.biopha.2015.12.004.
115. Murooka, T.T., Rahbar, R., and Fish, E.N. (2009). CCL5 promotes proliferation of MCF-7 cells through mTOR-dependent mRNA translation. Biochem Biophys Res Commun *387*, 381–386. https://doi.org/10.1016/j.bbrc.2009.07.035.
116. Aldinucci, D., Lorenzon, D., Cattaruzza, L., Pinto, A., Gloghini, A., Carbone, A., and Colombatti, A. (2008). Expression of CCR5 receptors on Reed–Sternberg cells and Hodgkin lymphoma cell lines: Involvement of CCL5/Rantes in tumor cell growth and microenvironmental interactions. Int J Cancer *122*, 769–776. https://doi.org/10.1002/ijc.23119.
117. Kato, T., Fujita, Y., Nakane, K., Mizutani, K., Terazawa, R., Ehara, H., Kanimoto, Y., Kojima, T., Nozawa, Y., Deguchi, T., et al. (2013). CCR1/CCL5 interaction promotes

invasion of taxane-resistant PC3 prostate cancer cells by increasing secretion of MMPs 2/9 and by activating ERK and Rac signaling. Cytokine *64*, 251–257. https://doi.org/10.1016/j.cyto.2013.06.313.

118. Ben-Baruch, A. (2012). The Tumor-Promoting Flow of Cells Into, Within and Out of the Tumor Site: Regulation by the Inflammatory Axis of TNFα and Chemokines. Cancer Microenvironment *5*, 151–164. https://doi.org/10.1007/s12307-011-0094-3.
119. Karnoub, A.E., Dash, A.B., Vo, A.P., Sullivan, A., Brooks, M.W., Bell, G.W., Richardson, A.L., Polyak, K., Tubo, R., and Weinberg, R.A. (2007). Mesenchymal stem cells within tumour stroma promote breast cancer metastasis. Nature *449*, 557–563. https://doi.org/10.1038/nature06188.
120. Yi, E.H., Lee, C.S., Lee, J.-K., Lee, Y.J., Shin, M.K., Cho, C.-H., Kang, K.W., Lee, J.W., Han, W., Noh, D.-Y., et al. (2013). STAT3-RANTES Autocrine Signaling Is Essential for Tamoxifen Resistance in Human Breast Cancer Cells. Molecular Cancer Research *11*, 31–42. https://doi.org/10.1158/1541-7786.MCR-12-0217.
121. Xiang, P., Jin, S., Yang, Y., Sheng, J., He, Q., Song, Y., Yu, W., Hu, S., and Jin, J. (2019). Infiltrating CD4+ T cells attenuate chemotherapy sensitivity in prostate cancer via CCL5 signaling. Prostate *79*, 1018–1031. https://doi.org/10.1002/pros.23810.
122. Suffee, N., Hlawaty, H., Meddahi-Pelle, A., Maillard, L., Louedec, L., Haddad, O., Martin, L., Laguillier, C., Richard, B., Oudar, O., et al. (2012). RANTES/CCL5-induced pro-angiogenic effects depend on CCR1, CCR5 and glycosaminoglycans. Angiogenesis *15*, 727–744. https://doi.org/10.1007/s10456-012-9285-x.
123. Velasco-Velázquez, M., Jiao, X., De La Fuente, M., Pestell, T.G., Ertel, A., Lisanti, M.P., and Pestell, R.G. (2012). CCR5 Antagonist Blocks Metastasis of Basal Breast Cancer Cells. Cancer Res *72*, 3839–3850. https://doi.org/10.1158/0008-5472.CAN-11-3917.
124. Casagrande, N., Borghese, C., Visser, L., Mongiat, M., Colombatti, A., and Aldinucci, D. (2019). CCR5 antagonism by maraviroc inhibits Hodgkin lymphoma microenvironment interactions and xenograft growth. Haematologica *104*, 564–575. https://doi.org/10.3324/haematol.2018.196725.
125. Zi, J., Yuan, S., Qiao, J., Zhao, K., Xu, L., Qi, K., Xu, K., and Zeng, L. (2017). Treatment with the C-C chemokine receptor type 5 (CCR5)-inhibitor maraviroc suppresses growth and induces apoptosis of acute lymphoblastic leukemia cells. Am J Cancer Res *7*, 869–880.
126. Jiao, X., Velasco-Velázquez, M.A., Wang, M., Li, Z., Rui, H., Peck, A.R., Korkola, J.E., Chen, X., Xu, S., DuHadaway, J.B., et al. (2018). CCR5 Governs DNA Damage Repair and Breast Cancer Stem Cell Expansion. Cancer Res *78*, 1657–1671. https://doi.org/10.1158/0008-5472.CAN-17-0915.
127. Ledley, F.D., Shonka McCoy, S., Vaughan, G., and Galinka Clearly, E. (2020). Profitability of Large Pharmaceutical Companies Compared With Other Large Public Companies. JAMA *323*, 834–843. https://doi.org/10.1001/jama.2020.0442.
128. Sriram, K., and Insel, P.A. (2018). G Protein-Coupled Receptors as Targets for Approved Drugs: How Many Targets and How Many Drugs? Mol Pharmacol *93*, 251–258. https://doi.org/10.1124/mol.117.111062.
129. Liu, S., Kong, C., Wu, J., Ying, H., and Zhu, H. (2012). Effect of CCR5-Δ32 Heterozygosity on HIV-1 Susceptibility: A Meta-Analysis. PLoS One *7*, e35020. https://doi.org/10.1371/journal.pone.0035020.

130. Lieberman-Blum, S.S., Fung, H.B., and Bandres, J.C. (2008). Maraviroc: A CCR5-receptor antagonist for the treatment of HIV-1 infection. Clin Ther *30*, 1228–1250. https://doi.org/10.1016/S0149-2918(08)80048-3.
131. Garcia-Perez, J., Rueda, P., Alcami, J., Rognan, D., Arenzana-Seisdedos, F., Lagane, B., and Kellenberger, E. (2011). Allosteric Model of Maraviroc Binding to CC Chemokine Receptor 5 (CCR5). Journal of Biological Chemistry *286*, 33409–33421. https://doi.org/10.1074/jbc.M111.279596.
132. Garcia-Perez, J., Rueda, P., Staropoli, I., Kellenberger, E., Alcami, J., Arenzana-Seisdedos, F., and Lagane, B. (2011). New Insights into the Mechanisms whereby Low Molecular Weight CCR5 Ligands Inhibit HIV-1 Infection. Journal of Biological Chemistry *286*, 4978–4990. https://doi.org/10.1074/jbc.M110.168955.
133. Kanmogne, G., and Woollard, S. (2015). Maraviroc: a review of its use in HIV infection and beyond. Drug Des Devel Ther, 5447. https://doi.org/10.2147/DDDT.S90580.
134. Westby, M., Lewis, M., Whitcomb, J., Youle, M., Pozniak, A.L., James, I.T., Jenkins, T.M., Perros, M., and van der Ryst, E. (2006). Emergence of CXCR4-Using Human Immunodeficiency Virus Type 1 (HIV-1) Variants in a Minority of HIV-1-Infected Patients following Treatment with the CCR5 Antagonist Maraviroc Is from a Pretreatment CXCR4-Using Virus Reservoir. J Virol *80*, 4909–4920. https://doi.org/10.1128/JVI.80.10.4909-4920.2006.
135. Hartley, O., Gaertner, H., Wilken, J., Thompson, D., Fish, R., Ramos, A., Pastore, C., Dufour, B., Cerini, F., Melotti, A., et al. (2004). Medicinal chemistry applied to a synthetic protein: Development of highly potent HIV entry inhibitors. Proceedings of the National Academy of Sciences *101*, 16460–16465. https://doi.org/10.1073/pnas.0404802101.
136. KUNA, P., ALAM, R., RUTA, U., and GORSKI, P. (1998). RANTES Induces Nasal Mucosal Inflammation Rich in Eosinophils, Basophils, and Lymphocytes *In Vivo*. Am J Respir Crit Care Med *157*, 873–879. https://doi.org/10.1164/ajrccm.157.3.9610052.
137. Gaertner, H., Lebeau, O., Borlat, I., Cerini, F., Dufour, B., Kuenzi, G., Melotti, A., Fish, R.J., Offord, R., Springael, J.-Y., et al. (2008). Highly potent HIV inhibition: engineering a key anti-HIV structure from PSC-RANTES into MIP-1 /CCL4. Protein Engineering Design and Selection *21*, 65–72. https://doi.org/10.1093/protein/gzm079.
138. Gaertner, H., Cerini, F., Escola, J.-M., Kuenzi, G., Melotti, A., Offord, R., Rossitto-Borlat, I., Nedellec, R., Salkowitz, J., Gorochov, G., et al. (2008). Highly potent, fully recombinant anti-HIV chemokines: Reengineering a low-cost microbicide. Proceedings of the National Academy of Sciences *105*, 17706–17711. https://doi.org/10.1073/pnas.0805098105.
139. Rico, C.A., Berchiche, Y.A., Horioka, M., Peeler, J.C., Lorenzen, E., Tian, H., Kazmi, M.A., Fürstenberg, A., Gaertner, H., Hartley, O., et al. (2019). High-Affinity Binding of Chemokine Analogs that Display Ligand Bias at the HIV-1 Coreceptor CCR5. Biophys J *117*, 903–919. https://doi.org/10.1016/j.bpj.2019.07.043.
140. Choi, W.-T., Nedellec, R., Coetzer, M., Colin, P., Lagane, B., Offord, R.E., Hartley, O., and Mosier, D.E. (2012). CCR5 Mutations Distinguish N-Terminal Modifications of RANTES (CCL5) with Agonist versus Antagonist Activity. J Virol *86*, 10218–10220. https://doi.org/10.1128/JVI.00353-12.
141. Haag, G.M., Halama, N., Springfeld, C., Grün, B., Apostolidis, L., Zschaebitz, S., Dietrich, M., Berger, A.-K., Weber, T.F., Zoernig, I., et al. (2020). Combined PD-1 inhibition (Pembrolizumab) and CCR5 inhibition (Maraviroc) for the treatment of refractory microsatellite stable (MSS) metastatic colorectal cancer (mCRC): First

results of the PICCASSO phase I trial. Journal of Clinical Oncology *38*, 3010–3010. https://doi.org/10.1200/JCO.2020.38.15_SUPPL.3010.
142. Miao, M., De Clercq, E., and Li, G. (2020). Clinical significance of chemokine receptor antagonists. Expert Opin Drug Metab Toxicol *16*, 11–30. https://doi.org/10.1080/17425255.2020.1711884.
143. Noble, C.A., Biesemier, A.P., McClees, S.F., Alhussain, A.M., Helms, S.E., and Brodell, R.T. (2024). The history of the microscope reflects advances in science and medicine. Semin Diagn Pathol. https://doi.org/10.1053/j.semdp.2024.01.002.
144. Rosenthal, C.K. (2009). The beginning. Nat Cell Biol *11*, S6–S6. https://doi.org/10.1038/ncb1938.
145. Rowbury, R. (2012). Robert Hooke, 1635–1703. Sci Prog *95*, 238–254. https://doi.org/10.3184/003685012X13454653990042.
146. Robertson, L.A. (2015). van Leeuwenhoek microscopes—where are they now? FEMS Microbiol Lett *362*. https://doi.org/10.1093/femsle/fnv056.
147. Davis, I.M. (2022). Antoni van Leeuwenhoek: defining proportion in the microscopic realm during the 17th century. FEMS Microbiol Lett *369*. https://doi.org/10.1093/femsle/fnac025.
148. Porter, J.R. (1976). Antony van Leeuwenhoek: tercentenary of his discovery of bacteria. Bacteriol Rev *40*, 260–269. https://doi.org/10.1128/br.40.2.260-269.1976.
149. Kutschera, U. (2023). Antonie van Leeuwenhoek (1632–1723): Master of Fleas and Father of Microbiology. Microorganisms *11*, 1994. https://doi.org/10.3390/microorganisms11081994.
150. Stephens, D.J., and Allan, V.J. (2003). Light Microscopy Techniques for Live Cell Imaging. Science (1979) *300*, 82–86. https://doi.org/10.1126/science.1082160.
151. Thorn, K. (2016). A quick guide to light microscopy in cell biology. Mol Biol Cell *27*, 219–222. https://doi.org/10.1091/mbc.e15-02-0088.
152. Lichtman, J.W., and Conchello, J.-A. (2005). Fluorescence microscopy. Nat Methods *2*, 910–919. https://doi.org/10.1038/nmeth817.
153. Diaspro, A., Chirico, G., Usai, C., Ramoino, P., and Dobrucki, J. (2006). Photobleaching. In Handbook Of Biological Confocal Microscopy (Springer US), pp. 690–702. https://doi.org/10.1007/978-0-387-45524-2_39.
154. Zheng, Q., and Lavis, L.D. (2017). Development of photostable fluorophores for molecular imaging. Curr Opin Chem Biol *39*, 32–38. https://doi.org/10.1016/j.cbpa.2017.04.017.
155. Royer, C.A. Fluorescence Spectroscopy. In Protein Stability and Folding (Humana Press), pp. 65–90. https://doi.org/10.1385/0-89603-301-5:65.
156. Givan, A.L. (2011). Flow Cytometry: An Introduction. In, pp. 1–29. https://doi.org/10.1007/978-1-61737-950-5_1.
157. Adan, A., Alizada, G., Kiraz, Y., Baran, Y., and Nalbant, A. (2017). Flow cytometry: basic principles and applications. Crit Rev Biotechnol *37*, 163–176. https://doi.org/10.3109/07388551.2015.1128876.
158. Zimmer, M. (2002). Green Fluorescent Protein (GFP): Applications, Structure, and Related Photophysical Behavior. Chem Rev *102*, 759–782. https://doi.org/10.1021/cr010142r.
159. Lippincott-Schwartz, J., and Patterson, G.H. (2003). Development and Use of Fluorescent Protein Markers in Living Cells. Science (1979) *300*, 87–91. https://doi.org/10.1126/science.1082520.

160. SHIMOMURA, O. (2005). The discovery of aequorin and green fluorescent protein. J Microsc *217*, 3–15. https://doi.org/10.1111/j.0022-2720.2005.01441.x.
161. Kremers, G.-J., Gilbert, S.G., Cranfill, P.J., Davidson, M.W., and Piston, D.W. (2011). Fluorescent proteins at a glance. J Cell Sci *124*, 157–160. https://doi.org/10.1242/jcs.072744.
162. Ashoka, A.H., Aparin, I.O., Reisch, A., and Klymchenko, A.S. (2023). Brightness of fluorescent organic nanomaterials. Chem Soc Rev *52*, 4525–4548. https://doi.org/10.1039/D2CS00464J.
163. MIZUTA, K., GALLAGHER, S., WANG, A., CHANG, N., MORINAGA, S., SATO, M., KANG, B.M., and HOFFMAN, R.M. (2024). Head-to-head Comparison of Green Fluorescent Protein (GFP) Imaging With Luciferase-luciferin Imaging *In Vivo* Using Single-nanometer Laser-excitation Tuning and an Ultra-low-light-detection Camera and Optics Demonstrates the Superiority of GFP. Anticancer Res *44*, 2823–2826. https://doi.org/10.21873/anticanres.17094.
164. Sample, V., Newman, R.H., and Zhang, J. (2009). The structure and function of fluorescent proteins. Chem Soc Rev *38*, 2852. https://doi.org/10.1039/b913033k.
165. Hoffman, R.M. (2005). Advantages of multi-color fluorescent proteins for whole-body and in vivo cellular imaging. J Biomed Opt *10*, 041202. https://doi.org/10.1117/1.1992485.
166. Blanpain, C., Vanderwinden, J.-M., Cihak, J., Wittamer, V., Le Poul, E., Issafras, H., Stangassinger, M., Vassart, G., Marullo, S., Schlo÷ndorff, D., et al. (2002). Multiple Active States and Oligomerization of CCR5 Revealed by Functional Properties of Monoclonal Antibodies. Mol Biol Cell *13*, 723–737. https://doi.org/10.1091/mbc.01-03-0129.
167. Gómez-Moutón, C., Lacalle, R.A., Mira, E., Jiménez-Baranda, S., Barber, D.F., Carrera, A.C., Martínez-A., C., and Mañes, S. (2004). Dynamic redistribution of raft domains as an organizing platform for signaling during cell chemotaxis. Journal of Cell Biology *164*, 759–768. https://doi.org/10.1083/jcb.200309101.
168. Andersson, Baechi, Hoechl, and Richter (1998). Autofluorescence of living cells. J Microsc *191*, 1–7. https://doi.org/10.1046/j.1365-2818.1998.00347.x.
169. Surre, J., Saint-Ruf, C., Collin, V., Orenga, S., Ramjeet, M., and Matic, I. (2018). Strong increase in the autofluorescence of cells signals struggle for survival. Sci Rep *8*, 12088. https://doi.org/10.1038/s41598-018-30623-2.
170. Heppert, J.K., Dickinson, D.J., Pani, A.M., Higgins, C.D., Steward, A., Ahringer, J., Kuhn, J.R., and Goldstein, B. (2016). Comparative assessment of fluorescent proteins for in vivo imaging in an animal model system. Mol Biol Cell *27*, 3385–3394. https://doi.org/10.1091/mbc.E16-01-0063.
171. Kim, T.K., and Eberwine, J.H. (2010). Mammalian cell transfection: the present and the future. Anal Bioanal Chem *397*, 3173–3178. https://doi.org/10.1007/s00216-010-3821-6.
172. Irfan Maqsood, M., Matin, M.M., Bahrami, A.R., and Ghasroldasht, M.M. (2013). Immortality of cell lines: challenges and advantages of establishment. Cell Biol Int *37*, 1038–1045. https://doi.org/10.1002/cbin.10137.
173. Leake, M.C., and Quinn, S.D. (2023). A guide to small fluorescent probes for single-molecule biophysics. Chemical Physics Reviews *4*. https://doi.org/10.1063/5.0131663.
174. Grimm, J.B., and Lavis, L.D. (2022). Caveat fluorophore: an insiders' guide to small-molecule fluorescent labels. Nat Methods *19*, 149–158. https://doi.org/10.1038/s41592-021-01338-6.

175. Panchuk-Voloshina, N., Haugland, R.P., Bishop-Stewart, J., Bhalgat, M.K., Millard, P.J., Mao, F., Leung, W.-Y., and Haugland, R.P. (1999). Alexa Dyes, a Series of New Fluorescent Dyes that Yield Exceptionally Bright, Photostable Conjugates. Journal of Histochemistry & Cytochemistry *47*, 1179–1188. https://doi.org/10.1177/002215549904700910.
176. Donaldson, J.G. (2015). Immunofluorescence Staining. Curr Protoc Cell Biol *69*. https://doi.org/10.1002/0471143030.cb0403s69.
177. Dreyer, R., Pfukwa, R., Barth, S., Hunter, R., and Klumperman, B. (2023). The Evolution of SNAP-Tag Labels. Biomacromolecules *24*, 517–530. https://doi.org/10.1021/acs.biomac.2c01238.
178. Uckert, W., Pedersen, L., and Günzburg, W. Green Fluorescent Protein Retroviral Vector: Generation of High-Titer Producer Cells and Virus Supernatant. In Gene Therapy of Cancer (Humana Press), pp. 275–285. https://doi.org/10.1385/1-59259-086-1:275.
179. Tomasova, L., Guttenberg, Z., Hoffmann, B., and Merkel, R. (2019). Advanced 2D/3D cell migration assay for faster evaluation of chemotaxis of slow-moving cells. PLoS One *14*, e0219708. https://doi.org/10.1371/journal.pone.0219708.
180. Saimi, D., and Chen, Z. (2023). Chemical tags and beyond: Live-cell protein labeling technologies for modern optical imaging. Smart Molecules *1*. https://doi.org/10.1002/smo.20230002.
181. Adame-Gallegos, J.R., Shi, J., McIntosh, R.S., and Pleass, R.J. (2012). The generation and evaluation of two panels of epitope-matched mouse IgG1, IgG2a, IgG2b and IgG3 antibodies specific for Plasmodium falciparum and Plasmodium yoelii merozoite surface protein 1–19 (MSP119). Exp Parasitol *130*, 384–393. https://doi.org/10.1016/j.exppara.2012.02.003.
182. Melan, M.A. (1994). Overview of Cell Fixation and Permeabilization. In Immunocytochemical Methods and Protocols (Humana Press), pp. 55–66. https://doi.org/10.1385/0-89603285-X:55.
183. Nwaneshiudu, A., Kuschal, C., Sakamoto, F.H., Rox Anderson, R., Schwarzenberger, K., and Young, R.C. (2012). Introduction to Confocal Microscopy. Journal of Investigative Dermatology *132*, 1–5. https://doi.org/10.1038/jid.2012.429.
184. Verdaasdonk, J.S., Stephens, A.D., Haase, J., and Bloom, K. (2014). <scp>B</scp> ending the Rules: Widefield Microscopy and the Abbe Limit of Resolution. J Cell Physiol *229*, 132–138. https://doi.org/10.1002/jcp.24439.
185. Heintzmann, R., and Ficz, G. (2006). Breaking the resolution limit in light microscopy. Brief Funct Genomic Proteomic *5*, 289–301. https://doi.org/10.1093/bfgp/ell036.
186. Möckl, L., Lamb, D.C., and Bräuchle, C. (2014). Super-resolved Fluorescence Microscopy: Nobel Prize in Chemistry 2014 for Eric Betzig, Stefan Hell, and William E. Moerner. Angewandte Chemie International Edition *53*, 13972–13977. https://doi.org/10.1002/anie.201410265.
187. Vangindertael, J., Camacho, R., Sempels, W., Mizuno, H., Dedecker, P., and Janssen, K.P.F. (2018). An introduction to optical super-resolution microscopy for the adventurous biologist. Methods Appl Fluoresc *6*, 022003. https://doi.org/10.1088/2050-6120/aaae0c.
188. Gustafsson, M.G.L. (2000). Surpassing the lateral resolution limit by a factor of two using structured illumination microscopy. J Microsc *198*, 82–87. https://doi.org/10.1046/j.1365-2818.2000.00710.x.

189. Samanta, K., and Joseph, J. (2021). An overview of structured illumination microscopy: recent advances and perspectives. Journal of Optics *23*, 123002. https://doi.org/10.1088/2040-8986/ac3675.
190. Heintzmann, R., and Huser, T. (2017). Super-Resolution Structured Illumination Microscopy. Chem Rev *117*, 13890–13908. https://doi.org/10.1021/acs.chemrev.7b00218.
191. O'Holleran, K., and Shaw, M. (2014). Optimized approaches for optical sectioning and resolution enhancement in 2D structured illumination microscopy. Biomedical Optics Express, Vol. 5, Issue 8, pp. 2580-2590 *5*, 2580–2590. https://doi.org/10.1364/BOE.5.002580.
192. Shaw, M., Zajiczek, L., and O'Holleran, K. (2015). High speed structured illumination microscopy in optically thick samples. Methods *88*, 11–19. https://doi.org/10.1016/J.YMETH.2015.03.020.
193. Chozinski, T.J., Gagnon, L.A., and Vaughan, J.C. (2014). Twinkle, twinkle little star: Photoswitchable fluorophores for super-resolution imaging. FEBS Lett *588*, 3603–3612. https://doi.org/10.1016/j.febslet.2014.06.043.
194. Tam, J., and Merino, D. (2015). Stochastic optical reconstruction microscopy (<scp>STORM</scp>) in comparison with stimulated emission depletion (<scp>STED</scp>) and other imaging methods. J Neurochem *135*, 643–658. https://doi.org/10.1111/jnc.13257.
195. Zlatanova, J., and van Holde, K. (2006). Single-Molecule Biology: What Is It and How Does It Work? Mol Cell *24*, 317–329. https://doi.org/10.1016/j.molcel.2006.10.017.
196. Shashkova, S., and Leake, M.C. (2017). Single-molecule fluorescence microscopy review: shedding new light on old problems. Biosci Rep *37*. https://doi.org/10.1042/BSR20170031.
197. Scalisi, S., Pisignano, D., and Cella Zanacchi, F. (2023). Single-molecule localization microscopy goes quantitative. Microsc Res Tech *86*, 494–504. https://doi.org/10.1002/jemt.24281.
198. Schnitzer, B., Welkenhuysen, N., Leake, M.C., Shashkova, S., and Cvijovic, M. (2022). The effect of stress on biophysical characteristics of misfolded protein aggregates in living Saccharomyces cerevisiae cells. Exp Gerontol *162*, 111755. https://doi.org/10.1016/j.exger.2022.111755.
199. Dresser, L., Hunter, P., Yendybayeva, F., Hargreaves, A.L., Howard, J.A.L., Evans, G.J.O., Leake, M.C., and Quinn, S.D. (2021). Amyloid-β oligomerization monitored by single-molecule stepwise photobleaching. Methods *193*, 80–95. https://doi.org/10.1016/J.YMETH.2020.06.007.
200. Plank, M., Wadhams, G.H., and Leake, M.C. (2009). Millisecond timescale slimfield imaging and automated quantification of single fluorescent protein molecules for use in probing complex biological processes. Integrative Biology *1*, 602. https://doi.org/10.1039/b907837a.
201. Syeda, A.H., Wollman, A.J.M., Hargreaves, A.L., Howard, J.A.L., Brüning, J.-G., McGlynn, P., and Leake, M.C. (2019). Single-molecule live cell imaging of Rep reveals the dynamic interplay between an accessory replicative helicase and the replisome. Nucleic Acids Res *47*, 6287–6298. https://doi.org/10.1093/nar/gkz298.
202. Reyes-Lamothe, R., Sherratt, D.J., and Leake, M.C. (2010). Stoichiometry and Architecture of Active DNA Replication Machinery in *Escherichia coli*. Science (1979) *328*, 498–501. https://doi.org/10.1126/science.1185757.

203. Plank, M., and Leake, M.C. (2010). Fast Millisecond Imaging of Single Fluorescent Protein Molecules Using a Simple “Slimfield” Optical Trick. Biophys J *98*, 588a. https://doi.org/10.1016/j.bpj.2009.12.3197.
204. Wollman, A.J.M., Miller, H., Foster, S., and Leake, M.C. (2016). An automated image analysis framework for segmentation and division plane detection of single live *Staphylococcus aureus* cells which can operate at millisecond sampling time scales using bespoke Slimfield microscopy. Phys Biol *13*, 055002. https://doi.org/10.1088/1478-3975/13/5/055002.
205. Payne-Dwyer, A.L., Jang, G.-J., Dean, C., and Leake, M.C. (2024). SlimVar: rapid *in vivo* single-molecule tracking of chromatin regulators in plants. Preprint, https://doi.org/10.1101/2024.05.17.594710 https://doi.org/10.1101/2024.05.17.594710.
206. Payne-Dwyer, A.L., and Leake, M.C. (2022). Single-Molecular Quantification of Flowering Control Proteins Within Nuclear Condensates in Live Whole Arabidopsis Root. In M.C. (eds) Chromosome Architecture. Methods in Molecular Biology, pp. 311–328. https://doi.org/10.1007/978-1-0716-2221-6_21.
207. Hu, Y.S., Zimmerley, M., Li, Y., Watters, R., and Cang, H. (2014). Single-Molecule Super-Resolution Light-Sheet Microscopy. ChemPhysChem *15*, 577–586. https://doi.org/10.1002/cphc.201300732.
208. Tokunaga, M., Imamoto, N., and Sakata-Sogawa, K. (2008). Highly inclined thin illumination enables clear single-molecule imaging in cells. Nat Methods *5*, 159–161. https://doi.org/10.1038/nmeth1171.
209. Axelrod, D. (2001). Total Internal Reflection Fluorescence Microscopy in Cell Biology. Traffic *2*, 764–774. https://doi.org/10.1034/j.1600-0854.2001.21104.x.
210. Mack, M., Luckow, B., Nelson, P.J., Cihak, J., Simmons, G., Clapham, P.R., Signoret, N., Marsh, M., Stangassinger, M., Borlat, F., et al. (1998). Aminooxypentane-RANTES Induces CCR5 Internalization but Inhibits Recycling: A Novel Inhibitory Mechanism of HIV Infectivity. Journal of Experimental Medicine *187*, 1215–1224. https://doi.org/10.1084/JEM.187.8.1215.
211. Momboisse, F., Nardi, G., Colin, P., Hery, M., Cordeiro, N., Schwartz, O., Sauvonnet, N., Arenzana-Seisdedos, F., Lagane, B., Olivo-Marin, J.-C., et al. Single-molecule imaging reveals distinct effects of ligands on 3 CCR5 dynamics depending on its dimerization status. https://doi.org/10.1101/2021.12.20.473455.
212. Jin, J., Momboisse, F., Boncompain, G., Koensgen, F., Zhou, Z., Cordeiro, N., Arenzana-Seisdedos, F., Perez, F., Lagane, B., Kellenberger, E., et al. (2018). CCR5 adopts three homodimeric conformations that control cell surface delivery. Sci Signal *11*, 2869. https://doi.org/10.1126/SCISIGNAL.AAL2869.
213. Fooksman, D.R., Vardhana, S., Vasiliver-Shamis, G., Liese, J., Blair, D.A., Waite, J., Sacristán, C., Victora, G.D., Zanin-Zhorov, A., and Dustin, M.L. (2010). Functional Anatomy of T Cell Activation and Synapse Formation. Annu Rev Immunol *28*, 79–105. https://doi.org/10.1146/annurev-immunol-030409-101308.
214. Kasprowicz, R., Rand, E., O’Toole, P.J., and Signoret, N. (2018). A correlative and quantitative imaging approach enabling characterization of primary cell-cell communication: Case of human CD4+ T cell-macrophage immunological synapses. Scientific Reports 2018 8:1 *8*, 1–17. https://doi.org/10.1038/s41598-018-26172-3.
215. Gustafsson, M.G.L., Shao, L., Carlton, P.M., Wang, C.J.R., Golubovskaya, I.N., Cande, W.Z., Agard, D.A., and Sedat, J.W. (2008). Three-dimensional resolution

doubling in wide-field fluorescence microscopy by structured illumination. Biophys J *94*, 4957–4970. https://doi.org/10.1529/BIOPHYSJ.107.120345.

216. Pageon, S. V., Nicovich, P.R., Mollazade, M., Tabarin, T., and Gaus, K. (2016). Clus-DoC: a combined cluster detection and colocalization analysis for single-molecule localization microscopy data. Mol Biol Cell *27*, 3627–3636. https://doi.org/10.1091/mbc.e16-07-0478.
217. Kiskowski, M.A., Hancock, J.F., and Kenworthy, A.K. (2009). On the use of Ripley's K-function and its derivatives to analyze domain size. Biophys J *97*, 1095–1103. https://doi.org/10.1016/J.BPJ.2009.05.039.
218. Jin, X., Lee, J.E., Schaefer, C., Luo, X., Wollman, A.J.M., Payne-Dwyer, A.L., Tian, T., Zhang, X., Chen, X., Li, Y., et al. (2021). Membraneless organelles formed by liquid-liquid phase separation increase bacterial fitness. Sci Adv *7*. https://doi.org/10.1126/SCIADV.ABH2929.
219. Lenn, T., and Leake, M.C. (2012). Experimental approaches for addressing fundamental biological questions in living, functioning cells with single molecule precision. Open Biol *2*. https://doi.org/10.1098/RSOB.120090.
220. Delalez, N.J., Wadhams, G.H., Rosser, G., Xue, Q., Brown, M.T., Dobbie, I.M., Berry, R.M., Leake, M.C., and Armitage, J.P. (2010). Signal-dependent turnover of the bacterial flagellar switch protein FliM. Proceedings of the National Academy of Sciences *107*, 11347–11351. https://doi.org/10.1073/pnas.1000284107.
221. Wollman, A.J.M., Hedlund, E.G., Shashkova, S., and Leake, M.C. (2020). Towards mapping the 3D genome through high speed single-molecule tracking of functional transcription factors in single living cells. Methods *170*, 82–89. https://doi.org/10.1016/J.YMETH.2019.06.021.
222. Leake, M.C., Chandler, J.H., Wadhams, G.H., Bai, F., Berry, R.M., and Armitage, J.P. (2006). Stoichiometry and turnover in single, functioning membrane protein complexes. Nature *443*, 355–358. https://doi.org/10.1038/nature05135.
223. Miller, H., Zhou, Z., Wollman, A.J.M., and Leake, M.C. (2015). Superresolution imaging of single DNA molecules using stochastic photoblinking of minor groove and intercalating dyes. Methods *88*, 81–88. https://doi.org/10.1016/j.ymeth.2015.01.010.
224. Payne-Dwyer, A.L., Syeda, A.H., Shepherd, J.W., Frame, L., and Leake, M.C. (2022). RecA and RecB: probing complexes of DNA repair proteins with mitomycin C in live *Escherichia coli* with single-molecule sensitivity. J R Soc Interface *19*. https://doi.org/10.1098/rsif.2022.0437.
225. Wollman, A.J.M., and Leake, M.C. (2015). Millisecond single-molecule localization microscopy combined with convolution analysis and automated image segmentation to determine protein concentrations in complexly structured, functional cells, one cell at a time. Faraday Discuss *184*, 401–424. https://doi.org/10.1039/C5FD00077G.
226. Leake, M.C., Wilson, D., Gautel, M., and Simmons, R.M. (2004). The Elasticity of Single Titin Molecules Using a Two-Bead Optical Tweezers Assay. Biophys J *87*, 1112–1135. https://doi.org/10.1529/biophysj.103.033571.
227. Leake, M.C., Wilson, D., Bullard, B., and Simmons, R.M. (2003). The elasticity of single kettin molecules using a two-bead laser-tweezers assay. FEBS Lett *535*, 55–60. https://doi.org/10.1016/S0014-5793(02)03857-7.
228. Shashkova, S., Andersson, M., Hohmann, S., and Leake, M.C. (2021). Correlating single-molecule characteristics of the yeast aquaglyceroporin Fps1 with environmental perturbations directly in living cells. Methods *193*, 46–53. https://doi.org/10.1016/j.ymeth.2020.05.003.

229. Leake, M.C. (2014). Analytical tools for single-molecule fluorescence imaging in cellulo. Phys. Chem. Chem. Phys. *16*, 12635–12647. https://doi.org/10.1039/C4CP00219A.
230. Wollman, A.J.M., Shashkova, S., Hedlund, E.G., Friemann, R., Hohmann, S., and Leake, M.C. (2017). Transcription factor clusters regulate genes in eukaryotic cells. Elife *6*. https://doi.org/10.7554/ELIFE.27451.
231. Dyer, D.P., Salanga, C.L., Volkman, B.F., Kawamura, T., and Handel, T.M. (2016). The dependence of chemokine-glycosaminoglycan interactions on chemokine oligomerization. Glycobiology *26*, 312–326. https://doi.org/10.1093/glycob/cwv100.
232. Martínez-Muñoz, L., Villares, R., Rodríguez-Fernández, J.L., Rodríguez-Frade, J.M., and Mellado, M. (2018). Remodeling our concept of chemokine receptor function: From monomers to oligomers. J Leukoc Biol *104*, 323–331. https://doi.org/10.1002/JLB.2MR1217-503R.
233. Li, J., Ding, Y., Liu, H., He, H., Yu, D., Wang, X., Wang, X., Yu, X., Ge, B., and Huang, F. (2021). Oligomerization-Enhanced Receptor-Ligand Binding Revealed by Dual-Color Simultaneous Tracking on Living Cell Membranes. Journal of Physical Chemistry Letters *12*, 8164–8169. https://doi.org/10.1021/ACS.JPCLETT.1C01844.
234. Im, D.J., and Jeong, S.-N. (2017). Transfection of Jurkat T cells by droplet electroporation. Biochem Eng J *122*, 133–140. https://doi.org/10.1016/j.bej.2017.03.010.
235. Bloemberg, D., Nguyen, T., MacLean, S., Zafer, A., Gadoury, C., Gurnani, K., Chattopadhyay, A., Ash, J., Lippens, J., Harcus, D., et al. (2020). A High-Throughput Method for Characterizing Novel Chimeric Antigen Receptors in Jurkat Cells. Mol Ther Methods Clin Dev *16*, 238–254. https://doi.org/10.1016/j.omtm.2020.01.012.
236. Momboisse, F., Nardi, G., Colin, P., Hery, M., Cordeiro, N., Blachier, S., Schwartz, O., Arenzana-Seisdedos, F., Sauvonnet, N., Olivo-Marin, J.-C., et al. (2022). Tracking receptor motions at the plasma membrane reveals distinct effects of ligands on CCR5 dynamics depending on its dimerization status. Elife *11*. https://doi.org/10.7554/eLife.76281.
237. Sánchez, M.F., Els-Heindl, S., Beck-Sickinger, A.G., Wieneke, R., and Tampé, R. (2021). Photoinduced receptor confinement drives ligand-independent GPCR signaling. Science (1979) *371*. https://doi.org/10.1126/science.abb7657.
238. Adler, J., Bernhem, K., and Parmryd, I. (2024). Membrane topography and the overestimation of protein clustering in single molecule localisation microscopy – identification and correction. Commun Biol *7*, 791. https://doi.org/10.1038/s42003-024-06472-3.
239. Tilton, J.C., Wilen, C.B., Didigu, C.A., Sinha, R., Harrison, J.E., Agrawal-Gamse, C., Henning, E.A., Bushman, F.D., Martin, J.N., Deeks, S.G., et al. (2010). A Maraviroc-Resistant HIV-1 with Narrow Cross-Resistance to Other CCR5 Antagonists Depends on both N-Terminal and Extracellular Loop Domains of Drug-Bound CCR5. J Virol *84*, 10863–10876. https://doi.org/10.1128/JVI.01109-10.
240. Arberas, H., Guardo, A.C., Bargallo, M.E., Maleno, M.J., Calvo, M., Blanco, J.L., Garcia, F., Gatell, J.M., and Plana, M. (2013). In vitro effects of the CCR5 inhibitor maraviroc on human T cell function. Journal of Antimicrobial Chemotherapy *68*, 577–586. https://doi.org/10.1093/jac/dks432.
241. Secchi, M., and Vangelista, L. (2022). Rational Engineering of a Sub-Picomolar HIV-1 Blocker. Viruses *14*, 2415. https://doi.org/10.3390/v14112415.

242. Bosch, P.J., Corrêa, I.R., Sonntag, M.H., Ibach, J., Brunsveld, L., Kanger, J.S., and Subramaniam, V. (2014). Evaluation of Fluorophores to Label SNAP-Tag Fused Proteins for Multicolor Single-Molecule Tracking Microscopy in Live Cells. Biophys J *107*, 803–814. https://doi.org/10.1016/j.bpj.2014.06.040.
243. Jatzlau, J., Burdzinski, W., Trumpp, M., Obendorf, L., Roßmann, K., Ravn, K., Hyvönen, M., Bottanelli, F., Broichhagen, J., and Knaus, P. (2023). A versatile Halo- and SNAP-tagged BMP/TGFβ receptor library for quantification of cell surface ligand binding. Commun Biol *6*, 34. https://doi.org/10.1038/s42003-022-04388-4.
244. Siddig, S., Aufmkolk, S., Doose, S., Jobin, M.-L., Werner, C., Sauer, M., and Calebiro, D. (2020). Super-resolution imaging reveals the nanoscale organization of metabotropic glutamate receptors at presynaptic active zones. Sci Adv *6*. https://doi.org/10.1126/sciadv.aay7193.
245. Calebiro, D., Rieken, F., Wagner, J., Sungkaworn, T., Zabel, U., Borzi, A., Cocucci, E., Zürn, A., and Lohse, M.J. (2013). Single-molecule analysis of fluorescently labeled G-protein–coupled receptors reveals complexes with distinct dynamics and organization. Proceedings of the National Academy of Sciences *110*, 743–748. https://doi.org/10.1073/pnas.1205798110.
246. Basu, S., Campbell, H.M., Dittel, B.N., and Ray, A. (2010). Purification of Specific Cell Population by Fluorescence Activated Cell Sorting (FACS). Journal of Visualized Experiments. https://doi.org/10.3791/1546.
247. Skuhersky, M., Tao, F., Qing, R., Smorodina, E., Jin, D., and Zhang, S. (2021). Comparing Native Crystal Structures and AlphaFold2 Predicted Water-Soluble G Protein-Coupled Receptor QTY Variants. Life *11*, 1285. https://doi.org/10.3390/life11121285.
248. Abramson, J., Adler, J., Dunger, J., Evans, R., Green, T., Pritzel, A., Ronneberger, O., Willmore, L., Ballard, A.J., Bambrick, J., et al. (2024). Accurate structure prediction of biomolecular interactions with AlphaFold 3. Nature *630*, 493–500. https://doi.org/10.1038/s41586-024-07487-w.
249. Valitutti, S., Müller, S., Cella, M., Padovan, E., and Lanzavecchia, A. (1995). Serial triggering of many T-cell receptors by a few peptide–MHC complexes. Nature *375*, 148–151. https://doi.org/10.1038/375148a0.
250. Frauwirth, K.A., and Thompson, C.B. (2002). Activation and inhibition of lymphocytes by costimulation. Journal of Clinical Investigation *109*, 295–299. https://doi.org/10.1172/JCI14941.
251. Trickett, A., and Kwan, Y.L. (2003). T cell stimulation and expansion using anti-CD3/CD28 beads. J Immunol Methods *275*, 251–255. https://doi.org/10.1016/S0022-1759(03)00010-3.
252. Chen, B.-C., Legant, W.R., Wang, K., Shao, L., Milkie, D.E., Davidson, M.W., Janetopoulos, C., Wu, X.S., Hammer, J.A., Liu, Z., et al. (2014). Lattice light-sheet microscopy: Imaging molecules to embryos at high spatiotemporal resolution. Science (1979) *346*. https://doi.org/10.1126/science.1257998.
253. Aldinucci, D., Borghese, C., and Casagrande, N. (2020). The ccl5/ccr5 axis in cancer progression. Preprint at MDPI AG, https://doi.org/10.3390/cancers12071765 https://doi.org/10.3390/cancers12071765.